
Using MTP measurements to characterise atmospheric gravity waves in the tropopause region

Mareike Kenntner



Dissertation
an der Fakultät für Physik
der Ludwig-Maximilians-Universität
München

vorgelegt von
Mareike Kenntner
aus Bonn

München, den 03. November 2017

Erstgutachter: Prof. Dr. Markus Rapp

Zweitgutachter: Prof. Dr. Bernhard Mayer

Tag der mündlichen Prüfung: 29. Januar 2018

Zusammenfassung

Atmosphärische Schwerewellen, die nahe am Erdboden angeregt werden, können weit in die Atmosphäre propagieren. Wenn sie brechen, übertragen sie ihre Energie und ihren Impuls an die Hintergrundströmung und treiben damit die globale Zirkulation der mittleren Atmosphäre. Um das Verständnis über die Entstehung und Ausbreitung von Schwerewellen durch die Atmosphäre weiter zu vergrößern, werden u.a. Messkampagnen mit Forschungsflugzeugen durchgeführt, bei denen besonders die Tropopausen-Region im Fokus steht. Diese ist als Barriere für die Ausbreitung von Schwerewellen in größere Höhen bekannt. Mit Hilfe eines passiven Mikrowellenradiometers, dem Microwave Temperature Profiler (MTP), können vom Flugzeug aus Temperaturmessungen sowohl ober- als auch unterhalb der aktuellen Flughöhe gemacht werden. Da atmosphärische Schwerewellen Temperaturschwankungen hervorrufen, bieten die Messungen des MTP eine gute Möglichkeit Schwerewellen direkt messen und charakterisieren zu können.

In der folgenden Arbeit wird untersucht, welche Temperaturfluktuationen vom MTP erfasst werden können und wie gut die Eigenschaften von Schwerewellen, wie ihre horizontale und vertikale Wellenzahl und die intrinsische Frequenz, aus den Temperaturdaten des MTP abgeleitet werden können. Hierzu wird eine Kalibrationsmessung im Labor ausgewertet, um die Detektionsgrenze für Temperaturstörungen festlegen zu können. Des Weiteren wird mit Hilfe von Strahlungstransportsimulationen bestimmt, über welchen Bereich der Atmosphäre Informationen in den MTP-Daten enthalten sind. Es wird gezeigt, dass das MTP atmosphärische Temperaturen mit einer Präzision von 0.37 K messen kann, und eine Analyse von Welleneigenschaften für Temperaturfluktuationen von mindestens 1.5 K Amplitude möglich ist. Das MTP kann über einen Bereich von 2-3 km um die Flughöhe Informationen über die potentielle Temperatur, die Stabilität der Schichtung der Luftmassen, sowie dort auftretende Wellen sammeln.

Um Schwerewellen charakterisieren zu können, wurde ein neuer Algorithmus zur Auswertung der aus den MTP-Daten abgeleiteten Temperaturprofilen entwickelt. In dieser Arbeit wird der Algorithmus vorgestellt und seine Kapazitäten in der Erkennung von Welleneigenschaften in MTP-Daten in einer Studie mit synthetischen Daten getestet. Es wird gezeigt, dass die vertikale Wellenlänge und intrinsische Frequenz mit einer Unsicherheit von maximal 30 % bestimmt werden können. Mit Hilfe von MTP-Daten ist es damit möglich, die Bedingungen für Wellen-Ausbreitung innerhalb der Tropopausen-Region zu bewerten. Schließlich wird der neue Algorithmus benutzt, um Messdaten der DEEPWAVE-Kampagne, die 2014 in Neuseeland stattfand, auszuwerten. Hier zeigt die Auswertung der MTP-Daten, dass auf Flug-Niveau gemessene Impulsflüsse nicht immer bis zur Stratosphäre gelangen. Die Messungen des MTP bieten einen einzigartigen und wichtigen Einblick in die vorherrschenden Bedingungen für Wellenausbreitung durch die Tropopausenregion.

Abstract

Atmospheric gravity waves, which have sources close to the Earth's surface, can propagate deep into the atmosphere. When these waves break, the energy and momentum they carry is transferred to the background wind. Thus, they drive the global circulation within the middle atmosphere. As one approach to enhance the understanding of the source processes and the propagation of gravity waves through the atmosphere, measurement campaigns with research aircraft have been conducted, which focus on the troposphere region. This region is known to be a barrier for propagation of gravity waves into higher altitudes. With the help of a passive microwave radiometer, the Microwave Temperature Profiler (MTP), measurements of temperature, both, above and below the aircraft can be conducted. As atmospheric gravity waves cause temperature fluctuations, the MTP provides the possibility to directly measure and characterise gravity waves.

In the following thesis it will be assessed, which temperature fluctuation signals can be resolved by the MTP instrument and how well characteristics of gravity waves, such as their horizontal and vertical wavenumbers and the intrinsic frequency, can be derived. Calibration measurements in a laboratory will be analysed to define the lower threshold of detectable temperature fluctuation amplitudes. Moreover, radiative transfer calculations will be carried out to investigate which part of the atmosphere the MTP measurements are sensitive to. It will be shown that the MTP is able to measure atmospheric temperatures with a precision of 0.37 K, and that an analysis of wave characteristics is possible from temperature fluctuations with amplitudes of at least 1.5 K. The MTP is sensitive to a vertical altitude region of 2-3 km around the research aircraft, and is able to collect information on the potential temperatures and static stability of the air masses surrounding the aircraft, as well as on gravity waves within this region.

To characterise the gravity waves, a new algorithm for further analysis of the temperature profiles derived from MTP measurements has been developed. This algorithm will be described within this thesis and its capabilities of detecting wave characteristics will be tested in a synthetic data study. It will be shown, that the vertical wavelengths and intrinsic frequencies can be derived with a maximum uncertainty of 30 %. Hence, through the use of MTP data, it is possible to assess propagation conditions for gravity waves within the tropopause region. Finally, the algorithm will be used to evaluate measurements from the DEEPWAVE campaign, which took place in New Zealand in 2014. For these data, the analysis shows that momentum fluxes derived from flight-level measurements, do not always reach the stratosphere. The measurements by the MTP instrument provide a unique and important insight to the prevailing conditions of wave propagation through the tropopause region.

Contents

1	Introduction	1
2	Properties of atmospheric gravity waves	5
2.1	Sources, scales and interaction with the atmosphere	5
2.2	Atmospheric gravity wave characteristics in linear theory	7
3	Experimental approach to measuring gravity waves: MTP	13
3.1	Radiometry	14
3.2	The Microwave Temperature Profiler: Instrument description	18
3.3	DLR-MTP campaign deployments	21
3.3.1	ML CIRRUS 2014	21
3.3.2	ACRIDICON 2014	21
3.4	MTP data products	22
3.4.1	Previous studies involving MTP data products	23
3.4.2	New approach to MTP data usage	25
4	Temperature profile retrieval	27
4.1	Raw Data preparation for Retrieval	27
4.2	Brightness temperature calculations	28
4.2.1	Instrument characteristics	29
4.2.2	Description of calibration methods and MTP calibration parameters	34
4.2.3	Error estimation	44
4.2.4	Discussion	48
4.3	Retrieval performances	49
4.3.1	Performance of JPL retrieval	52
4.3.2	Performance of the TIRAMISU algorithm	56
4.4	MTP range of sensitivity	57
5	Altitude-resolved characterisation of waves	66
5.1	Wave characterisation using aircraft mission data	66
5.1.1	Wave characterisation from MTP data	67
5.1.2	Aircraft measurement system data	72
5.1.3	Comparison of methods	74

5.2	Sensitivity study: Analysis of simulated data	76
5.2.1	Analysis of synthetic temperature data	77
5.2.2	Analysis of processed temperature fields	80
5.3	Case study: DEEPWAVE campaign data	87
5.3.1	The DEEPWAVE campaign 2014	88
5.3.2	RF16 - July 4 th , 2014	90
5.3.3	RF12 - June 29 th , 2014	98
5.4	Discussion	104
6	Summary	106
A	Appendix	111
A.1	Retrieval methods	111
A.1.1	Statistical retrieval	111
A.1.2	Inversion of the forward problem	114
A.2	Wavelet analysis	118
A.3	DEEPWAVE model runs	122

1 Introduction

There are numerous types of atmospheric waves affecting our climate and weather in different ways. The scales of these waves range from centimetres in wavelength (e.g. turbulence) to several thousands of kilometres (e.g. tidal waves), and their periods can last seconds to days (e.g. Nappo, 2013; Fritts and Alexander, 2003). While all of these waves have effects on our weather or even the Earth's climate (e.g. U. Schumann (ed.), 2012), the focus of this thesis lies on gravity waves (GWs), which are oscillations of air parcels, with the buoyancy force as the restoring force. See Fritts and Alexander (2003); Alexander et al. (2010); Plougonven and Zhang (2014), or Durran (2015) for comprehensive reviews of the current state of knowledge concerning GW sources and their interaction with the atmosphere.

In atmospheric sciences, GWs have been recognised to have impact on “transporting energy and momentum, in contributing turbulence and mixing, and in influencing the mean circulation and thermal structure of the middle atmosphere” (Fritts and Alexander, 2003). GWs, which are created within the troposphere or lower stratosphere, are able to propagate to higher altitudes of the atmosphere and interact with the mean flow at altitudes as high up as 80 km or higher (e.g. Holton, 1982, 1983; Nappo, 2013). The decreasing pressure of the atmosphere with altitude causes the amplitudes of the GWs to increase, following the law of energy conservation (Nappo, 2013). Ultimately, the waves break, depositing their energy and momentum at the altitude where the breaking occurs. The horizontal momentum carried by the wave is added to the mean flow, when the wave breaks, while the energy is contributing to the heating of the air masses in which the wave breaking occurs (e.g. Holton, 1982, 1983; Fritts and Alexander, 2003; Nappo, 2013). This has been found to be the explanation of the quasi-biennial oscillation (QBO) - a periodic change of mean flow direction in the tropical stratosphere (e.g. Baldwin et al., 2001; Ern et al., 2014). GWs have also been identified to drive the global circulation in the middle atmosphere (e.g. Dunkerton, 1978; Butchart, 2014), causing the cold summer mesopause and warm winter stratopause (Lindzen, 1981; Siskind, 2014), which distinctly differ from the radiative equilibrium state (Holton, 1982, 1983).

Also, circumstances that allow the waves to travel to the middle atmosphere (or prevent that) have not been fully understood and are a focus of ongoing research (e.g. Kruse and Smith, 2015; Kruse et al., 2016; Bramberger et al., 2017), resulting in a continuous call for observations of GWs to improve the understanding of the GW life cycle, and their representation in climate models (e.g. Fritts and Alexander, 2003; Sato et al., 2009; Geller et al., 2013). Ongoing research is performed evaluating model studies as well as observational data to assess the life cycle of GWs.

A linear theory, describing the characteristics of GWs, has been developed (described in e.g. Fritts and Alexander, 2003; Nappo, 2013), and its validity as a description of mountain waves has been shown for a number of cases (e.g. Smith et al., 2008, 2016).

Some research campaigns, dedicated to the investigation of GWs, have been conducted, such as the Gravity Wave Life Cycle I (GW LCYCLE I) campaign in 2013 (e.g. Wagner et al., 2017), or the Deep Propagating Gravity Wave Experiment (DEEPWAVE) campaign in 2014 (Fritts et al., 2016). Within these missions, research aircraft are equipped with a variety of in situ and remote sensing instruments, tracking wave signals on their way through the atmosphere, from the source region close to the ground, up to the mesosphere, often in combination with ground-based measurements. One of these instruments, deployed within the DEEPWAVE campaign in 2014 is the Microwave Temperature Profiler (MTP) (Denning et al., 1989; Mahoney and Denning, 2009). This is a passive radiometer, monitoring the air temperature of air masses both above and below the flight level of the research aircraft it is mounted on.

The first MTP was built in the late 1970s, with the goal of detecting clear air turbulence (CAT) at flight level (Denning et al., 1989; Gary, 1989). The data products were soon used to interpret the meteorological situation on research flights investigating the Antarctic ozone hole, leading to the deployment of MTP instruments as a ‘standard’ instrumentation on many research campaigns. The capability of the instrument to provide valuable information on the background state of the atmosphere during research flights has long been acknowledged within the atmospheric research community (Lim et al., 2013; Haggerty et al., 2014). Recently, the German Aerospace Center, [Deutsches Zentrum für Luft- und Raumfahrt e.V.] (DLR) has purchased an MTP, after recognising the potential of tracking down wave signals in the temperature data. Including the DLR-MTP deployments on the High Altitude and Long Range Research Aircraft (HALO) in 2014, MTP instruments have participated in over 60 scientific campaigns conducted with eight different aircraft, including the National Center for Atmospheric Research (NCAR)’s aircraft NCAR Gulfstream-V (NCAR GV), and the Global Hawk of the National Aeronautics and Space Administration (NASA) (Lim et al., 2013).

The full capabilities of the MTP instrument concerning the characterisation of GWs within a recording of two-dimensional temperature data has not yet been investigated. This will be the main focus of this thesis; answering the question:

What contribution does the MTP make to the characterisation of gravity waves around the tropopause?

This thesis presents the results of an assessment of the capabilities of the MTP, based on answering the following sub-questions:

Question 1: What is the precision of the MTP temperature measurements?

This question will be answered through the evaluation of data from calibration measurements in the laboratory. Changing instrument conditions, as experienced during research flights, are simulated in a cold chamber and their influence on the calibration and data quality are assessed.

The standard retrieval algorithm, used to process MTP data so far, is based on a statistical approach. This method does not rely on exact radiative transfer (RT) calculations with well-calibrated input of brightness temperatures (BTs). As a result, an in-depth assessment of the calibration process has not yet been published.

It is the first time that such a thorough calibration of the MTP instrument is performed, and an error estimation of derived BTs is made. From this error estimation a lower threshold of detectable temperature changes in a time series of data, such as temperature perturbations caused by GWs, can be derived.

Question 2: Which altitude region around the flight level of the research aircraft is the MTP sensitive to?

To find the answer, RT calculations are used to determine the origin of the temperature signals reaching the instrument. Again, the statistical approach within the standard retrieval algorithm, used so far, has not made a thorough investigation of RT necessary. The evaluation of weighting functions presented within this thesis is the first assessment of range of sensitivity of the MTP instrument using RT calculations.

As the focus of the evaluation of MTP data within this thesis lies on the characterisation of GWs, the data analysis is a second focus of this study. Earlier studies using MTP data sets to characterise GWs have always made use of meteorological data recorded by the aircraft measurement system. Within this thesis a new algorithm solely based on MTP data is developed, focussing on extracting wave signals from the two-dimensional temperature data provided by the MTP, and deriving the wave properties from these signals. The idea of the algorithm is to extract the phase line orientation (PLO) of the wave, from which the vertical wave number and the intrinsic frequency of the detected wave packet can be derived. So naturally a third question must be answered:

Question 3: How well can various wave characteristics, such as the vertical wave length or the intrinsic frequency, be derived from existing MTP data?

A study using synthetic temperature data and RT calculations to simulate MTP measurements is used to determine whether the PLO of a wave can be correctly determined, using the newly developed algorithm. Through this study, detection limits as well as uncertainty estimations for the derived wave properties are obtained.

Finally, a set of observation data from research flights of the DEEPWAVE campaign in 2014 is analysed using the new algorithm. The evaluation of this data set is compared to already published results from flight level data evaluation, as well as to results of studies combining a larger number of observations from other instruments and models.

It will be shown that the MTP provides data that supports the understanding of GW activity around flight level of the research aircraft. Through MTP data analysis insight can be gained to atmospheric conditions responsible for wave reflection, refraction, and ducting in the vicinity of the research aircraft's flight level.

In the following, within Chapter 2, an overview of sources and typical scales of GWs is given, along with a description of their propagation through and interaction with the atmosphere. Also, the linear theory of waves is briefly explained in this chapter, followed by the introduction of the measurement principle in Chapter 3. Here, earlier results from the evaluation of MTP data are summarised, and the idea of the new algorithm to analyse MTP data is introduced. Various approaches to the calibration of the instrument as well as the RT calculation, leading to the answers of questions 1 and 2 above are given in Chapter 4. This is followed by a description of the new analysis algorithm as well as of the established method of deriving wave properties from flight level measurements in Chapter 5. Within this chapter, the new algorithm is tested, using synthetic data. In the final section of Chapter 5 the results of analysing MTP data, using the new algorithm, are shown in comparison to the results of model studies and flight level data analysis. The thesis is concluded by a short summary of the answers to the questions stated above.

2 Properties of atmospheric gravity waves

As mentioned in the introduction, GWs have large impact on the Earth's climate and have thus been in the focus of atmospheric research for many years. The first section of this chapter will give a brief overview of the most common sources of GWs, their resulting scales, and their interaction with the atmosphere.

While to this day there is no full mathematical description of GWs and their interaction with the atmosphere that can be solved analytically, a linear theory exists, which describes the main characteristics of atmospheric waves in simple environments. This theory can be applied to analyse measurements of GWs in many real cases. The main features of this theory are explained in Section 2.2 of this chapter. Even though this theory is excluding nonlinear interactions with the atmosphere or between different wave packets, it still allows to derive wave characteristics, such as the frequency, phase and group velocities, or even energy and momentum fluxes from some measurable parameters. The equations that link all properties of GWs, and hence enable a full characterisation of GWs from measurement data, are presented in Section 2.2.

2.1 Sources, scales and interaction with the atmosphere

In the introduction to his book, Nappo (2013) summarises that waves within the atmosphere are always present, and range over a variety of scales and periods, moving in all different directions. Wave periods range from minutes to hours, their amplitudes can stretch between just above or below the detection limit to very large.

Fritts and Alexander (2003) give an overview of dominant GW sources, and the scales of the resulting waves. They list topography, convection, and wind shear as the most common sources of GW, but acknowledge that in the vicinity of specific local sites, or within larger-scale dynamics, other sources may also play significant roles. In close proximity to jet systems or fronts wave-wave interaction, wave dissipation, or adjustment of unbalanced flows, can also lead to the creation of GWs (Fritts and Alexander, 2003).

Mountain waves, created by flow over lifted topography are well-understood, as there have been many observations (e.g. Hoffmann et al., 2013, 2016), model studies (e.g. Dörnbrack et al., 2002; Wagner et al., 2017) and dedicated field campaigns (e.g. Fritts et al., 2016) to study orographic waves.

Horizontal wavelengths of orographic waves span between ten and hundreds of kilometres (Fritts and Alexander, 2003), and the temperature differences are known to cause formation of polar stratospheric clouds (PSC) (Dörnbrack et al., 2002). Those mountain waves, carrying momentum fluxes to the middle atmosphere, are identified to have horizontal scales of 10 – 100 km (Fritts and Alexander, 2003).

While orographic GWs are often dominated by very few frequencies, Fritts and Alexander (2003) summarise the findings on convective GWs differently: Here the whole spectrum of frequencies is created through convection, and those waves are able to travel large distances, making it hard to link them to their convective sources. The wave creation mechanism is a complicated interaction of thermal forcing, wind shear, and convection acting as a barrier to mean flow.

The third main source of GWs is known to be within the vicinity of jet and front systems (e.g. Fritts and Alexander, 2003; Plougonven and Zhang, 2014). Here, a number of mechanisms is thought to be creating GWs, which mostly contribute to the mean flow adjusting towards a balanced state. Diversions from the balanced state can be due to sheared flow, convective heating or absorption of other GWs (Plougonven and Zhang, 2014).

GWs can propagate both vertically and horizontally through the atmosphere (e.g. Sato et al., 2009; Ehard et al., 2017). The vertical propagation of GWs through the atmosphere is influenced by the stability profile, as well as vertical wind gradients and gradients of static stability (e.g. Fritts and Alexander, 2003; Birner, 2006; Nappo, 2013; Kruse et al., 2016). Temporal changes in horizontal wind can lead to a change of the wave phase speed, while horizontal wind and thermal gradients can induce reflection or refraction of waves (Fritts and Alexander, 2003). The tropopause as well as a tropopause inversion layer (TIL), which is a layer of enhanced stability just above the tropopause, can be such reflection levels, as these are layers of changing stability with height (Birner, 2006). Still, even simple temperature gradients can form a wave duct (Nappo, 2013). The condition for the reflection of a wave is that the observed frequency of the wave $\omega = k \cdot c_{\text{ph},x}$ with horizontal wavenumber k and horizontal phase speed $c_{\text{ph},x}$, is zero. Various layers with such conditions can lead to wave trapping or ducting, confining the wave to a small altitude region of the atmosphere. If the waves between two reflecting levels interfere positively, they are called ducted waves. The reflecting levels act as a wave guide (Nappo, 2013), allowing the ducted wave to travel large horizontal distances. Ducted waves are frequently found within the vicinity of frontal systems (Plougonven and Zhang, 2014). The possibility of ducting is largest for small horizontal wavelengths ($\lambda_{\text{hor}} \sim 20$ km), and decreases with increasing horizontal scales (Swenson et al., 2000; Fritts and Alexander, 2003). According to Fritts and Alexander (2003), ducted waves “have intrinsic frequencies near N , may have only a gradual decay of wave amplitude away from the duct, and have little or no associated momentum flux”.

Two main mechanisms lead to the breaking of GWs, stopping their propagation: As the wave travels towards higher altitudes, and lower pressures, energy conservation leads to increased amplitudes of the wind and temperature perturbations. This can finally lead to instabilities, causing the wave to overturn and break (Kaifler et al., 2015).

The second cause for wave breaking is the interaction with the background flow. From linear theory (see next section), it can be derived that, whenever the mean background flow has the same magnitude as the horizontal phase speed of the wave, but opposite direction, the wave breaks (Nappo, 2013). Thus, the vertical wind profile acts as a filter of the upward propagating waves, which, for example, is the explanation of the QBO (Baldwin et al., 2001; Ern et al., 2014; Kruse et al., 2016).

In their review, Fritts and Alexander (2003) discuss spectra and typical scales of propagating GWs: While the horizontal scales of all GWs differ greatly over a span of tens of kilometres to over 1000 km, the frequency, as well as the horizontal scale spectrum often follows a $-5/3$ -law, from which the scale spectrum often diverges at large scales, due to dynamical effects. Intrinsic frequencies Ω are limited to $f < \Omega < N$, with f denoting the Coriolis parameter, and N representing the Brunt-Väisälä frequency. The various creation mechanisms lead to GWs with low phase speeds typical for orographic waves, and considerably higher phase speeds of GWs originating from other sources (Plougonven and Zhang, 2014).

According to Fritts and Alexander (2003), vertical wavelengths of energy-carrying waves are found to have scales of 2 – 5 km in the lower stratosphere, increasing to 10 – 30 km towards the mesosphere. For a single observed wave field, Fritts and Alexander (2003) discuss evidence that only few scales contribute to the observed temperature and wind velocity variations, rather than a broad spectrum of scales. However, they also conclude that discussion on this question is still ongoing.

2.2 Atmospheric gravity wave characteristics in linear theory

The linear theory, describing atmospheric gravity waves, and the derivation of its main formula, the Taylor-Goldstein-equation is well known, and described in numerous scientific books and articles (e.g Holton et al., 1995; Fritts and Alexander, 2003; Nappo, 2013). Here, only the relevant equations concerning the analysis of MTP data will be presented.

The Taylor-Goldstein-equation describes the wave through the perturbation of the vertical wind w' , which is defined as $w' = \tilde{w} \exp(-i(kx - \omega t))$, using the horizontal wavenumber k and the observed frequency of the wave ω .

The final derived equation describing the wave is:

$$\frac{d^2 \hat{w}}{dz^2} + \left[\frac{k^2 N^2}{\Omega^2} + \frac{k}{\Omega} \frac{d^2 u_0}{dz^2} - k^2 - \frac{k}{\Omega H_S} \frac{du_0}{dz} - \frac{1}{4H_S^2} \right] \hat{w} = 0 \quad (2.1)$$

using the static stability $N^2 = -\frac{g}{\rho_0} \frac{d\rho_0}{dz} = \frac{g}{\theta_0} \frac{d\theta_0}{dz}$, derived from the background state, the intrinsic frequency of the wave Ω , which is related to the observed frequency ω via the background wind u_0 as $\Omega = \omega - u_0 k$, and the scale height H_S .

This is the differential equation of a harmonic oscillator $\hat{w} = Ae^{imz} + Be^{-imz}$ with the vertical wavenumber m equalling the expression within the brackets in Eq. (2.1). To derive the equation, the ansatz

$$\tilde{w} = \hat{w} \cdot \exp(z/2H_S) \quad (2.2)$$

has been used, which already implies, that the wave \tilde{w} has a growing amplitude with altitude z due to the decreasing pressure.

Still, more can be learned from Eq. (2.1), which is the mathematical expression defining the vertical wavenumber m :

$$m = \pm \left[\frac{N^2}{(c_{\text{ph},x} - u_0)^2} + \frac{u_0''}{(c_{\text{ph},x} - u_0)} - \frac{1}{H_S} \frac{u_0'}{(c_{\text{ph},x} - u_0)} - \frac{1}{4H_S^2} \right]^{\frac{1}{2}} \quad (2.3)$$

in which the intrinsic frequency Ω has been replaced by the observed frequency as $\Omega = \omega - u_0k = k(c_{\text{ph},x} - u_0)$, using the horizontal phase speed $c_{\text{ph},x}$ of the wave. Following the usual definition, positive m denote upward moving waves.

In case of a negative expression within the brackets, m becomes imaginary, which describes an exponentially decreasing amplitude of the wave with altitude, corresponding to a dampened wave that does not transport energy through the atmosphere. Such waves are called *evanescent* waves. Only waves with real solutions for m transport energy within the atmosphere. Those waves are called *propagating* waves.

As stated in the introduction to this thesis, those waves that contribute to the mean flow at high altitudes are of interest to the research community. If the source of the wave lies within the troposphere or lower stratosphere, it has to have a real vertical wavenumber m in order to be able to transport its energy to mesospheric altitudes.

It must be noted, that the solution of Eq. (2.1) is not straightforward, since N^2 can vary with z , as can u_0 . It can also be seen that in Eq. (2.3) singularities result, if the magnitude of the mean flow u_0 equals that of $c_{\text{ph},x}$, only with opposite signs. If this criterion is met, the wave breaks, leading to the deposition of energy and momentum at the altitude level at which the critical wind speed $u_0 = -c_{\text{ph},x}$ is met.

The easiest case to solve the Taylor-Goldstein equation is that with a constant N^2 and constant background horizontal wind. In that case the terms with derivatives of the horizontal wind in Eq. (2.1) are eliminated. Additionally, only considering so-called medium- and high-frequency waves with $\Omega \gg \Omega_{\text{Earth}}$ and with vertical wavenumbers $|m| \gg 1/(2H_S) \simeq 7 \cdot 10^{-5} \text{ m}^{-1}$ leads to a much easier equation in which only two terms remain (Fritts and Alexander, 2003):

$$\hat{w}'' + \left[\frac{k^2 N^2}{\Omega^2} - k^2 \right] \hat{w} = 0 \quad (2.4)$$

This is the equation describing plane waves, and it leads to the dispersion relation that links the wave's frequency Ω to the wavenumbers as:

$$\Omega = \pm \frac{kN}{(m^2 + k^2)^{1/2}} \leftrightarrow \omega = u_0 k \pm \frac{kN}{(m^2 + k^2)^{1/2}} \quad (2.5)$$

which can also be expressed using the angle β' between the wave vector and the horizontal plane:

$$\Omega = \pm \frac{kN}{(m^2 + k^2)^{1/2}} = \pm N \cos(\beta') \quad (2.6)$$

The sign before the fraction depends on the vertical wavenumber m , with the positive branch denoting an upward moving wave (positive m). From this relation, the range of possible frequencies of the atmospheric wave is limited to $0 \leq \Omega \leq N$.

The more general, three-dimensional dispersion relation is (Fritts and Alexander, 2003):

$$\Omega^2 = \pm \frac{N^2(k_x^2 + l_y^2) + f^2(m^2 + \frac{1}{4H_S^2})}{k_x^2 + l_y^2 + m^2 + \frac{1}{4H_S^2}} \quad (2.7)$$

in which k_x and l_y denote the two horizontal wavenumbers and $f = 2\Omega_{\text{Earth}} \sin(\phi)$ represents the Coriolis parameter of latitude ϕ . Using these equations, all unknown characteristics of the wave can be determined, as long as the horizontal and vertical wavenumbers, along with N are known.

In the two-dimensional case, the phase- and group-velocities of the wave can be derived from the observed frequency as:

$$c_{\text{ph},x} = \frac{\omega}{k} = u_0 \pm \frac{N}{(k^2 + m^2)^{1/2}} = u_0 \pm \frac{N}{k} \cos(\beta) \quad (2.8)$$

$$c_{\text{gr},x} = \frac{\partial \omega}{\partial k} = u_0 \pm \frac{Nm^2}{(k^2 + m^2)^{3/2}} = u_0 \pm \frac{m^2}{N^2} (c_{\text{ph},x} - u_0)^3 \quad (2.9)$$

$$c_{\text{ph},z} = \frac{\omega}{m} = u_0 \frac{k}{m} \pm \frac{kN}{m(k^2 + m^2)^{1/2}} = \pm u_0 \frac{k}{|m|} + \frac{N}{|m|} \cos(\beta) \quad (2.10)$$

$$c_{\text{gr},z} = \frac{\partial \omega}{\partial m} = \mp \frac{Nk|m|}{(k^2 + m^2)^{3/2}} = \mp \frac{k|m|}{N^2} (c_{\text{ph},x} - u_0)^3 \quad (2.11)$$

Again, whenever there is a choice of signs, the upper branch stands for positive m , the lower branch for negative m .

In general, $c_{\text{ph},z}$ and $c_{\text{gr},z}$ have opposite signs. While the phase-velocity shows the direction of movement of the wave, the group-velocity shows the direction of transport of energy. Hence, waves with negative vertical wavenumber m transport energy upwards through the atmosphere. Moreover, the scalar product of the wave-vector \vec{k} and the group-velocity vector of the wave results in zero, showing that the two are perpendicular. Thus, the energy transport takes place parallel to the phase lines of the wave.

From the basic equations used to derive the Taylor-Goldstein equation (2.1), phase relations of the perturbations in wind, pressure, and temperature can be derived. The relations are given as:

$$u' = -\frac{m}{k}w' \quad (2.12)$$

$$p' = -\frac{\rho_0 m(\omega - u_0 k)}{k^2}w' = -\frac{\rho_0 m \Omega}{k^2}w' \quad (2.13)$$

$$w' = \frac{i\Omega g}{N^2}\tilde{T}' \quad (2.14)$$

of which the last equation is taken from Wang et al. (2006), and \tilde{T}' denotes the temperature perturbation divided by the background temperature.

Knowing k and m , and any of the perturbation quantities, e.g. the temperature, all other perturbations can be calculated. Thus, more information can be gained, which is of much interest to the research in GWs: The horizontal momentum and the energy transported by the wave, expressed as momentum flux, \mathbf{MF} , and energy flux, \mathbf{EF} . These are calculated directly from pressure and wind perturbations:

$$\mathbf{MF}_x = \rho_0 \int u'(s')w'(s') ds' \quad (2.15)$$

$$\mathbf{MF}_y = \rho_0 \int v'(s')w'(s') ds' \quad (2.16)$$

$$\mathbf{EF}_x = \int p'(s')u'(s') ds' \quad (2.17)$$

$$\mathbf{EF}_y = \int p'(s')v'(s') ds' \quad (2.18)$$

$$\mathbf{EF}_{\text{vert}} = \int p'(s')w'(s') ds' \quad (2.19)$$

In the linear case, both quantities are related, following the Eliassen-Palm-theorem, as:

$$\mathbf{EF}_{\text{vert}} = -\vec{U} \cdot \vec{\mathbf{MF}} \quad (2.20)$$

with mean flow speed \vec{U} at level of flux measurement and $\vec{\mathbf{MF}} = (\mathbf{MF}_x, \mathbf{MF}_y)$ (Eliassen and Palm, 1960). This relation is used to test the linearity of the cases encountered during flight, as both sides of the equation can be calculated independently. If the relation stated by Eliassen and Palm (1960) is valid, the encountered waves are probably well described by the equations derived from linear theory (e.g. Smith et al., 2008; Kruse and Smith, 2015; Smith et al., 2016). In this case, the relations given above can be expressed in terms of T' as:

$$\mathbf{MF}_{\text{hor}} = \rho_0 \int -\frac{m}{k} w'^2 ds' = \rho_0 \frac{g^2}{N^4} \int \frac{m\Omega^2}{k} \tilde{T}'^2 ds' \quad (2.21)$$

$$\mathbf{EF}_{\text{hor}} = \int \frac{\rho_0 m^2 \Omega}{k^3} w'^2 ds' = -\rho_0 \frac{g^2}{N^4} \int \frac{m^2 \Omega^3}{k^3} \tilde{T}'^2 ds' \quad (2.22)$$

$$\mathbf{EF}_{\text{vert}} = \int -\frac{\rho_0 m \Omega}{k^2} w'^2 ds' = \rho_0 \frac{g^2}{N^4} \int \frac{m\Omega^3}{k^2} \tilde{T}'^2 ds' \quad (2.23)$$

Note, that the phase relations assume that the wave vector \vec{k} is aligned with the x -axis. Thus, the wavenumber k represents the horizontal component, defining the momentum flux vector as $\vec{\mathbf{MF}} = (\mathbf{MF}_{\text{hor}}, 0)$. Since using the phase relations to calculate the energy and momentum fluxes already assumes the validity of linear theory, the Eliassen-Palm relation must be true, if tested with the quantities derived using Eq. (2.21) and (2.23).

In the mid-frequency approximation, which assumes, that $N \gg \Omega \gg f$, the dispersion relation (2.7) takes the simplified form of:

$$\Omega = N \left| \frac{k}{m} \right| \quad (2.24)$$

with horizontal wavenumber $k = k_x + l_y$. With this approximation the momentum and energy flux can be calculated using:

$$\mathbf{MF}_{\text{hor}} = \frac{1}{2} \rho_0 \frac{g^2}{N^2} \int \frac{k}{m} \tilde{T}'^2 ds' \quad (2.25)$$

A mathematical derivation of Eq. (2.25) from the three-dimensional linear theory can be found in Ern et al. (2004). As mentioned above, when using the phase relations to derive the vertical flux of momentum, the assumption of linearity is already made, meaning that $\mathbf{EF}_{\text{vert}} = -u_0 \mathbf{MF}_{\text{hor}}$ must be true. The two values are related by the horizontal background wind, and the relation will follow the strength patterns of u_0 , meaning that nothing new is learned by separately calculating $\mathbf{EF}_{\text{vert}}$.

However, if temperature data is available, it can be used to calculate the gravity wave potential energy density per mass (GWPED)

$$E_\rho = \frac{1}{2} \frac{g^2}{N^2} \overline{\left(\frac{T'}{T_0} \right)^2} \quad (2.26)$$

This is used as an estimation of over-all wave activity (Kaifler et al., 2015).

All quantities needed in the above equations, are part of, or can be derived from the data products of the MTP, which is described in the following chapter. The two-dimensional temperature measurements of the MTP provide all information needed to derive the phase-angle β' , and with it the absolute values of the wavenumbers k and m .

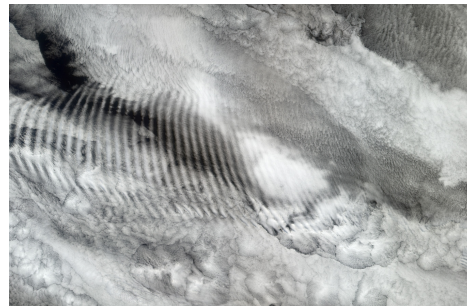
Based on extrapolation of the flight level pressure or the pressure profile used in the RT calculation within the retrieval algorithm, potential temperature profiles and from these the Brunt-Väisälä frequency, N , can also be derived. This is already enough information to use the dispersion relation, Eq. (2.6), to derive the intrinsic frequency, Ω , and apply equations (2.21) - (2.23) to derive the magnitude of momentum and energy fluxes. The direction of propagation can only be known if the signs of k and m are known. However, these are not revealed by the stationary picture of the wave provided by MTP temperature measurements. Probable propagation directions can only be estimated by interpreting the phase line tilt relative to the mean flow direction and by analysing wind measurements.

3 Experimental approach to measuring gravity waves: MTP

The wave-motion of the affected air parcels leads to temperature, pressure, and density differences in comparison to the surroundings, which can be detected in nearly all atmospheric measurements, as long as they provide sufficient resolution in time or space. For example, the difference in air temperature compared to the surroundings can lead to visible wave-patterns in cloud structures, as shown in Figure 3.1.



(a) Wave clouds seen from passenger aircraft¹.



(b) Satellite image of wave clouds².

Figure 3.1: Examples of visible wave patterns in clouds.

On horizontal flight legs, in situ measurements of certain trace gases might also show a wave pattern, when cutting through the air masses containing different concentrations of the targeted trace gas (e.g. Heller et al., 2017). However, most data is available from the measurement of temperature and wind fields, in which deviations from a smooth background are analysed to find and characterise wave signals.

Large coverage in space and time is provided when using remote sensing instruments to measure these temperature and wind fields. Satellite observations are used to gain insight into geographical hot-spots of wave activities, and their seasonal variability (e.g. Eckermann and Preusse, 1999; Hoffmann et al., 2013, 2016).

Ground-based or airborne Light Detection And Ranging (LIDAR) instruments provide measurements over a large vertical extent within the atmosphere, with good spatial resolution (Kaifler et al., 2015, 2017; Witschas et al., 2017), providing two-dimensional measurement time-series.

¹by Ilya Katsman; <https://www.instagram.com/p/BPNCLMjEUH/?taken-by=theonlyilya>, (last access: 13-March-2018). Printed with personal permission by Ilya Katsman.

²by NASA/GSFC/LaRC/JPL, MISR Team; <https://earthobservatory.nasa.gov/IOTD/view.php?id=4117>, (last access: 11-July-2017).

However, active remote sensing instruments often only provide data with considerable distance to their location (i.e. above or below flight level). Moreover, they are often sensitive to the surrounding atmospheric conditions, often only able to measure during darkness, in cloud-free atmosphere with sufficient aerosol concentration (e.g. Kaifler et al., 2015; Witschas et al., 2017). Here, radio sonde measurements can provide valuable data, as they cover an altitude region between ground level and up to ~ 30 km. Still, radiosonde measurements are only available at fixed time intervals (usually around 3 h during intensive measurement periods, or 12 h on regular schedules). They cover a horizontal range that depends on the winds in the altitudes they pass. This can pose a problem to interpret the wave activity over a certain, narrow region of interest.

To investigate the sources of waves and their propagation through the atmosphere, measurements are needed that have a high resolution in time and space, and can be done over a longer period of time, but variable in space. This is provided by aircraft-based measurements. While air-borne LIDAR measurements only cover one viewing direction with some distance to the actual flight level of the aircraft, passive microwave radiometers, such as the one described in section 3.2 of this chapter, can be used in a limb-sounding geometry, covering both, altitude regions above, as well as below the aircraft. With typical flight levels just below the tropopause, those measurements cover the tropospheric source region of many GWs, while also probing possible barriers that prevent the vertical propagation of a wave, such as a TIL, or jet stream winds. Additionally, it is largely independent from the prevailing atmospheric conditions, as clouds or sunlight hardly interfere with the measurement.

The MTP is the realisation of such a passive microwave radiometer. In the following, the basic principles of passive radiometry are explained in Section 3.1, followed by a description of the instrument design of the DLR-MTP in Section 3.2 and an overview of the DLR-MTP campaign deployments in Section 3.3. Also, a brief overview of the MTP's data products and their usage in the past is given in Section 3.4. This leads to a short introduction of the new approach that is taken to analyse the data provided by the MTP instrument, with respect to the characterisation of GWs.

3.1 Radiometry

Radiometry is a well-known, and well-documented remote-sensing measurement method, which has been developed since the use of the first active Radio Detection And Ranging (RADAR) instruments as early as 1903 (Ulaby et al., 1981). A 'standard' giving a thorough overview to the theory of measurements, the history, and common apertures is Ulaby et al. (1981), of which a new version has been available since 2015. A sometimes easier-to-read book on the topic is written by Iain Woodhouse (2005). In the following, the main principles of passive radiometry are presented as a summary of the common knowledge found in both of these books.

The microwave spectrum is part of the radio spectrum, and covers the frequency range between 0.3 GHz and 300 GHz, corresponding to wavelengths between a meter and millimetres. This part of the electromagnetic spectrum is used in navigation, broadcasting and for scientific purposes. In the atmosphere, there are a number of absorbers in this wavelength region. The strongest are oxygen and water vapour, making water vapour mixing ratio and atmospheric temperature (from measurements at oxygen absorption lines) the main data products of passive radiometric measurements.

All radiometers measuring atmospheric temperature use frequencies of the strong absorption lines of the 60 GHz oxygen complex ('V-band'), which are caused by magnetic-dipole transitions (Liebe et al., 1992). Passive radiometers pick up the energy transported by the photons emitted in these transitions. The change to the initial intensity of the emitted radiation while travelling through the atmosphere is described by the radiative transfer (RT) equation, which links the (frequency-dependent) intensity of incoming radiation $I(\nu)$ to the strength of the source, $B(\nu, T)$, and the distance to the source, s , with respect to alterations caused by absorption along the way:

$$I(\nu) = I_b(\nu)e^{-\tau(\nu,s)} + \int_0^s B(\nu, T) \cdot e^{-\tau(\nu,s')} \alpha(\nu, s') ds' \quad (3.1)$$

Here, $I_b(\nu)e^{-\tau(\nu,s)}$ denotes the background radiation either emitted from the Earth's surface, or picked up from space - depending on the instrument's viewing direction. In case of microwave radiometry, the background radiation from space results in a 2.7 K temperature signal (Waters, 1976). Other quantities are the volume absorption coefficient α , the optical depth $\tau = \int_0^s \alpha(\nu, s') ds'$, and the source function $B(\nu, T)$, depending on frequency ν , and temperature T .

The volume absorption coefficient α is defined as:

$$\alpha(\nu, s) = \sum_m k_m(\nu, p(s), T(s)) \cdot n_m(s) \quad (3.2)$$

depending on the absorption cross-section k_m , that is a measure of the effectiveness of absorption, which depends on frequency ν , pressure p , and temperature T . The sum is taken over the various relevant absorbers, e.g. different trace gases, and their abundance n_m along the path s . The magnitude of $\alpha(\nu, s)$ states the amount of radiation at frequency ν , which is extracted from the radiation entering a volume, on the way towards the observer. The largest source of losses is absorption by molecules within the volume. However, those same molecules can also emit radiation at the same frequency, and add to the signal again.

Another cause of decreasing intensity on the way is scattering. This is not accounted for in Equation (3.1), due to the following reasons:

The collision with molecules and aerosols within the volume can not only cause a change of direction of the photons through elastic scattering (Rayleigh- or Mie scattering), but can also cause a change of frequency (Raman scattering) at very small rates. The efficiency of both scattering processes depends on the wavelength of the radiation in focus.

Rayleigh and Raman scattering can occur if a photon collides with air molecules, which in the case of microwaves is negligible compared to the effect of absorption of the photon (Melsheimer et al., 2005). Mie scattering is most efficient, if the scattering particle is about the same size as the wavelength of the scattered light. However, the wavelength of interest for the MTP measurements is $\lambda \sim 5$ mm, which is an extremely rare size for aerosols (Chapter 3 in U. Schumann (ed.), 2012). Only hydrometeors (liquid or frozen water particles) might reach diameters large enough to become relevant for scattering, however, on cruising altitudes, they should not be encountered by research aircraft, and are usually being avoided by pilots. Hence, scattering can be neglected in the description of microwave radiative transfer concerning the vast majority of airborne operations.

Using the absorption coefficient α , the transmission is defined as:

$$\mathcal{T}(\nu, s) = e^{-\tau(\nu, s)} = \exp\left(-\int_0^s \alpha(\nu, s') ds'\right) \quad (3.3)$$

The transmission defines how far radiation of a certain frequency can reach into an opaque medium, such as the atmosphere.

The weighting function is the derivative of the transmission, using both, optical depth, τ , and absorption, α :

$$W(\nu, s) = \frac{\partial \mathcal{T}}{\partial s} = \alpha(\nu, s) \cdot \exp\left(-\int_0^s \alpha(\nu, s') ds'\right) = \alpha(\nu, s) \cdot e^{-\tau(\nu, s)} \quad (3.4)$$

which equals the components of the RT equation within the integral, except the source function $B(\nu, T)$, hence the name ‘weighting function’. It shows where the changes in transmission are largest, and as a result, which altitudes measurements at the current frequency are most sensitive to. Ideally, there is a peak in the weighting function at those altitudes. As a simplified approach for the MTP, Gary (1989) uses the approximation of the distance, by which $W(\nu, s)$ has dropped to $1/e$ for the range of sensitivity.

By applying the RT equation, the amount of radiation reaching the antenna of the instrument from a certain distance can be calculated. This can be translated into a brightness temperature (BT), T_B . This is the temperature a black body would have that emits the measured amount of radiation. As the atmosphere can be treated as a black body, the absolute temperatures of the atmospheric sources can be derived by applying the RT equation, and by reconstructing the temperatures needed in the term $B(\nu, T)$ to create the same signal as measured by the sensor.

The source function, describing the amount of energy emitted by a black body with a temperature, T , is given by Planck’s law, depicted in Figure 3.2a:

$$B(\nu, T) = \frac{2h\nu^3}{c^2} \cdot \frac{1}{\exp\left(\frac{h\nu}{k_B T}\right) - 1} \quad (3.5)$$

Here, c represents the speed of light, h is the Planck constant, and k_B denotes the Boltzmann constant. This is a highly non-linear relationship between the emitted radiation and the temperature. However, in the microwave frequency region, the expression of the exponent becomes very small, so that the exponential function can be expressed as:

$$\exp\left(\frac{h\nu}{k_B T}\right) \cong 1 + \frac{h\nu}{k_B T} \quad (3.6)$$

This leads to the linear expression also known as Rayleigh-Jeans relation:

$$B(\nu, T) = \frac{2h\nu^3}{c^2} \cdot \frac{1}{\exp\left(\frac{h\nu}{k_B T}\right) - 1} \cong 2\frac{\nu^2}{c^2} \cdot k_B T \quad (3.7)$$

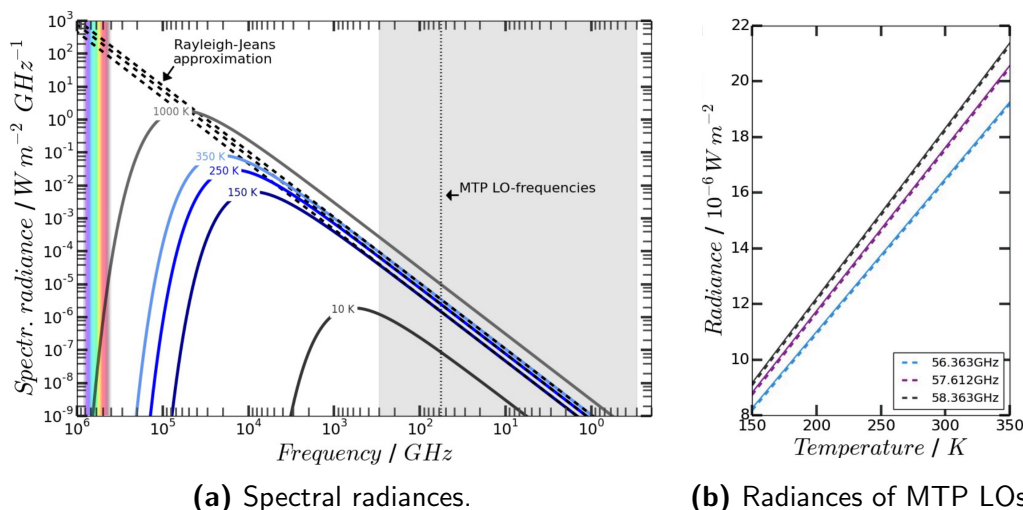


Figure 3.2: a) Planck curves at different temperatures. The black dashed lines indicate the Rayleigh-Jeans approximation for the atmospheric temperature range (blue lines). Also indicated are the MTP LOs (3 vertical dashed lines; showing as a single line). b) Radiance at the MTP LOs at atmospheric temperatures. Values are calculated using the Planck equation (dashed lines) and the Rayleigh-Jeans approximation (solid lines).

With the established linear relationship between the amount of radiation emitted by the black body and its temperature, an exact measurement of the emitted thermal radiation in the microwave region is sufficient to derive this body's temperature, referred to as BT. However, grey bodies would emit less radiation, meaning colder temperatures would be associated with measurements of their microwave radiation. Fortunately, the atmosphere is an almost perfect black body in the microwave region, so the Planck function is the correct source function for the RT, and measurements within the 60 GHz oxygen absorption complex can be used to derive the atmospheric temperature.

When modelling the radiance a microwave radiometer would measure in a defined atmospheric state, the instrument's characteristics have to be taken into account.

This is usually done by convolving the radiative transfer equation with an instrument function that describes how much of the signal reaching the front of the receiver is picked up and being processed by the instrument. The MTP uses a local oscillator frequency (LO) to transform the incoming frequency signal to the base-band, where a spectral filter can be applied, that defines the frequency region the measurement is taken at. This region is usually centred around the frequency of a strong oxygen absorption line, which in case of the MTP corresponds to the LO. The instrument function typically consists of a measurement of the filter characteristics, together with the antenna diagram, which shows how sensitive the receiver is to the different directions in the half-sphere it is pointing towards.

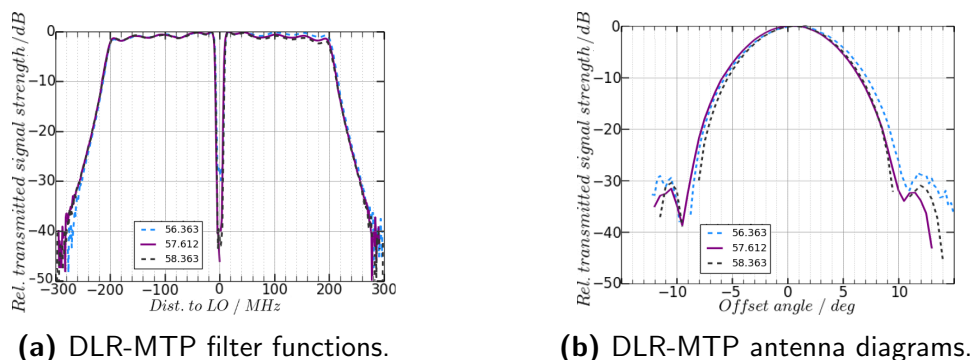


Figure 3.3: (a) filter function and (b) antenna diagram of the DLR-MTP at the standard LOs.

Exemplary measurements of the filter functions and antenna diagrams of the DLR-MTP are shown in Figure 3.3. The radiative power reaching the radiometer’s antenna is translated by the radiometer to a voltage that is measured and stored in a data file as digital counts. Those counts can be translated into BTs through calibration of the instrument (see Chapter 4.2). To derive absolute temperature profiles from the measurements of the MTP, a retrieval algorithm has to be used. This algorithm applies the RT equation, and finds the vertical temperature profile that most likely caused the measured BTs.

3.2 The Microwave Temperature Profiler: Instrument description

The MTP was developed in the late 1970s by Bruce Gary and Richard Denning at the Jet Propulsion Laboratory (NASA-JPL) for research on CAT (Gary, 1989). After the discovery of the Antarctic ozone hole in the 1980s, the MTP was part of the instrumentation on various research missions conducted in the late 1980s and has been deployed on many research missions since then. It provides measurements of temperature profiles both, above and below the flight altitude of the research aircraft. From this, information on the tropopause height, lapse rate around flight altitude, or the mesoscale structure of potential temperature can be derived (see Section 3.4 ff.).

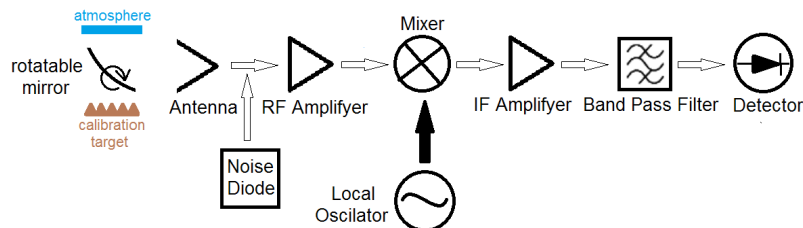


Figure 3.4: Block diagram of the DLR-MTP.

The concept of measurements of the MTP as a passive total-power radiometer (Denning et al., 1989) is straightforward. A horn antenna is used as a receiver of incoming atmospheric radiation. Through down-conversion with a defined frequency, the LO, and low pass filtering a part of the incoming radiation spectrum is chosen. The passing signal is converted to a voltage, which is proportional to the squared input intensity. This voltage is finally translated to a digital count number, stored in the MTP data file. Using a rotatable mirror in front of the instrument’s antenna, the direction from which the radiation is collected can be changed, making the measurement of altitude-resolved temperature profiles possible. Furthermore, a heated calibration target is built into the instrument, to which the mirror points after each cycle of atmospheric measurements. The signals recorded while pointing towards the heated target are combined with a noise diode signal and used for calibration. A thorough discussion of the MTP’s calibration is given in Chapter 4. In its standard deployment settings, ten viewing angles are being used during one measurement cycle; five above the horizon, four underneath, and one pointing exactly towards the horizon. At each angle, measurements at three LOs, corresponding to the frequencies of three strong oxygen absorption lines are made (see Table 3.1). That adds up to thirty measurements, which are combined to provide the input for the retrieval algorithm, which calculates the absolute temperature profiles from the MTP raw measurements.

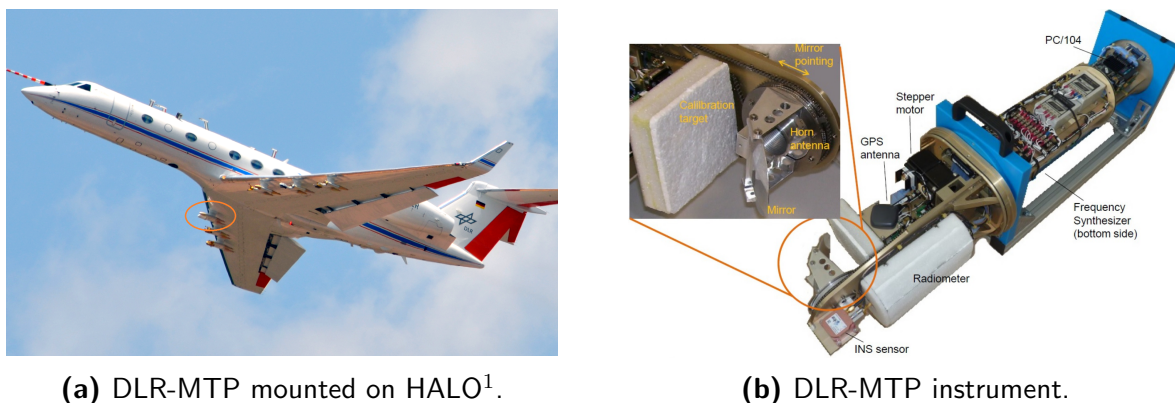
LO frequencies	(limb-) elevation angles
56.363 GHz	+80°, +55°, +42°, +25°, +12°
57.612 GHz	±0°, -12°, -25°, -42°, -80°
58.363 GHz	

Total number of measurements per cycle: 30

Table 3.1: Standard settings of MTP measurements

The measuring concept has not changed significantly over the years - with one exception. As explained in Lim et al. (2013), the radiometric and electric components have improved significantly, leading to much less noise on the measured data, as well as a much more compact design of the instrument itself. With less noisy data, the measurement strategy allowed for a re-definition of the instrument’s filter function. The earlier MTP instruments used LOs between two strong absorption lines of the oxygen absorption complex near 60 GHz.

The filter-width was then chosen in a way that the two strong absorption lines were within the filter bandwidth, so that they were sampled at the same time, increasing the signal-to-noise ratio of the instrument. However, as there are no oxygen absorption lines with exactly the same strength, the two sides of the filter probe slightly different parts of the atmosphere. With better system parts that induce less noise on the signal, this set-up could be changed, so that the LO is now defined as a frequency near an oxygen absorption line centre and the two flanks that are measured belong to the same line. This was included in a new instrument design, presented in 2008, which allowed to mount the MTP inside a canister underneath the wing of a research aircraft. It is pointing forward, measuring the temperatures of air masses in front of the aircraft. Details of the instrument design can be found in Mahoney and Denning (2009). Two instruments were built using this new design. One has been deployed on the NCAR GV since 2008 (e.g. Lim et al., 2013; Davis et al., 2014; Haggerty et al., 2014), the other was bought by the DLR, and has been flown on HALO in two recent campaigns.



(a) DLR-MTP mounted on HALO¹.

(b) DLR-MTP instrument.

Figure 3.5: The DLR-MTP instrument.

Two parts were added to the DLR-instrument after the purchase from NASA-JPL: An embedded computer and an inertial measurement system including a Global Positioning System (GPS) antenna. They provide the opportunity to operate the DLR-MTP instrument independent from the aircraft cabin in a self-sufficient flight-mode. These changes have implied modifications to the instrument’s software. In the original set-up a Visual Basic software package was provided by NASA-JPL to run the instrument during research flights. With the on-board computer and integration of the inertial sensor, this software was translated to a LabView code, which was adjusted to use the additional data provided by the inertial sensor and run independently from a connection to a cabin computer (which is still provided, and can be used, e.g. to adjust settings during research flights). Besides the hardware additions and some software-induced differences in the measurement routine, both wingpod-instruments, the one operated by NCAR, and the DLR-MTP are built with similar radiometric hardware components, and are thus considered to have the same instrument characteristics.

¹Photograph by Maximilian Dollner; Printed with personal permission by M. Dollner.

Their filter band-width is fixed to ± 200 MHz, however, the radiometer architecture using a mixer to down-shift the incoming signal allows measurements at various frequencies, depending on the chosen LO. The synthesizer used to generate the LO can be tuned between 12 GHz and 16 GHz. The output signal is doubled twice, allowing a frequency range of 48 GHz to 64 GHz for atmospheric measurements. At each elevation angle used during measurements, the synthesizer is successively tuned to the desired LOs, before moving to the next elevation.

Since the NCAR-MTP is part of the HIAPER Airborne Instrumentation Solicitation (HAIS), used as a set of standard instruments deployed on the NCAR GV, it has been in use in a variety of scientific campaigns since 2008, including the DEEPWAVE campaign in New Zealand in June/July 2014 (see section 5.3.1).

3.3 DLR-MTP campaign deployments

The DLR-MTP has been deployed twice, since its purchase. The first deployment was during the Mid-Latitude CIRRUS experiment (ML CIRRUS) campaign in March and April 2014. The second deployment was during the Aerosol, Cloud, Precipitation, and Radiation Interaction and Dynamics of Convective Cloud Systems (ACRIDICON) campaign in September and October of the same year.

3.3.1 ML CIRRUS 2014

The very first deployment of the DLR-MTP was during the ML CIRRUS campaign in 2014 (Voigt et al., 2017). The focus of this mission was to probe natural cirrus clouds as well as contrail cirrus throughout various stages of their life-cycles. The MTP was part of the wing-probe instrumentation and recorded data during all mission flights.

Due to software issues, parts of several mission flights are missing in the MTP data. During the last flight of the campaign, a brief period of icing occurred, during which the front of the MTP was covered in a thin layer of freezing water. This influenced the measurements, as liquid water is a strong absorber within the 60 GHz frequency range.

In total, the DLR-MTP produced almost 63 hours of data during 13 mission flights, recording 17476 individual measurement cycles. In the following, a measurement cycle is defined as a single sequence of measurements at each of the used elevation angles and LOs. Due to a cold soldered-joint connecting the built-in noise diode, used for calibration, the processing of the data with the standard retrieval algorithm provided by NASA-JPL (see Appendix A.1), is not possible for some parts of the data set.

3.3.2 ACRIDICON 2014

The ACRIDICON campaign took place in September and October of 2014 in Manaus, Brazil. A detailed description of the campaign was published in Wendisch et al. (2016). The main focus of the campaign was on aerosol effects on deep convective clouds.

For this purpose, large convective clouds were probed on varying altitude levels, which often resulted in very short flight legs, at partially very low altitudes.

The DLR-MTP was operating during all 18 mission flights. However, due to the high temperatures in the Amazon region, the MTP experienced over-heating problems, and was shut down during flight legs below 5000 m. During the last five mission flights of the ACRIDICON campaign, a different measurement set-up was chosen, focussing on the atmosphere above the aircraft. The number of elevation angles was reduced, as well as the number of LOs the MTP operated at. This resulted in shorter measurement cycles (7 s instead of 13 s), but the data format could not be processed by the MTP retrieval software provided by NASA-JPL, which expects input resulting from the standard measurement strategy at ten elevation angles and three LOs. Moreover, the instrument software occasionally got confused by non-standard timing of the measurement cycles, and sometimes did not send the correct data for mirror pointing. This resulted in recorded profiles during which solely the signal from the hot calibration target of the MTP instrument was measured. This only occurred for single measurement cycles at a time, leaving enough usable measurements to construct valid time-series of temperature profiles for all flight legs on which the MTP was operating.

In total, the MTP produced almost 86 hours of data during 18 mission flights, recording 26399 individual measurement cycles. Due to the formatting of data, the standard retrieval software cannot be used for further processing of all data. Thus, to date no absolute temperature profiles are available from the ACRIDICON campaign.

3.4 MTP data products

The main data product of all MTPs is a time-series of vertical temperature profiles along the flight track of the research aircraft. These profiles have to be derived by using a retrieval algorithm (see Appendix A.1). From the temperature profiles some important values can be derived and used to interpret other measurements, or perform analyses of the atmospheric state at the time of the measurement.

The most obvious parameter that can be derived from the temperature profiles is the tropopause altitude. This is defined as the lowest level at which the lapse rate decreases to 2 K km^{-1} or less, provided that the average lapse rate between this level and all higher levels within 2 km does not exceed 2 K km^{-1} (World Meteorological Organization, 1957). The lapse rate can be easily derived from the temperature profiles, and the lapse rates at each altitude can be checked whether they fulfil the criterion. Thus, the tropopause can be found, and used to interpret other measurements. Often, it is necessary to know whether tropospheric or stratospheric air masses were probed during flight. If only in situ measurements are available, this determination is often made from measurements during ascends or descends of the aircraft, or close-by radio sondes. Still, the flight pattern can be such that those aircraft ascends or descends are over 100 km away from the point where measurements were taken, and radio sondes are only released twice a day, which can imply large temporal and spacial distance from the aircraft's flight path.

The MTP provides a measurement at the position of the aircraft, which is more reliable.

Another important secondary MTP data product are profiles of potential temperature. With a known pressure profile (e.g. the hydrostatic extrapolation of the flight level pressure), the potential temperature can be calculated at each altitude level as:

$$\theta(z) = T(z) \cdot \left(\frac{p_{\text{ref}}}{p(z)} \right)^{\frac{R_L}{c_p}} \quad (3.8)$$

with the absolute temperature T , a reference pressure $p_{\text{ref}} \equiv 1000$ hPa, the gas constant of dry air $R_L \cong 287$ Jkg⁻¹K⁻¹ and the specific heat capacity of air $c_p \cong 1005$ Jkg⁻¹K⁻¹. Typically the exponent is approximated by $R_L/c_p \cong 2/7$ (Ch. 1 in U. Schumann (ed.), 2012). To be consistent with the way the absolute temperatures are retrieved, the pressure used in this equation should be the same as used to define the atmosphere within the retrieval algorithm. From the profiles of potential temperature the buoyancy frequency can be derived as:

$$N^2 = \frac{g}{\theta} \cdot \frac{d\theta}{dz} \quad (3.9)$$

These values are valuable in interpreting the atmospheric state around the aircraft, as the vertical profile of static stability yields information on the strength of the TTL. Furthermore, the static stability is an important variable when applying the equations from Chapter 2.2 to characterise wave packets encountered during flight.

As a result, the MTP provides information on the atmospheric state at flight altitude, valid for the same air masses as probed by the aircraft's in situ instrumentation. In that the MTP remains unique.

3.4.1 Previous studies involving MTP data products

Since its first deployment in the Stratospheric-Tropospheric Exchange Project (STEP) in Australia, 1987, the MTP has widely been regarded as an instrument providing valuable background information on the state of the atmosphere. It has been used to interpret in situ measurements of trace gases (e.g. Marcy et al., 2007; Thornton et al., 2007; Spinei et al., 2015), aerosols, (e.g. Gamblin et al., 2006; Popp et al., 2006; Schwarz et al., 2008), and assist the study of cloud physics (e.g. Corti et al., 2008; Jensen et al., 2010; Schumann et al., 2017; Urbanek et al., 2017), and dynamics in the atmosphere (e.g. Tuck et al., 1997, 2003; Sitnikova et al., 2009). In many cases, the MTP data were solely used to determine the tropopause height, to distinguish measurements of tropospheric or stratospheric air masses in the data set of interest. In the studies focussing on cirrus clouds or atmospheric dynamics, the (potential-) temperature gradient or derived buoyancy frequency N^2 is of particular interest to facilitate interpretations of measurements from other participating instruments.

There are also a number of studies focussing directly on the analysis of MTP data, e.g. to derive the boundary layer height from MTP potential temperature isentropes (Nielsen-Gammon et al., 2008).

After the Airborne Antarctic Ozone Experiment (AAOE), Hartmann et al. (1989) combined MTP measurements with pressure and wind measurements provided by the meteorological measurement system of the aircraft. They calculated potential vorticity on potential temperature isentropes to gain insight in mixing processes within the polar vortex. Davis et al. (2014) investigated the cold point temperature and mesoscale temperature fluctuations, derived as the difference to the mission average temperature, in the upper troposphere and lower stratosphere (UTLS), in connection to tropical weather disturbances.

Furthermore, MTP measurements have already been utilised to investigate GWs in the atmosphere. One of the earliest studies was published by Murphy and Gary (1995). They investigate mesoscale temperature fluctuations observed with the MTP during the Airborne Arctic Stratospheric Experiment (AASE II) campaign, with regard to the effects of rapid temperature changes (even by small amounts) on PSC. As a follow-up, Tabazadeh et al. (1996) further investigated the mechanism for the formation of PSC, combining the previous analyses of mesoscale temperature fluctuations in MTP data with modelled synoptic-scale temperature variations and lee wave forecasts. A more general overview on mesoscale temperature fluctuations measured by the MTP is given in two publications by Gary (2006, 2008). In these studies, systematic analysis of occurrence and amplitudes of mesoscale temperature fluctuations, related to the terrain below the aircraft, as well as aircraft altitude, season, and latitudes were presented and compared to synoptic-scale model output.

Much effort has been taken in utilising the MTP's ability to resolve mesoscale temperature fluctuations in the analysis of wave events encountered during research flights: In their analysis of a wave event observed during the AASE II in 1991/92, Chan et al. (1993) made use of the two-dimensional data provided by MTP measurements. Here, the horizontal wavelength of the wave event was identified from potential temperature cross sections derived from the MTP data along the flight track. This approach was already proposed by Gary (1989), who identified wave events in altitude changes of specific potential temperature isentropes along the flight track, which mark the adiabatic movement path of air parcels. He identified 12 encounters of mountain waves during the AAOE campaign and investigated mountain wave effects in the formation of the ozone hole. Similar approaches in the analysis of MTP data have been made by other studies as well (e.g. Bacmeister et al., 1990), who investigated the wave structures found in potential temperature isentropes altitudes derived from MTP measurements of both, the AAOE and AASE II campaigns in relation to the ground topography. This was followed by the aforementioned case study of Chan et al. (1993), and similar studies by Dean-Day et al. (1998) and Wang et al. (2006).

Based on these mesoscale temperature fluctuation analyses, a number of modelling studies have been performed and compared to cases in which MTP measurements are available. These studies aimed at improving the understanding and numerical description of GWs. Such studies have been undertaken by Bacmeister et al. (1990, 1996, 1999), Pfister et al. (1993), Cho et al. (1999), Leutbecher and Martin (2000), Dörnbrack et al. (2002), and Eckermann et al. (2006).

In the most recent study, basing the characterisation of GWs encountered during flight on MTP measurements, much the same goal was to be achieved as in this thesis. In their analysis Wang et al. (2006) use the S-transform method to identify wave events in aircraft measurement data. This is a variant of the wavelet analysis, which will be used in the new algorithm to analyse MTP data, presented in this thesis. Wang et al. also estimate the vertical wavelengths from MTP data through:

$$\lambda_z = 2\pi \left\| \frac{iT'}{dT'/dz} \right\| \sim \frac{\sigma(T')}{\sigma(dT'/dz)} \quad (3.10)$$

in which T' is derived by linear de-trending of the temperature measurements. The standard deviation σ is used to avoid singularities that can occur if the left part of the equation is used. They derive the intrinsic frequency $\hat{\omega}$ through the GW dispersion relation in the form:

$$\frac{1}{\lambda_z^2} = \frac{1}{\lambda_h^2} \frac{(N^2 - \hat{\omega})}{(\hat{\omega} - f)} - \frac{1}{4H_\rho^2} \quad (3.11)$$

which is a variant of Eq. (2.3), using the Coriolis parameter f and density scale-height H_ρ . The derived intrinsic wave frequency is then used to determine the vertical flux of horizontal momentum as

$$\mathbf{MF}_x = \frac{1}{2}\bar{\rho}(1 - f^2/\hat{\omega}^2)\tilde{u}\tilde{w}(\Phi_w - \Phi_u) \quad (3.12)$$

in which the amplitudes of the wind perturbations are denoted as \tilde{u} and \tilde{w} and their phase-shift as $(\Phi_w - \Phi_u)$. All three quantities are derived using the S-transform of aircraft data. Substituting the \tilde{u} values by the corresponding properties of \tilde{v} obviously leads to \mathbf{MF}_y . The horizontal direction of propagation of a wave packet, ϕ , was estimated using two different methods. One is the simple relation $\tan(\phi) = \mathbf{MF}_y/\mathbf{MF}_x$, the other “using a variant of the Stokes parameter method with the aid of the cross S-transform” (Wang et al., 2006), in which the propagation direction of a GW is derived from the major axis orientation of the wind perturbation hodograph as

$$\phi' = \frac{1}{2} \arctan \left(\frac{\tilde{u}^2 - \tilde{v}^2}{2\tilde{u}\tilde{v} \cos(\Phi_v - \Phi_u)} \right) \quad (3.13)$$

3.4.2 New approach to MTP data usage

The new algorithm, developed within this thesis, is based purely on MTP data. The Altitude-resolved characterisation of waves in atmospheric sounding (ACHWAS) algorithm uses wavelet analysis of temperature perturbation (T') signals within the MTP temperature data. Those are defined by individual linear de-trending of the temperature time series at all available altitudes. Within the algorithm, all secondary parameters, such as the potential temperature, and N^2 , are derived using the background-state T_0 , defined by the linear trend, that is used to find the temperature fluctuations.

Using the static stability, N , a vertical profile of the GWPED can be calculated, indicating the overall wave activity around flight altitude. The GW scales associated with the temperature perturbation signals are analysed by applying the wavelet transform and reconstructing T' signals at dominant scales. Within these reconstructed temperature perturbation signals, the (non-directional) orientation of the GW phase lines can be determined. The phase line orientation (PLO), β , is extracted as the angle between the phase line and the vertical. It provides a direct relation of the horizontal and vertical wavelengths, of which the former is already known from the spectral analysis within the wavelet transform. As the direction of propagation of the GW cannot be extracted from temperature data alone, the PLO is confined to $-90^\circ \leq \beta \leq 90^\circ$.

Once the PLO is identified, and with it the wavenumbers k and m are known, the dispersion relation of GWs, Eq. (2.5), is used to derive the intrinsic frequency of the wave. Knowing these quantities, Eq. (2.21) is applied to derive the absolute value of momentum flux contribution within the current wavelength scales at the position of the analysed phase line. This approach to estimate momentum fluxes of GWs has been applied in the analysis of satellite data (e.g. Ern et al., 2004, 2016) as well as interpretation of three dimensional tomography measurements (Krisch et al., 2017), but not in the analysis of MTP data. Basing the analysis on the reconstructed signals of dominant wave modes within the wavelet transform allows for individual characterisation of the wave packets encountered during flight, and also the interpretation of their individual contribution to the overall energy and momentum fluxes.

This is the first approach that makes use of the MTP's ability to provide a two-dimensional data set of temperatures above and below flight level, and solely use the temperature measurements to derive wave characteristics.

In Chapter 5 a more detailed description of the ACHWAS algorithm used to analyse MTP data is given. The capabilities of the new analysis method of MTP data will be assessed using synthetic data, before it is applied to data from the 2014 DEEPWAVE campaign. The results of these case studies will be compared to the findings of already published studies of these cases. Those studies have analysed flight level measurements (Smith et al., 2016) as well as remote sensing data and model output (Bramberger et al., 2017; Portele et al., 2017).

To allow for correct interpretation of MTP data, and assist in the estimation of uncertainties and capabilities of the new algorithm, the calibration of raw data is assessed in the following chapter, leading to a threshold value of detectable temperature perturbations in MTP time series. The capabilities of available retrieval algorithms are tested, and the altitude range covered by MTP measurements is investigated to identify the best practice when applying the new algorithm.

4 Temperature profile retrieval

Before the analysis of absolute temperature profiles derived from the measured data recorded with the DLR-MTP, the raw data has to be processed. The raw measurements of the instrument are stored as digital counts in individual files for each flight. Those raw counts have to be translated into profiles of absolute temperature, using a retrieval algorithm as described in Appendix A.1. However, a number of data processing steps, such as quality control, described in Section 4.1, and conversion to brightness temperatures (BTs), as described in Section 4.2, have to be undertaken before the retrieval algorithm can be applied. As there are currently two different retrieval algorithms available to process data of the DLR-MTP, the performance of the two algorithms will be compared in Section 4.3. The results of this section lead to a more general investigation of the abilities of the MTP instrument, concerning the range of sensitivity. Radiative transfer (RT) calculations are used to investigate the altitude range from which the measured signal originates, leading to a discussion of possible adaptations to the measurement strategy in Section 4.4.

4.1 Raw Data preparation for Retrieval

The raw data produced by the DLR-MTP cannot be used as input for any available retrieval algorithm without pre-processing. First, several steps of quality checks and corrections have to be performed.

In a first step, the housekeeping data from a mission flight are checked to make sure that all instrument parameters were within their usual range during the recording of the data. Data has to be excluded, if there was an obvious problem with the electronics or if the pointing of the instrument prevented a correct measurement of the atmosphere's temperature. The former manifests in the data, whenever '0' counts are stored as signal (the usual range is between '15000' and '25000'). The latter was the case, if the stored counts only differ by less than ~ 20 counts during an entire measurement cycle. This happens, if an error in the communication between the computer and the instrument occurs. That results in the mirror pointing towards the built-in calibration target instead of the given angle towards the atmosphere. This error has frequently occurred during the recording of data in some of the ACRIDICON mission flights in 2014, but only affects single measurement cycles at a time. A measurement cycle consists of a set of 30 measurements, recorded under each of the ten elevation angles, and using each of the three LOs used in the standard measurement setting (see Table 3.1).

In a second step, the time stamps of the recorded profiles have to be corrected for the case that the GPS antenna did not provide an accurate Coordinated Universal Time (UTC) time stamp, e.g. after (re-) starting the instrument.

This can be seen in the housekeeping data, in which the control flags set by the GPS receiver itself are logged. The correction is important to make sure that MTP data are comparable to other measurements of the research flight. If there is no correct GPS signal available, the PC time is used to store the data. To find the correct GPS time stamp for those measurement cycles, the mean recording time of all measurement cycles recorded during the same flight is calculated. This is subtracted from the time stamp of the first measurement cycle with correct UTC time stamp and the resulting value is used as that of the last recorded measurement cycle without valid UTC time. Then, the difference between the originally stored time, before this correction, to the stored time stamp of the preceding cycle is used to determine its correct time stamp, and so on, until the beginning of the period without valid GPS signal (usually the beginning of the data file) is reached.

With the time-corrected data set the aircraft parameters corresponding to each measurement cycle, can be extracted from the aircraft data files. For all relevant parameters the mean values between the time of the last recorded measurement cycle and the current one is calculated. These parameters are stored in an extra line of data, which is added to each block of data in the raw data file. Now, the retrieval algorithm provided by NASA-JPL can be used to retrieve the absolute temperature profiles from the raw data file. No further calibration or processing of raw data is needed here. However, other retrieval algorithms rely on well-calibrated BTs as input. These have to be derived from the raw data through a calibration process, as discussed in the following section.

4.2 Brightness temperature calculations

The raw data product from the MTP is a series of numbers (‘counts’) related to the intensity of the incoming radiation at the antenna. Those counts have to be related to BTs by using a calibration curve, determined from calibration measurements made either in the laboratory or during the mission flights. The retrieval code provided by NASA-JPL already has an implemented translation of raw counts to BTs. However, the statistical approach taken within this retrieval algorithm does not depend on well-calibrated input data. It is assumed that changes in the instrument state are small enough that any shifts in the calibration coefficients are negligible. Additionally, the underlying statistics provide the basis for the assumption that the retrieved temperature profiles still resemble the atmospheric situation well. On the contrary, any retrieval algorithm based on inverting the forward-problem

$$\vec{y} = \mathbf{F}(\vec{x}) \quad (4.1)$$

with the measurement vector \vec{y} , the forward model \mathbf{F} , and the atmospheric state \vec{x} , will react very sensitive to changes in the BT input. Such an inversion algorithm is the Temperature InveRrsion Algorithm for Microwave SoUunding (TIRAMISU) (Xu et al., 2016). To process MTP data with this algorithm the BTs have to be calculated separately, before using them as input. To ensure a correct error estimation of the retrieval output, the relative input error, associated with the MTP BTs, must be known.

In the following, some general characteristics of the DLR-MTP will be presented, followed by a description of possible calibration methods. Finally, the uncertainty of derived BTs will be discussed. A realistic estimation of BT errors will lead to a qualified assumption to what extent small temperature perturbations, for example such created by GWs, can be resolved with the MTP instrument.

4.2.1 Instrument characteristics

Before discussing the various possibilities of calibration strategies to determine the calibration parameters of the MTP instrument, some general characteristics of the DLR-MTP will be analysed. These can have an influence on the accuracy of the measurements, and have to be included in an error estimation of the BTs that will be the result of the calibration. The two major sources of errors in the calibration are non-linearity of the sensor and noise.

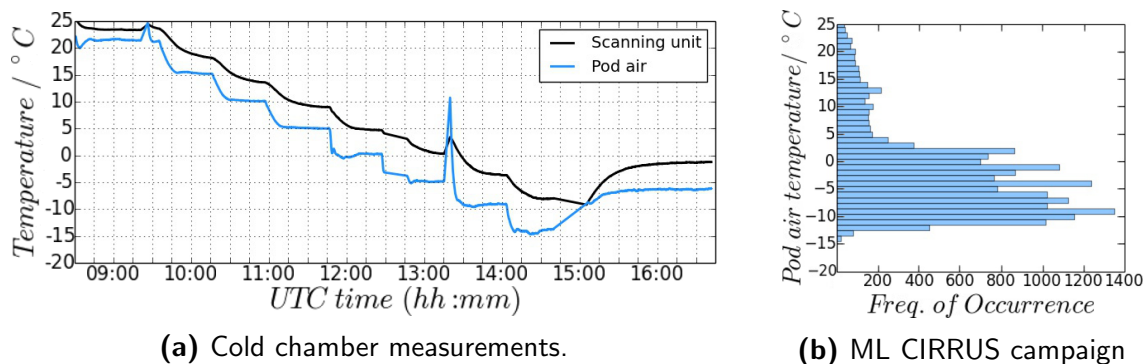


Figure 4.1: Temperature sensor measurements during (a) cold chamber measurements (black line: Scanning unit sensor, blue line: Pod air sensor) and (b) during all ML CIRRUS campaign flights

To determine these characteristics, as well as the typical calibration parameters of the DLR-MTP instrument, a series of measurements inside a cold chamber has been performed. During this measurement series, the temperature of the cold chamber was successively lowered from 21 °C to -15 °C in steps of 5 K, followed by a longer time at -7.5 °C (see Fig. 4.1a). This temperature range resembles the temperatures the MTP experienced during its deployment in the ML CIRRUS campaign in 2014, as shown in Figure 4.1b. The pod air temperature sensor monitors the temperature inside the MTP's housing during the flight. In the cold chamber, the housing was not installed, to minimize influence from the microwave window on the calibration. As a result, the readings of this sensor show the air temperature inside the cold chamber. The scanning unit temperature sensor keeps track of the temperature of the MTP instrument within close proximity to the crucial parts of the radiometer, such as amplifiers or the mixer. The readings of this sensor give an impression of the state of the instrument and its thermal stability. The temperatures of other important parts of the radiometer, such as the mixer, synthesizer, or calibration target are stabilised, so that their temperatures do not reflect the overall instrument state.

It can be seen that whenever the chamber temperature is lowered, both sensors pick up that temperature change. However, the response is different. This difference is caused by the placement of the sensors, one being closer to some heated parts of the instrument. From the readings of the scanning unit temperature sensor (black line in Fig. 4.1a) it can be seen that the MTP instrument takes some time to stabilize under the new temperature conditions. At 0° the cold chamber software had to be restarted, causing a longer stabilisation period, and at -7°C the cold chamber was opened to re-fill the liquid nitrogen in the cold target causing the spikes in the temperature measurements at 13:20 UTC.

Along with the MTP instrument two microwave absorbers at ambient temperature (hereafter referred to as ‘ambient targets’), and one microwave absorber submerged in liquid nitrogen (hereafter referred to as ‘cold target’) were placed in the chamber, in order to perform calibration measurements throughout the complete measurement series (see also Section 4.2.2). The third calibration target used in this measurement series is the built-in calibration target of the MTP instrument, which is heated to $\sim 45^\circ\text{C}$, and is hereafter referred to as ‘hot target’.

For all considerations of the calibration analysis that will be shown in this and the following sections, only those parts of the measurement series are used in which the scanning unit temperature is stable (the difference between two readings being smaller than an empirical threshold value of 0.04K). This way, effects from the instrument adjusting to new environmental conditions do not influence the calibration. This adjustment can take up to 15 minutes after the initial temperature change. Also, the very last segment of measurements is excluded from the studies, because the instrument had to be restarted due to a software error. The restart caused a long ‘warming-up’ period; during such a period the instrument is generally unstable. Moreover, towards the end of the measurements the liquid nitrogen in the cold target had nearly completely evaporated, so that the absorber material inside the target was not completely submerged any more. Thus, the measured BT, when looking at this target, is not equal to the evaporation temperature of liquid nitrogen, and the measurements cannot be used for calibration.

Linearity of the sensor

All calibration methods discussed later in this Chapter, assume a linear relationship between the radiation signal picked up by the horn antenna and the processed signal. Indeed, as the amount of radiation emitted by a microwave absorber is linear in temperature, a linear relationship between any target temperature and the measurement signal should be found. Using the measurements of the two ambient targets installed within the chamber, it can be shown that for the DLR-MTP the linear relation between the source temperature and the measurement output is given at all standard LOs, as shown in Fig. 4.2.

Since not only the temperature of the target changed in this test, but also the temperature of the sensor unit itself (see Fig. 4.1), it can also be established that the linear relationship between the measured signal and the source temperature is maintained throughout changing conditions, as they appear during a measurement flight, e.g. due to altitude changes.

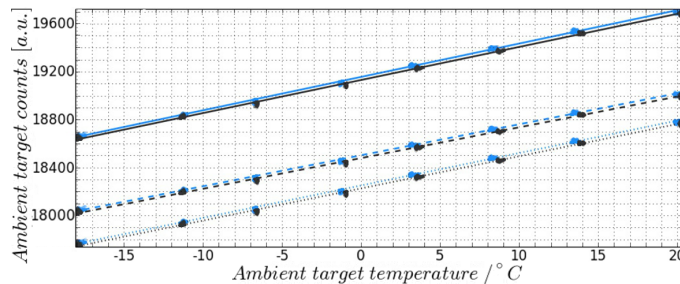


Figure 4.2: Ambient target temperature vs. measured signal (counts) of the two ambient targets for all three standard LOs of the DLR-MTP (different line styles). Different line colours correspond to the measurement of the two individual ambient targets.

The calibration parameters that link the measurement signal to the BTs are therefore the slope of a line and this line's y-intercept. Since a line is completely defined by any two known points, a calibration method using two calibration targets at known temperatures will determine the calibration parameters of the DLR-MTP. The stability of the calibration parameters in connection with changing instrument conditions will be discussed later, in Section 4.2.2. However, the lines in Fig. 4.2 already indicate that no large changes of the calibration parameters with the instrument state are to be expected.

Noise characterisation

Having shown that there is indeed a linear relationship between the temperature of the signal source and the output signal of the MTP instrument, the main remaining instrument characteristic of interest is the noise on the measurement signal.

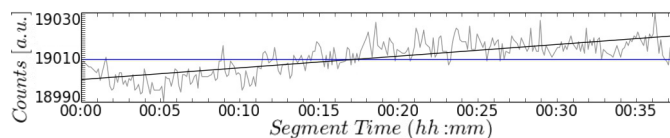


Figure 4.3: Measured signal (grey line) at LO 56.363 GHz while looking at ambient target inside the cold chamber as well as mean value (blue line) and linear fit (black line).

Obviously, system-induced noise affects the resolution of the measurements. It limits what changes in source temperature can be picked up by the instrument. Ideally, the noise added by the system is a Gaussian white noise. The noise can be seen in a time series of recorded data (see Fig. 4.3), and can be characterised from measurement data. The approach used to characterise the noise figure of the DLR-MTP is to use time-series of measurements at (nearly) stable instrument states, such as during the cold chamber measurements.

When pointing towards a calibration target at a stable temperature, the mean measurement signal should not change over time, and the deviation from the mean represents the noise added by the instrument.

An example of the measured signal while looking at one of the ambient targets during one segment is shown as the grey line in Fig. 4.3. Obviously, absolute stability can hardly be reached in a cold environment, while parts of the sensor unit are heated to $\sim 40^\circ\text{C}$. As a result, the measured signal cannot simply be divided into a mean value (blue line in Fig. 4.3) and a noise signal. The slight changes in system temperature over time have to be taken into account by applying a linear fit to the measured data of one segment (black line in Fig. 4.3). Now the measurement noise can be determined by subtracting this linear fit. Using this approach to analyse the cold chamber measurements at nearly stable conditions, reveals that the DLR-MTP noise figure, as shown in Figure 4.4, can be characterised by a Gaussian distribution with a standard deviation of ~ 6 cnts and the mean at 0 cnts.

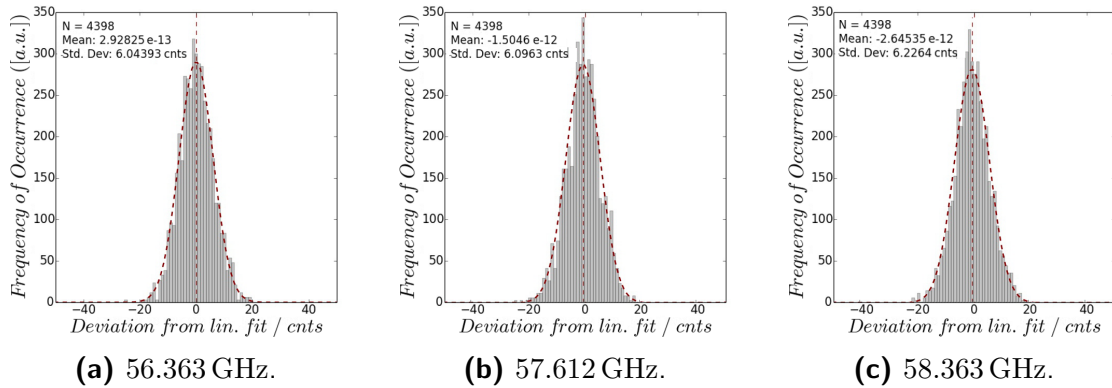


Figure 4.4: DLR-MTP noise figures from cold chamber measurements at the three standard LOs. Red dashed line: Gauss-fit to data. Fit parameters are shown in the upper left-hand corners.

The same method as for the cold chamber measurements is used for DLR-MTP data, recorded during the ML CIRRUS campaign in 2014. Here, the criterion used to determine flight segments with nearly stable instrument states is a difference of the scanning unit temperature of less than 0.04 K between two cycles. Additionally, it was made sure that no altitude changes were made ($\Delta z \leq 25$ m) or curves were flown during these segments. From all ML CIRRUS mission and test flights, 61 segments could be identified that satisfied the criteria and were at least 5 minutes long. Obviously, there is no ambient target available during flight. Instead, only the measured signal while pointing towards the built-in calibration target (without noise diode (ND) offset signal) is used to determine the noise figure. Again, a linear fit value is subtracted to determine the noise.

In Fig. 4.5 the noise characteristics at the three standard LOs are shown, along with a Gaussian function with a mean at 0.0 cnts, and a standard deviation of 6 cnts, as implied by the cold chamber noise figure. The Gaussian distribution of the noise values is found again, even with a slightly smaller standard deviation as in the cold chamber measurements, but still in excellent agreement with the values found in the laboratory environment. While the measurement noise of the DLR-MTP can be described by a Gaussian distribution, its spectral characteristics have to be known, to be able to distinguish between periodic signals in the time series due to GWs and those resulting from noise. For the spectral analysis the ML CIRRUS mission flight segments are used again.

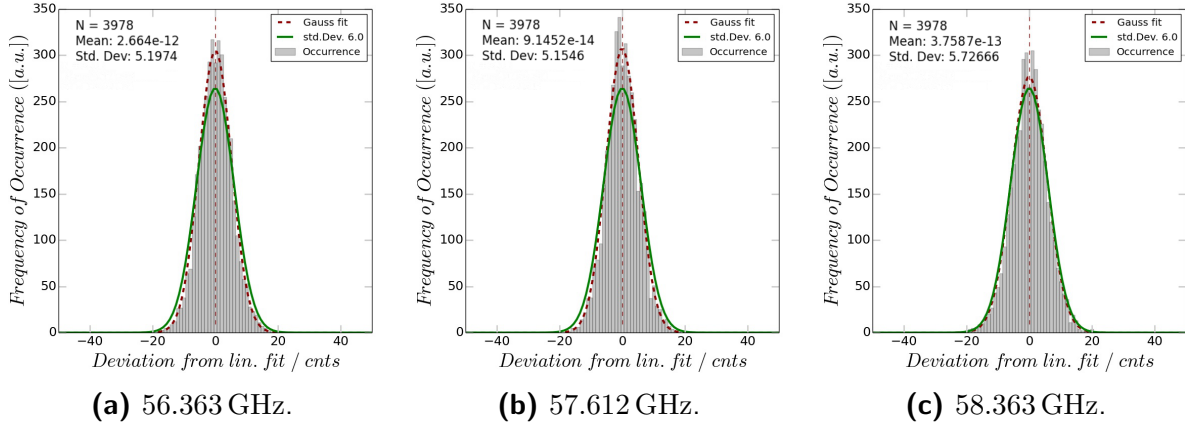


Figure 4.5: DLR-MTP noise figures from ML CIRRUS flight data. Red dashed line: Gauss-fit to data (fit parameters are shown in the upper left-hand corners). Green line: Ideal Gauss function with the mean at 0.0 cnts and 6 cnts standard deviation.

Due to the varying lengths of the individual flight legs, the data is concatenated to a single time line for spectral analysis. The power spectra of the noise signals at the three standard LOs of the DLR-MTP, as shown in Fig. 4.6, reveal that the measurement noise can best be described as a red noise, rather than a white noise with completely independent noise values in a time series.

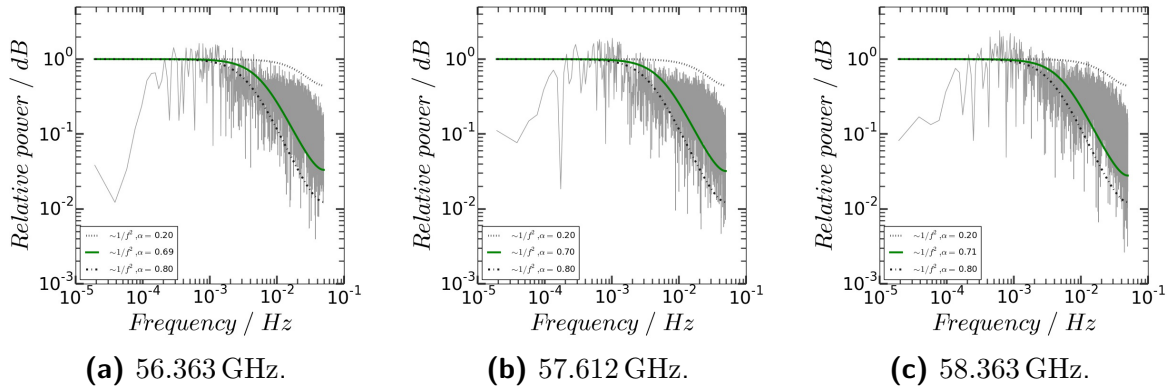


Figure 4.6: Power spectra of DLR-MTP noise figures from ML CIRRUS flight data at the three standard LOs. Black, dashed lines: theoretical power spectra of $1/f^2$ noise with lag1-correlations of $\alpha = 0.2$ and $\alpha = 0.8$. Green, solid line: theoretical power spectrum of $1/f^2$ noise with lag1-correlation of input data.

Red noise is characterised by a $\sim 1/f^2$ dependency of spectral power on frequency. It is characterised by the auto-correlation α between a data point of the time series and its precursors. According to Torrence and Compo (1998) the corresponding theoretical noise power spectrum is given by:

$$P_k = \frac{1 - \alpha^2}{1 + \alpha^2 - 2\alpha \cos(2\pi k/N)} \quad (4.2)$$

Knowing the noise power spectrum of the MTP allows to determine whether periodic structures in the time series, identified with the ACHWAS algorithm described in Chapter 5.1, are significant (high probability that they result from atmospheric temperature fluctuations), or noise-induced. Additionally, the standard deviation of the Gaussian distribution of noise values can be used to determine the variance of BTs derived from the raw signals, once the calibration parameters are known.

4.2.2 Description of calibration methods and MTP calibration parameters

Since there is a linear response in the measured signal to changes in the source temperature, the brightness temperatures, T_B , have a linear dependency on the measured counts (c):

$$T_B = s_{cal} \cdot c - T_R \quad (4.3)$$

with the slope of the line, s_{cal} , and the receiver noise temperature, T_R , represented by the y -intercept of the line. Since the receiver noise temperature represents an offset that is added to the measured temperature, it is subtracted in the equation. While a line can be fitted through any two known points, which makes the calibration process very simple, the determination of the line parameters also bears the danger of inconsistencies under rapidly changing measurement conditions, which could lead to large errors in the calculated BTs.

For the DLR-MTP there are three possible calibration strategies that can be used to determine the line parameters:

1. Hot-cold calibration, using a cold target (microwave absorber submerged in liquid nitrogen) and an ambient target (microwave absorber at room temperature)
2. MTP built-in hot target (microwave absorber with a heated metal plate in the back) combined with a noise diode offset signal
3. MTP built-in hot target combined with HALO static temperature (HALO TS)

The first method can only be deployed on the ground, since it uses external calibration targets. However, it is needed to determine the ND characteristics used in the second method. Both, the second and third method can be applied during flight (i.e. derived from parameters recorded during flight), representing the instrument state at the time of measurement better than calibration parameters from laboratory measurements can.

The three calibration methods are described in detail in the following subsections, starting with the hot-cold method, which is applied to the data from the measurement series in a cold chamber. From these a possible dependency of the calibration parameters on the instrument state can be derived along with the characteristics of the parts used in the other two calibration methods (i.e. ND characteristics and hot target BT).

Hot-cold-calibration in a cold chamber

The hot-cold calibration method is the standard calibration method used for a wide range of radiometers. When applying this method, an ambient target at room temperature is used together with a cold target. The calibration parameters are derived using the temperature of the ambient and the cold target, T_{amb} , and T_{cold} , as well as the measured signal stored as counts, c_{amb} and c_{cold} :

$$s_{\text{cal}} = \frac{T_{\text{amb}} - T_{\text{cold}}}{c_{\text{amb}} - c_{\text{cold}}} \quad (4.4)$$

$$T_{\text{R}} = T_{\text{amb}} - s_{\text{cal}} \cdot c_{\text{amb}} \quad (4.5)$$

Using this method to calibrate the sensor, before making measurements in the atmosphere, provides the calibration parameters based on two temperatures which lie on the upper edge and below the expected measurement range. Thus, the validity of the calibration for the following measurements can be ensured, as long as the sensor itself is in the same surrounding conditions during the calibration as during the atmospheric measurements, and sufficient instrument stability is given.

Obviously, a radiometer mounted on the outside of an aircraft will not experience the same environmental conditions during an entire mission flight. Hence the necessity to investigate how the calibration parameters change under different atmospheric conditions surrounding the sensor. During a mission flight there are two parameters that change significantly whenever the aircraft changes altitudes: pressure and temperature. While the influence of the changing pressure cannot easily be simulated in a laboratory, the changing temperatures surrounding the aircraft can be simulated by placing the instrument inside a cold chamber, which has been done with the DLR-MTP (see Section 4.2.1), simulating the surrounding temperatures as found during the mission flights of the ML CIRRUS campaign in 2014 (see Figure 4.1). From this measurement series, the calibration parameters for different states of the instrument can be derived. Moreover, the built-in calibration target and ND, used for in-flight calibration, can also be characterised under varying instrument states. This permits the best possible accuracy and estimation of error, when applying in-flight calibration.

One important consideration is necessary, when looking at hot-cold calibration measurements: Due to partial reflection at the surface of the liquid nitrogen, a standing wave is present between the horn antenna and the surface of the fluid. As liquid nitrogen has a boiling temperature of ~ 77 K at standard pressure, it is constantly boiling and thus evaporating. With the change of the surface level, the wavelength of the standing wave between the sensor's antenna and the liquid nitrogen surface is modulated and with it the way it interferes with the signal from the absorber. When looking at a time series of measurements, this changing interference can be seen in a modulation of the measured time series, as shown in Fig. 4.7.

As the DLR-MTP is a total-power radiometer (Denning et al., 1989), the output voltage of the detector is proportional to the square of the incoming intensity (Ulaby et al., 1981; Woodhouse, 2005). Thus, the times with least interference of the original signal and the standing waves are defined by minima in the measured signal time series.

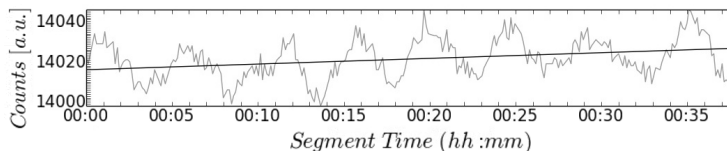
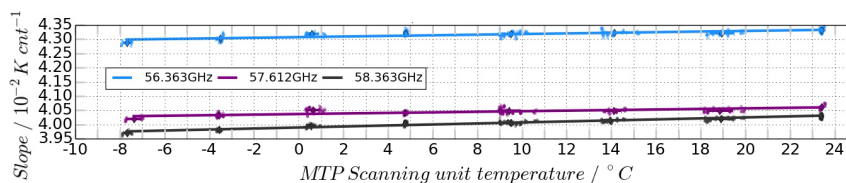
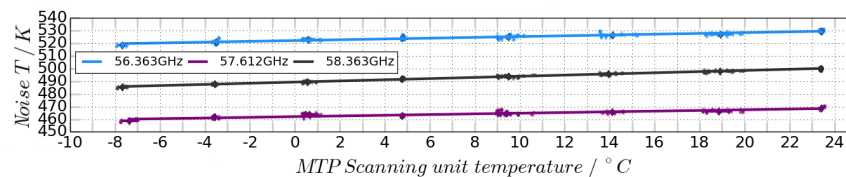


Figure 4.7: Time series of measurements of liquid nitrogen target. Grey line: original measurement; black line: linear trend in data

To find those minima in the cold chamber measurement time series, first a running average ($N = 15$) is used to minimise the noise on the data. Then, a spline-fit is used to find a smooth curve, representing the measurements. Finally, the minima of this smooth curve, interpolated to a high time-resolution, are used to identify those individual measurement cycles closest to the minima in the time series on which the calibration will be based. Note, that the modulation of the measured signal is different for each LO used in the measurements. Due to noise, the calibration becomes more reliable, if a mean of more than one cycle close to a minimum in the time series is used, hence, the five closest points to the position of a minimum are always included in the analysis.



(a) Slopes of calibration lines for standard LOs during cold chamber measurements.



(b) Receiver noise temperature for standard LOs of the MTP instrument.

Figure 4.8: Calibration parameters resulting from hot-cold calibration in cold chamber.

Following the considerations about changing calibration parameters with changing system states, the resulting calibration parameters are plotted over the corresponding scanning unit temperatures at the time the minimum in the cold target measurements occurred. Fig. 4.8a and 4.8b clearly show that the parameters do indeed change with the scanning unit temperature. That confirms the assumption, that DLR-MTP flight data cannot simply be calibrated by using fixed calibration line parameters from laboratory measurements at arbitrary room temperatures.

Still, it is possible to apply a linear fit to the data, providing a relationship between the MTP scanning unit temperature and the calibration parameters to be used at these temperatures. The same is true when using the hot target measurement signal as a reference, which might better represent the current state of the instrument than the scanning unit temperature. The linear fit parameters are summarised in Tables 4.1 and 4.2.

	Scanning unit temperature T_{sc}			Hot target counts c_{hot}		
	ref. T_{sc} [°C]	ref. s_{cal} [K cnts ⁻¹]	Lin. fit slope [10 ⁻⁵ cnts ⁻¹]	ref. c_{hot} [cnts]	ref. s_{cal} [K cnts ⁻¹]	Lin. fit slope [10 ⁻⁶ K cnts ⁻²]
LO [GHz]						
56.363	7.518	0.043154	1.0937	19486	0.043154	2.0141
57.612	7.527	0.040446	0.9989	19292	0.040446	1.8964
58.363	7.474	0.040031	1.7775	20213	0.040031	3.4361

Table 4.1: Linear fit values linking calibration slope values to MTP scanning unit temperature and hot target counts.

However, due to the changing conditions during a measurement flight, it cannot be ascertained that the hot-cold calibration in a laboratory provides valid calibration parameters for an entire data set recorded during measurement flight.

	Scanning unit temperature T_{sc}			Hot target counts c_{hot}		
	ref. T_{sc} [°C]	ref. T_R [K]	Lin. fit slope [K °C ⁻¹]	ref. c_{hot} [cnts]	ref. T_R [K]	Lin. fit slope [K cnts ⁻¹]
LO [GHz]						
56.363	7.518	524.492	0.3132	19486	524.492	0.0647
57.612	7.527	464.104	0.2716	19292	464.104	0.0559
58.363	7.474	492.777	0.4599	20213	492.777	0.0922

Table 4.2: Linear fit values linking T_R (calibration y -intercept) to MTP scanning unit temperature and hot target counts.

The linear fit is linking only the stable measurement conditions, which are not given throughout an entire measurement flight, e.g. after flight level changes. Hence, other methods, based on measurements taken during flight, might be more adequate. For this purpose, the hot-cold calibration from the cold chamber measurements is used to characterise the ND that is part of the instrument. It provides an offset signal that can be used as fitting point for the calibration line during flight (see next section). To characterise the ND offset signal, the ND is repeatedly activated during the cold chamber calibration measurements, enabling an offset signal characterisation under varying instrument conditions. Since the calibration parameters are already known from the hot-cold calibration, the temperature offset connected to the measurement signal offset created by the ND can be calculated. The ND characteristics of the DLR-MTP instrument will be discussed in the following section.

Calibration using the MTP built-in target

As mentioned in the previous section, a calibration with only one target at known temperature is possible, if the measurement of the calibration target is performed twice: Once in the usual way, and once with a noise diode, which adds a noise signal to the measurement signal behind the antenna, switched on. If the temperature offset associated with this noise signal, T_{ND} , is known, the calibration parameters can be derived from the measurements of the calibration target with and without the noise signal switched on:

$$s_{\text{cal}} = \frac{T_{\text{ND}}}{c_{\text{ND}} - c_{\text{hot}}} \quad (4.6)$$

$$T_{\text{R}} = T_{\text{hot}} - s_{\text{cal}} \cdot c_{\text{hot}} \quad (4.7)$$

Here, the measured signal of the built-in hot target at temperature T_{hot} is denoted as c_{hot} , and with the ND switched on as c_{ND} . This method is the default way to calibrate MTP measurements: There is a built-in calibration target, which is constantly heated to $\sim 45^\circ\text{C}$ at its rear side, to which the MTP's mirror is pointing after each measurement cycle during flight. This way, the calibration roughly follows the individual state of the instrument, whatever conditions the aircraft meets. Within the NASA-JPL retrieval algorithm, the readings from the calibration measurements using the ND are taken when converting the raw counts to BTs.

When applying this calibration method with MTP data, everything builds on two assumptions that will be tested in the following. The first is that the BT measured when pointing towards the heated target corresponds to the measurements of the temperature sensors at the back of the target. The second assumption is that the ND offset signal is the same each time the calibration measurements are performed. However, if this assumption is incorrect, large calibration errors can occur due to the fact that the two points used to determine the calibration line parameters are both at quite high temperatures: The built-in calibration target is up to 100 K warmer than the outside air temperatures during flight, and T_{ND} is added to this temperature.

First, the measured BT when pointing towards the built-in hot target is analysed using the cold chamber measurement data. Here, the calibration parameters, determined from the hot-cold calibration method, are used to calculate the hot target BT associated with the current measurement signal.

There are two Pt100 temperature sensors placed at the metal back of the target. The readings of these sensors confirm a constant temperature of the calibration target's back of $\sim 45^\circ\text{C}$ during entire mission flights. However, the housekeeping data of the sensor unit temperature indicate cold surrounding temperatures the MTP is experiencing during flight. These create a large temperature difference of up to 55 K between the heated back of the target and its front. As the calibration measurement is most influenced by the front of the absorber, of which the exact temperature is unknown, the interpretation of the Pt100 sensor readings as the true BT measured during calibration would lead to errors in the calibration calculation.

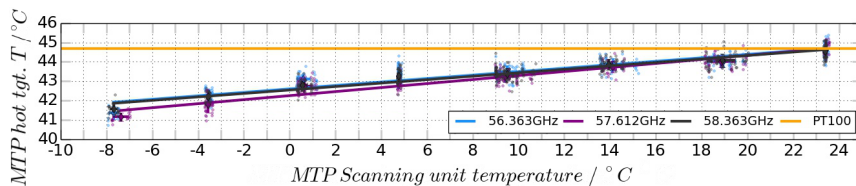


Figure 4.9: Calculated hot target BTs at different scanning unit temperatures during cold chamber measurements. Small dots: Single measurements contributing to the average at one scanning unit temperature. Orange line: Pt100 sensor readings.

Figure 4.9 shows the clear trend towards colder BTs with lower scanning unit temperatures, which correspond to a colder environment of the MTP instrument. The difference between the readings of the Pt100 sensors in the rear of the target and the correct BTs measured during calibration can be as large as 3 K. Still, the linearity of the sensor again allows for a linear fit between the current scanning unit temperature and the average associated hot target BT. Thus, in-flight calibration can be performed, using a corrected hot target BT, according to the MTP instrument’s housekeeping data.

LO [GHz]	ref. T_{sc} [°C]	ref. T_{hot} [°C]	Lin. fit slope [°C °C ⁻¹]
56.363	7.518	43.271843	0.089124
57.612	7.527	43.036542	0.103719
58.363	7.474	43.211868	0.088969

Table 4.3: Linear fit values used to correct the MTP hot target brightness temperature.

The parameters to correct the hot target BTs used in the calibration are shown in Table 4.3. Using wrong hot target BTs in the calibration process causes offsets in the calculated BTs, or even changes the slope of the calibration line derived from the in-flight calibration measurements. The error resulting from using a wrong hot target BT will be thoroughly discussed in Section 4.2.3, along with all other uncertainties in the calibration process.

The second assumption, that the ND offset signal is the same each time the calibration measurements are performed, still has to be tested. The calculated noise diode offset temperatures of the DLR-MTP, derived from the cold chamber calibration measurements, are shown in Fig. 4.10. For better comparability, the mean of the temperature- and count values have been removed. Those correspond to the reference values in Table 4.4. The ND offset temperature obviously depends on the count offset resulting from the induced noise on the input signal, which shows a clear dependency on the sensor unit temperature (colouring of the dots in Fig. 4.10). Again, it is possible to apply a linear fit between the recorded ND offset signal, $\hat{c}_{ND} = c_{ND} - c_{hot}$, and the associated ND offset temperature, derived from the hot-cold calibration method. This fit can be used to find the correct ND offset temperature required in the calibration of mission data. The linear fit values of this correction are shown in Table 4.4.

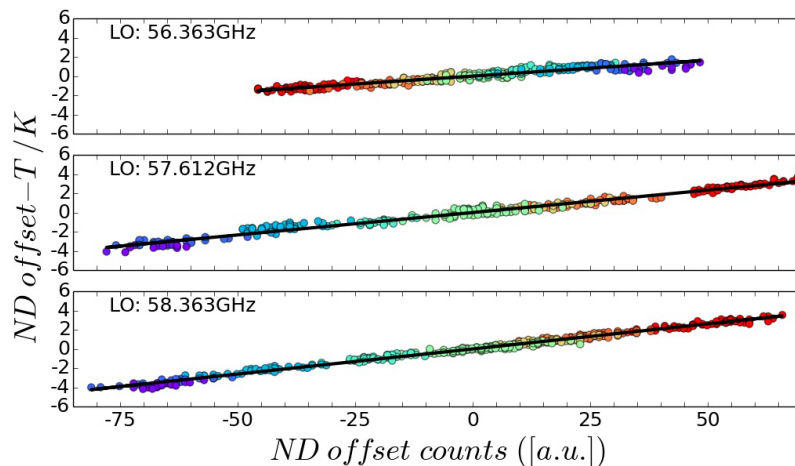


Figure 4.10: Calculated ND offset temperature for occurring ND count offsets (mean removed from both values). Colour-coding: MTP scanning unit temperature (Blue: colder - red: warmer). Black line: Linear fit, linking ND offset temperature to offset counts.

In Fig. 4.10 the deviation of noise diode counts from the linear fit can be seen as being as large as 20 counts for any of the three LOs. This spread translates into the remaining uncertainty in the ND offset temperature. The impact on the overall BT error will be discussed in Section 4.2.3.

LO [GHz]	ref. \hat{c}_{ND} [cnts]	ref. T_{ND} [K]	Lin. fit slope [K cnts ⁻¹]
56.363	2799	120.90706	0.033089
57.612	3049	123.43799	0.046590
58.363	2932	117.53960	0.052118

Table 4.4: Linear fit values linking noise diode offset temperature to MTP noise diode offset counts.

Unfortunately, during its deployment in the ML CIRRUS campaign in 2014, occasional failures of the ND were experienced. As shown in Fig. 4.11, the signal was not stable, caused by a faulty soldered joint, which was not identified before the campaign. Hence, the ND signal cannot be used for calibration of all flight data from this campaign.

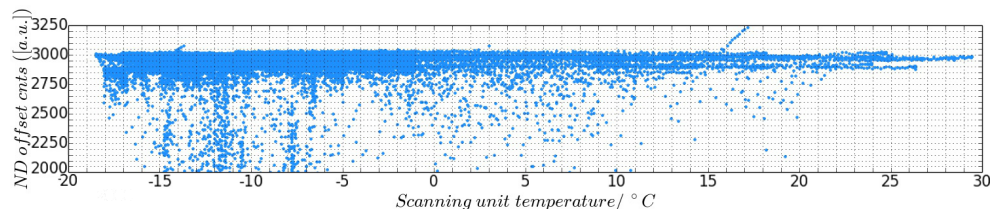


Figure 4.11: Noise diode offset counts at LO 57.612 GHz during all ML CIRRUS mission flights.

However, in-flight calibration is still possible, if another reference temperature for the determination of the calibration parameters is found.

This reference temperature can be provided by using the static temperature, measured by the HALO aircraft measurement system (HALO TS), interpreted as the BT measured at the 0° elevation (horizontal measurement). At this elevation, the MTP is pointing forward, measuring the same air masses, as the HALO nose-boom instruments. In Section 4.4 it will be shown that the MTP measurements at all standard LOs are most sensitive to the air directly in front of the sensor (less than 2 km distance). Thus, the average HALO TS value of the 13 s - period it takes to record an entire MTP measurement cycle (with the 0° measurement being in the middle of the cycle), is representative of the air masses probed by the 0° elevation measurements. Hence, the calibration parameters can be derived by:

$$s_{\text{cal}} = \frac{T_{\text{hot}} - TS}{c_{\text{hot}} - c_{0^\circ}} \quad (4.8)$$

$$T_{\text{R}} = T_{\text{hot}} - s_{\text{cal}} \cdot c_{\text{hot}} \quad (4.9)$$

Comparison of calibration methods using mission flight data

Basically, three methods to derive the correct BTs from MTP raw counts have been discussed. Calibration parameters linked to either the scanning unit temperature or the hot target measurement signal, have been derived from measurements in a cold chamber. Also, the calibration using the built-in hot target has been investigated. It has been found that the ND offset signal is linearly depending on the scanning unit temperature (T_{sc}) readings. The same has been found for the hot target brightness temperature. Corrections for the values of T_{ND} (depending on \hat{c}_{ND}) and of T_{hot} (depending on T_{sc}) have been introduced.

	lab. calib.		MTP tgt + ND				MTP tgt + TS	
	'CCS'	'CCH'	'TND0'	'TND1a'	'TND1b'	'TND2'	'TTS0'	'TTS1'
lab s_{cal}	T_{sc}	c_{hot}	-	-	-	-	-	-
lab T_{R}	T_{sc}	c_{hot}	-	-	-	-	-	-
T_{ND}	-	-	(u)	(c)	(u)	(c)	-	-
T_{hot}	-	-	(u)	(u)	(c)	(c)	(u)	(c)
TS	-	-	-	-	-	-	(u)	(u)

Table 4.5: Calibration methods tested with MTP data. T_{sc} indicates linking of the parameters to the scanning unit temperature, c_{hot} indicates linking to hot target measurement signal. Usage of uncorrected data is denoted with a '(u)', applied corrections with a '(c)'.

There are eight different ways to perform the calibration calculations with and without applying the corrections discussed in the previous sections, summarised in Table 4.5. All methods need to be compared to find the best practice of deriving BTs from MTP raw counts. All eight methods have been applied to the same set of mission data, using segments from all ML CIRRUS mission flights, during which the altitude of the aircraft did not change by more than 50 m between cycles, and no curves were flown (roll smaller than 5°).

Note that the definition of usable legs is not based on any parameters connected to the DLR-MTP, leading to the inclusion of measurement cycles with possibly unstable measurement conditions, e.g. shortly after altitude changes. The only exception is that only those segments are used, during which the ND did not show failures, which lead to faulty calibration values causing non-realistic BTs as large as 400 K or below 0 K. This way, 38 flight segments of at least 10 minutes length could be identified. The BTs are calculated based on each individual measurement cycle, but using the calibration coefficients calculated from the average of the relevant data from the seven previous cycles, the seven following cycles, and the cycle itself ($N = 15$), to account for noise on the calibration measurement signals.

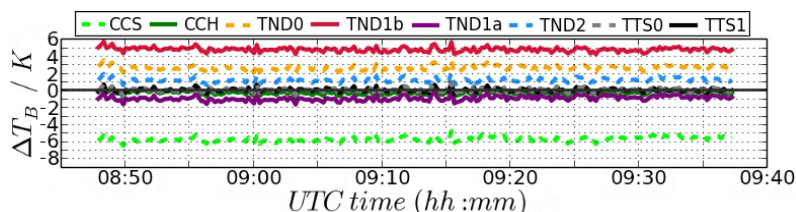


Figure 4.12: Difference between HALO TS and BTs derived from the 56.363 GHz measurements at 0° during ML CIRRUS mission flight 10, using the eight calibration strategies defined in Table 4.5.

As an example, the resulting BTs of the 56.363 GHz measurements at limb-viewing angle 0° during one selected segment of ML CIRRUS flight MLC10 on April 11th, 2014, are shown in Fig. 4.12. For plotting purposes, the difference between the BTs derived with each individual calibration method to the HALO TS is shown. The BTs resulting from all calibration methods show the same time-dependent variations, and mainly differ in their offset to HALO TS. This leads to the assumption that differences in the respective calibration coefficients affect the accuracy of the derived BTs more than the precision.

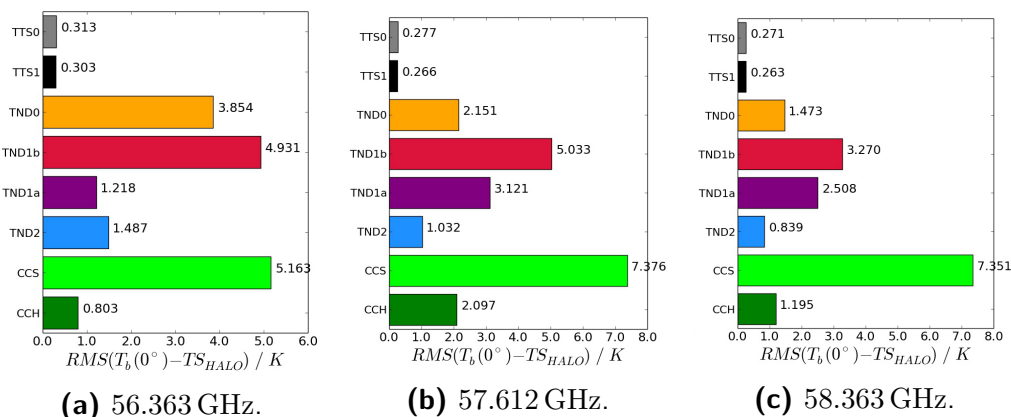


Figure 4.13: RMS difference between HALO TS and BTs, derived from MTP measurement signal at limb-viewing angle 0° at the three standard LO during all ML CIRRUS flight segments with no altitude changes, curves, or ND failures, longer than 10 min.

To compare the performances of the eight calibration methods, the root mean square (RMS) difference between the 0° BTs and HALO TS is shown in Fig. 4.13 for all three LOs.

The same colour-coding of the methods is used as in Fig. 4.12. The calibration methods producing BTs that deviate most from HALO TS under 0° are methods ‘*CCS*’ (light green bar) and ‘*TND1b*’ (red bar). They are obviously heavily influenced by systematic offsets, as seen in Fig. 4.12.

The systematic offset between the BTs can be removed by comparison to HALO TS. To do so, a leg-mean value of the HALO TS and the BTs of the 0° elevation measurements is used to determine the offset, which is subtracted from the BTs at all elevation angles:

$$T_B^{\text{corr}}(\nu_{\text{LO}}, \alpha) = T_B(\nu_{\text{LO}}, \alpha) - \left(\overline{T_B(\nu_{\text{LO}}, 0^\circ)} - \overline{TS} \right) \quad (4.10)$$

with $T_B(\nu_{\text{LO}}, \alpha)$ and $T_B^{\text{corr}}(\nu_{\text{LO}}, \alpha)$ denoting the original and the corrected BTs under elevation angle α and at a specific LO, respectively. $\overline{T_B(\nu_{\text{LO}}, 0^\circ)}$ denotes the leg-mean of the original BTs, measured under 0° elevation, and \overline{TS} represents the leg-mean HALO TS. By using leg-mean values to determine the offset, the corrected BTs will still contain individual small-scale structures, which might differ from those in the HALO TS measurements. As a result, this correction will not influence further analysis of the data concerning wave-like structures. Moreover, the corrected BTs resulting from using all eight strategies differ by less than 1 K at all elevation angles (see Fig. 4.14).

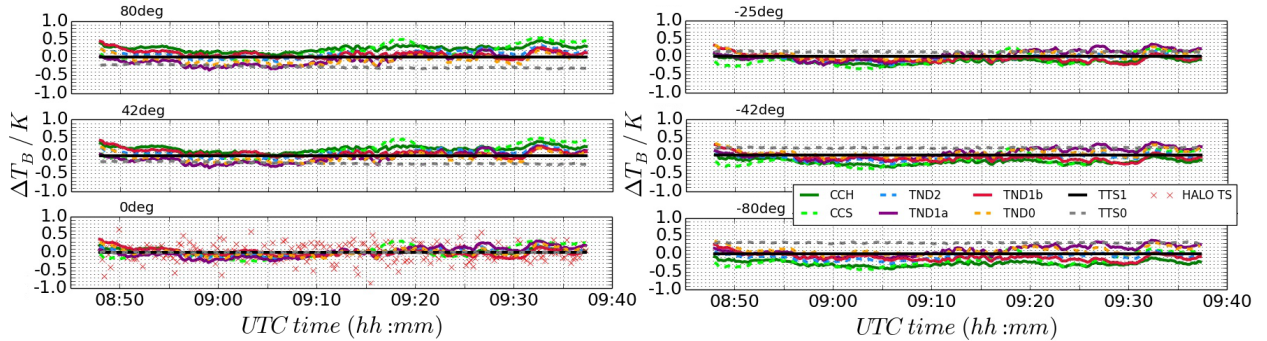


Figure 4.14: Difference between offset-corrected BTs derived with the eight calibration methods defined in Table 4.5 and the offset-corrected BTs of ‘*TTS1*’ at six different elevation angles. Red crosses in lower left panel: difference between method ‘*TTS1*’ and HALO TS.

Since the individual offsets differ by up to 7 K (cf. Fig. 4.13), this clearly indicates that removing the offset will not significantly change the shape of the temperature profile calculated in the retrieval. Now, plotting the RMS difference between the 0° BTs and HALO TS, shown in Fig. 4.15, gives a much better impression of the capabilities of the different calibration strategies.

Based on these findings, a decision is made, which strategy is to be preferred for calibration of mission flight data of the DLR-MTP instrument. Obviously, the methods that make use of HALO TS show the smallest deviation from HALO TS readings (see Fig. 4.15). However, if the least possible dependence on the HALO measurements is to be maintained, it is best to use method ‘*CCH*’, which uses the calibration values from the cold chamber measurements, related to the current hot target measurement signal.

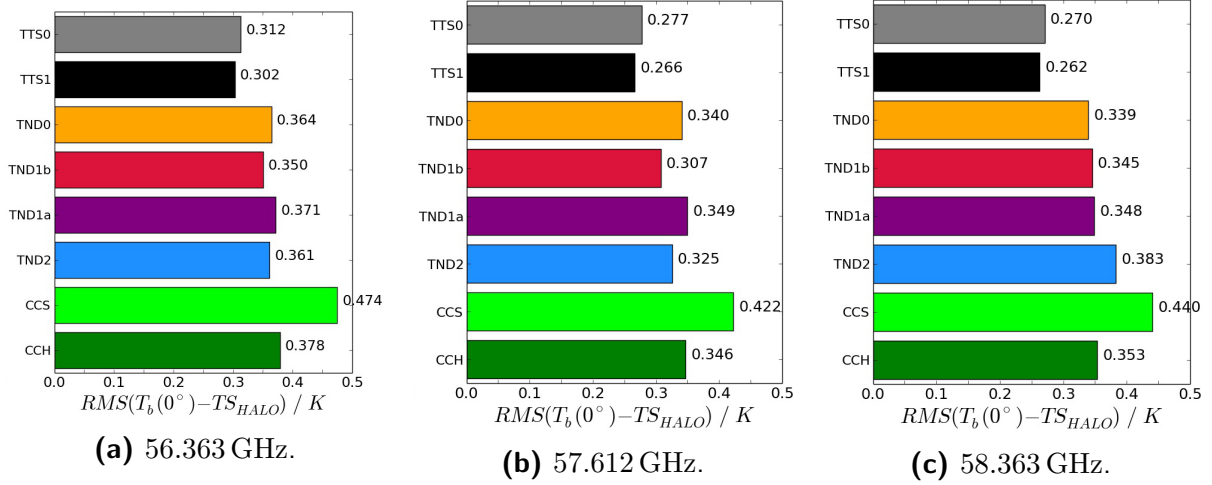


Figure 4.15: Same as Figure 4.13, but for offset-corrected brightness temperatures.

Whenever reliable ND measurements are available, method ‘*TND2*’, which uses the hot target measurement together with the ND offset (both with applied corrections as discussed in Section 4.2.2), also provides reliable results. Applying the corrections to T_{ND} or T_{hot} does not significantly change the result, but slightly smaller deviations from HALO TS are seen for the BTs derived using only the T_{hot} correction (method ‘*TND1b*’) or both corrections (method ‘*TND2*’).

Still, considering the unreliable ND signal during the ML CIRRUS campaign, the favoured calibration strategy is method ‘*CCH*’, also applying the offset-correction between the leg-mean 0° BT and the leg-mean HALO TS. The deviation between the resulting 0° elevation BTs and HALO TS is ~ 0.35 K at all three LOs for all ML CIRRUS flight legs with stable instrument conditions. Further investigation is needed to consider whether this value already represents the error in BT calculations. This will be discussed in the following.

4.2.3 Error estimation

To estimate the uncertainty of the calibrated BTs used as input to the retrieval algorithm, a number of uncertainties have to be taken into account. Those arise from the use of the different reference temperatures used in the calibration process. The three proposed calibration strategies are:

$$\begin{aligned}
 T_{\text{B}}^{\text{TS}}(c) &= s_{\text{cal}} \cdot c - (T_{\text{hot}} - s_{\text{cal}} \cdot c_{\text{hot}}) \\
 s_{\text{cal}} &= (T_{\text{hot}} - TS) / (c_{\text{hot}} - c_{0^\circ})
 \end{aligned}
 \tag{4.11}$$

$$\begin{aligned}
 T_{\text{B}}^{\text{ND}}(c) &= s_{\text{cal}} \cdot c - (T_{\text{hot}} - s_{\text{cal}} \cdot c_{\text{hot}}) \\
 s_{\text{cal}} &= (T_{\text{ND}}) / (c_{\text{ND}} - c_{\text{hot}})
 \end{aligned}
 \tag{4.12}$$

$$T_B^{\text{CCh}}(c) = s_{\text{cal}}^{\text{CCh}}(c_{\text{hot}}) \cdot c - T_R^{\text{CCh}}(c_{\text{hot}}) \quad (4.13)$$

Here, Eq. (4.11) represents the calibration methods based on the built-in calibration target with temperature T_{hot} and measurement signal c_{hot} , as well as HALO TS, associated with the measurement signal at 0° elevation (c_{0°). Eq. (4.12) represents the calibration using the built-in calibration target together with the ND signal with associated offset temperature T_{ND} . Finally, Eq. (4.13) represents the use of calibration parameters derived from the cold chamber measurements, referenced through the current measurement signal when pointing at the built-in target c_{hot} .

error source	name	estimation method	uncertainty	ref. value
Hot target brightness temperature	ΔT_{hot}	RMS to lin. fit in cold-chamber measurements	0.23 K	315.84 K
HALO static temperature	ΔT_S	RMS to 13s running average	0.13 K	250.0 K
ND offset temperature	ΔT_{ND}	RMS to lin. fit in cold-chamber measurements	0.25 K	120.63 K
Cold-chamber slope	$\Delta s_{\text{cal}}^{\text{CCh}}$	RMS to lin. fit in cold-chamber measurements	$8.244 \times 10^{-5} \text{ K cnt}^{-1}$	$0.04121 \text{ K cnt}^{-1}$
Cold chamber Y-intercept	ΔT_R^{CCh}	RMS to lin. fit in cold-chamber measurements	1.205 K	493.79 K
Measurement noise	Δc	Deviation from lin. fit in stable flight segments	6 cnts	18500 cnts

Table 4.6: Individual uncertainties of values used in brightness temperature calculation.

While individual uncertainties can be assigned to each of the contributing values (summarised in Table 4.6), it is clear that their uncertainties are not all independent. The most prominent example is the uncertainty of the y -intercept (T_R). It directly follows from the uncertainty of the slope of the line, but is also influenced by changing instrument states. Hence, a quadratic sum of the individual errors is not suitable and will lead to a large over-estimation of the total BT error.

To investigate the error contribution of the individual uncertainties to the calculated BTs, a sensitivity analysis is performed. Reference values (see last column in Table 4.6) for all parameters with uncertainties are used in a reference calculation. With these values, BTs are calculated for a range of counts between 17500 and 19725, which corresponds to the measurement signal range for atmospheric temperatures. Then, two control calculations are made, adding the corresponding uncertainties (see second-to-last columns in Table 4.6) in a way that the slope of the calibration line becomes as steep as possible ($s_{\text{cal}}^{\text{max}}$, red lines in Fig. 4.16 and 4.17), or as flat as possible ($s_{\text{cal}}^{\text{min}}$, blue lines in Fig. 4.16 and 4.17):

$$s_{\text{cal}}^{\text{max}} = \frac{(T_1 + \Delta T_1) - (T_2 - \Delta T_2)}{(c_1 - c_2) - 2\Delta c} \quad (4.14)$$

$$\rightarrow T_{\text{R}}^{\text{max}} = (T_2 - \Delta T_2) - s_{\text{cal}}^{\text{max}} \cdot (c_2 + \Delta c) \quad (4.15)$$

$$s_{\text{cal}}^{\text{min}} = \frac{(T_1 - \Delta T_1) - (T_2 + \Delta T_2)}{(c_1 - c_2) + 2\Delta c} \quad (4.16)$$

$$\rightarrow T_{\text{R}}^{\text{min}} = (T_2 + \Delta T_2) - s_{\text{cal}}^{\text{min}} \cdot (c_2 - \Delta c) \quad (4.17)$$

assuming that T_1 (with associated measurement signal c_1) is the warmer temperature used in the calibration. Comparing the BTs of the reference calculation to those of the two control calculations reveals the maximum uncertainty in the derived BTs.

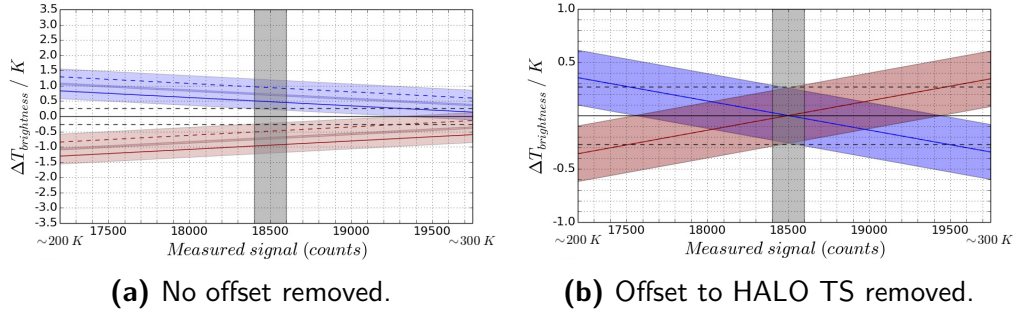


Figure 4.16: Error estimation of Calibration method using hot target brightness temperature combined with ND offset signal (a) uncorrected, and (b) with applied HALO TS (assumed to be at 250 K) offset correction. Vertical, grey shaded region: Expected range of measurement signals, if 0° measurement signal is at 18500 cnts (≈ 250 K). Black, dashed horizontal lines: Expected error induced by measurement noise of 6 cnts. Note the different y -scales.

As an example, the resulting differences between the reference run and the two runs with the steepest-possible slope of the calibration line, and the least steep slope are plotted in Figure 4.16. Here, the calibration method combining the built-in target with the ND is used (Eq. (4.12)). The shading around the two lines resulting from the two control calculations indicate the error range induced by 6 cnts uncertainty of the measurement signal that is to be calibrated. The range of uncertainty for a BT derived at a specific measurement signal is the range between the largest and the smallest BT calculated for this measurement signal in any of the control runs. From Fig. 4.16a it becomes obvious, that this range of uncertainty depends on the difference between the temperatures of the calibration targets and the measured atmospheric temperature.

In parallel to the offset correction introduced in the previous section, a BT correction for the control calculations is introduced. The resulting differences to the reference run are shown in Figure 4.16b. Here, the offset correction is calculated from the difference between the BTs of the control calculation ($T_{\text{B}}^{\text{ctr}}$), and that of the reference calculation ($T_{\text{B}}^{\text{ref}}$), at 18500 cnts:

$$T_{\text{B}}^{\text{corr}}(c) = T_{\text{B}}^{\text{ctr}}(c) - (T_{\text{B}}^{\text{ctr}}(18500) - T_{\text{B}}^{\text{ref}}(18500)) \quad (4.18)$$

This results in a shift of the blue and red lines in Fig. 4.16. Now, the minimal range of uncertainty in the BTs is around 18500 cnts, where the correction value is taken from. The vertical grey shaded region indicates the usual spread of measurement signals during the recording of one MTP measurement cycle. Within this region, the resulting error, indicated by the upper-most and lower-most edges of the blue- or red-shaded region, is smaller than the expected error from the measurement noise itself, indicated by the horizontal black dashed lines.

The same approach is applied to the calibration methods based on the MTP hot target in combination with HALO TS (Fig. 4.17a), and the calibration using parameters from the cold chamber measurements, related to the hot target measurement signal (Fig. 4.17b).

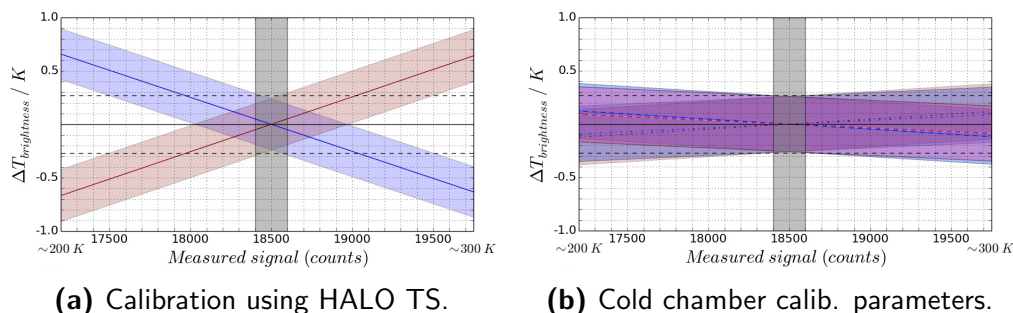


Figure 4.17: Same as Figure 4.16b, for calibration method (a) using MTP hot target and HALO TS and (b) using cold chamber calibration parameters.

The three approaches to calibrating MTP measurements produce comparable uncertainties in the derived BTs, once the offset to HALO TS has been corrected. Using this correction, the calibration method relating to the cold chamber measurements is most reliable in the case that the measured signals deviate largely from the measurement signal at the horizontal elevation. However, as indicated by the vertical grey shading in the figures, the usual range of counts in a single measurement cycle is small enough that the performance of all three calibration methods remains comparable, and the overall uncertainty is below the already established value of $\sim 0.35 K$ for all methods.

Other error sources

Besides the uncertainty error in the calibration, there is one more error source that should be considered, when creating the input for a retrieval algorithm: The pointing of the antenna beam is not exact, because the software controlling the pointing of the mirror assumes that the instrument is aligned with the horizontal plane. Considering the position of the DLR-MTP underneath the wing of the aircraft, however, this assumption is not correct. The mounting of the instrument leads to an offset between the horizontal plane of the instrument and the pitch angle measured by the aircraft system. Moreover, this offset is depending on the altitude and speed of the aircraft, which alters the pressure underneath the wing.

On the ground, the offset between the pitch measured by the aircraft system, and the actual pitch of the DLR-MTP can easily be determined. Furthermore, the inertial sensor, which is part of the DLR-MTP, constantly records the current pitch angle of the instrument. However, the measurement is disturbed by the electromagnetic signal caused by the near-by mounted stepper motor, making the data not reliable enough to allow for a real-time correction of the pointing of the MTP instrument. Thus, the real pointing has to be determined after the flight. Analysing the few reliable data points available after the two campaign deployments reveals that the relative deviation from the true horizontal plane was less than $1^\circ - 2^\circ$ during entire mission flights. The small antenna built into the sensor unit has a field of view that is relatively large (7.5° full width half maximum value (FWHM) of a Gaussian-shaped antenna function, see Fig. 3.3b). This leads to a wide altitude range that is covered by one measurement. Thus, it is safe to assume, that a deviation of the elevation angle of $1^\circ - 2^\circ$ from the assumed angle does not have a considerable influence on the retrieval performance. In the interpretation of already recorded DLR-MTP data the pointing error can thus be neglected.

4.2.4 Discussion

Three basic calibration strategies to derive the BTs recorded by the MTP have been presented and compared. While the linearity of the sensor could be established, the need to correct reference values of the hot target BT, the ND offset temperature, as well as adjusting the calibration parameters from laboratory environments according to the current instrument state has been demonstrated. All calibration strategies, with and without applied corrections, have been tested using a real data set from the ML CIRRUS campaign in 2014. The necessity of an offset-correction relative to HALO TS has been identified. The correction procedure has been introduced as comparing the leg-mean of the calculated BTs at 0° elevation angle to the leg-mean of HALO TS.

When comparing offset-corrected BTs to HALO TS of all ML CIRRUS mission flights, the RMS difference to the HALO TS is found to be between 0.25 K and 0.37 K. This range is valid for all calibration methods, as long as the ND functions properly. Otherwise the calibration methods using the ND offset signal cannot be applied and will lead to false results. It has been shown that the offset-corrected BTs of all calibration methods agree well within this specified RMS range at all elevation angles used during the ML CIRRUS campaign in 2014. At 0° elevation, the smallest deviation from HALO TS is seen in the BTs derived with the calibration methods that use the 0° measurements as one of the fitting points for the calibration line. The largest deviations from HALO TS (during flight legs with properly working ND), is seen in the calibration method that uses calibration parameters from the cold chamber measurements, linked to the system state via the readings of the MTP scanning unit temperature sensor.

The relative errors that remain after offset correction are clearly dominated by the contribution from measurement noise. Other uncertainties, such as the pointing of the instrument, are negligible compared to this uncertainty.

In the literature, another approach to derive the variance of measurement noise, σ_N , is:

$$\sigma_N = \frac{T_{\text{sys}}}{\sqrt{\Delta f \cdot \tau}} = \frac{T_R + T_{\text{atmo}}}{\sqrt{\Delta f \cdot \tau}} \quad (4.19)$$

in which Δf denotes the filter bandwidth, and τ represents the integration time (e.g. Ulaby et al., 1981; Woodhouse, 2005). The DLR-MTP has an ideal filter width of $\Delta f = 400$ MHz (see Fig. 3.3a) and uses an integration time of 200 ms. Assuming a receiver noise temperature of 493.79 K (see Table 4.6), and a mean atmospheric temperature of 250 K, this leads to a theoretical value of $\sigma_{N,\text{theo}} = 0.0827$ K, which is about four times smaller than the value established through the calibration of mission data. However, values used to derive the theoretical variance do not take into account, that the effective filter band width is smaller than the ideal value due to small deviations depending on frequency, and because of the gap in the centre. Moreover, it does not consider gain fluctuations (Ulaby et al., 1981). This is not representative of any real radiometric system, such as the MTP which explains the deviation from the value found through flight data analysis. It also shows that the uncertainty of derived BTs is dominated by the gain fluctuations. Using the standard deviation of the Gaussian distribution that describes the noise on the MTP measurements (see reference values in Table 4.6), a much larger value of $\Delta T_B = \Delta c \cdot s_{\text{cal,ref}} = 0.247$ K is found. This is still smaller than the value derived from mission flight analysis. However, when deriving the noise figures, only measurement sequences with nearly stable instrument parameters were used. This was not done in the mission flight analysis, which leads to a higher value of uncertainty in derived BTs, but also presents the most realistic value.

Considering the desire for mostly independent MTP measurements from other measurements (such as the HALO TS, which can then be used as reference), and the technical problems with the ND, experienced during the ML CIRRUS campaign in 2014, the favoured method of calibration is to use calibration parameters from the cold chamber measurement series, linked to the system state via the measurement signal while pointing towards the MTP built-in target. Using this method, BTs can be derived with a precision better than 0.37 K, and an accuracy matching that of the HALO TS measurements, which have an estimated overall error of 0.5 K (Ungermann et al., 2015).

4.3 Retrieval performances

The calibrated set of BTs measured by the MTP during one measurement cycle has to be converted to absolute temperatures of the atmosphere at different altitudes, using a retrieval software that links an absolute temperature profile to the measured BTs.

Currently, two algorithms are available to process MTP data: A statistics-based algorithm provided by NASA-JPL together with the instrument, and a new inversion algorithm developed at DLR. Detailed descriptions can be found in Appendix A.1. Here, only a brief summary of the underlying concepts is given.

Brief description of the JPL retrieval

The current standard MTP retrieval algorithm, provided by NASA-JPL with the purchase of the instrument (Mahoney and Gary, 2003), is based on a statistical approach, using radiosonde data as input. Figure 4.18 shows the working principle of the retrieval algorithm.

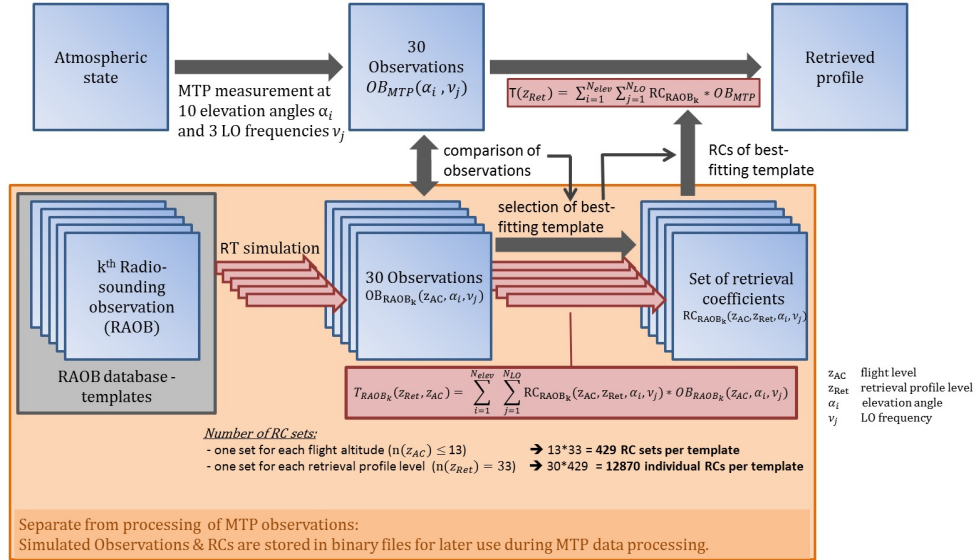


Figure 4.18: Schematic of the statistical retrieval method provided by NASA-JPL.

As stated in Denning et al. (1989), RT calculations are performed for a large number of radio sonde measurements typical for the time and region of the scientific measurement campaign. From the simulated measurements and the known absolute temperature profiles used in the RT calculation, so-called retrieval coefficients (RCs) are derived for each template profile. These RCs link the known absolute temperature at an altitude $T(z)$ to the simulated measurements of the current measurement cycle $T_B(\alpha, \nu)$ taken under the elevation angles α , and at LO ν :

$$T(z) = \sum_{\nu=1}^{N_{\nu}} \sum_{\alpha=1}^{N_{\alpha}} RC_{\alpha, \nu} \cdot T_B(\alpha, \nu) \quad (4.20)$$

After a measurement flight, the simulated BTs are compared to the real observations to find the best-fitting template by a multiple regression algorithm, following Strand and Westwater (1968). Once, the best-fitting template is found, the corresponding set of RCs is used, to calculate the absolute temperature profile, using Eq. (4.20).

The so-called ‘MRI’-value is the RMS difference between the observations \vec{y} and the previously simulated BTs of the best-fitting template, \vec{y}_{sim} . It is used as a control value to indicate whether the simulated BTs derived from the available radio sonde data used to establish the RCs fit well to the observations made during the research flight. Typically, ‘MRI’-values below one are considered to indicate good retrieval quality.

Brief description of the TIRAMISU retrieval

The Temperature InveRsion Algorithm for Microwave SoUnding (TIRAMISU) algorithm, (Xu et al., 2016), has been developed at DLR as an alternative to the statistical approach, which heavily depends on a priori knowledge of the atmospheric state. The working principle of TIRAMISU is depicted in Fig. 4.19. The goal of the algorithm is the inversion of the forward problem $\vec{y} = \mathbf{F}(\vec{x})$, in which \vec{y} represents the observations, \vec{x} represents the true state of the atmosphere, and \mathbf{F} is the forward function, known through the RT equation (see Chapter 3.1).

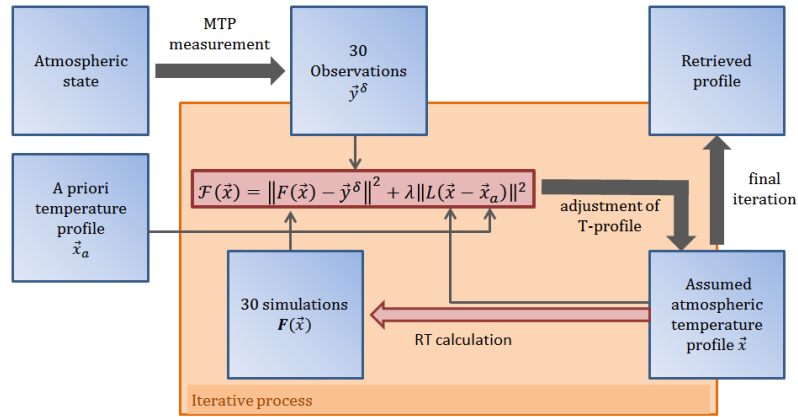


Figure 4.19: Schematic of the TIRAMISU algorithm.

Due to measurement errors, and the possibility that different states of the atmosphere can lead to the same set of observations, this equation cannot be mathematically inverted. Hence, an iterative process is used, minimising the Tikhonov cost function

$$\mathcal{F}(\vec{x}) = \|\mathbf{F}(\vec{x}) - \vec{y}^\delta\|^2 + \lambda \|\mathbf{L}(\vec{x} - \vec{x}_a)\|^2 \quad (4.21)$$

in which the index δ indicates that the observations contain uncertainties. The equation also contains the a priori temperature profile \vec{x}_a , e.g. taken from a climatology, and the regularisation parameter λ , which influences the weight of the penalty term in Eq. (4.21). \mathbf{L} denotes a regularisation matrix, which can be set to choose which properties of the a priori state influence the penalty term. The iterative process starts with a first guess, which can be freely chosen, e.g. as constant temperature at all altitudes or equal to the a priori. The observations that would be made in the corresponding atmosphere $\vec{x}_{i=0}$ are simulated and then compared to the real observations made during the research flight (first term in Eq. (4.21)). The Jacobian matrix with entries $\mathbf{J}_{ij} = \partial F_i / \partial x_j$ is used to determine which changes to the current atmospheric state \vec{x} have most impact on the simulated BTs. This, together with the value of $\mathcal{F}(\vec{x})$, is used to adjust the atmospheric state. The next iteration starts with the simulation of observations that would be made with the new state of the atmosphere. The algorithm terminates, if the change in $\mathcal{F}(\vec{x})$ between two iterations is sufficiently small.

For the testing of the retrieval methods, a set of 24 different mean radio sonde profiles, shown in Fig. 4.20, are used. These temperature profiles represent the templates on which the processing of ML CIRRUS campaign data with the statistical retrieval algorithm provided by NASA-JPL is based. Thus, they are chosen to represent a variety of atmospheric states during spring in Western Europe, while being distinctly different from each other, e.g. differing in tropospheric and stratospheric lapse rates, tropopause altitudes or tropopause layer thickness.

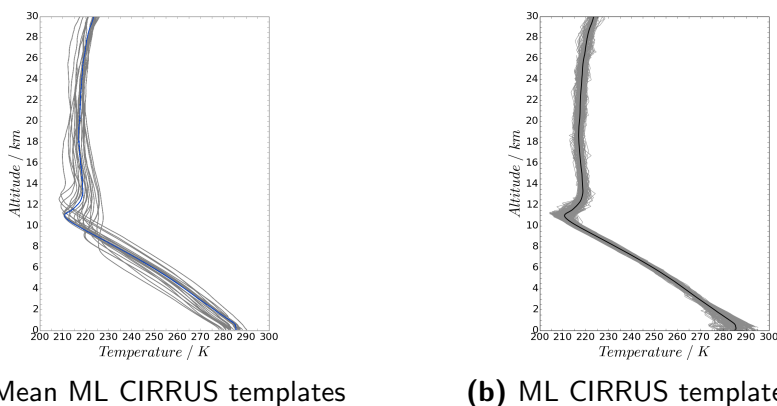


Figure 4.20: (a): T-profiles used in retrieval performance study. Blue line: Mean profile of the single template shown in (b). Black line in (b): mean profile; thin, grey lines: Individual profiles.

The forward calculation of MTP measurements based on the provided temperature profiles at flight altitudes 8 km, 11 km, and 14 km are carried out using the simulation-mode of the TIRAMISU retrieval. That uses the radiative transfer model Generic Atmospheric Radiation Line-by-line Infrared Code (GARLIC) (Schreier et al., 2014), and includes all known instrument characteristics of the MTP instrument (filter function and antenna characteristics). The simulated MTP BTs are then prepared for input to the two retrieval algorithms to test their performance in varying atmospheric conditions and flight levels.

4.3.1 Performance of JPL retrieval

First, the standard retrieval algorithm for MTP data, the statistical retrieval provided by NASA-JPL, is tested. The processing of simulated BTs has to be prepared, as will be described in the following, before showing the results of the study.

Data preparation for processing synthetic data with JPL retrieval

To be able to process data with the NASA-JPL retrieval algorithm, the simulated BTs have to be converted to the MTP raw data format. This also contains several housekeeping parameters, from which a calibration is calculated within the retrieval routines. Hence, when preparing the input for this algorithm, it has to be made sure that it contains housekeeping data that will not induce large errors that influence the outcome of the comparison of the two methods.

To ensure that the input data is processed correctly, the simulated BTs are converted to the correct input format by using real measurements from the ML CIRRUS campaign. This means that one block of real MTP data is copied, and only the line containing the actual measurements is replaced. Since this line has to contain raw counts, not BTs, a re-calibration has to be done in a way that ensures that the retrieval algorithm will come up with the correct BTs from the raw counts. The conversion of raw data to BTs within the retrieval algorithm is heavily depending on the user interface settings, and is repeatedly performed within the retrieval, following the relation:

$$T_B(\nu_{LO}, \alpha) = TS + \frac{c(\nu_{LO}, \alpha) - c(\nu_{LO}, 0^\circ)}{G(\nu_{LO})} \quad (4.22)$$

based on the outside air temperature HALO TS, and a gain value, $G(\nu_{LO})$, that is determined in each cycle, using many iterations and smoothing corrections. This complicated routine was replaced by a simple equation with fixed parameters:

$$T_B(\nu_{LO}, \alpha) = 313.15 + \frac{c(\nu_{LO}, \alpha) - c_{\text{hot}}(\nu_{LO})}{20} \quad (4.23)$$

which corresponds to using fixed values for HALO TS and $G(\nu_{LO})$. The numbers are chosen according to typical values and temperatures, assuming a calibration target temperature of $40^\circ\text{C} = 313.15\text{ K}$, and a gain of about 20, which is within the typical region of calculated gains in the retrieval algorithm. This way, it can be ensured that the BTs are calculated the same way in each cycle, and the simulated BTs can be easily converted to raw counts, while ensuring that the checking routines to filter out bad cycles (bad gain values, too large or too low count numbers, corrupt housekeeping values, ...) do not flag the measurements as faulty. The input data for the retrieval can now be based on any real measurement that has been made with the MTP, simply replacing the line containing the original measurement signal with the counts that represent the simulated BTs, T_B^{sim} :

$$c(\nu_{LO}, \alpha) = (T_B^{\text{sim}}(\nu_{LO}, \alpha) - 313.15) \cdot 20.0 + c_{\text{hot}}(\nu_{LO}) \quad (4.24)$$

using the value of $c_{\text{hot}}(\nu_{LO})$ from the real data block.

Results

One has to keep in mind that the statistical retrieval uses a simplified radiative transfer calculation, which is not as detailed as the radiative transfer model GARLIC, used by the TIRAMISU simulation mode. As both RT calculations use different instrumental settings and consider different amounts of trace gases in the atmosphere, the output of simulated BTs can differ strongly, especially for individual test profiles as seen in Fig. 4.21. Here, the mean differences between the simulated BTs of the two RT models at three different flight altitudes and under the ten different (limb-) elevation angles are shown. The differently simulated BTs display a fixed offset of around 3 K at the three standard LOs. The two additional LOs at 54.671 GHz and 55.221 GHz may be considered in a changed measurement strategy of the MTP (see Section 4.4).

The simulated BTs of these frequencies differ more strongly, especially at higher altitudes. This implies that the NASA-JPL retrieval is not ready to be used with settings different from the long-time standard.

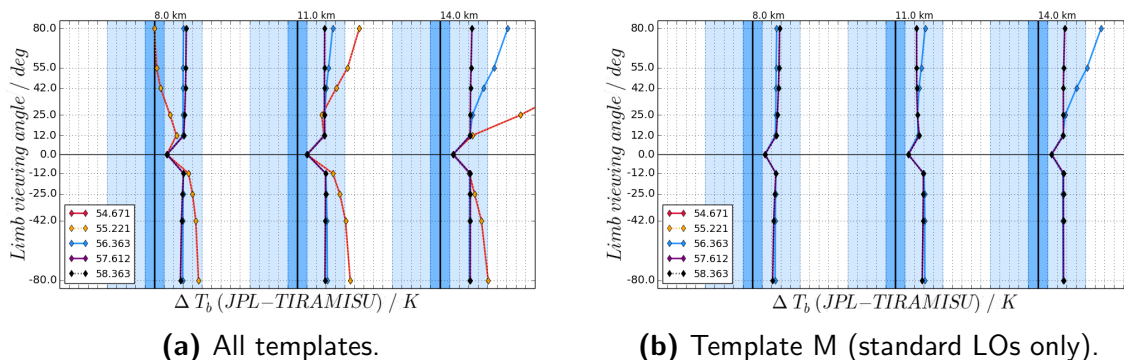


Figure 4.21: Mean difference between simulated BTs for (a) all ML CIRRUS templates and (b) template 'M', calculated with GARLIC and the built-in radiative transfer model of the statistical retrieval. Blue-shaded regions: ± 5 K interval around zero difference at the flight altitude indicated above the plot. Darker shading: ± 1 K region. Note that the lines representing the 54.671 GHz and 57.612 GHz data are covered by the 55.221 GHz and 58.363 GHz lines, respectively.

Also, it is striking, that the BTs at 0° elevation differ much less than at other viewing angles. This is due to the way the NASA-JPL RT calculation is set up: Here, the absolute temperature of the input profile at flight altitude is set as BT of the 0° measurement. When creating the input files with simulated BTs, this is represented by subtracting the offset between the 0° measurement and the outside air temperature from all observations.

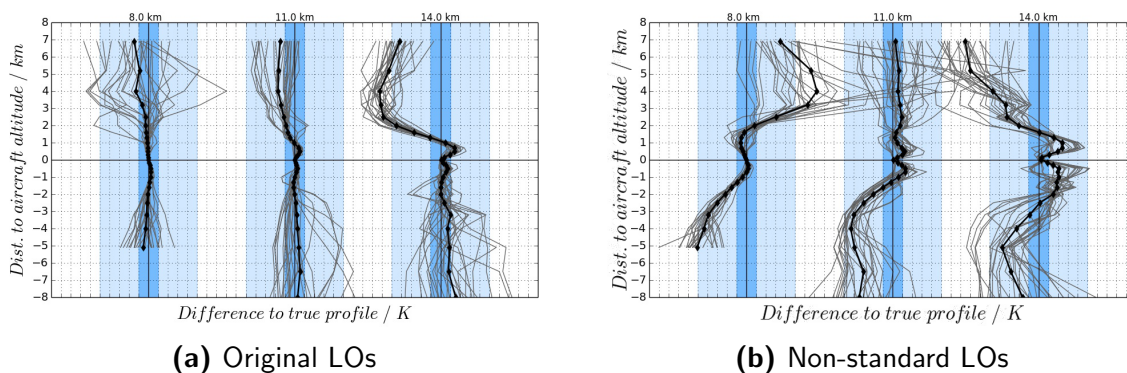


Figure 4.22: Difference between true and retrieved temperature profiles at three typical altitudes of the HALO aircraft. Blue-shaded regions: ± 5 K interval around zero difference at the flight altitude indicated above the plot. The darker shading shows the ± 1 K region.

As explained before, the NASA-JPL retrieval algorithm chooses the best-fitting template by calculating the RMS difference between the simulated BTs (from its own RT simulation) and the observations simulated with the simulation mode of TIRAMISU, \vec{T}_B^{obs} .

This can result in the choice of a template that is different from the true profile, but which has a similar average temperature and RMS between its simulated BTs and the \vec{T}_B^{obs} as the true profile. Still, the final retrieved temperature profiles usually agree well with the true profiles, especially within an altitude region of ± 1 km around the aircraft (see Fig. 4.22a). Further away, they diverge towards the profiles of the used templates, which can result in large differences to the true state. This behaviour can be explained when taking a closer look at the radiative transfer calculations in a study to investigate the instrument's sensitivity to various layers of the atmosphere (see Section 4.4).

When replacing the observation at 57.612 GHz with simulated BTs at 55.221 GHz, the retrieved temperature profiles are much less comparable to the true states (see Fig. 4.22b). This was already implied by the large difference of the NASA-JPL BT calculations to those of the TIRAMISU simulation mode at non-standard LOs.

All in all, when using the standard measurement settings, temperature profiles retrieved with the NASA-JPL retrieval algorithm usually represent the true profile well within a $\sim \pm 1$ km-region around flight altitude, even if RCs of templates are chosen, which are different from the true profile the BT simulation was based on. Still, the assumption that the 0° BT always equals the outside air temperature, that is made within the NASA-JPL retrieval, explains the little 'kink' towards 0 K difference to the true profile, that is visible at 11 km and 14 km flight altitude. This can influence the derived quantities based on lapse rates, as the absolute temperature profile will have the same 'kink' at flight altitude.

As mentioned in Section 4.3, the 'MRI'-value, giving the, RMS difference of the two vectors containing the simulated BTs of the used template, and the vector containing the input observations, can be used as indicator of retrieval quality. In the processing of the 24 temperature profiles used in this study, all MRI values are below 1, indicating good quality retrievals in all runs. However, there are still small differences, which could lead to the impression, that certain runs produced better-quality retrievals than others. From the comparison of the resulting temperature profile with the true profile, however, it can be seen that this value is not lower (better) in cases in which the template corresponding to the true profile was chosen. This implies that a low MRI does not indicate that the retrieved temperature profile is likely to have the correct shape or no offset to the true temperature profile. Hence, when using MTP data that was processed with the statistical retrieval, the MRI value is more of an indicator whether the RT calculations to derive the RCs are based on templates that resemble the atmospheric state during the observation well (MRI smaller than 1) or whether all simulated observations of the available templates already differ strongly from the real observations (MRI close to 2). The last case is a strong indication that the RT simulation has to be performed again, using different settings, regarding the template choices or the set of flight altitudes the RT calculations are based on, to better represent the conditions under which the observations were made. This situation could occur when covering remote locations during a measurement flight, such as open ocean or large deserts without radio sonde stations nearby.

4.3.2 Performance of the TIRAMISU algorithm

The same basic tests as described above, are performed using the TIRAMISU algorithm. While the optimal regularisation settings have already been tested by Xu et al. (2016), Zhang (2016), and Szajkowski (2016), the user still has many freedoms in their choice of the first guess, a priori temperature profile, and the requested output grid. Following Xu et al. (2016), the chosen set-up for the sensitivity study is a regularisation parameter based on expected error estimation, a first-order difference regularisation matrix, and a 0K initial guess at all altitudes. As would be done when retrieving real observations, the a priori temperature profile is based on the Committee on Space Research (COSPAR) International Reference Atmosphere (CIRA) climatology, in this case: April at 40°N, as the test-profiles represent radio sondes during Spring in Western-Europe.

Ideally, iterative algorithms are programmed to work independently from the user-defined output grid. However, TIRAMISU, as well as many other iterative retrieval algorithms, is implemented in a way that is very sensitive to the requested altitude resolution. At 11 km flight altitude, this sensitivity can be depicted by plotting the difference of the retrieved temperature profiles to the respective known true states for a number of different output grids, as shown in Figure 4.23. Here, the range of the output grids tested with TIRAMISU has been restricted to an area of roughly ± 1.5 km relative to flight altitude. The following section will give insight into the reasons for this decision. The tests have shown that using grid points further away from the aircraft leads to large oscillations in the retrieved temperature profiles, indicating that the MTP measurements provide too little information on the requested altitudes. Still, even when restricting the number of grid points and the distance to the aircraft at which output is requested, the performance of the retrieval of 24 radio sonde profiles differs distinctly, resulting in a large spread between the individual profiles, e.g. at grid ‘Grid01R’ or ‘Grid06R’ in Fig. 4.23.

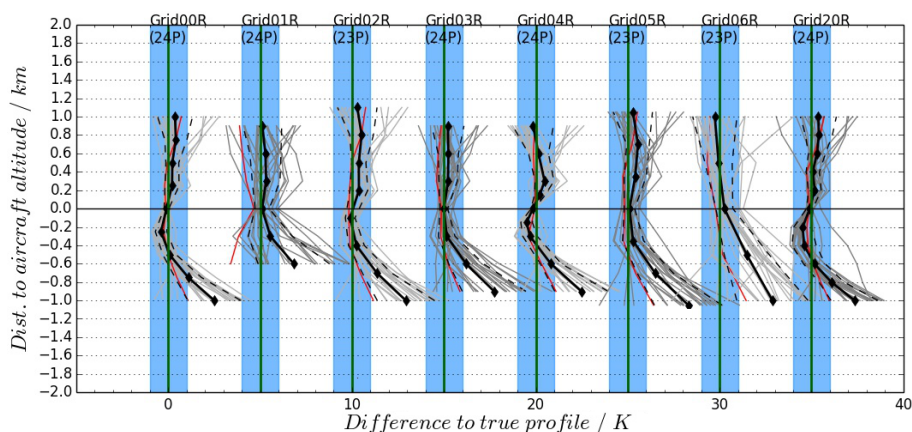


Figure 4.23: Difference between true and retrieved temperature profiles at 11 km flight altitude, using different output grids for TIRAMISU (indicated above the plot). Thick, black lines with diamond markers: average difference to true profile, taken from 24 individual profiles (thin grey lines). The profile marked in red is used as background in the 2D simulations, described in Chapter 5.2.

While the mean (thick black lines in Fig. 4.23) usually indicates robust results, at least above the aircraft, there are still large deviations from the true profiles for individual radio sonde templates (thinner, grey lines in Fig. 4.23). Of the tested output grids the grid ‘Grid3R’ is the most reliable, based on point-to-point RMS of the average difference to the true state and the small overall spread of the individual profiles. Thus, this grid is used in the sensitivity studies with two-dimensional input data, described in Chapter 5.2.

With the current set-up, every single grid shows considerable deviations of up to 3 K between the individual retrieved temperature profiles and the respective true states below the aircraft. Especially the fact that this deviation grows with the distance to the aircraft, even within a ± 1 km distance to the aircraft, gives reason to doubt that a correct determination of lapse rates or potential temperatures at these altitudes will be possible with data processed with the TIRAMISU algorithm using its current settings. Further sensitivity studies to determine the optimal user settings are required, before the algorithm can be utilised to analyse MTP measurements, in which the true state of the atmosphere is not known. However, when comparing the spread of the individual profiles, the tests with the TIRAMISU algorithm show that once the best settings are found, the output is probably more robust than that from the NASA-JPL retrieval algorithm, especially at higher aircraft altitudes. Moreover, the inversion algorithm is a more physics-based approach than the statistical algorithm, which heavily depends on the given radio sonde data base and has proven to be not suited to process MTP data recorded at non-standard LOs.

4.4 MTP range of sensitivity

The output of the statistical retrieval, which has been provided by NASA-JPL with the purchase of the MTP instrument, suggests measurement sensitivity to a region of up to ± 8 km around the aircraft. However, the retrieval performance, as shown in Section 4.3.1, shows that the retrieval results for simulated measurements of known temperature profiles only agree reasonably well with the correct result within a region of about ± 1 km around the aircraft. The tests conducted with TIRAMISU support this by showing non-realistic outputs for grid points outside a $\sim \pm 1.5$ km range. This is in agreement with implications given in the analysis of data from older MTP instruments. The MTP flown on the ER-2 research aircraft at ~ 20 km altitude only has a measurement range of $\sim \pm 2 - 3$ km around flight altitude, while using similar LOs as the current instrument (i.e. 57.3 GHz and 58.8 GHz) (Gary, 1989). Likewise, the height range of the DC-8 instrument, with LOs at 55.51 GHz, 56.66 GHz, and 58.79 GHz has an ‘applicable range’ (within which the weighting function drops to $1/e$) of roughly ± 2.8 km (Gary, 2006). In their conclusion of analysis of data recorded with the NCAR-MTP Davis et al. (2014) mention that “it appears that more than about 3 km below the aircraft, the MTP may have difficulty identifying subtle mesoscale variations of temperature”.

Taking a closer look at the RT equation (Eq. (3.1) in Chapter 3.1) will help to find out which altitude range around the flight altitude of the aircraft the measurements of the current MTP instrument really is sensitive to. Within the RT equation, all terms in the integrand, except the Planck function, are defined as the weighting function (WF):

$$W(\nu, s) = \alpha(\nu, s) \cdot e^{-\tau(s)} = \alpha(\nu, s) \cdot \exp\left(-\int_0^s \alpha(s') ds'\right) \quad (4.25)$$

The WFs for the three standard LOs used by the DLR-MTP under the nine non-horizontal viewing angles used in the standard measurement strategy are shown in Figure 4.24. For RT calculations needed to derive the WFs, the Python scripts for Computational Atmospheric Spectroscopy (Py4CATS)¹ tool (Schreier and Gimeno García, 2013) is used. The WFs are derived from absorption coefficients calculated using high-resolution transmission molecular absorption database (HITRAN) values for line parameters, and assuming a mid-latitude summer atmosphere. For better comparison they are scaled to equal 1 at flight altitude. For comparison, WFs of the Advanced Microwave Sounding Unit-A (AMSU-A) (Karbou et al., 2005), used on satellites, are shown in Fig. 4.24d. In this reference case, the altitude from which the most information within the measurement is gathered corresponds to the altitude of the peak in the WF.

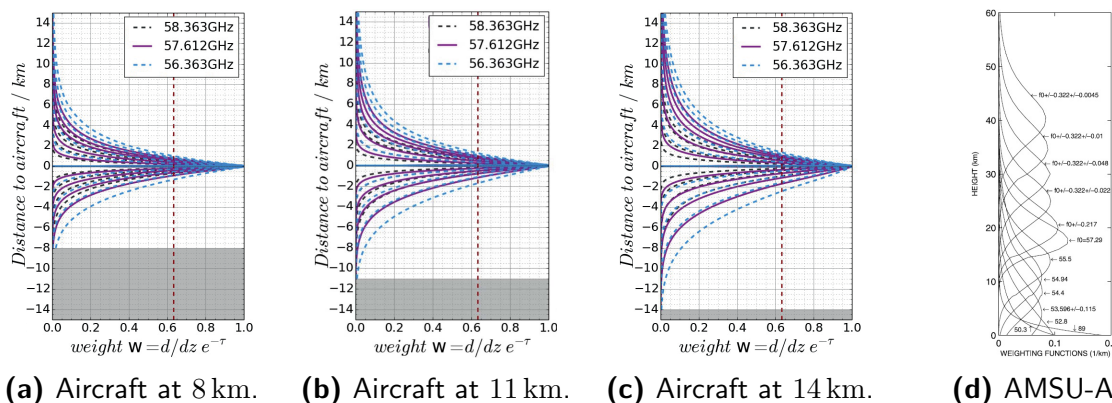


Figure 4.24: Relative WFs of the three MTP standard LOs (nine lines each, for each non-horizontal viewing angle), calculated at aircraft altitudes of (a) 8 km, (b) 11 km, and (c) 14 km. Red, dashed lines indicate where W has dropped by $1/e$. Grey areas at the bottom: altitude ranges that would be below the surface at the respective aircraft altitudes. (d): WFs of the AMSU-A2 instrument, adapted from Fig. 1b in Karbou et al. (2005). Note the different y-axis limits.

The MTP WFs look nearly symmetrical above and below flight level (differences do not show due to the scaling of the plots), and do not show any peaks, indicating that most information is gathered at flight altitude. Nonetheless, from the difference between measurements under varying elevation angles and using different LOs, information on the vertical temperature profile can still be gathered.

¹available at <http://atmos.eoc.dlr.de/tools/Py4CATS/>; downloaded on 15 Oct. 2015

The influence of decreasing pressure with altitude is clearly depicted by the larger spread of the lines in Figure 4.24c than in Figure 4.24a. Still, even at an aircraft altitude of 14 km, which is just below HALO's ceiling altitude, the values of the WFs have dropped by $1/e$ at roughly ± 2 km distance to the aircraft. Considering that all measurements receive at least 50 % of the signal from within this altitude region, it is reasonable to assume, that not much additional information can be found further away, which has already been indicated by the results of the retrieval of simulated BTs, shown in Sections 4.3.1 and 4.3.2. Here, the spread between the individual retrieved temperature profiles started to grow considerably with larger distance to the aircraft, beginning at $\sim 1.5 - 2$ km distance.

As already mentioned in Chapter 3.2, the current measurement settings of the DLR-MTP have not always been the standard of MTP measurements. The very first MTP, as described in Denning et al. (1989), was flown during the STEP in 1984. It used two LOs at 57.3 GHz and 58.8 GHz. It already used ten limb viewing angles within a range of -50° and $+60^\circ$. Later, another MTP instrument was flown on NASA's DC-8, which already used three LO frequencies at 55.51 GHz, 56.65 GHz, and 58.80 GHz, while scanning within a limb angle range of $\pm 80^\circ$ (Mahoney, 2004). Only the latest versions of the MTP use the LOs positioned at the centre frequencies of strong oxygen absorption lines (Lim et al., 2013). The hard- and software of the DLR-MTP allow for changes to the set of LOs as well as the set of elevation angles. Possible adaptations will be discussed in the following.

Possible changes to the set of LOs

In the research of GW propagation within the UTLS it would be of great interest to provide measurements that are sensitive over a larger vertical layer of the atmosphere than with standard settings of the MTP. In the present setting, the LOs are chosen as the centre frequencies of the three strongest oxygen absorption lines within the 60 GHz oxygen complex. For those frequencies, the atmosphere is optically thick, even at a flight altitude of 14 km, as indicated by the WFs shown in Fig. 4.24c.

Logically, the best idea to widen the range of sensitivity would be to use different LOs that are located at weaker absorption lines, on the edge of the 60 GHz oxygen absorption complex (cf. peaks in Fig. 4.25b), or even between two lines, as was done with the older MTP instruments. However, to maintain a good quality of the retrieved temperature profiles, an LO has to be chosen around which the absorption strength is somewhat symmetrical (i.e. similar shapes of the flanks of the lines within the filter range). If an LO were chosen so that a strong absorption line would be close enough to just be included on the edge of the filter, the measured signal could be strongly influenced by a small error in the placement of the LO (synthesizer errors). Since the 60 GHz oxygen absorption complex is composed of strong absorption lines, that are located close to each other, pressure broadening at lower altitudes, which can lead to overlapping of lines, has to be considered as well, when deciding about a new measurement strategy. This influence is also smallest, if the centre frequency of a line is chosen as LO. Concerning the threshold of possible frequencies, water vapour absorption becomes important in RT calculations, whenever frequencies close to 50 GHz are chosen.

Here, the oxygen absorption is not dominant over the water vapour absorption any more. Hence, the best place to look for more LO candidates are the oxygen absorption lines at the weaker edge of the V-Band, i.e. those lines between 52.021 GHz and the weakest absorption line already in use, the 56.363 GHz line. According to Liebe et al. (1992), there are eight strong oxygen absorption lines between 52 GHz and the 56.363 GHz line, which is already used as MTP LO frequency. Figure 4.25 shows the simulated BTs the MTP would measure in an atmosphere with a constant temperature of 250 K up to 110 km altitude. The simulation is made, using the simulation mode of TIRAMISU, for the whole spectrum of frequencies between 50 GHz and 60 GHz with 0.01 GHz resolution at six different flight altitudes between 2 km and 15 km, which is the ceiling altitude of the HALO aircraft.

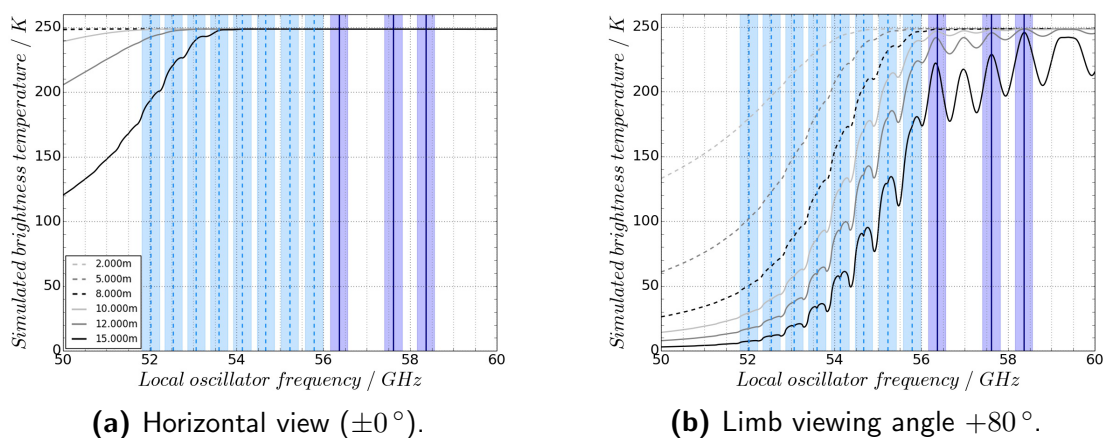


Figure 4.25: Simulated BTs at LOs between 50 GHz and 60 GHz at different flight altitudes (different line styles). Solid, vertical lines: Standard LOs of the MTP; dashed vertical lines: strong lines that could be used as new MTP LO. Shading around vertical lines: MTP filter width.

In the figure, the resulting BTs at limb-viewing angle 0° and $+80^\circ$ are shown. The centre frequencies of the oxygen absorption lines are indicated by vertical lines, with an indication of the filter bandwidth as shaded regions around the lines. Whenever the simulated BT is lower than the constant temperature of the assumed atmosphere, at 250 K, the atmosphere is partly transparent for the current frequency, meaning that part of the measured signal originates from the cold space at 2.7 K (Waters, 1976). If the transparency of the atmosphere is too large, only a small part of the measured signal originates from air masses close to the aircraft. Measurements at too weak absorption lines cannot contribute much to the information on the temperature profile. Furthermore, when measuring downwards, the signal could be dominated by the surface temperature, which might not be well-known, e.g. over open ocean. Moreover, if the atmosphere is partly transparent for an LO at the $\pm 0^\circ$ limb measurement, it cannot be used for calibration any more, as the measured BT is lower than the outside air temperature. This would lead to errors in the retrieval input. Hence, for adding LOs to the MTP measurement strategy, only oxygen absorption lines between 54 GHz and 56 GHz are tested. The weighting functions of the complete set of possible LOs at the three aircraft altitudes of 8 km, 11 km, and 14 km are shown in Figure 4.26.

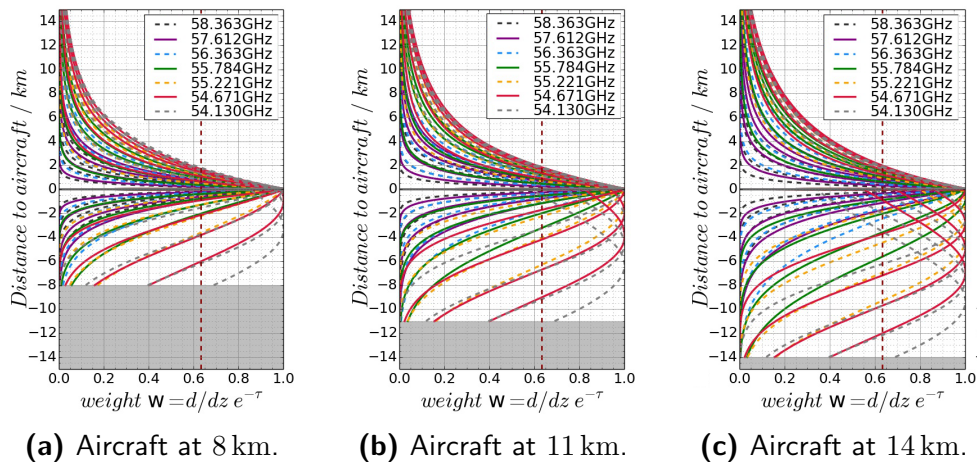


Figure 4.26: Relative WFs of possible MTP LOs, calculated at aircraft altitudes of (a) 8 km, (b) 11 km, and (c) 14 km. Red, dashed lines indicate where W has dropped by $1/e$. Grey areas at the bottom: altitude ranges that would be below the surface at the respective aircraft altitudes.

Obviously, the new LOs at weaker oxygen absorption lines (light grey, red, yellow, and green lines in Fig. 4.26), are sensitive to a much wider range of altitude layers, especially below the aircraft. However, the figure shows, that even for the measurements at 54.13 GHz and 54.671 GHz, (light grey and red lines in Fig. 4.26) the range of sensitivity above the aircraft is not much larger than for the standard LOs. This is due to the partial transparency of the atmosphere at these frequencies, indicated by low BTs in Fig. 4.25b.

In Section 4.2 it has been shown that a good way of calibrating the MTP measurements is to use the HALO TS. However, this method can only be applied, if the atmosphere is not partly transparent at the chosen LO at the $\pm 0^\circ$ measurement, even at the aircraft's ceiling altitude of 15 km. From Fig. 4.25a it can be seen that this is still true for LOs at frequencies larger than 54 GHz. The WFs for the horizontal measurements at the possible MTP LOs are shown in Fig. 4.27.

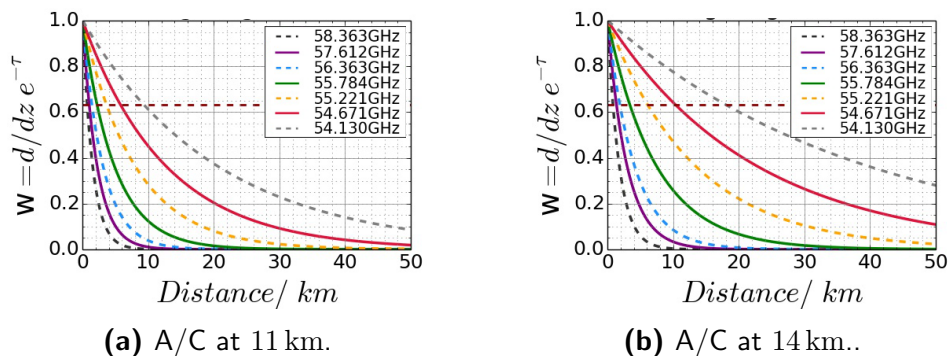


Figure 4.27: Relative WFs of all possible LOs at $\pm 0^\circ$ limb angle at aircraft altitudes of (a) 11 km and (b) 14 km. The horizontal, red, dashed line indicates where W has dropped by $1/e$.

It shows, that measurements at the weaker absorption line frequencies are influenced by atmospheric air much further away from the aircraft, than the standard LO measurements are. If frequencies of weaker absorption lines are used as LOs, one has to be cautious when including the HALO TS in the calibration process, as air from distances up to several tens of kilometres contributes to the measured MTP signal. While for long enough legs this is not likely to affect the offset correction with the leg-mean HALO TS, the large distance of air masses contributing to the signal has to be considered in the calibration process.

Finally, if new LOs are added to the MTP measurement strategy, a new balance between vertical and horizontal resolution of measurements has to be found. Just adding LOs will extend the time it takes to record the data of one profile. Simply exchanging LOs might reduce the vertical resolution of the retrieved temperature profile close to the aircraft. The best approach will probably be a mix of more LOs and less elevation angles.

Possible changes to the set of elevation angles

When discussing changes to the set of elevation angles to be used in the MTP measurements, the changes to the signal path through the atmosphere have to be considered. Basic geometric considerations show, that changing the angle under which the measurement is taken, changes the length of the path the signal travels through one layer of the atmosphere. By hardware-design limitations, the range of MTP viewing angles is limited to $\pm 80^\circ$. To consider a new, feasible set of elevation angles, it makes sense to compare the path lengths of all possible elevation angles α with the shortest possible path length at maximum elevation ($\pm 80^\circ$):

$$l_{\text{rel}80^\circ} = \frac{\cos(10^\circ)}{\cos(90^\circ - \alpha)} \quad (4.26)$$

The relative path lengths to the $\pm 80^\circ$ angle are shown in Table 4.7. Those elevation angles used in the MTP standard strategy are underlined. Especially the three largest elevation angles used in the standard MTP measurement strategy do not differ much in their path lengths. Choosing an inappropriate set of elevation angles results in the WFs of different measurements being very similar (over-laying lines, e.g. below aircraft altitude in Fig. 4.24). Two measurements with similar WFs will hold nearly the same information on the atmospheric temperature profile and are redundant.

Taking the assumptions about the signal path length into consideration, leads to a set of elevation angles, resulting in measurements with as much independent information as possible. To derive a new set of elevation angles for MTP measurements, a rule of thumb can be used, that with each new angle the length of the signal path at 80° should be added, meaning that $l_{\text{rel}80^\circ}$ is close to an integer. Corresponding rows are highlighted in green in Table 4.7. Using the elevation angles 11° , 14° , 19° , 30° , 41° , and 80° would give factors of ≈ 5 , ≈ 4 , ≈ 3 , ≈ 2 , ≈ 1.5 , and 1. However, this set would still produce redundant information, due to the fact, that the antenna beam of the MTP instrument has a field of view of $\approx 7.5^\circ$. The measurements at 11° and 14° would thus overlap, and probably also not differ much from the measurement at 19° .

α	$l_{\text{rel}80^\circ}$								
1°	56.428	13°	4.378	19°	3.025	28°	2.098	41°	1.501
[...]		14°	4.071	20°	2.879	29°	2.031	42°	1.472
5°	11.299	15°	3.805	[...]		30°	1.97	[...]	
[...]		16°	3.573	25°	2.33	31°	1.912	55°	1.202
11°	5.161	17°	3.368	26°	2.247	[...]		[...]	
12.0°	4.737	18°	3.187	27°	2.169	40°	1.532	80°	1.0

Table 4.7: Signal path lengths relative to $\pm 80^\circ$. Underlined: Elevation angles used in the standard measurement strategy. Green numbers: Possible candidates for a new strategy.

Since it might be of use to reduce the total number of measurements in favour of better horizontal resolution, it is worthwhile considering to use only the 14° angle to replace all three measurements at 11° and 14° , and 19° . Thus, including the horizon measurement, only nine elevation angles would be left. Furthermore, in the standard measurement strategy, the down-looking angle set is reduced by leaving out the -55° limb-angle. Since the up-looking WFs of all possible LOs are very similar, the opposite would be more feasible: use more down-looking angles to enhance the resolution of measurements below the aircraft, but reduce the number of up-looking angles, e.g. by leaving out the $+41^\circ$ measurement.

Proposal of new MTP measurement strategy

When putting together the findings of the above sections, redundancy in information within one measurement cycle can be reduced. Moreover, at least below the aircraft, the range of sensitivity of the MTP measurements can be significantly enlarged by using at least one LO at the frequency of a weaker oxygen absorption line. As the MTP is mounted on a moving platform, it is necessary to consider the time it takes to record one complete measurement cycle, in order to maintain the best possible horizontal resolution of the measurements. The time it takes to record a profile is the integration time (t_{int}) multiplied by the number of elevation angles (A) and the number of LOs (L). Currently, the MTP uses an integration time of 200 ms, to which a waiting-time of 100 ms has to be added. This waiting-time is used to make sure that the LO signal from the synthesizer is stable after changing the frequency between measurements. At the end of each profile recording, the calibration measurement is done twice (with and without ND signal) for each LO, and some time for the stepper motor to find the current viewing angle position (t_{step}) has to be added after each viewing angle adjustment:

$$t_{\text{cyc}} = A \cdot L \cdot (t_{\text{int}} + t_{\text{wait}}) + 2 \cdot L \cdot (t_{\text{int}} + t_{\text{wait}}) + A \cdot t_{\text{step}} \quad (4.27)$$

At the moment, the recording of one profile takes about 13 s, which indicates that the time to set the stepper motor position takes about 0.2 s, in total. Purely adding one LO to the measurement strategy would increase the time to record a profile to ~ 16.5 s, decreasing the horizontal resolution by ~ 700 m compared to the standard strategy.

However, already reducing the set of elevation angles from 10 to 8, while using 4 LOs brings the recording time down to ≈ 14 s, which would leave the horizontal resolution comparable to the standard settings.

Name	Elevation angles	LOs [GHz]	t_{cyc}
standard	$+80^\circ, +55^\circ, +42^\circ, +25^\circ, +12^\circ,$ $\pm 0^\circ, -12^\circ, -25^\circ, -42^\circ, -80^\circ$	56.363, 57.612, 58.363	~ 13 s
'10E3LO'	$+80^\circ, +42^\circ, +25^\circ, +12^\circ, \pm 0^\circ,$ $-12^\circ, -25^\circ, -42^\circ, -55^\circ, -80^\circ$	55.784, 56.363, 58.363	~ 13 s
'8E4LOa'	$+80^\circ, +30^\circ, +16^\circ,$ $\pm 0^\circ, -16^\circ, -30^\circ, -41^\circ, -80^\circ$	54.671, 56.363, 57.612, 58.363	~ 14 s
'8E4LOB'	$+80^\circ, +30^\circ, +16^\circ,$ $\pm 0^\circ, -16^\circ, -30^\circ, -41^\circ, -80^\circ$	54.671, 55.221, 56.363, 58.363	~ 14 s

Table 4.8: Proposed measurement strategies for future missions of the DLR-MTP.

Three possible new measurement strategies are summarized in Table 4.8, which could be worthwhile to test for future missions of the similarly built MTP instruments at DLR and NCAR. The WFs, calculated for all those strategies at aircraft altitude 11 km, are shown in Fig. 4.28 along with WFs calculated for the standard strategy as used in the 2014 HALO campaigns (Fig. 4.28a). All three new strategies have the advantage of using at least one weaker absorption line frequency, and thus having an increased range of sensitivity.

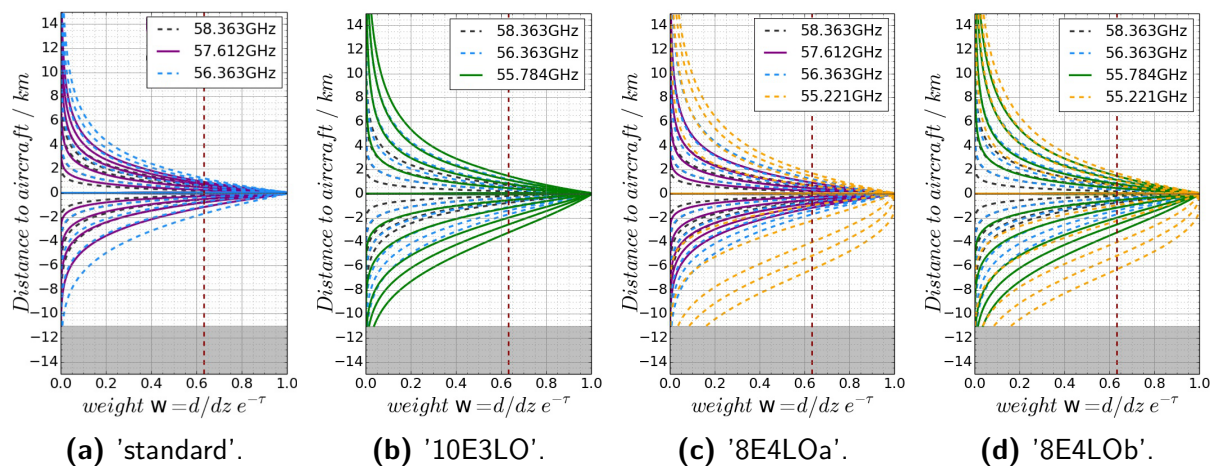


Figure 4.28: Relative WFs at flight altitude 11 km of (a) standard MTP measurement settings and possible new strategies (b) '10E3LO', (c) '8E4LOa', and (d) '8E4LOB'. Red, dashed lines indicate where W has dropped by $1/e$. Grey areas at the bottom: altitude ranges that would be below the surface at the respective aircraft altitudes.

Strategy '10E3LO' would enlarge the range of sensitivity, while allowing for processing of data with the NASA-JPL retrieval algorithm, which expects measurements at ten elevation angles, and three LOs.

However, the tests in Section 4.3 have shown, that the RT calculations have to be improved, in order to achieve reasonable results with the NASA-JPL retrieval.

Once the new retrieval algorithm TIRAMISU is set up to produce reliable results with MTP data, more variations within the measurement strategy can be applied, such as the other two suggested strategies.

Strategy ‘8E4LOa’ is still using the three LOs of the standard strategy, thus providing much (partially redundant) information on the ± 1 km region around the aircraft. Still, possibly up to three grid points in considerable distance (up to 6 km) to the aircraft could be added to the retrieved temperature profile below flight level, when including the weaker absorption line frequency at 55.221 GHz

Strategy ‘8E4LOb’ only uses two LOs of the standard strategy, adding more information on the air masses further away from the aircraft. Using this strategy, a higher resolution of the retrieved temperature profile at a larger distance to the aircraft can be gained.

Even better measurement results could be achieved, if hardware at the current state of technology could be used in a new design of the MTP. The current state of technology already allows for parallel measurements to record BTs at multiple LOs at the same time. Noise figures of modern amplifiers and receivers used in radiometry are improved, compared to the standards of the time when the DLR-MTP instrument was built. This could lead to a reduced integration time, improving the horizontal resolution of measurements even further. This, combined with a powerful retrieval algorithm that chooses the appropriate parts of the recorded spectrum as input, according to the requested output altitudes, would provide a much better resolved picture of the atmosphere than the current instrument, while containing the reliability and compactness of the already known MTP instrument.

5 Altitude-resolved characterisation of waves

As stated in the introduction, as well as Chapter 3, the MTP has far better capabilities than to just serve as a meteorological background indicator, giving tropopause heights and lapse rates at flight altitude. Even with the limited region of sensitivity, the altitude-resolved temperature data can be used to derive the static stability, and derive the lapse rate, which can be used as indicator for tropospheric or stratospheric air masses. The advantage of MTP data, compared to other remote-sensing instruments, is to provide time series of temperature data at different altitude levels, both above and below flight altitude of the research aircraft. Within these time-series of data at different altitude levels, wave-like structures can be identified, and an analysis of the propagation conditions for GWs within the UTL is possible.

As a tool to analyse these time series the Altitude-resolved characterisation of waves in atmospheric sounding (ACHWAS) algorithm has been developed. It uses wavelet analysis to extract wave signals from a time series of data, following the method presented in Torrence and Compo (1998) (see Appendix A.2). The detected wave signals can then be identified at each altitude where MTP data are available, so that wave signals can be characterised. This algorithm is described in the first section of this chapter.

The first section also introduces aircraft data analysis, following Smith et al. (2008) which is currently used to interpret flight level data with focus on wave activity. This is followed by a comparison of the two methods of aircraft mission data analysis. In section two of this chapter, the capabilities of the new analysis method of MTP data are assessed by applying it to synthetic data. Finally, this is followed by two case studies, in which the ACHWAS algorithm is applied to real mission data. The results will be compared to the findings of the well established method by Smith et al. (2008), which has already been used to analyse DEEPWAVE data (Smith et al., 2016). It will be assessed how well the two methods agree, and in which way they are able to complement each other.

5.1 Wave characterisation using aircraft mission data

Analysis of GWs on flight level of aircraft paths is performed to investigate GW propagation in the upper troposphere and lower stratosphere. A research question of interest is whether the low-level tropospheric conditions can be connected to wave activity measured by satellites or other instruments in high altitudes, up to the mesosphere. Especially the tropopause region, as well as the stratospheric jet region constitute possible barriers or filters to the vertical propagation of waves.

They are regions of changing static stability and background wind, which are both important parameters in the linear theory of waves. As aircraft flight levels are typically close to the tropopause, the interpretation of data collected during flight can give valuable insight as to which wave modes could pass the tropopause and propagate into the stratosphere or even on to the mesosphere. In this section, both, an already existing approach to characterise waves found in aircraft measurement system data, as well as a newly developed algorithm for analysing MTP data will be explained. A comparison will be made, showing how both methods complement each other.

5.1.1 Wave characterisation from MTP data

The idea of the ACHWAS algorithm, developed within this thesis, is to find dominant wave modes at the various altitudes on which MTP data are available for a flight segment of the research flight. To do so, a wavelet transform of the temperature perturbation signal $T'(x)$, found by subtracting a linear trend from the input data $T(x)$, is performed on each output level of the retrieval algorithm used to calculate the absolute temperature profiles. Temperature perturbation signals of the dominant scales found in the wavelet analysis of MTP data at flight level, as well as user-defined fixed scale intervals are reconstructed on all grid altitudes. The reconstructed signals are further analysed to extract the phase line orientation (PLO), β , of the reconstructed wave, which is defined as the angle between the wave vector κ and the vertical, confined to values between $-90^\circ \leq \beta \leq 90^\circ$. A description of the wavelet transform and its application to atmospheric data is given in Appendix A.2. The main processing steps of the ACHWAS algorithm are shown in Fig. 5.1.

Since the retrieval output levels are defined as fixed distances relative to the current aircraft altitude, they can differ slightly in a time series of measurements along a flight leg. However, as a main criterion in the definition of a flight leg is that the aircraft altitude must not change by more than 50 m between two MTP cycles, the output levels are still very similar for all temperature profiles of a single flight leg. In order to perform a valid wavelet analysis of the temperatures along the flight leg, it is still necessary to interpolate all individual temperature profiles to the same vertical grid. This grid is determined by using the average retrieval output levels of all profiles of the current flight leg. The interpolation of each individual temperature profile is done using the ‘interp1d’ function provided by the `scipy.interpolate` module from the `scipy` library (Jones et al., 2001). To be able to respect curved structures in the vertical temperature profile, such as the tropopause, a cubic interpolation scheme is used. Interpolation grid points that extend the range of the current retrieved temperature profile range are filled with nan-values. At this point, the temperatures are also converted to potential temperatures, which will later be used to define the background state and investigate the static stability around the flight altitude. Now, the temperatures at each altitude level of the common grid can be extracted to form the ‘horizontal’ input data for the wavelet analysis, which is performed on each altitude layer in the vertical grid.

As the wave numbers of GWs are to be derived, the algorithm uses the flown distance as default unit of the x -axis, calculated as the great-circle distance between the current coordinates and those of the first MTP cycle in the time series. Obviously, a time series of measurements taken on a moving platform provides even more options, such as time or latitudinal- or longitudinal coordinates. Often, it is useful to define a reference point to which the distance of each profile is calculated. In mountain wave analysis, this reference point is most commonly set at the highest mountain that has been passed during flight.

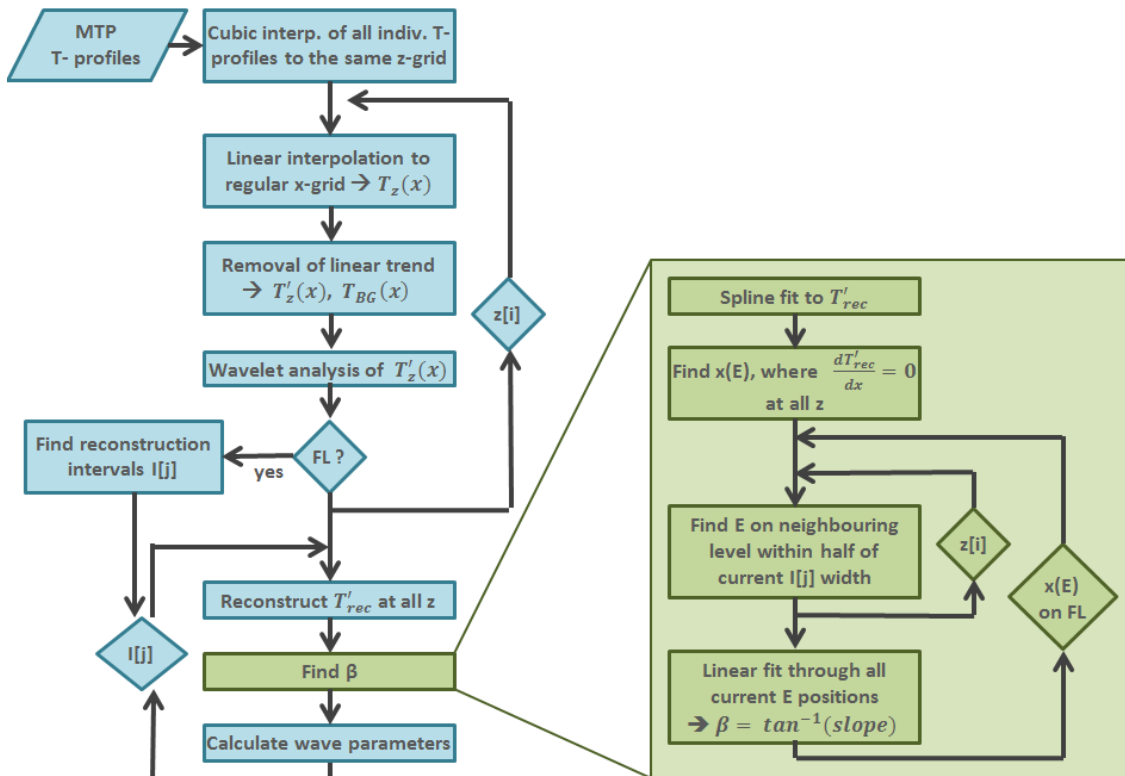


Figure 5.1: Schematic of the ACHWAS algorithm.

In preparation for the wavelet transform, a regular x -axis with 1 km grid spacing is defined, to which the current time series of temperatures is linearly interpolated. This is a more narrow spacing than provided by the data set which has a ~ 1.5 km - 2 km resolution depending on the aircraft speed. However, the Fourier analysis, which is part of the wavelet analysis, makes a regular spacing mandatory, and choosing the 1 km spacing provides data with the same information content as the original, without largely oversampling the information provided by the measurements.

From the interpolated temperature data a background, $T_{BG}(x)$, has to be removed (see Fig. 5.2), since the wave structures are only analysed from temperature perturbations, $T'(x)$. A number of options are implemented in the code, such as only removing a mean temperature value, but the default mode is to subtract a linear fit to the temperature data.

The background values of the potential temperature, $\theta_{BG}(x)$, are calculated in the same way, and stored for later use in deriving wave characteristics and atmospheric background conditions. As $\theta_{BG}(x)$ is derived at each altitude level z , the potential temperature lapse rate can be derived, and used to calculate $N^2 = \frac{g}{\theta_0} \frac{d\theta_0}{dz}$ from the background state.

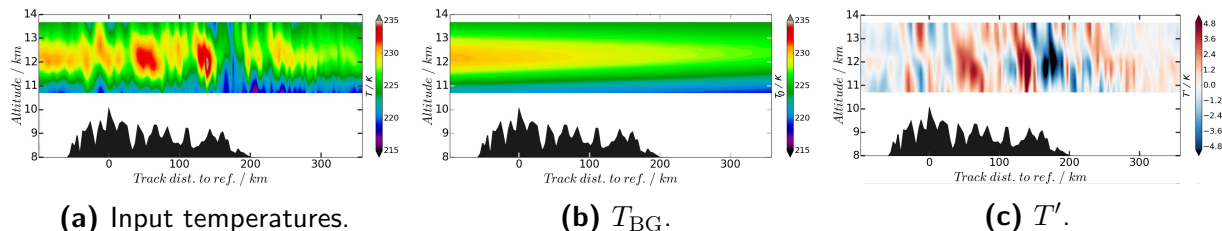


Figure 5.2: a) Original temperature data of DEEPWAVE flight RF16, leg 8, as provided by MTP retrieval output. b) Background temperature field (horizontal linear trends at each altitude level) and c) remaining temperature perturbation signal. The topography has correct scaling, but is lifted.

Now the wavelet transform is applied to the $T'(x)$ time series at each available altitude level z . The implementation of the wavelet transform is provided by Torrence and Compo (1998)¹. The results of the wavelet transforms at the various altitude levels are stored to be used in the later steps of the analysis. At flight level, which is always included in the retrieval output grid, the global power spectrum of the wavelet transform is analysed to find the intervals which will be used to reconstruct the T' signals of dominant scales, and derive the corresponding wave characteristics.

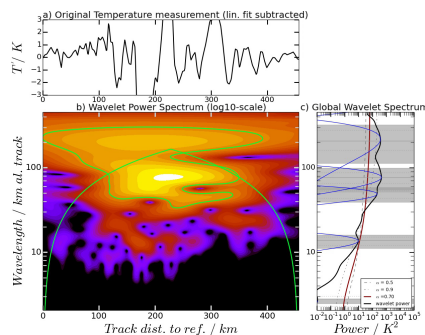


Figure 5.3: Wavelet analysis of MTP data of DEEPWAVE flight RF16, leg 8 at flight level: a) input T' data, b) wavelet power, and c) global power spectrum.

Since the power spectrum is a smooth data set, a spline fit can be used to describe the global wavelet power spectrum and find minima, maxima, and inflexion points by examining the first and second derivative of the spline fit. One option is to choose reconstruction intervals between two inflexion points with a maximum in between. However, this is often found to be too narrow to reconstruct the full amplitude of temperature perturbations within the synthetic data study, described below.

¹Source code available at <http://paos.colorado.edu/research/wavelets/>, accessed on 08-Oct-2015.

Another option is to apply a Gauss-fit to the data, which is the default option. In this case, a Gauss curve is calculated, which has its mean value at the respective peak in the global power spectrum, and the same standard deviation as the data between the two inflexion points next to this maximum. The reconstruction interval is then defined as those scales, at which the values of the Gauss curve exceed an empiric value of the maximum power divided by 1000. All reconstruction intervals found this way are stored for further processing. The spline fit is performed using the ‘splrep’ function of the `scipy.interpolate` module. For the evaluation of the function and its derivatives the ‘splev’ function of the same module is used. In the synthetic data study (see Section 5.2) with input signals only consisting of a single horizontal wave length, the expected reconstruction interval width connected to a given wavelength is derived. If the width of an interval found by the algorithm exceeds this expected width (linked to the median scale of the detected reconstruction interval), it is divided into sub-intervals of the expected width, to evaluate whether the structure in the power spectrum originates from more than one wave packet. This procedure provides better confidence in the resulting wave characteristics. Moreover, fixed reconstruction intervals can be defined by the user, enabling a scale analysis, as proposed by Smith et al. (2016). In this case, the user-defined interval limits are adopted.

Once all altitude levels have been processed with the wavelet analysis, the temperature perturbation signals at each respective altitude, T'_R , are reconstructed within the stored wavelength intervals. This way, a wave signal seen at flight level can be observed over various altitudes around the aircraft altitude and its properties can be derived. An example of T'_R , from processing DEEPWAVE campaign data is given in Fig. 5.4. Now the reconstructed T'_R signals of each wavelength interval can be analysed with respect to wave characteristics (right-hand side of Fig. 5.1).

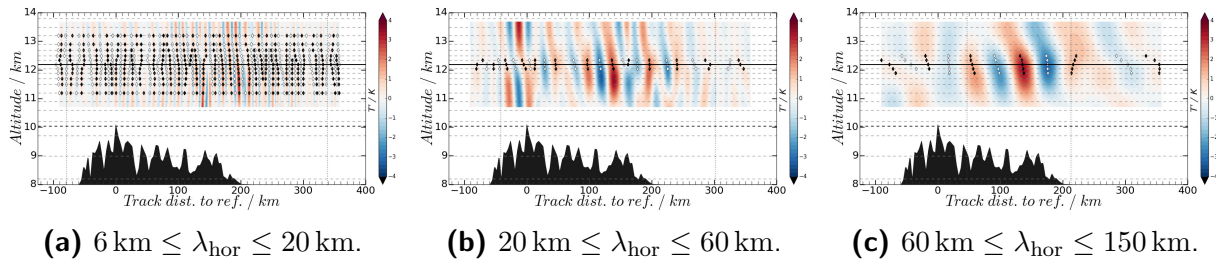


Figure 5.4: Reconstructed T'_R signal of three different fixed reconstruction intervals after wavelet analysis of DEEPWAVE flight RF16, leg 8 data. Markers indicate minima (white) and maxima (black) used for determination of β . Horizontal grey lines in the background: Altitudes at which retrieval output is available. The topography has correct scaling, but is lifted to be visible in the plots. Note the different colour scales.

In the next step the PLO β is determined. It is derived from the slope of the phase line, defined by the positions of all minima (maxima) belonging to the same wave-phase (black and white markers in Fig. 5.4): To do so, the positions of minima and maxima in the T'_R signal at each altitude level are identified through a spline fit to the data. The derivative is used to find the extrema.

The PLO is then determined for each individual wave-phase, always following the same procedure (here, assuming that the current wave-phase is defined by minima in T'_R): First, the closest position of a minimum above the current flight level minimum is identified, and then the closest position of the minimum above this one, and so on, up to a distance of 1 km above the aircraft. The positions are all stored, as long as the distance to the next-lower minimum is smaller than half the maximum wavelength of the reconstruction interval, to make sure that they all belong to the same wave-phase. The same procedure is followed downwards, beginning at flight level, to a distance of -1 km below the aircraft. When all positions of minima, x_E , belonging to the same wave-phase are identified, linear fits through the pairs of (x_E, z) are calculated. More than one fit is used, as the number of points included into the fit is successively increased, beginning with the three points closest to the flight level, and finally using all available points within ± 1 km distance to the aircraft. This way, the results can be compared to find a measure of confidence in the fit result, and the derived wave characteristics. The PLO of the current wave-phase, β , is calculated as the inverse tangent of the slope of the fit lines (see Figure 5.4). Knowing the slope of a phase line from the linear fit, the vertical wave number m , the intrinsic frequency Ω , and the absolute momentum flux contribution of the wave can be calculated, according to the equations in Chapter 2.2.

It is worth noting that it is possible to perform the analysis twice, based on the meridional and zonal distances flown. This way, the absolute values of the three-dimensional wave numbers can be extracted, as long as the identified wave packets can be linked in both analyses. That is especially interesting in the case that the aircraft is not moving along the mean flow. Obviously, the data has to be split in two different orthogonal directions, when the aircraft is moving in near-exact longitudinal or latitudinal direction. Also, since most flight legs dedicated to measuring GWs are designed to follow the mean flow of air, the two-dimensional analysis is expected to lead to the same results as a three dimensional analysis. Moreover, if the analysis is done in a horizontal direction not parallel to the flight direction, the resolution of data drops, and the interpretation of the analysis must include the question whether the measured GWs are stationary.

Furthermore, it is important to mention, that the algorithm only reveals the magnitude of the wave numbers k and m . While the analysis of wind and pressure perturbation co-spectra from aircraft in situ data allows for an analysis of the direction of the derived fluxes, the analysis of MTP data, using the ACHWAS algorithm, only provides insight into the magnitude of wave activity through the reconstructed temperature perturbation amplitudes and the resulting GWPED, as well as by determining absolute momentum flux contributions. As the PLO is a non-directional value, wind measurements and observations by other instruments have to be used in order to interpret possible direction of propagation of the observed GWs. However, the two-dimensional data provided by the MTP measurements still enable a better understanding of the processes of wave propagation, reflection or dissipation around flight altitude, as will be shown in the real-data analysis in Section 5.3. A discussion of uncertainties connected to resulting wave characteristics will be given after testing the algorithm with synthetic data, in Section 5.2.

5.1.2 Aircraft measurement system data

The evaluation of in situ aircraft measurements concerning GWs has been established since almost ten years. It was developed and first described by Smith et al. (2008), and further developed in Smith et al. (2016). They use meteorological data provided by aircraft in situ measurements to identify and characterise GWs encountered during flight.

The detection of waves within these data utilises vertical streamline displacement. This is determined by analysing the vertical wind measurements along the flight segment S as:

$$\eta(x) = \int_0^S \frac{w'(x)}{U_B(x)} dx \quad (5.1)$$

Following the definitions of Smith et al. (2008), U_B is the horizontal wind along line-of-flight, and w' denotes the vertical wind perturbation.

Also, momentum- and energy fluxes can be derived from aircraft measurement data in the same way as described in chapter 2.2, following Eq. (9a), (9b), and (10) from Smith et al. (2008), respectively:

The momentum flux in x - and y direction is determined as:

$$\mathbf{MF}_{x_B} = \bar{\rho} \int_0^S u(x)'w(x)' dx \quad [\text{Nm}^{-1}] \quad (5.2)$$

$$\mathbf{MF}_{y_B} = \bar{\rho} \int_0^S v(x)'w(x)' dx \quad [\text{Nm}^{-1}] \quad (5.3)$$

The energy flux is calculated from the pressure and vertical wind perturbations:

$$\mathbf{EF} = \int_0^S p(x)'w(x)' dx \quad [\text{Wm}^{-1}] \quad (5.4)$$

which can also be calculated from the momentum flux according to Eliassen and Palm (1960) as:

$$\mathbf{EF} = -\vec{U} \cdot \vec{\mathbf{MF}} \quad (5.5)$$

with the mean flow speed \vec{U} at the level of flux measurement, u' and v' representing the horizontal wind perturbations, $\bar{\rho}$ representing the leg-mean air density, and p' denoting the pressure perturbation.

The most important aspect of this flight level data analysis is the way the perturbations of the wind components and the pressure are derived. In their analysis of campaign data from the Terrain-Induced Rotor Experiment (T-REX) campaign in 2006 (Smith et al., 2008), and from DEEPWAVE data (Smith et al., 2016), they derive the variables by subtracting the leg-mean of the flight leg data. An exception to this is the estimation of the pressure perturbation p' . In Smith et al. (2008) it is discussed that the autopilot of the aircraft follows a constant static pressure, which leads to small altitude changes during the flight leg, caused by the wave-induced pressure changes within the atmosphere.

Hence, before deriving the pressure perturbation, a correction is applied to the pressure data (Eq. (12) in Smith et al., 2008), following:

$$p_{\text{corr}} = p_{\text{static}} + \bar{\rho}g(z - z_{\text{REF}}) \quad (5.6)$$

in which p_{static} denotes the static pressure measured by the aircraft, $\bar{\rho}$ stands for the leg-mean air density, g is the gravitational acceleration, and z and z_{REF} represent the GPS height of the aircraft and the leg-mean GPS altitude respectively. In their analysis of DEEPWAVE data (Smith et al., 2016), this correction is extended, facilitated by the availability of more precise differential GPS data. After applying the above correction for slight flight level adjustments during the flight leg, another correction is applied to account for possible cross-track winds (geostrophic correction). This correction (Eq. (8) in Smith et al., 2016), is calculated as:

$$p_g = 2\bar{\rho}\Omega_{\text{Earth}} \sin(\phi) \int_0^s u_{\text{cross}} ds' \quad (5.7)$$

using the Earth's angular velocity Ω_{Earth} , latitude ϕ , and the cross-track wind u_{cross} . The final corrected pressure used to derive energy and momentum fluxes is the difference between p_{corr} and p_g , which is almost identical to detrending p_{corr} (Smith et al., 2016).

Some important variables for GW characterisation, such as the tropopause height, or static stability N^2 cannot easily be derived from flight level measurements, as their estimation is based on vertical gradients of temperature. However, the tropopause height can be derived from close-by radio sondes, or from ozone measurements during flight level changes. In their analysis of T-REX data, Smith et al. utilise the vertical displacement η to estimate the static stability through the relation to the potential temperature at flight altitude (Eq. (3) in Smith et al., 2008):

$$\frac{d\theta}{dz} = - \left(\frac{d\theta}{d\eta} \right)_{\text{AC}} \quad (5.8)$$

which they derive as the slope of a linear fit between the two variables. They state that this method only works for strong waves and during flight legs parallel to the mean flow, as there is no linear relationship between θ and η in case of weak waves.

From the given random errors of the sensor readings used in the analysis, Smith et al. (2016) estimate worst-case errors of the calculated momentum flux of up to 11%, which is dramatically reduced by an increased number of samples within the wave.

The errors in horizontal and vertical energy fluxes are estimated to be in the same order of magnitude, around 10% in the worst-case scenarios. As there are redundant sensor measurements available in the data set of the DEEPWAVE campaign, Smith et al. (2016) use the difference between results from calculations utilizing the different sensors to estimate uncertainties in the calculated energy and momentum fluxes.

They derive a difference of $\sim 5\%$ in the energy fluxes calculated with data from redundant sensors.

Using the above formulae to derive momentum and energy fluxes gives an impression on the wave activity on the flight level. However, contributions come from a variety of different wavelengths. While wavelet analysis is used in the evaluation of individual special cases, Smith et al. (2016) utilise spectral decomposition of wind measurements throughout the whole campaign to derive dominant modes and determine which part of the wave spectrum contributes to the vertical energy flux. They apply high- or low-pass filters to the perturbation signals to separate the scales. Moreover, a new coefficient is generally defined as

$$CC(f', g') = \overline{f'g'} / (\overline{f'f'} \cdot \overline{g'g'})^{1/2} \quad (5.9)$$

This coefficient can be used to estimate the direction of propagation, and can be applied to the filtered signals to derive which part of the spectrum contributes to the transport of energy and momentum. For example $CC(p', w')$ indicates upward propagation in case of positive results. Analogous, $CC(p', u') < 0$ indicates westward wave propagation.

5.1.3 Comparison of methods

Two methods of detecting and characterising GWs in data sets of aircraft mission data have been discussed. The presented method to analyse MTP measurements uses a different approach than the already established flight-level data analysis, as 2D temperature data are available for analysis. The temperature perturbations can be used to identify both the horizontal and vertical wave numbers of the observed GWs. Together with the static stability, N^2 , which can also be directly derived from the temperature profiles, the intrinsic frequency of the wave, Ω , can be calculated. Also, the vertical profile of GWPED can be calculated as a measure of overall wave activity around the aircraft altitude. Absolute momentum flux contributions of the individual phases can be derived by using the phase relations between the temperature and wind perturbations (Eq. (2.21) in Chapter 2).

The established method of analysing aircraft system data, as described by Smith et al. (2008, 2016), is capable of identifying wave events and deriving momentum and energy fluxes. They relate these to the wave scales found during the flight leg by using wavelet analysis or spectral decomposition. The direction of propagation of a wave is derived through the use of a coefficient, which links the flight level pressure to the flight level winds, or by directly comparing the directions of momentum and energy flux.

While both methods differ in their approach and use of available data (see Table 5.1), they both provide valuable information on the waves encountered during flight. When used together, a nearly complete picture of the wave characteristics can be drawn.

The most obvious difference in the two approaches is the data they are based on. While aircraft in situ measurements are only available at flight level, MTP measurements are also available within some distance both above and below the current flight level.

Param.	Smith et al. (2008, 2016)	MTP analysis
w'	De-trended in situ wind measurement of GV	(Phase relation between $\frac{T'}{T_0}$ and w')
u'	De-trended in situ wind measurement of GV	(Phase relation to w' , using wave numbers k and m)
p'	De-trended in situ static pressure measurement of GV, with correction accounting for flight level adjustments	(Phase-relation to w' , using Ω , wave numbers k and m , and $\bar{\rho}$ derived from MTP output)
T'	De-trended in situ static temperature of GV	Horizontally de-trended T_{MTP}
θ'	De-trended potential temperature of GV data	Horizontally de-trended θ_{MTP} , calculated from T_{MTP}
β	Ratio of vert. and hor. EF	Linear fit in reconstructed 2D T' field
$\lambda_{\text{hor}}; k$	Spectral analysis (wavelet transform, Fourier analysis)	Dominant modes of wavelet analysis
$\lambda_{\text{vert}}; m$	-	$\lambda_{\text{hor}} \cdot \tan(\beta)$
Ω	-	Derived from wave numbers k and m
EF_{hor}	Cumulative sum of $p'u'$ in leg-direction	(Absolute value, derived through phase relations between $\frac{T'}{T_0}$, w' , and p')
EF_{vert}	Cumulative sum of $p'w'$ in leg-direction	(Absolute value, derived through phase relations between $\frac{T'}{T_0}$, u' , and p')
MF_{hor}	Cumulative sum of $u'w'$ and $v'w'$ in leg-direction	Absolute value, derived through phase relations between $\frac{T'}{T_0}$, w' , and u'
Propagation dir.	Correlation coefficient relating wind perturbation and pressure perturbations	-
Linearity	Correlation of EF with $\vec{U} \cdot \vec{\text{MF}}$	Basic assumption
N^2	Upwind radio sondes	Derived from $d\theta_{\text{MTP}}/dz$ at position of measurement
z_{TP}	Nearby radio sondes or ozone profiles from ascend/descend	Derived from dT_{MTP}/dz at position of measurement

Table 5.1: Parameters derived during gravity wave analysis from aircraft mission data. Entries in parentheses are not implemented in the ACHWAS algorithm.

Thus, the method used by Smith et al. (2008, 2016) only draws a picture of the state at flight level at the time of the passing of the research aircraft. On the other hand, MTP data covers a 2-3 km thick altitude region around the aircraft, in which changing T' amplitudes, e.g. such caused by reflection or breaking of waves, can be resolved. Through those changing T' amplitudes possible wave interactions with the atmosphere become visible, that cannot be picked up by the aircraft sensors.

Another important difference between the methods is the resolution of available data. Aircraft measurement systems of the NCAR GV and HALO provide high resolution data with a frequency better than 1 Hz. This is a 10 - 100 times better resolution than the MTP provides with measurement cycles of 13 s for the DLR-MTP or 17 s for the NCAR-MTP. This mainly influences the lower threshold of detectable wave scales, which is at least 10 km in case of the DLR-MTP measurements.

Furthermore, a clear difference is the availability of meteorological parameters that characterise the atmospheric state. One-dimensional data series at flight level will not provide any information on temperature lapse rates. Thus it is not possible to determine the tropopause altitude, which is defined by the change of the lapse rate with altitude (World Meteorological Organization, 1957). For the same reason, the static stability of the probed air masses cannot be determined by flight level measurements. The approximation used by Smith et al. (2008) is only an indication, and is only applicable in very specific conditions. Both of these quantities can be derived from MTP measurements, which provide enough vertical resolution to derive the temperature gradient and with it the static stability around flight altitude. However, knowing that the MTP is only sensitive to the atmosphere within a $\sim 2 - 3$ km layer around the current flight level, the tropopause height is mainly interpreted from the a priori knowledge provided in the radio sonde database of the retrieval algorithm (see Chapter 4.4), unless the aircraft flight level is close enough to the tropopause, (within ~ 1.5 km distance to the current flight level). The estimation of tropopause height from MTP data, depending on a priori knowledge, is thus comparable to using nearby radio sondes or in situ measurements of aircraft ascends and descents.

5.2 Sensitivity study: Analysis of simulated data

Before applying the new ACHWAS algorithm to real data, it is tested how well the PLO β can be determined using synthetic data. To do so, a stationary 2D temperature field is calculated, using a background temperature profile from radio sondes, $T_{\text{BG}}(z)$, and a temperature perturbation:

$$T(x, z) = T_{\text{BG}}(z) + T'(x, z) = T_{\text{BG}}(z) + A \cdot \sin\left(\frac{2\pi x}{\lambda_{\text{hor}}} + \frac{2\pi z}{\lambda_{\text{vert}}}\right) \quad (5.10)$$

As the algorithm is constructed to find β , its value is used as an input parameter, together with the horizontal wave length, from which the vertical wavelength used in Eq. (5.10) can be constructed by:

$$\lambda_{\text{vert}} = \lambda_{\text{hor}} \cdot \tan(\beta) \quad (5.11)$$

To simulate a flight through the two-dimensional temperature field, the aircraft position x is defined as travelled distance for a fixed aircraft speed of 200 m/s. At each position x after one second of flight the vertical temperature profile of the temperature field defined by Eq. (5.10) is calculated to construct the synthetic temperature data used to test the ACHWAS algorithm. Synthetic data files are constructed for 150 combinations of horizontal wavelengths, ranging from 5 km to 50 km in steps of 5 km, and 60 km to 100 km in steps of 10 km, combined with PLOs β of $5^\circ, 15^\circ, 25^\circ, 35^\circ, 40^\circ, 50^\circ, 55^\circ, 65^\circ, 75^\circ$, and 85° .

In a first test, the input data are stored at the standard output levels of the statistical retrieval, assuming a flight altitude of 11 km, and processed with the ACHWAS algorithm. This way it can be shown that the algorithm is able to detect the true wave characteristics from a given set of data. However, this study is not representative for real MTP measurements, since those are processed with a retrieval algorithm before the ACHWAS algorithm is applied. Also, one DLR-MTP measurement cycle contributing to a single temperature profile, takes ~ 13 s. This is accounted for by adding another step to the synthetic data study: 13 s average absolute temperature profiles from the ‘flight’ through the 2D temperature field are stored in an external data file and used as input for the simulation mode of TIRAMISU. The resulting brightness temperatures (BTs) are then processed with the retrieval algorithms available for processing of MTP data (see Chapter 4.3) to derive the absolute temperature profiles. Here, the influence of the retrieval algorithm can be seen in the results after applying the ACHWAS algorithm.

In a final step, noise is added to the BTs before processing the data with the retrieval algorithm. Thus, the simulation resembles real atmospheric measurements as close as possible. Again, the ACHWAS algorithm is applied to find out the effect of the noise. Results from applying the algorithm to real atmospheric measurements taken during the DEEP-WAVE campaign in 2014 will be presented in the next section.

5.2.1 Analysis of synthetic temperature data

When directly processing the 2D temperature data without BT simulation and retrieval, it can be tested, whether the ACHWAS algorithm works correctly. Using the 1 Hz input data, the result of the processing with the ACHWAS algorithm is that the correct wavelength intervals for reconstruction (with the median wavelength equalling the input wavelength) are found during wavelet analysis, and also the correct β is derived in all cases, which is the expected result. From this test, the global wavelet power spectra are used to establish the relation between the reconstruction interval width W_I and the known horizontal wavelength of the input signal, as shown in Fig. 5.5c. A quadratic relationship is found:

$$W_I = 0.0006 \cdot \lambda_{\text{hor}}^2 + 0.4427 \cdot \lambda_{\text{hor}} - 0.2249 \quad (5.12)$$

The broadening of the reconstruction interval is an effect of the wavelet basis used in the analysis, which has a Gaussian shape in the frequency domain (see Fig. A.3) that becomes wider at larger wavelengths.

Thus, the power, which in case of the synthetic data is contributed purely by one single wavelength, is interpreted to belong to a number of neighbouring wavelengths. This means that the ACHWAS algorithm cannot distinguish between monochromatic waves and wave packets of different characteristics. Hence, the median wavelength of the reconstruction interval is always interpreted as the horizontal wavelength of the GW observed during flight, that causes the peak in the global power spectrum.

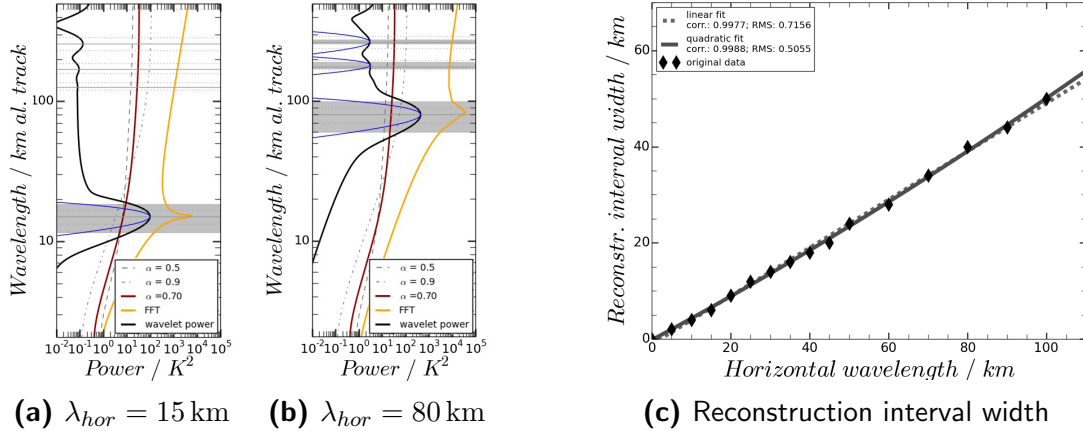


Figure 5.5: Power spectra of wavelet analysis of flight level data with different horizontal wavelengths of (a) $\lambda_{hor} = 15$ km, and (b) $\lambda_{hor} = 80$ km. Grey shaded areas: reconstruction intervals found by the algorithm. Blue lines: Gauss-curves fitted to power spectrum. Right panel: Reconstruction interval width vs. true horizontal wave length.

Another interesting effect of the wavelet analysis is seen in Figure 5.5, which is the fact that the global wavelet power spectrum has more than one single maximum, even with the purely monochromatic input signal. Each of these peaks results in a reconstruction interval within the ACHWAS algorithm. However, only the one corresponding to the horizontal wavelength of the input signal is significantly larger than the theoretical noise power spectrum. Details of the wavelet analysis and the definition of the theoretical noise power spectrum are described in Appendix A.2.

The noise figure of the DLR-MTP raw data has been analysed in Chapter 4.2.1. It has been found that the noise follows a Gauss distribution and can be represented by a theoretical red-noise power spectrum. The DLR-MTP noise spectra are shown in Fig. 5.6. For plotting purposes, the spectral power is normalised to 1 at a frequency of 10^{-3} Hz, here. The MTP noise figure implies that there is an auto-correlation between successive data points, which causes a spectral behaviour as described by Eq. 4.2, with $\alpha \cong 0.7$. The corresponding noise power spectrum is shown as solid, green line in Fig. 5.6. The lag-1 autocorrelation, α , of the MTP data is calculated as the slope of a linear fit between the original time series and the same data set shifted by one point. The black dashed lines show the same theoretical spectrum for lag-1 coefficients of 0.2 and 0.8. Within the wavelet analysis, only peaks in the global power spectrum that are larger than the theoretical line scaled by the variance of the time series are significant.

Still, the ACHWAS algorithm stores all peaks for further processing, leaving the evaluation of significance to the user. In Fig. 5.5, showing the global power spectra from the processing of 1 Hz input data, the theoretical noise power spectrum is shown as solid red line. In all analyses of the un-processed input data, only the peak at the wavelength of the given input signal is considered significant over a theoretical red-noise with lag-1 autocorrelation $\alpha = 0.7$.

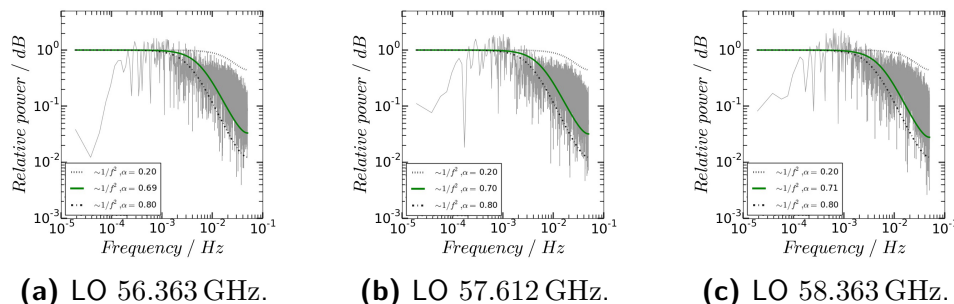


Figure 5.6: Spectra of DLR-MTP noise from ML CIRRUS flight data at the three standard LOs. Black dashed lines: theoretical power spectra of $1/f^2$ noise with lag-1 autocorrelations of $\alpha = 0.2$ and $\alpha = 0.8$. Green, solid line: theoretical power spectrum of $1/f^2$ noise with lag-1 autocorrelation of input data.

The performance of the ACHWAS algorithm can be shown, when plotting the difference between the derived PLO and the known β in the input data, as shown in Fig. 5.7. In the processing of the 13s average temperature profiles, the impact of measurement resolution can be seen.

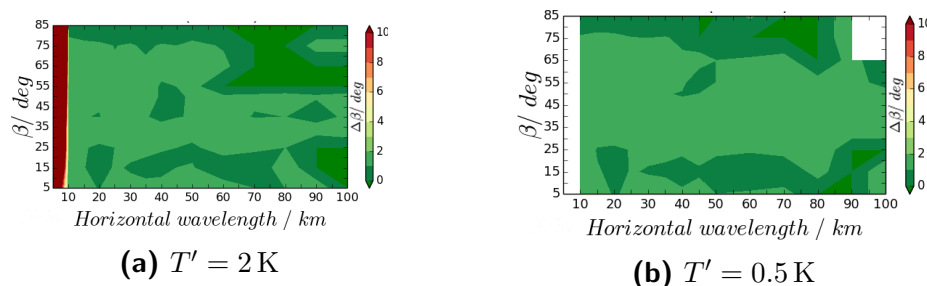


Figure 5.7: Absolute RMS difference of the true phase line orientation and the derived β from analysis of 13s average input signals with amplitudes of (a) $T' = 2\text{ K}$ and (b) $T' = 0.5\text{ K}$.

While the correct β is still derived within a maximum uncertainty of $\pm 2^\circ$ at all combinations of horizontal wavelengths larger than 10 km and all possible PLOs, the sampling is not sufficient to correctly analyse the shorter waves, neither with a temperature perturbation amplitude of 0.5 K (cf. Fig 5.7b), nor at a larger amplitude of 2 K (cf. Fig 5.7a). As a fairly short leg length was chosen for the synthetic data, sometimes the large wavelengths only show one single minimum or maximum within the leg. Those cases are excluded from the analysis (white areas in Fig. 5.7), due to weak statistical meaning.

In case of the very short horizontal wavelength and small amplitude (Fig. 5.7b) The reconstruction interval found by the algorithm is found to be a single wave length and hence discarded or not found at all, so that no further analysis of the reconstructed signal was possible.

5.2.2 Analysis of processed temperature fields

In the second part of the synthetic data study, the input data sets are processed by a retrieval algorithm before applying the ACHWAS algorithm. To do so, the simulation mode of TIRAMISU is used to calculate BTs from the 13s average temperature profiles. This corresponds to what the MTP would measure when flying through the temperature field. A flight altitude of 11 km is assumed. The simulated BTs are then stored, and used as input for the retrieval routines. When using TIRAMISU, the CIRA 40N April temperature profile is chosen as a priori and a constant 220 K atmosphere as initial guess.

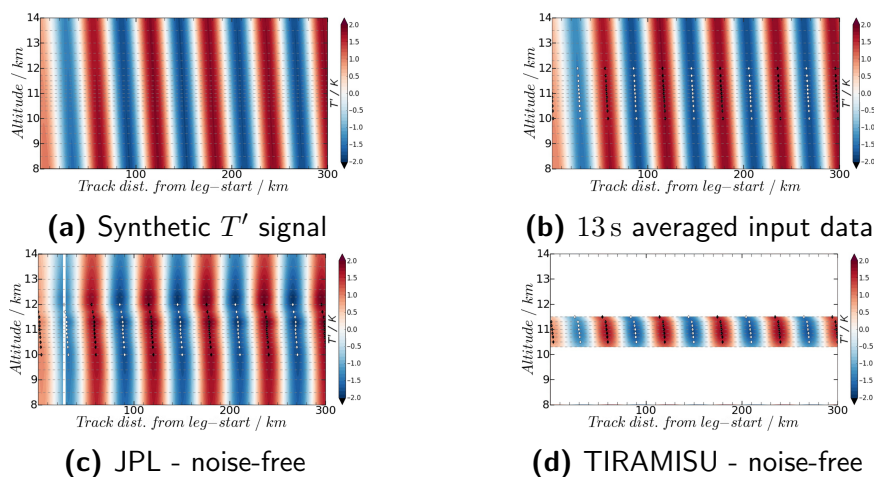


Figure 5.8: Original (a), and reconstructed T' signals, as depicted in Figure 5.4: reconstructions of wave signals after wavelet analysis of (b) input signal, and noise-free BTs processed with (c) the JPL retrieval and (d) TIRAMISU.

For processing with the NASA-JPL retrieval, the data is prepared in the same way as during the retrieval testing described in Section 4.1. Since one of the template profiles used in the processing of ML CIRRUS data is also used as background temperature profile in the calculation of the 2D temperature field, the same templates as for processing of the ML CIRRUS data are used to evaluate the synthetic data, providing a similar retrieval set-up as used in the processing of atmospheric measurements.

A first look at how well the ACHWAS algorithm works can be taken when comparing the reconstructed signals to the input signal at a given wavelength and β combination. In Fig. 5.8, the original and reconstructed T'_R signals at $\lambda_{\text{hor}} = 60$ km and with $\beta = 55^\circ$ are depicted. Of most interest are the reconstructed T'_R signals after wavelet analysis of the data processed with a retrieval algorithm (Figure 5.8c and 5.8d).

There are a number of differences to the original input data. The most prominent difference between the unprocessed data and any of the other reconstructions is the range in which the PLO is visible at all. The data processed with the NASA-JPL retrieval show a distinct change towards vertical phase lines at distances to the aircraft larger than 1 km, which is in accordance to the sensitivity of the instrument to a 1 km - 1.5 km distance to the aircraft, discussed in Chapter 4.4. The output at larger distances is almost exclusively based on a priori knowledge and does not allow for meteorological interpretation of the T'_R signals.

The data processed with TIRAMISU only exist up to a distance of about 1 km from the aircraft, as the output grids that extend further lead to non-realistic retrieval output. Still, within the available altitude range, the tilt of the phase lines is visible. However, towards larger distances from the flight level, there is a sort of ‘rounding’, implying that only very few grid levels close to the flight altitude can be used to extract β .

Two sets of synthetic data are processed with TIRAMISU, one including a temperature perturbation with amplitude $T' = 1$ K, the other with an amplitude of $T' = 2$ K. The RMS difference of the derived PLOs to the true angles in the input data is shown in Fig. 5.9.

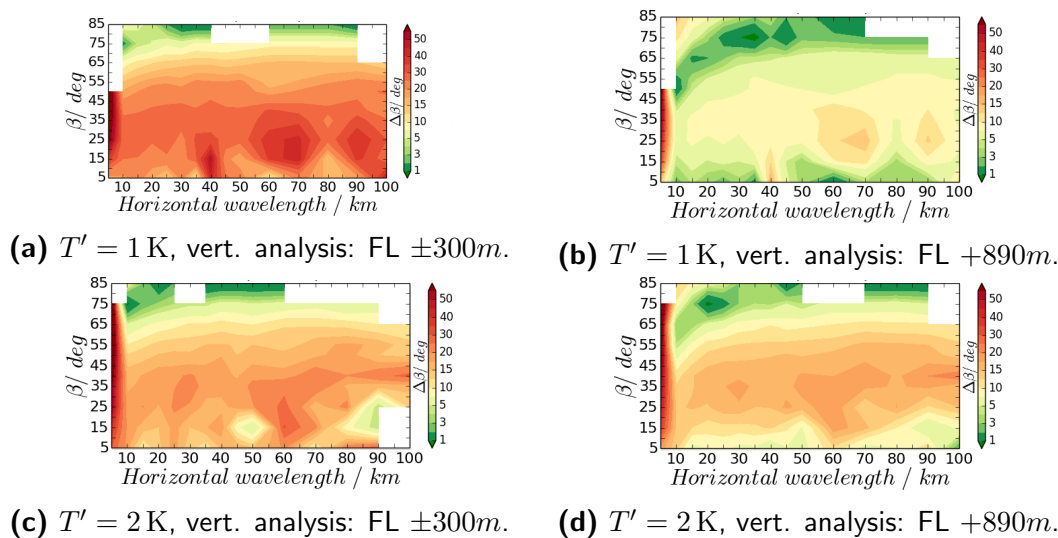


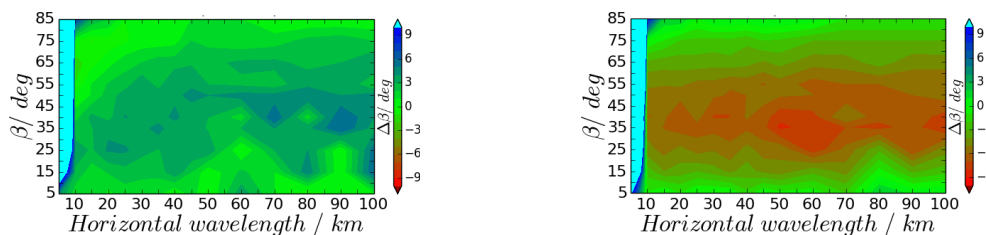
Figure 5.9: Absolute RMS difference (colour-coded, in deg) of the true phase line orientation and the derived β resulting from the analysis of noise-free synthetic data processed with TIRAMISU.

Obviously, there is a large dependence on the choice of the number of altitude levels included in the analysis. The left-hand panels in Figure 5.9 show the results of the analyses including all available levels between ± 300 m around flight level. The right-hand panels show the results when including only altitudes at or above the flight level, up to a distance of +890 m. In both shown cases, including only levels at or above flight level produces better results. The effect is larger for the 1 K amplitude than for the 2 K amplitude. The retrieval testing, shown in Chapter 4.3, revealed that in its current set-up there is a large bias in the absolute temperatures retrieved below flight level, if TIRAMISU is used as retrieval algorithm.

This is an explanation for the better performance of the ACHWAS algorithm, if no levels below flight altitude are included.

The fact that the analysis of wave signals with smaller amplitudes works better than for larger amplitudes seems counter-intuitive. However, a possible explanation is that the TIRAMISU retrieval is much less dependent on a priori information, and reacts more strongly to a change between two successive input BT profiles than the NASA-JPL retrieval algorithm. With the current set-up of the TIRAMISU retrieval, the larger amplitude of the wave signal results in bigger differences between the derived absolute temperature profiles of two successive measurement cycles, not necessarily reflecting the temperature differences caused by GWs. Hence, the ACHWAS algorithm fails to detect the correct PLO. However, the test also shows, that once the correct settings for processing of MTP data are found, TIRAMISU can be a valuable and quite powerful retrieval algorithm, able to resolve even small temperature perturbation signals with amplitudes of ~ 1 K.

A different result is achieved in the analysis of noise-free data processed with the statistical retrieval developed by NASA-JPL. Looking at the mean difference of β , derived by the ACHWAS algorithm, to the true PLO (Fig. 5.10), reveals that good results can be achieved. Here, the results from processing input data with an amplitude of $T' = 2$ K are shown. The left panel shows the results achieved when including data from altitudes around flight level up to a distance of ± 500 m.



(a) $T' = 2$ K, vert. analysis: FL ± 500 m. (b) $T' = 2$ K, vert. analysis: FL ± 700 m.

Figure 5.10: RMS difference (colour-coded, in deg) of the true phase line orientation and the derived β resulting from the analysis of noise-free synthetic data processed with the JPL retrieval.

In the analysis that produces the output shown in Figure 5.10b, two more data points are included in the linear fit to derive β , extending the analysis to an altitude region of ± 700 m around flight level. Including slightly less data points results in slightly smaller differences to the true β . However, most striking is the fact that by changing the altitude range included in the analysis, the derived PLO is deviating in a different direction: the smaller altitude range results in less steep phase lines (blue colours in Fig. 5.10a). Two more data points result in steeper phase lines (red colours in Fig. 5.10b). This indicates that when analysing real data, the ACHWAS algorithm should be applied several times, including different numbers of altitude levels, in order to estimate an uncertainty of the derived slope of the phase lines, and the resulting β through comparison of the results.

The RMS difference between the (phase line-) slope of the linear fit and the true slope (plotted as percentage of the true slope) gives an idea of the magnitude of the relative uncertainty. This is shown in Figure 5.11. Unsurprisingly, the relative error becomes smaller with growing amplitude of the wave-signal. Also, smaller errors are found in the upper left-hand corners of the plots, corresponding to a combination of smaller λ_{hor} and large β . This combination results in short vertical wavelengths, which can be much better resolved in the MTP data than large vertical wavelengths, which only induce very small changes in T' between different altitude levels. The best results are achieved, if the vertical wavelength is shorter than $\sim 50 - 75$ km (dark, blue colours in Figure 5.11a). This is already larger than what is expected to be found in measurements ($\lambda_{\text{vert}} \leq 30$ km; indicated by dashed lines in the following figures), unless the encountered wave is a trapped wave, which would result in nearly vertical phase-lines ($\beta \rightarrow 0$ and $\lambda_{\text{vert}} \rightarrow \infty$).

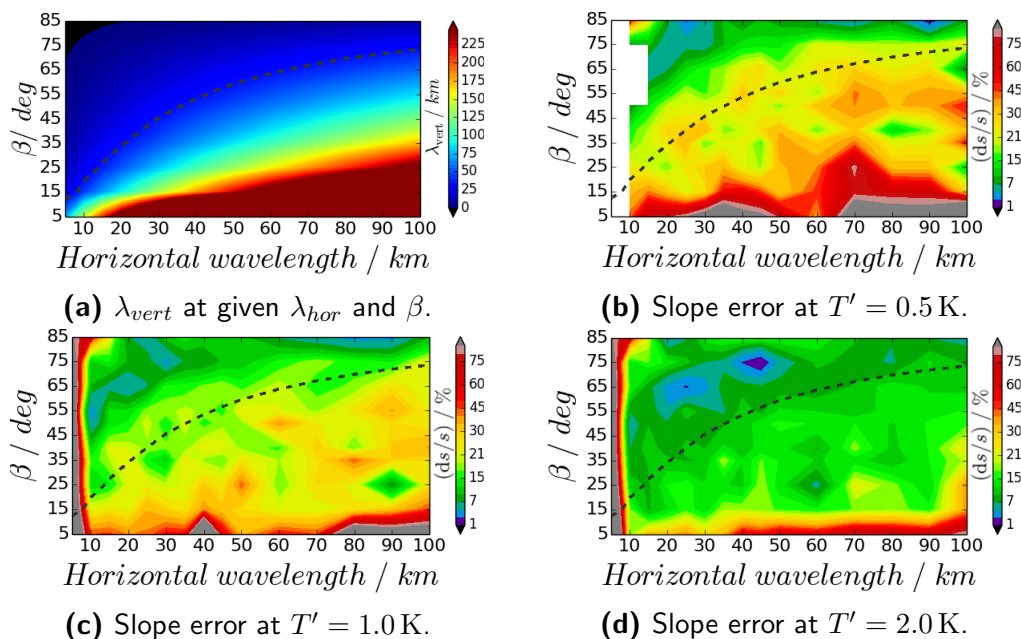


Figure 5.11: (a) expected vertical wavelength at given λ_{hor} and β and relative error (in %), of derived phase line slopes resulting from noise-free synthetic data processed with the JPL retrieval, with given T' -amplitudes of (b) 0.5 K, (c) 1.0 K, and (d) 2.0 K. The dashed lines indicate $\lambda_{\text{vert}} = 30$ km.

The linear fit through the extrema, defining the phase lines, is obviously much more reliable, if the amplitude of the reconstructed signal is larger. In this case, the location of an extreme can be defined much clearer than with small amplitudes, inducing much smaller uncertainties in the linear fit.

Finally, the influence of measurement noise on the retrieval performance, and the ability to derive wave characteristics, is tested. Since the ACHWAS algorithm already struggles to find the correct β in noise-free data processed with TIRAMISU, the test with noisy data is only made with data processed with the NASA-JPL retrieval.

For this test the input is modified by adding a time series of noise to the raw counts before processing the data. This time series of noise is constructed following the rules of the Markov process (Eq. (A.19)). The lag-1 autocorrelation $\alpha \approx 0.7$ of the MTP data is calculated as the slope of a linear fit between the original time series and the same data set shifted by one point. The data is then processed by the retrieval in the same way as described above. Results are shown in Fig. 5.12.

When processing noisy data, the relative error in the derived phase line slopes is clearly larger than in the noise-free case. This is caused by the noise on the input data, which can result in a shift of the positions of the extrema at single altitude levels, making the linear fit procedure more difficult. Again, the errors are much smaller for larger amplitudes (e.g. 2 K, in Fig. 5.12d) than for small amplitudes (e.g. 1 K, in Fig. 5.12c). In the noisy case it is even clearer, that only small vertical wavelengths can be resolved in the MTP data.

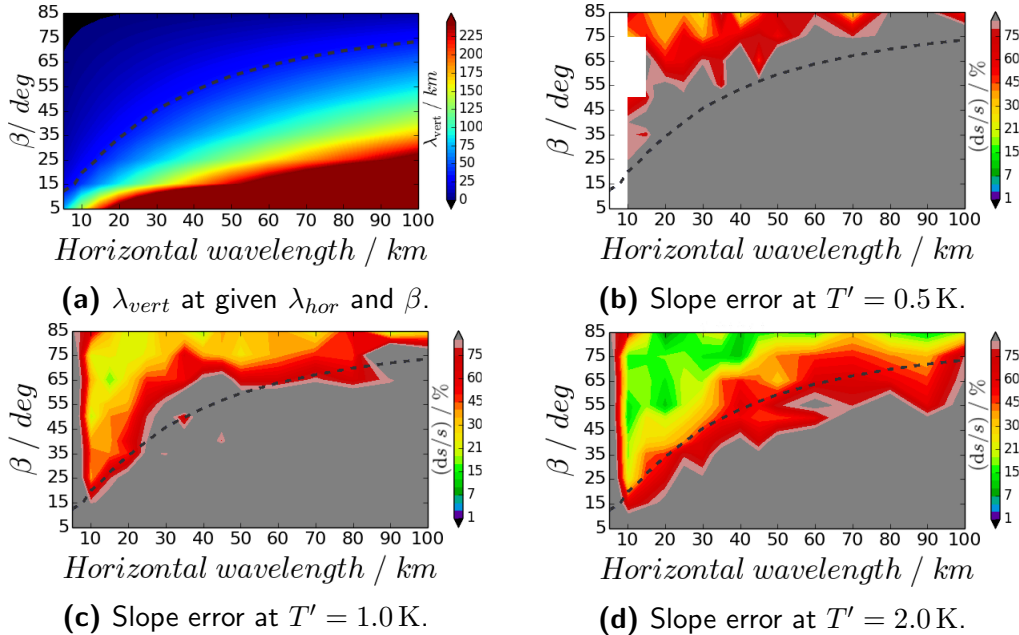


Figure 5.12: (a) expected vertical wavelength at given λ_{hor} and β and relative error (in %), of derived phase lines resulting from noisy synthetic data processed with the JPL retrieval, with given T' -amplitudes of (b) 0.5 K, (c) 1.0 K, and (d) 2.0 K. The dashed lines indicate $\lambda_{vert} = 30$ km

From this study it becomes clear that the amplitude of the temperature perturbation strongly influences the quality of the derived characteristics of the wave. In the case of processing wave signals with an amplitude of $T' = 0.5$ K (Fig. 5.12b), the derived PLOs diverge from the true β by 50% or more in almost all cases, leading to the conclusion that the T' signal is too small to be resolved within the noisy data. In Chapter 4.2, the measurement noise was found to induce fluctuations on the measured BTs with a magnitude of ~ 0.37 K. This means that for a wave-induced temperature fluctuation with amplitude 0.5 K, the signal-to-noise ratio is less than 2.

This explains the large errors in the analysis, and implies that the detection limit of temperature perturbations in MTP data only permits the correct detection of wave-induced temperature perturbations with amplitudes of at least 1-1.5 K. Only with large enough temperature perturbation amplitudes, the signal can be picked up by the sensor, and the ACHWAS algorithm is able to perform well.

Uncertainty of derived wave quantities

When analysing the uncertainties of the derived quantities, it must be noted that the RT model used to create the synthetic data (RT model GARLIC, within TIRAMISU) differs from the RT model within the NASA-JPL retrieval, which uses a simplified approach with less altitude levels and different trace gas amounts than GARLIC (see Chapter 4.3 or Appendix A.1). This can influence the conversion from observations to absolute temperatures. In Fig. 4.21b in the previous chapter, the difference between the BTs simulated with the two RT models are shown. The little kink towards a slightly smaller differences between the BTs calculated with the two RT models at flight level can induce a similar structure in the derived absolute temperature profiles, and the reconstructed temperature perturbation signals within this study (cf. Fig. 5.8c). This may handicap the linear fit through the extrema defining a phase line, from which the wave characteristics are derived. That probably adds to the over-all error seen in the present study, leading to an over-estimation of uncertainty in the following. When processing mission data, the ACHWAS algorithm is expected to perform better than what is possible to show within this synthetic data study.

The vertical wavelength of the observed GW, λ_{vert} is derived by multiplying the (phase line-) slope of the linear fit, s_{fit} , with the horizontal wavelength, λ_{hor} , interpreted as the median wavelength of the reconstruction interval.

The uncertainty of λ_{hor} results from the width of the reconstruction interval: In the default settings, this interval is derived from a Gauss-fit to the power-spectrum. The interval width, W_{R} results from including those scales, at which the global wavelet power is larger than the maximum value divided by 1000. This is about 3 times larger than the $\text{FWHM} = \sigma \cdot 2\sqrt{2\ln 2}$, with the standard deviation σ . The synthetic data studies have shown that even with noisy data the reconstruction intervals are centred around the correct horizontal wavelength. Hence, the standard deviation of the Gauss fit is used to pick the interval in which the true wavelength is most likely to be found when processing mission data:

$$\Delta\lambda_{\text{hor}} = \frac{\text{FWHM}}{2\sqrt{2\ln 2}} = \frac{W_{\text{R}}/6}{2\sqrt{2\ln 2}} = \frac{\lambda_{\text{R}}^{\text{max}} - \lambda_{\text{R}}^{\text{min}}}{6\sqrt{2\ln 2}} \quad (5.13)$$

using the difference between the largest reconstruction wave length, $\lambda_{\text{R}}^{\text{max}}$, and the smallest, $\lambda_{\text{R}}^{\text{min}}$, to define the interval width. This uncertainty can easily be derived, knowing the relationship of the reconstruction interval width to the true horizontal wavelength (Eq. (5.12)). It is worth mentioning, that the wavenumber is calculated from the wavelengths through multiplication with an error-free constant, so that it has the same relative uncertainty as the wavelength.

The calculation of λ_{vert} , as well as the vertical wave number $m = 2\pi/\lambda_{\text{vert}}$, is straight forward, with the known slope of the linear fit, s_{fit} from the analysis and the estimated horizontal wave length λ_{hor} with associated wave number $k = 2\pi/\lambda_{\text{hor}}$:

$$\lambda_{\text{vert}} = \frac{\lambda_{\text{hor}}}{s_{\text{fit}}} \leftrightarrow m = k \cdot s_{\text{fit}} \quad (5.14)$$

The relative error of s_{fit} is already known from the previously shown results of the ACHWAS algorithm applied to synthetic data.

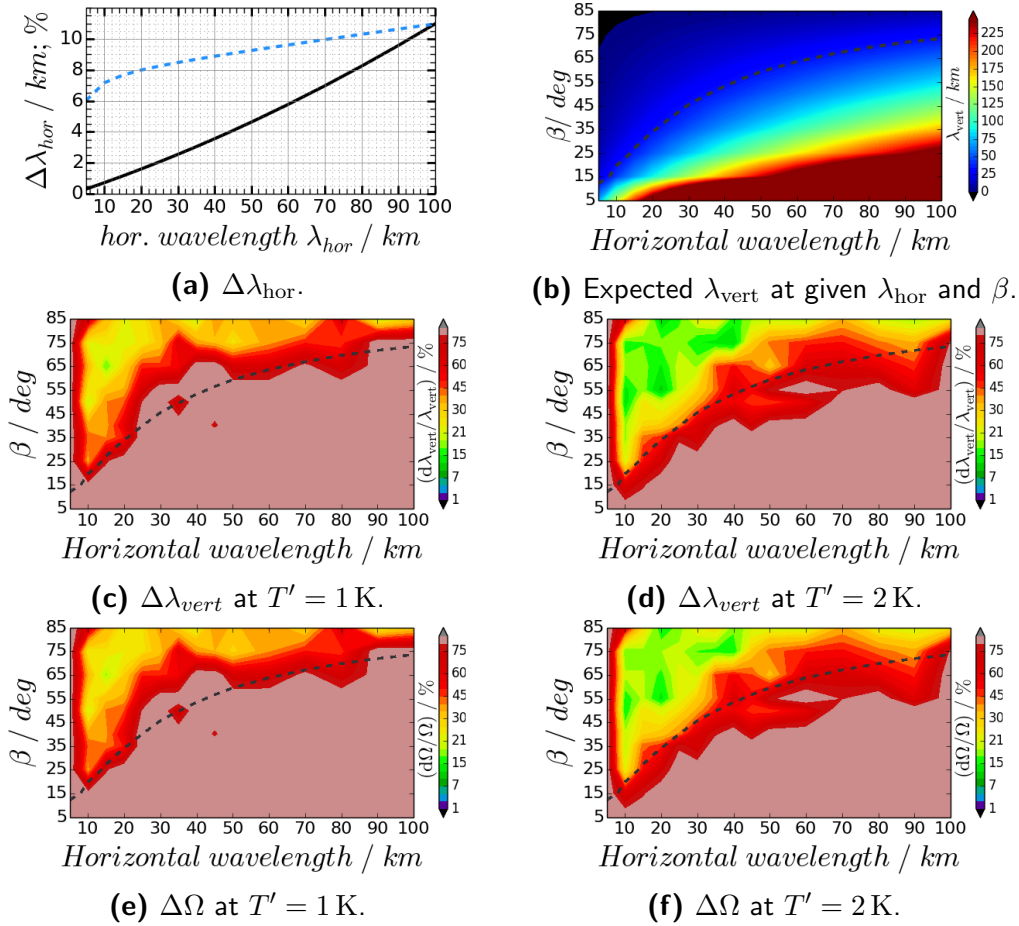


Figure 5.13: (a) uncertainty of λ_{hor} in km (black line) and % (blue, dashed line). (b) expected λ_{vert} . Also: relative error (in %), of derived λ_{vert} with given T' -amplitudes of (c) 1 K and (d) 2 K, and relative error (in %), of derived Ω with given T' -amplitudes of (e) 1 K and (f) 2 K. The dashed lines indicate $\lambda_{\text{vert}} = 30$ km

With this the overall uncertainty of the resulting vertical wavelength can be derived as:

$$\Delta\lambda_{\text{vert}} = \sqrt{\left(\frac{\Delta\lambda_{\text{hor}}}{s_{\text{fit}}}\right)^2 + \left(\frac{\lambda_{\text{hor}}}{s_{\text{fit}}^2} \cdot \Delta s_{\text{fit}}\right)^2} \quad (5.15)$$

Moreover, using the mid-frequency approximation to calculate the intrinsic frequency of the observed GW, $\Omega = N |k/m|$, the relative error can be calculated as:

$$\Delta\Omega = \sqrt{\left(\frac{\Delta k}{k}\right)^2 + \left(\frac{\Delta m}{m}\right)^2} \quad (5.16)$$

Both derived uncertainties, for $\Delta\lambda_{\text{vert}}$ and $\Delta\Omega$ are shown in Fig. 5.13 for temperature perturbation amplitudes of 1 K and 2 K. They are clearly dominated by the uncertainty of the fit to the phase lines. Again, best results are achieved for larger amplitudes and small vertical wavelengths (upper left corners of the plots in Fig. 5.13).

When analysing mission data, a typical error of $\sim 30\%$ or better can be assumed in the derived vertical wavenumber, given that the amplitude of the temperature perturbation signal is at least 1.5 K and the vertical wavelength of the encountered wave packet is smaller than 50 km. It is expected to find even better results for real data processed with the NASA-JPL retrieval algorithm, as the synthetic data study is influenced by differences in the RT calculations of the simulated data and the retrieval algorithm. Moreover, typical scales of GW vertical wavelengths are $\lambda_{\text{vert}} \leq 30$ km for which the error only becomes larger (up to $\sim 50\%$) when approaching this upper limit of vertical wavelengths.

Concerning derived momentum fluxes, an error estimation is not unambiguous. The NASA-JPL retrieval method used to calculate the absolute temperature profiles from the MTP measurements is heavily dependent on the available a priori data. Within the processing of a single flight leg, the a priori temperature profiles used in the conversion of raw data to absolute temperature profiles, can change from measurement cycle to measurement cycle. Also, if the a priori data base does not represent the real atmospheric conditions during measurement flights well, it is unclear what the error of the absolute temperatures in the MTP output really is. Hence, there is no way to derive a clear uncertainty connected to secondary data products, such as potential temperature or static stability, or even the amplitude of the reconstructed temperature fluctuations seen in MTP data, which was over-estimated by up to 0.4 K in the synthetic data runs. Still, as mentioned earlier, the ACHWAS algorithm performs the linear fit, which determines the slope of the phase line, multiple times with varying numbers of altitude levels included in the analysis. For any of the derived quantities, the differences between those analysis runs can be used to derive an uncertainty. This practice will be applied in the following case studies. It is expected that the TIRAMISU retrieval will be able to derive temperature profiles of better quality, once the correct settings are found.

5.3 Case study: DEEPWAVE campaign data

Since the two campaigns in which the DLR-MTP has been deployed were entirely focussed on research questions different from GWs, the data recorded by the DLR-MTP do not provide a good base to test the ACHWAS algorithm with real mission data.

Moreover, as mentioned in Chapter 3.3.1, the DLR-MTP experienced some technical problems during its first deployment in the ML CIRRUS campaign. Furthermore, a number of flights during the ACRIDICON campaign have been used to test different measurement strategies, which has prevented applying the NASA-JPL retrieval algorithm up to now. However, the research of this campaign was mostly focussed on cloud microphysics, and only few flights provide long enough flight legs to evaluate remote-sensing data from the MTP. Mountain wave signatures are not expected to be found in any of those flight legs, as the campaign took place in the Amazon region around Manaus, where there is no orographic source of GWs. As a result, the algorithm described in the previous section will be applied to campaign data from a different campaign, which also took place in 2014. During the DEEPWAVE campaign in New Zealand (NZ) the sister instrument to the DLR-MTP, owned and operated by NCAR, was part of the instrumentation on the NCAR GV. As mentioned in Chapter 3.2, that MTP instrument is a duplicate to the DLR-MTP, as it is built with similar hardware parts that make up the radiometer. This gives reason to the assumption that the measurements of the two instruments show the same characteristics in noise and instrument effects when used with the same standard measurement strategy. Additionally, the results concerning the range of sensitivity of the MTP measurements from Chapter 4.4, as well as the performance of the ACHWAS algorithm using MTP data processed with the NASA-JPL retrieval, can reasonably be assumed to be applicable to the NCAR instrument as well. However, the NCAR-MTP is providing data with slightly lower horizontal resolution than the DLR-MTP, due to the fact that one measurement cycle takes ~ 17 s instead of the 13 s of the DLR-MTP. This results in less ability to resolve small-scale waves up to ~ 10 km, which would only just be sampled by three data points.

Data from two research flights of the DEEPWAVE campaign, that have been thoroughly discussed in the literature, e.g. by Smith et al. (2016), Portele et al. (2017) and Bramberger et al. (2017) is analysed. For the first time, MTP data¹ is processed with the ACHWAS algorithm, and the results will be discussed in the context of already published results.

5.3.1 The DEEPWAVE campaign 2014

The DEEPWAVE campaign took place in NZ during June and July 2014. A description of the purpose of the campaign, the instrumentation used during the measurement phase, as well as a summary of the meteorological situation can be found in Fritts et al. (2016) and Gisinger et al. (2017). This section will only give a brief overview of what is relevant for MTP data evaluation of the two flights analysed within this thesis.

The DEEPWAVE campaign was “the first comprehensive measurement program devoted to quantifying the evolution of gravity waves [...] arising from sources at lower altitudes as they propagate, interact with mean and other wave motions, and ultimately dissipate from Earth’s surface into the mesosphere and lower thermosphere” (Fritts et al., 2016).

¹UCAR/NCAR - Earth Observing Laboratory. 2015. Microwave Temperature Profiler (MTP) Data. Version 1.0. UCAR/NCAR - Earth Observing Laboratory. <https://doi.org/10.5065/D6H70D56>. Accessed 08 Aug 2017.

The South Island (SI) of NZ was chosen as the location for the measurements, as it is known as a GW ‘hot spot’, due to its vicinity to the winter polar night jet during June, July, and August (Hoffmann et al., 2016). The mountain ridge of the Southern Alps, which spans over the entire SI in a roughly South-West to North-East direction, forms a natural barrier to low-level winds, which typically have wind directions perpendicular to the mountain ridge (Gisinger et al., 2017). With the polar night jet at higher altitudes, waves generated by the flow over the Southern Alps are expected to find favourable conditions for deep propagation throughout the stratosphere and into the mesosphere and lower thermosphere (Fritts et al., 2016; Gisinger et al., 2017). The research flights were targeting various flow conditions over the SI, as well as the Tasman sea, to investigate the atmospheric responses. A variety of instruments was used to observe mountain waves. These include ground-based LIDAR instruments and air-glow imagers, radio sondes, satellite measurements, and air-borne observations from the NCAR GV as well as aboard the DLR FALCON aircraft. A detailed list of participating instruments is given in Fritts et al. (2016), along with an overview of the intensive observation periods (IOPs). The overall meteorological condition during the DEEPWAVE campaign in June, July, and August 2014 is summarised in Gisinger et al. (2017). They state, that based on the Southern Oscillation Index the mean tropospheric flow showed a tendency to South-Westerly flows towards the beginning of the campaign. Also, the subtropical jet is identified as being dominant over the polar front jet, but characterised as slightly weaker-than-average, based on the values of the Southern Annular Mode. At the same time, the polar front jet is characterised to be slightly stronger than average. Both jets had a mean westerly flow direction over the SI of NZ.

Within this study, the MTP measurements from two research flights (RFs) of the NCAR GV are analysed. The first, RF12, took place on June 29th, 2014 within IOP9, during which wave activity was detected throughout the entire observed atmosphere (Fritts et al., 2016). The other research flight, RF16, belongs to IOP10 and took place on July 4th, 2014, again, with the observation of strong wave activities throughout the observed atmosphere (Fritts et al., 2016). During this research flight, Smith et al. (2016) report the largest energy fluxes measured throughout the entire campaign. On the other hand, RF12 is reported to show only small fluxes of energy and momentum in flight level measurements (Smith et al., 2016). A possible explanation of the low flux measurements is mountain wave breaking, which is indicated in the flight leg data of the highest flight legs at 13.7 km (Fritts et al., 2016). The meteorological conditions during the two research flights will be summarised within the case studies below. Already published individual results from the analysis of aircraft data and other instruments, as well as model studies connected to the two research flights will also be shown. The results of the analysis of MTP data with the ACHWAS algorithm will be discussed in comparison to the already known results.

In their discussion of NCAR GV flight leg data, Smith et al. (2016) divide the GW scales into four categories: the smallest scale, called ‘Turbulence’, includes scales of 0.1 km to 2 km and cannot be resolved with the MTP measurements. Also, the ‘short’ category ($6 \text{ km} \leq \lambda_{\text{hor}} \leq 20 \text{ km}$) is very close to the MTP’s detection limit of 10 km.

Thus, influence from the retrieval algorithm is expected to interfere with the analysis by the ACHWAS algorithm. As a result, the only wavelength scales discussed in the MTP data analysis are the ‘intermediate’ ($20 \text{ km} \leq \lambda_{\text{hor}} \leq 60 \text{ km}$), and the ‘long’ ($60 \text{ km} \leq \lambda_{\text{hor}} \leq 150 \text{ km}$) scales.

5.3.2 RF16 - July 4th, 2014

The results of the measurements taken during RF16 on July 4th, 2014 are summarised in Bramberger et al. (2017). Here, a thorough analysis of the meteorological situation, the measurement results, and the connection between observations at multiple different layers of the atmosphere is performed. Bramberger et al. (2017) analyse, whether the strong forcing situation in the lower troposphere caused the observation of one of the largest GW events in the middle atmosphere, reported by Kaifler et al. (2015), who analysed nearby ground-base Rayleigh-Lidar observations. For RF16, Smith et al. (2016) report the largest energy fluxes at flight level within the entire DEEPWAVE campaign.

The meteorological situation is described in detail by Bramberger et al. (2017): The research flight RF16 was part of the IOP10, during which winds with up to 35 ms^{-1} occurred in the troposphere, over the mountains of the NZ Southern Alps. The NCAR GV research flight took place between 07:00 UTC and 12:15 UTC, during which a low pressure system, as well as a zonal jet, causing the strong low-level winds, with a maximum around 09:00 UTC, approached the SI of NZ from South-West. During the time period between 00:00 UTC and 12:00 UTC, the wind direction changed from Westerly to South-Westerly. That affected the generation of GWs, as the horizontal wind speed, as well as the horizontal wind direction both changed. There was an increase in zonal wind speed to 50 ms^{-1} up to the tropopause, which is assumed to “favour the propagation of stationary mountain waves in the troposphere as no critical level exists in the ambient flow” (Bramberger et al., 2017). An analysis of the Scorer parameter, derived from European Centre for Medium-Range Weather Forecasts (ECMWF) model simulations is given, indicating that wave propagation was possible for waves with horizontal wavelengths larger than 2 km. From radio sonde profiles of $\partial\theta/\partial z$ Bramberger et al. (2017) derived regions of wave breaking, at altitudes with $\partial\theta/\partial z \approx 0$. From the moving direction of the sonde, they derive a “nearly permanent wave breaking above the main mountain ridge between 06UTC and 12UTC”, which is the time of the research flight analysed in the following.

MTP results

On the DEEPWAVE web page, it is stated that the MTP data for RF16 are “of moderate quality”¹, so some influence of the retrieval is expected in the analysis, e.g. from frequent changes of radiosonde templates to use in the conversion of BT measurements to absolute temperatures. However, this mostly impacts the analysis of small scales ($\lambda_{\text{hor}} \leq 20 \text{ km}$), which are not analysed within this study.

¹Source: <https://www.eol.ucar.edu/content/summary-mtp-results-deepwave> - accessed: 31st Aug. 2017

Moreover, as shown in the previous chapter, the MTP instrument has a more limited view of the atmosphere around the aircraft than indicated by the number of retrieval output levels. Thus, it is necessary to keep in mind that reconstructed T'_R signals are heavily influenced by a priori knowledge at distances to the aircraft larger than ~ 1.5 km. At these altitudes mainly a priori knowledge is used to derive absolute temperatures. Here, the phase lines of the waves always appear to be vertical and reconstructed T' amplitudes have values comparable to those at flight level. Therefore, within this analysis, any MTP data further away than 1.5 km from the aircraft are excluded.

Still, the analysis of MTP data reveals valuable information about the atmospheric state during the flight legs of RF16. While in the flight level data analysis by Smith et al. (2016) the highest EF_z values of the entire campaign are found during leg 1 of this flight, the MTP measurements reveal that these values are not representative of the overall situation.

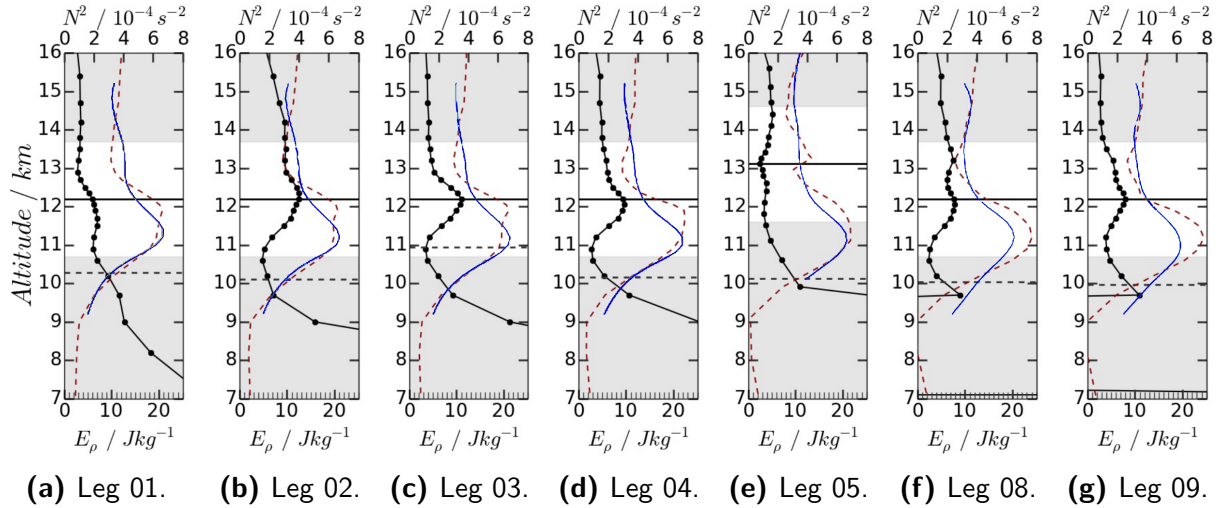


Figure 5.14: Static stability (red, dashed lines) and GWPED derived from MTP data (black, solid lines) during single legs of RF16. Thin, blue lines Static stability derived from high-resolution WRF model runs. Horizontal lines: current flight level (solid); tropopause altitude (dashed). Grey-shaded areas indicate where MTP data is dominated by a priori knowledge.

The static stability, derived from the background temperature of the MTP measurements are shown in Fig. 5.14, along with the GWPED derived from the overall temperature perturbation. During all flight legs there is a pronounced peak in N^2 , indicating the TIL, which spans roughly between ~ 10 km and ~ 12 – 13 km. The same profile of static stability is represented in high-resolution model data from the Weather Research and Forecasting (WRF) model (Skamarock and Klemp, 2008; Skamarock et al., 2008). Details of the model set-up are given in the next section. Whenever there is considerable wave activity at flight level (GWPED close to 10 Jkg^{-1} or larger), a decrease of the GWPED towards higher altitudes can be seen. The only exception is leg 5, where the GWPED stays about the same, but at a very low value of $\sim 3.8 \text{ Jkg}^{-1}$. While the varying conditions mentioned in Smith et al. (2016) and Bramberger et al. (2017) are reflected in the MTP measurements,

it even becomes clear, that the flight level measurements only provide snap shots of the overall atmospheric conditions. In some cases the derived values of energy and momentum fluxes do not represent the overall GW propagation conditions within the UTLS, especially during the first four flight legs of RF16.

The reconstructed temperature perturbations of the ‘intermediate’ and ‘long’ scales, according to the classification in Smith et al. (2016), derived from MTP measurements are shown in Fig. 5.15. Leg 3 and 9 are not shown, as they look similar to leg 2 and 8, respectively.

In the analysis of MTP data, evidence of ‘intermediate’ or ‘long’ scale waves propagating into the stratosphere is hardly found during leg 1 (Fig. 5.15a and 5.15b). While the amplitudes of the ‘intermediate’ T'_R signals at flight level are very large (almost 5 K at ~ 135 km distance to Mt. Aspiring), they drop to less than 1 K with growing distance to the aircraft altitude. The PLOs of the four ‘intermediate’ wave-phases with the strong amplitudes do not exceed 70° to the vertical, and show different orientations relative to the wind direction, some leaning into the wind, others not. This indicates that there is only little total upward propagation, if any. The T'_R signals of the ‘long’ scales have amplitudes around 1–1.8 K at flight level, and even derived PLOs of roughly 80° , that suggest upward propagation. However, the amplitude again decreases to less than 1 K above flight altitude, indicating wave dissipation and also little to no contribution to vertical fluxes of energy and momentum into the stratosphere.

Some evidence of propagation into the stratosphere by ‘intermediate’ and ‘long’ scale waves is found in leg 2 (Fig. 5.15c and 5.15d), over the Eastern edge of the island. There is also a slight reduction in the T'_R amplitudes at roughly 13 km altitude, which corresponds to the minimum in N^2 , defining the upper edge of the TIL. This is an indication that the waves are partly reflected or dissipated at the upper edge of the TIL. In the ‘long’ scale evaluation with the ACHWAS algorithm (Fig. 5.15d), the PLO of the warm phase at 118 km distance to Mt. Aspiring contributes strongest to the momentum flux ($MF_x \approx 0.65 - 0.8$ Pa), the neighbouring cold phase at ~ 170 km, contributing approximately 0.1 Pa. The spread of the MF_x contribution of a single wave-phase results from including different altitude ranges between 300 m and 1 km around flight altitude in the ACHWAS analysis.

During leg 4, the analysis of MTP data indicates possible upward propagation of ‘long’ scale waves over the Eastern edge of the island (Fig. 5.15f). The strong warm-phase at 125 km distance to Mt. Aspiring has an amplitude of ~ 2.8 K, the neighbouring cold-phase at 171 km one of ~ 2.3 K. Both phase lines lean into the wind at an angle of $\sim 80^\circ$. Their contributions to the momentum flux are 0.51–0.59 Pa and 0.33–0.41 Pa, respectively. The amplitude is reduced to about half above flight level, and the orientation of the phase line of the cold-phase appears to shift more towards the vertical. Still, the MTP data clearly indicate possible upward propagation of these wave modes encountered during flight. A similar situation is found during leg 8 and 9, with indication of upward propagating ‘long’ waves in the MTP data (Fig. 5.15j).

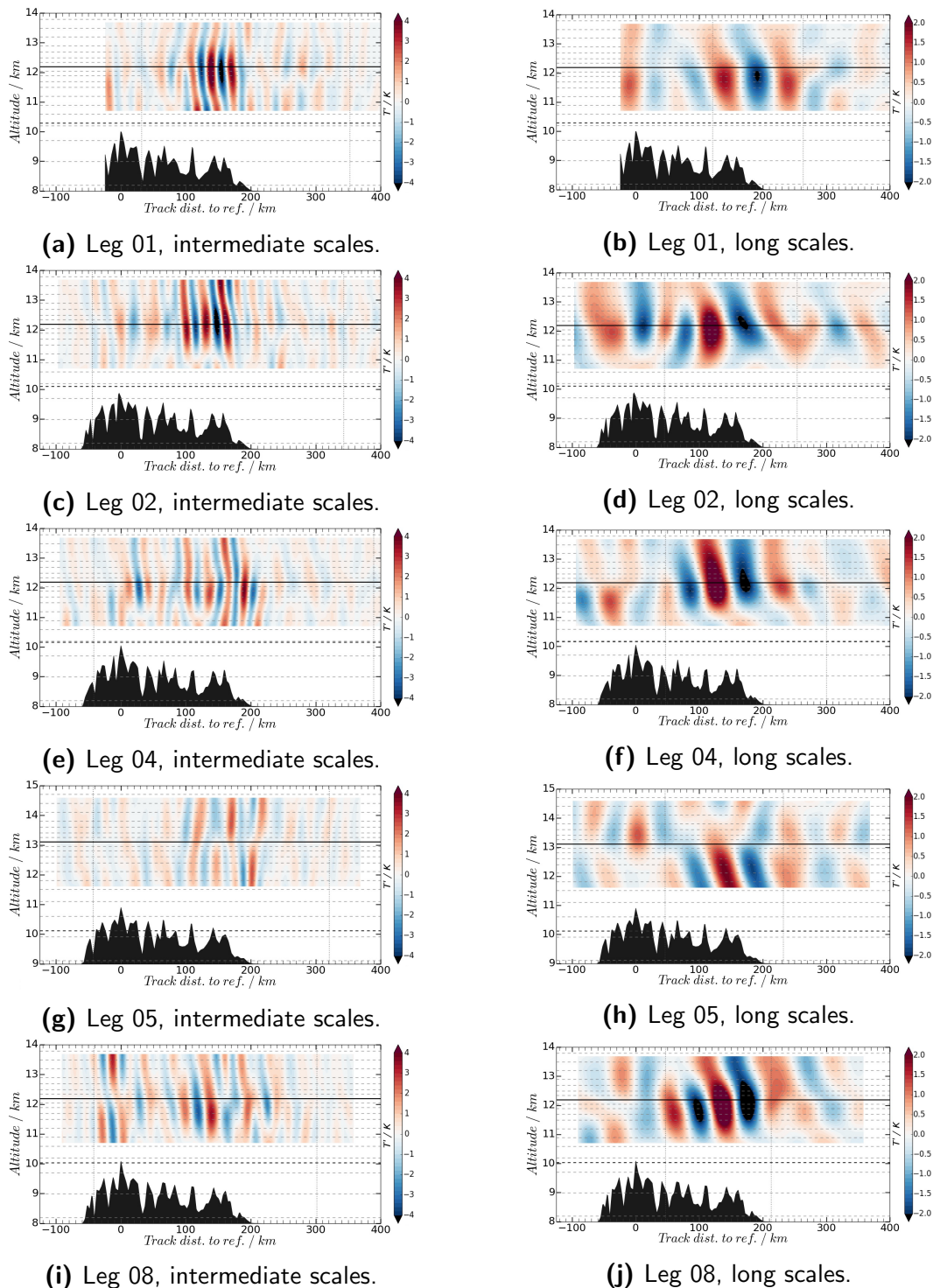


Figure 5.15: Reconstructed T' signals after wavelet analysis of MTP data. The x -scales are calculated distance to mt. Aspiring. Rows: different flight legs of RF16. Left column: Intermediate scales ($20 \text{ km} \leq 60 \text{ km}$); right column: Long scales ($60 \text{ km} \leq 150 \text{ km}$). Horizontal lines: current flight level (solid); leg-mean tropopause altitude (dashed). Dashed, grey lines in the background: MTP data output levels.

The T'_R signals of the MTP data from leg 5 (Fig 5.15g and 5.15h) only have amplitudes smaller than 1 K at and above flight level, which is in accordance with the small GWPED values shown in Fig. 5.14a. Moreover, dissipation of ‘long’ scale waves below flight level is indicated for three wave-phases with amplitudes of almost 2 K below flight level. Their amplitudes are dramatically reduced at flight level. Hence, no considerable contribution to vertical fluxes of energy and momentum are expected from the ‘intermediate’ or ‘long’ waves in this flight leg.

Comparison to model simulations

For this particular flight, high-resolution model data from the WRF model, set up with six-hourly ECMWF reanalysis data is available. The model run was initialised on July 3rd 2014 at 18:00 UTC and has a spacial resolution of 2 km, and temporal resolution of 5 min. The data was linearly interpolated to the flight track of RF16, and is available at 137 output levels. Only those within the applicable range of MTP data are used in the ACHWAS analysis.

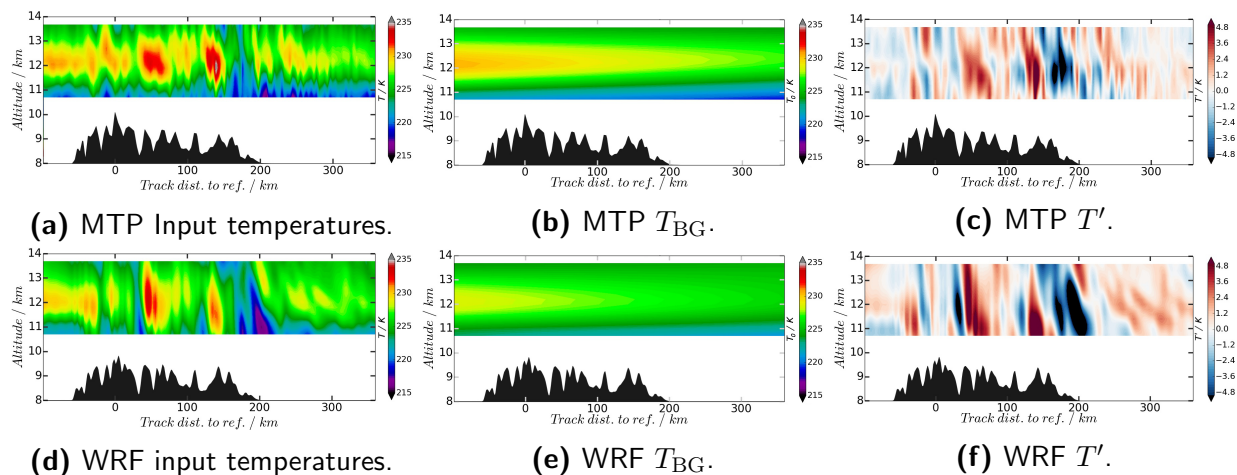


Figure 5.16: Temperature data of DEEPWAVE flight RF16, leg 8, as provided by MTP retrieval output (top row) and WRF simulations (bottom row). a)/d): Original input data; b)/e): Background temperature field (horizontal linear trends at each altitude level) and c)/f) remaining temperature perturbation signal. The topography has correct scaling, but is lifted.

In order to compare the model output to the MTP data, the interpolated WRF output is processed with the ACHWAS algorithm, using the same settings as for MTP data. The comparison of MTP data to model data shows similar results on every flight leg of RF16 (see Appendix A.3). As an example, the comparison of data from flight leg 8 are shown in the following. Figure 5.16 shows the original input data, the derived background temperatures and the remaining temperature perturbation signal for the MTP data, as well as for the WRF model data of flight leg 8. While the MTP data have decreasing vertical resolution with growing distance to the flight level, the model data are available at ~ 200 m resolution within the UTLS.

As only data with a maximum distance of 1.5 km distance to the flight level are shown, the vertical resolutions of both data sets are still comparable.

The input data of both, the MTP retrieval output, as well as the WRF model output, show similar structures. The model data (bottom row of Fig. 5.16) exhibit warm and cold temperature structures that extend further in the vertical. However, they are found at the same horizontal positions as in the MTP measurements. Moreover, there are more small-scale structures found in the MTP data (e.g. thin vertical ‘stripes’ between 200 km and 300 km distance to Mt. Aspiring), which are not displayed in the WRF model data. As mentioned earlier, it cannot clearly be determined whether these small structures are atmospheric signals, as they can also be imposed on the data set by the retrieval algorithm. There are only slight differences in the derived temperature signals of the background and the temperature perturbations in both data sets. The background signal derived from MTP data is slightly warmer than that from WRF data. At the same time the amplitudes of the remaining temperature perturbations are slightly larger in the WRF data. The same is found in the analysis of all other flight legs of RF16.

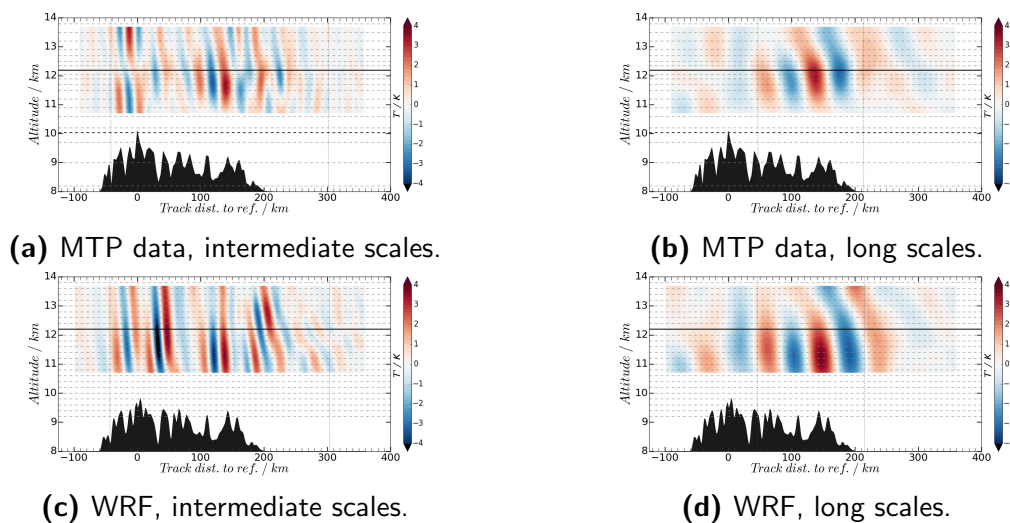


Figure 5.17: Reconstructed T' signals after wavelet analysis of MTP retrieval output (top row) and high resolution WRF model data (bottom row) of RF16 leg 8. The x -scales are calculated distance to Mt. Aspiring. Left column: Intermediate scales ($20 \text{ km} \leq 60 \text{ km}$); right column: Long scales ($60 \text{ km} \leq 150 \text{ km}$). Horizontal lines: current flight level (solid); leg-mean tropopause altitude (dashed). Dashed, grey lines in the background: available data output levels.

When analysing the reconstructed temperature perturbation signals at various wavelength scales, more differences between the data become visible. While the positions of the warm- and cold-phases of the encountered waves are the same, their amplitudes, as well as the general shapes do differ. Still, the phase-line orientations agree well in almost all cases, indicating the same direction of propagation, and the strength-pattern is the same in both data sets. Strong temperature perturbation signals are found at the same positions in both data sets.

Additionally, more wave activity in the intermediate scales is indicated by larger amplitudes in the reconstructed T'_{rec} signals of the WRF data over the Western part of the island. This is true for almost all flight legs of RF16. This is mainly due to the chosen colour-coding in the figures: At this part of the island, the effect of the stronger T'_{rec} amplitudes in the WRF data is more visible than at those parts of the flight leg, where there are also strong amplitudes in the MTP data. However, there is still a decrease in the temperature perturbation amplitudes above flight level in the model data, confirming the conclusion drawn from the analysis of MTP measurements, that flight level data analysis is sensitive to the chosen flight level, and might not represent well the amount of energy and momentum carried into the stratosphere by GWs. In general, the model data do not show as much variability between the different flight legs, as the MTP data. The amplitudes in the reconstructed temperature perturbation signals from WRF data are comparable between all legs, while the MTP data clearly show a decrease in wave activity in the ‘intermediate’ and ‘long’ scales towards flight leg 5 (c.f. Fig. 5.15 and Appendix A.3). A possible reason could be the temporal evolution of the wave field within the model. Choosing a different initialisation time of the model run could influence the wind field and change the output. The whole system seems to be slower in its evolution than what is seen in observations. The dependence on model output on run time since initialisation is already discussed in Portele et al. (2017).

Comparison to known wave properties from flight level data evaluation

To analyse the possible waves present within the troposphere, vertical wind measurements by the Doppler wind LIDAR measurements aboard the DLR FALCON aircraft (Witschas et al., 2017), are used by Bramberger et al. (2017). Here, a clear indication for the existence of mountain waves is given by vertical wind perturbations with a horizontal wavelength of 10 km - 20 km throughout the UTLS. The signal is found both, in the LIDAR measurements aboard the DLR-FALCON, as well as in the flight level measurements of the NCAR GV aircraft at 12 km, at the same locations on all analysed altitudes. Bramberger et al. (2017) conclude that this indicates that the wave pattern is stationary, as well as that the phase lines of the waves are nearly vertical, which is typical for high-frequency waves. In the analysis of flight level wind data from the DLR-FALCON, Bramberger et al. (2017) derive mainly positive EF_z values, which is an indication of upward propagation of the waves. However, they find largely varying EF_z values over time, as do Smith et al. (2016) in their analysis of NCAR GV flight-level data (see Fig. 5.18a). The same variability is found in the MTP data, indicated by the varying amplitudes of the reconstructed temperature perturbation signals.

Still, the picture drawn by the MTP measurements does differ from that of flight level analysis in some cases: Smith et al. (2016) report the “largest fluxes in the entire DEEPWAVE project” during leg 1 of RF 16. However, the MTP data indicate that while there are large amplitudes in T'_{rec} , that explain the large flux values found in the flight leg analysis, the amplitudes decrease towards higher altitudes. Hence, the measured fluxes are not expected to reach the stratosphere.

For possibly propagating waves during leg two, the momentum flux values derived from the MTP data show a large variability between different wave-phases, with values between 0.1 Pa and 0.8 Pa. The MF_x values shown in Smith et al. (2016) (Fig. 5.18b) indicate a leg-mean momentum flux of 0.3 – 0.5 Pa, which is around the mean value of the two flux contributions. Note, that from the MTP measurements only non-directional flux values can be derived. Here, the MTP measurements give evidence to strongly varying wave activity, depending on the position of the aircraft. This variability is not reflected in the leg-mean flux values often discussed in the literature.

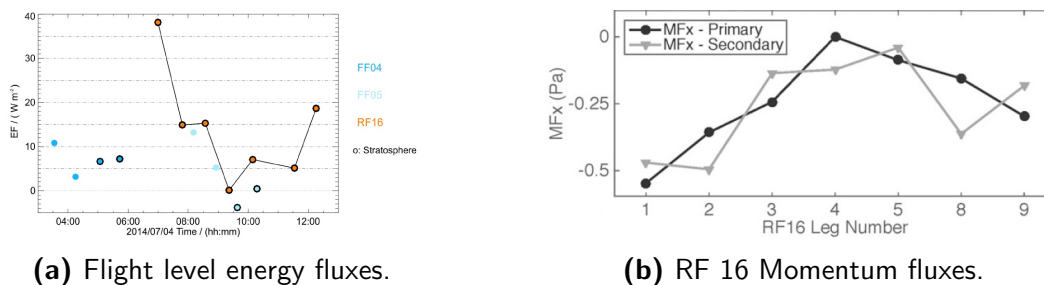


Figure 5.18: a) Energy fluxes derived from flight level data of GV flight legs during RF16 and Falcon data during FF04 and FF05. Adapted from Fig. 6a) in Bramberger et al. (2017). b) Momentum fluxes derived from flight level wind measurements during RF16, using two different sensor readings. Adapted from Fig. 7 (middle panel) in Smith et al. (2016, ©American Meteorological Society. Used with permission.) .

During leg 4, quite large momentum flux values of 0.33-0.59 Pa are found in the analysis of ‘long’ scale temperature perturbation signals in MTP data. In their analysis, (Smith et al., 2016) derive only small leg-mean MF_x values ($0 \text{ Pa} \leq |MF_x| \leq 0.2 \text{ Pa}$), which is lower than the values derived with the ACHWAS algorithm. At the time of this flight leg, Bramberger et al. (2017) find evidence for downward propagation of waves in leg 3 of DLR-FALCON research flight FF05, flown $\sim 1.3 \text{ km}$ below the NCAR GV flight track. The analysis of data from these flight legs is an example of the influence by contributions from both positive and negative momentum fluxes found during the flight leg and largely varying contributions within different wavelength scales. These varying contributions are an explanation of the large deviation of the momentum flux contributions derived with the ACHWAS algorithm for single wave-phases from the leg-mean values derived from flight level data analysis.

Finally, during leg 5, Smith et al. (2016) find a larger leg-mean upward energy flux than in leg 4, which is in contrast to the very low T'_{rec} amplitudes seen in the MTP data. However, the analysis of MTP data does not include the ‘small’ scales, suggesting that the values derived from flight level data are influenced by waves with $6 \text{ km} \leq \lambda_{\text{hor}} \leq 20 \text{ km}$.

In their analysis Bramberger et al. (2017) also show the spectral analysis of the energy flux, derived from DLR-FALCON flight level measurements, which shows significant maxima in spectral power at wavelength scales between 10 km and 40 km (see Fig 5.19a). Moreover, when analysing all available data from the research flights during IOP10, a strong peak in spectral power at the same scales is found.

This is in accordance to the results in Smith et al. (2016). In both studies, the flux-carrying waves are identified as those of ‘intermediate’ scales. The contribution by the ‘small’ scale waves is not investigated in the MTP data.

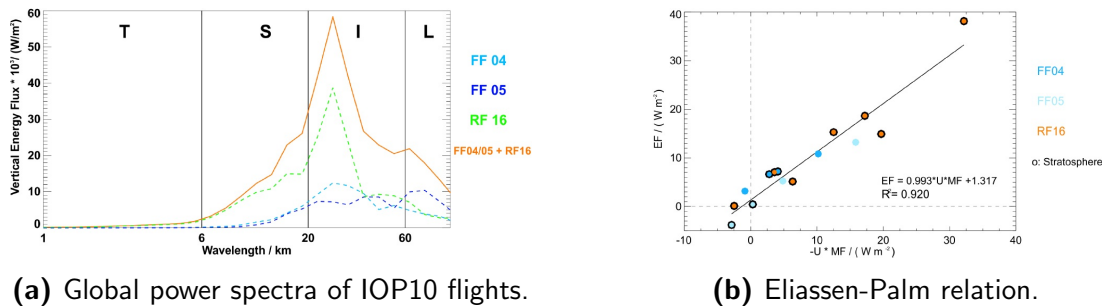


Figure 5.19: a) Power spectra of DEEPWAVE flights during IOP10. The letters correspond to the wavelength scales defined in Smith et al. (2016). Adapted from Fig. 7d Bramberger et al. (2017). b) Eliassen-Palm relation, derived from flight leg wind measurements during IOP10. Adapted from Fig. 6b in Bramberger et al. (2017).

Also, both studies show that the Eliassen-Palm relation $EF = \vec{U} \cdot \vec{MF}$ is fulfilled in the case of IOP10 (see Fig 5.18a), indicating that linear theory can be applied to describe the GWs and a comparison between flux values derived by flight level wind data analysis and those derived from MTP temperature data is valid.

5.3.3 RF12 - June 29th, 2014

The NCAR GV research flight RF12 belongs to the IOP9 from June 29th to July 1st, 2014, and is reported to have probed “one of the strongest mountain wave events during DEEP-WAVE” (Fritts et al., 2016). Gisinger et al. (2017) characterised the situation as belonging to a so-called Trough-North-West weather regime. In their analysis, large hydrostatic reflection coefficients were calculated around the tropopause, due to an enhanced TIL. This coefficient decreased over time, indicating more favourable conditions for wave propagation towards the end of RF12 (c.f. Fig. 5.20a).

The meteorological situation is also discussed by Portele et al. (2017), who found a transition from strong to moderate transient forcing over the Southern Alps during IOP9. They describe an Eastward-moving Rossby-wave ridge causing increasing North-Westerly and Westerly winds, almost perpendicular to the mountain ridge of the Southern Alps. According to Portele et al. (2017), the cross-mountain wind component was strongest at 10 UTC on June 29th, 2014. That falls within the time of RF12, which started at 07:53 UTC and landed at 17:09 UTC of that day. A double jet with peaks at ≈ 11 km and ≈ 15 km was causing quite complex propagating conditions for waves generated by the flow over the mountain ridge, due to increased wind shear over the lower wind maximum and the wind minimum in between the two jets (Portele et al., 2017).

The analysis of radio sonde data within the same study indicated “a nearly adiabatic layer at about 14 km altitude”, within which wave breaking is expected.

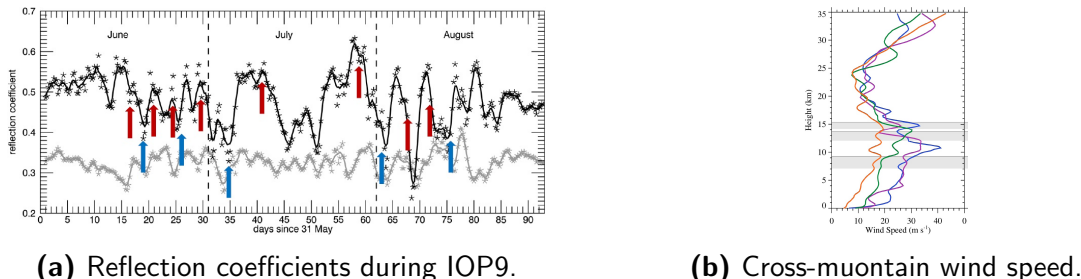


Figure 5.20: a) Hydrostatic reflection coefficients in June 2014. GW events with reflection coefficients ≥ 0.5 are marked with red arrows, GW events with reflection coefficients ≤ 0.4 are marked with blue arrows. Adapted from Fig. 5a in Gisinger et al. (2017, ©American Meteorological Society. Used with permission.). b) Upstream cross-mountain wind speed from ECMWF reanalysis. Adapted from Fig. 8 (left panel) in Portele et al. (2017, ©American Meteorological Society. Used with permission.). The blue, purple, and green lines represent the conditions on June 29th, between 08-10 UTC, 14-16 UTC, and 23-01 UTC, respectively; the orange line the period 17-19 UTC on June 30th.

MTP results

According to the summary on the DEEPWAVE web page, the MTP data for RF12 have “reasonable quality retrievals”¹. This indicates that the temperature profiles are trustworthy, although the control value given by the retrieval algorithm shows that the available radio sonde templates do not perfectly fit the measured data (MRI value close to 1). It can be assumed that the application of the ACHWAS algorithm provides reliable results for temperature perturbations with amplitudes of at least 1.5 K.

The profile of static stability together with the GWPED derived from the total T' signal and the background state at each altitude are shown in Fig. 5.21. Here, the development of background conditions between flight legs can be nicely illustrated. During RF12, a pronounced TIL is present between ~ 11 km and ~ 13 km during the first four flight legs. It is indicated by the strong peak in N^2 (red, dashed line in Fig. 5.21). In the data of legs 1, 6, and 10, a local minimum in N^2 is visible at or close to the current flight level. This is most likely an artefact from the retrieval algorithm, which forces the flight level temperature to equal the outside air temperature, measured by the aircraft. It can be seen that the overall GWPED always changes with altitude, showing that flight level measurements do not reflect the atmospheric state within the whole UTLS. Again, the influence of the retrieval can be seen in the GWPED, where local minima and maxima are induced around flight level. Still, from the general shape of the N^2 and GWPED profiles, the following development can be observed:

¹Source: <https://www.eol.ucar.edu/content/summary-mtp-results-deepwave> - accessed: 31st Aug. 2017

During leg 1 there is a peak in GWPED within the TIL, which is an indication of trapped waves. However, this peak becomes smaller in leg 6, and is not present at all during leg 10 and leg 14, where the shape of the N^2 profile still resembles that of leg 1. Hence, the change in the GWPED is probably due to changing wind conditions, which are not being observed by the MTP.

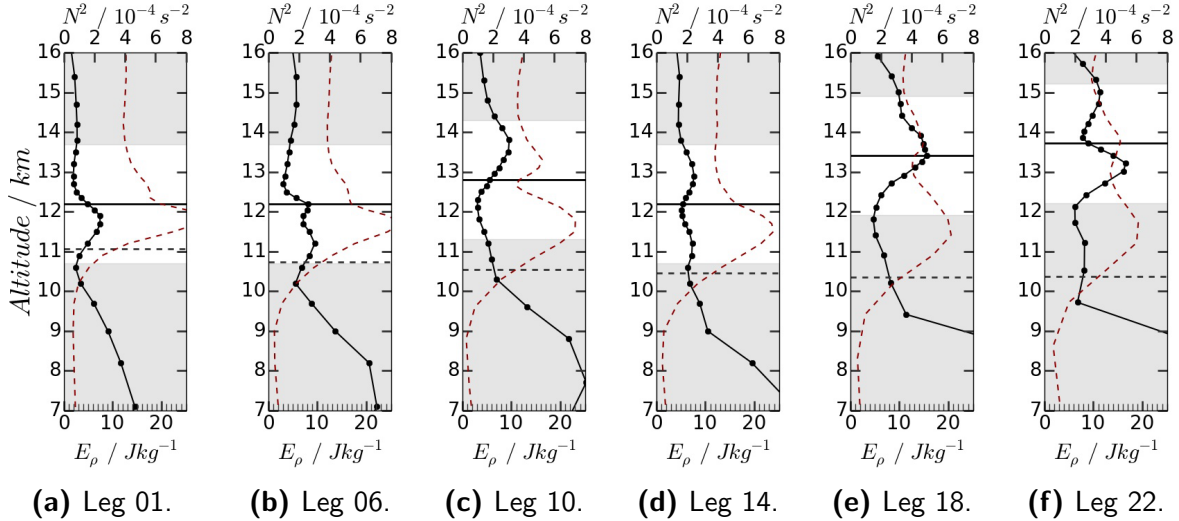


Figure 5.21: Static stability (red, dashed lines) and GWPED (black, solid lines) during single legs of RF12. Horizontal lines: current flight level (solid); tropopause altitude (dashed). Grey-shaded areas indicate where MTP data is dominated by a priori knowledge.

An overview of MTP results is given by showing the reconstructed T'_R signals after wavelet analysis. Figure 5.22 shows T'_R of five flight segments of RF12, passing over the Mt. Aspiring massif of the Southern Alps. Within these figures details of the temporal evolution of wave propagation conditions can be visualised.

In the plots of T'_R of the first flight leg (Fig. 5.22a and 5.22b), the influence of the TIL between 11 km and 13 km is visible in both wavelength scales. At the upper and lower edges of the TIL, the amplitudes in T'_R are very small. However, within the TIL, T'_R has up to four times larger amplitudes, indicating trapped waves within the TIL. In the ‘intermediate’ scale analysis (Fig. 5.22a), the strong warm-phase at 143 km and the strong cold-phase at 156 km distance to Mt Aspiring, over Mt. Pisgah (see Fig. 3 in Portele et al., 2017, for mountain peak identification), appear almost vertical within the TIL. However, the PLO at flight level, derived using the ACHWAS algorithm, is about $\sim 80^\circ$ to the vertical, leaning into the wind, which indicates upward propagation. The phase lines shift to a larger tilt just above flight level, indicating possible leakage to higher altitudes, but with largely reduced amplitudes, compared to the altitudes directly below flight level. The derived intrinsic frequencies for the two wave-phases are considerably lower than $N \approx 0.027 \text{ s}^{-1}$ ($0.003 \leq \Omega \leq 0.007 \text{ s}^{-1}$). The momentum flux contributions are $0.17 \text{ Pa} - 0.24 \text{ Pa}$ and $0.21 \text{ Pa} - 0.43 \text{ Pa}$ respectively.

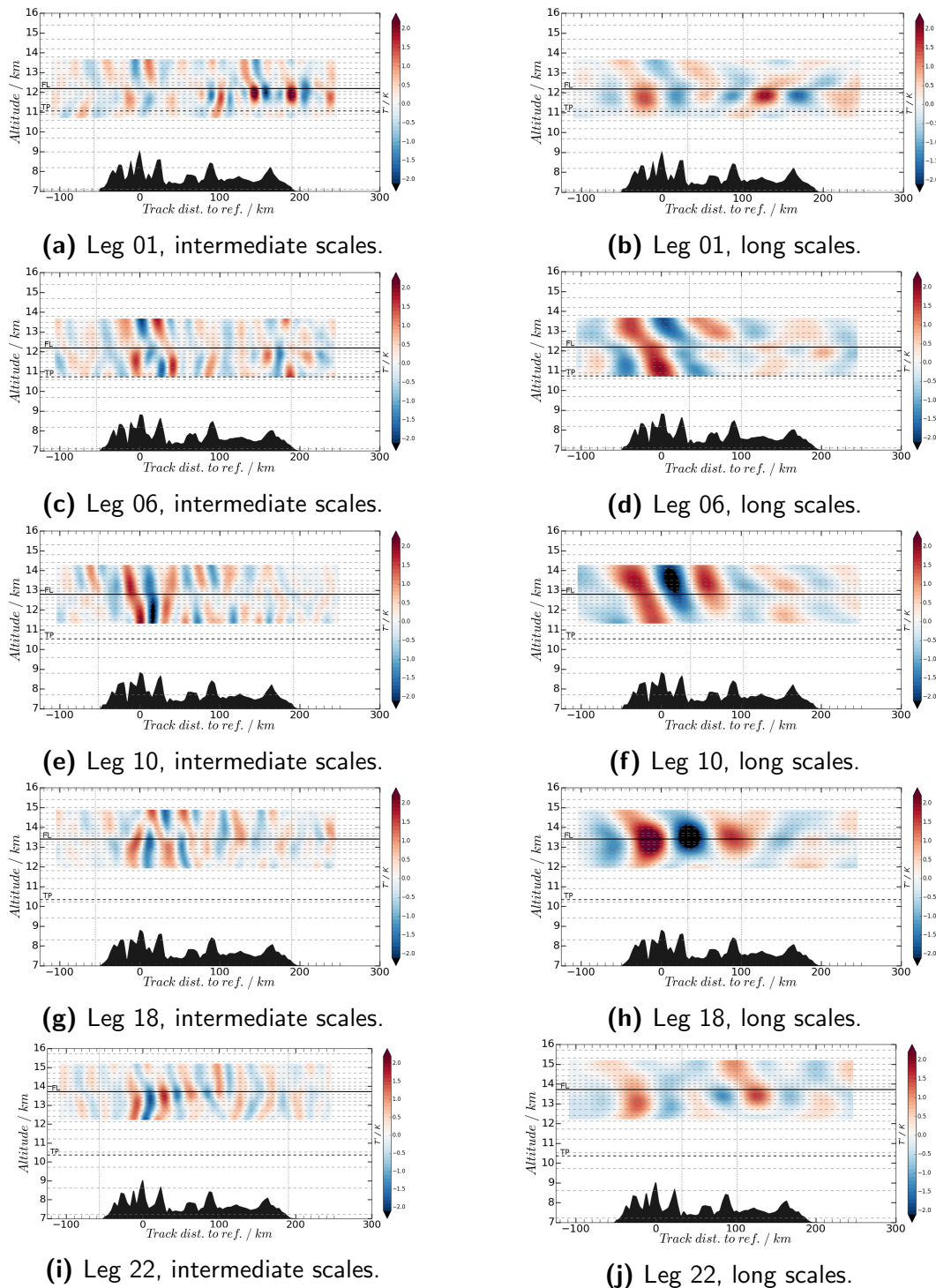


Figure 5.22: Reconstructed T' signals after wavelet analysis of MTP data. The x -scales are calculated distance to Mt. Aspiring. Rows: different flight legs of RF12. Left column: Intermediate scales ($20 \text{ km} \leq 60 \text{ km}$); right column: Long scales ($60 \text{ km} \leq 150 \text{ km}$). Horizontal lines: current flight level (solid); leg-mean tropopause altitude (dashed). Dashed, grey lines in the background: MTP data output levels.

Legs 6, 10, and 14 correspond to the maximum forcing phase, defined by Portele et al. (2017). The T'_R signals of leg 14 are not shown here, as they are similar to those of leg 10. There is clear indication of wave propagation in the T'_R signals, especially of the ‘long’ scales (Fig. 5.22d and 5.22f), through the upper boundary of the TIL directly above the Mt Aspiring massif between -50 km and 50 km track distance. For the two ‘intermediate’ wave-phases with strong amplitudes directly above Mt. Aspiring, the analysis of data from leg 10 with the ACHWAS algorithm reveals a tilt of the phase lines of about 80° to the vertical and intrinsic frequencies of $0.0022 \text{ s}^{-1} \leq \Omega \leq 0.0035 \text{ s}^{-1}$. This results in momentum flux contributions at flight level between 0.17 Pa and 0.31 Pa. The analysis of the ‘long’ scales in leg 10 (Fig. 5.22f) shows three wave-phases with strong amplitudes between 0 km and 80 km distance to Mt. Aspiring. The phase lines lean a bit more into the wind, with PLOs of $\sim 85^\circ$ to the vertical. The resulting intrinsic frequencies are $\Omega \approx 0.0012 \text{ s}^{-1}$, $\Omega \approx 0.0019 \text{ s}^{-1}$ and $\Omega \approx 0.0025 \text{ s}^{-1}$ for the wave-phases at -20 km, 20 km and 60 km distance to Mt. Aspiring respectively. Momentum flux contributions at flight level are ~ 0.12 Pa for the first and last of the three wave-phases, and ~ 0.24 Pa for the one in between.

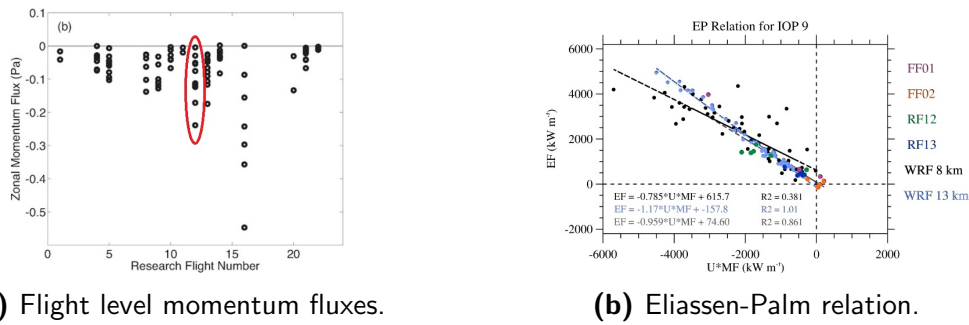
Only during leg 18, an indication of wave trapping within the ‘long’ scales is evident again (Fig. 5.22h), now between altitudes of 12 km and 15 km. Especially the cold wave-phase at 35 km shows no distinct tilt in the phase line, as the PLOs derived with the ACHWAS algorithm differ strongly between the analyses of different altitude ranges, with derived intrinsic frequency being close to N . Since the TIL lies below the altitude region in which the strong amplitudes are found, the trapping is more likely to be caused by the wind profile. Upstream cross-mountain wind profiles, derived by Portele et al. (2017), are shown in Fig. 5.20b. In the profiles of 08-10 UTC, there are two pronounced wind maxima at 11 km and 15 km altitude. The profile changes towards the next sonde at 14-16 UTC, where there is only one maximum at $\sim 11 - 12$ km, and a more pronounced minimum at ~ 14 km is seen. This change in wind conditions could explain the MTP measurements that result in such different T'_R signals in the ‘long’ scales between the different flight legs.

The T'_R signals of leg 22 (Fig. 5.22i and 5.22j) only show small amplitudes just above 1 K that do not allow for robust analysis with the ACHWAS algorithm. The overall wave activity within the ‘intermediate’ and ‘long’ scales during this leg is very low, and the T'_R signals show very small amplitudes above flight level. Hence, the waves within those two scale categories are expected to contribute only little to the energy and momentum flux into the stratosphere.

Comparison to known wave properties from flight level data evaluation

This research flight is discussed in Smith et al. (2016) and used as an example for low-flux events during the DEEPWAVE campaign in 2014. Also, Portele et al. (2017) analysed the forcing by low-level winds during this IOP. They used flight level measurements by both aircraft, as well as model simulations and concluded that the TIL was one characteristic responsible for wave reflection and breaking of waves. This influence of the TIL is also seen in the analysis of MTP data in the ‘intermediate’ and ‘long’ scales during leg 1.

However, the analysis of Portele et al. (2017) states that the TIL influences especially those waves with smaller horizontal scales. In accordance, Smith et al. (2016) observed that only waves with horizontal wavelengths larger than 40 km contributed to the vertical flux during RF12. They concluded that while the fluctuations of the vertical wind were dominated by short scales ($\lambda_{\text{hor}} \approx 8$ km), the flux-carrying waves fell within the ‘long’ category with dominant scales of $\lambda_{\text{hor}} \approx 80$ km. This is in concordance with the findings of Portele et al. (2017), who observed that only waves with scales above ≈ 60 km contributed to the vertical energy flux. In their wavelet analysis of the $p'w'$ cospectra, Portele et al. (2017) identified a significant peak in the global wavelet power located over the main ridge of the Southern Alps. This peak corresponds to scales of $60 \text{ km} \leq \lambda_{\text{hor}} \leq 80 \text{ km}$ and coincides with a negative momentum flux. Based on these findings the authors concluded that the encountered waves were upward propagating GWs with a mean wavelength of $\lambda_{\text{hor}} \approx 70$ km. In accordance, clear indication for upward propagating waves within the ‘intermediate’ and ‘long’ scales is found in MTP data, especially during legs 6, 10, and 14.



(a) Flight level momentum fluxes.

(b) Eliassen-Palm relation.

Figure 5.23: a) Flight level momentum fluxes during DEEPWAVE research flight. Adapted from Fig. 5b in Smith et al. (2016, ©American Meteorological Society. Used with permission.). RF12 flux values are encircled. b) Eliassen-Palm relation derived from different data sets during IOP9. Adapted from Fig. 12 in Portele et al. (2017, ©American Meteorological Society. Used with permission.).

In both analyses, the calculated leg-mean zonal momentum fluxes vary between 0 Pa and ~ 0.25 Pa (see Fig. 5.23a), with slightly smaller values reported by Portele et al. (2017). The values derived from MTP data during leg 1 compare well to the leg-mean MF_x values derived by Smith et al. (2016). As the momentum flux values of only two wave-phases are derived in the analysis of MTP data, there is indication of possible upward propagation of waves at flight level, however, confined to a small part of the flight leg, and with dissipation above flight level. The same is valid for the findings of leg 10.

Assuming that the wind perturbation signals behave analogous to the temperature fluctuations, as is indicated by Smith and Kruse (2017), the method applied by Smith et al. (2016) would only pick up considerable wave activity on flight legs 10 and 18, where the amplitudes in T'_R are largest. On the other hand, with the exception of leg 1 and leg 22, there are always considerable T'_R amplitudes ($T' \approx 2$ K) of the ‘long’ scale waves at flight level, explaining the observation by Smith et al. (2016) that “the energy flux is dominated by waves in the long category with $\lambda \approx 80$ km”.

In their linearity analysis, based on the Eliassen-Palm-relation, Smith et al. (2016) found “good agreement”, indicating that the GWs encountered during RF12 can be described using linear theory. This is confirmed by (Portele et al., 2017), using high-resolution Weather Research and Forecast model simulations (see Fig. 5.23b). Hence, the comparison between flight leg data analysis and MTP temperature data analysis is valid again.

5.4 Discussion

The case studies of the DEEPWAVE campaign show that the MTP provides valuable observations of the propagating conditions for GWs within the UTLS. The comparison with high resolution model data, available for DEEPWAVE flight RF16 confirms that the MTP is able to pick up changing atmospheric conditions above and below flight level, that are necessary to correctly interpret flight level data analysis.

There is indication of trapped waves within the TIL, giving the explanation for the already reported low flux values during RF12. Apart from clearly changing overall GW activity, wave reflection or dissipation at the TIL is also a possible explanation of the varying measurements of energy fluxes during RF16, reported by Smith et al. (2016). The MTP observations are unique in the way that the instrument constantly probes the same air masses as the aircraft in situ instruments, but yields information on an extended altitude layer from which information on the atmospheric background conditions can be derived. Thus it contributes greatly to the understanding of propagating conditions for GWs encountered during measurement flights.

Through the analysis of MTP data it is evident that GWs with wavelengths between 20 km and 150 km are present in the atmosphere around flight level of the RF12 flight legs passing over the Mt Aspiring massif. Decreasing amplitudes in the T'_R signals above flight level indicate wave reflection of both, ‘intermediate’ and ‘long’ scales within the TIL, explaining the low flux measurements described by Smith et al. (2016) and Portele et al. (2017). Gisinger et al. (2017), who use vertical profiles of static stability to derive a reflection coefficient, point out the influence of the TIL on GW propagation. The calculated reflection coefficient on June 29th is relatively large (c.f. Fig. 5.20a), indicating strong influence of the TIL. This can only be seen in the MTP data analysis of leg 1, where a peak in the GWPED within the TIL indicates possible trapping of waves. However, the TIL was still present during legs 6 - 14, where the MTP picked up temperature signals that clearly suggest leakage through the upper boundary of the TIL (e.g. ‘intermediate’ scales in leg 1), as well as propagation of waves through the TIL (e.g. ‘long’ scales in leg 10). The strong amplitudes of the T'_R signals of the ‘long’ scales in leg 18 with largely reduced amplitudes above and below the flight altitude cannot be explained through the MTP measurements alone, as the TIL was less pronounced during this leg. The wind minimum between the two arms of the jet, and especially the change in the wind profile, could be a possible explanation for difference in the measured temperature perturbation signals of leg 18 and leg 22.

The absolute values of momentum flux contribution, calculated for wave-phases with amplitudes larger than 1 K in the T'_R signals, compare well to the leg-mean values shown in Smith et al. (2016), which suggests that those are the dominant wave-phases contributing to the over-all momentum flux. As higher altitudes are not in sight of the MTP, it cannot be determined whether waves propagating upwards around flight level are propagating further through the ‘valve layer’ (Kruse et al., 2016), and the stratosphere.

In the case of RF16, the analysis of MTP data provides valuable information to interpret the flight level measurements of largely varying energy fluxes between single legs of RF16. The large energy fluxes, reported by Smith et al. (2016), derived from flight level measurements during leg 1 are caused by waves which are reflected at the upper edge of the TIL, and do not, or only partially propagate further into the stratosphere. Absolute values of flux contributions of single wave-phases resolved in the MTP data are higher than the leg-mean values derived by Smith et al. (2016), but large variations of the values derived for different wave-phases are observed, explaining the difference to the leg-mean values. The difference to the leg-mean values can further be explained by other down-ward propagating wave packets that are not included in the MTP data analysis, but lower the leg-mean values derived in the analysis of Smith et al. (2016). There is clear indication of possible up-ward propagating GWs of single wave-phases in the ‘long’ scale analysis of MTP data with the ACHWAS algorithm.

In their analysis of correlation coefficients of momentum and energy fluxes, Smith et al. (2016) conclude, that the small scale waves appear to be propagating upwind, while not contributing to the vertical fluxes. They conclude that the TIL, which is present in all radio sondes during the research flights RF12 and RF16, may act as a wave duct for those small-scale waves. However, from the same analysis they also derive that “the longer waves carry momentum and energy vertically and have the mountain wave signature of upwind propagation”. The analysis of MTP data shows that reflection or dissipation of waves at the upper boundary of the TIL, or even trapping within the TIL commonly happened during RF12 and partly during RF16. The reduced amplitudes of the T'_R signals above flight level are a clear indicator, that the flux of energy and momentum into the stratosphere is lower than suggested by the flight level measurements conducted within the TIL. Still, during both research flights, there is also evidence of leakage above the TIL.

Especially in the interpretation of observations from RF16, the analysis of MTP measurements provides valuable additional information that is needed to interpret the findings of flight level analysis. The combination of MTP data and flight level measurements proves to be a powerful tool in interpreting the propagation conditions of GWs through the tropopause region.

6 Summary

Within this thesis, the use of measurements from the DLR-MTP in characterising GW signatures within the tropopause region has been assessed. The MTP is an airborne passive radiometer, measuring thermal emission from the atmosphere within the 60 GHz oxygen absorption band. From the measurement signal the temperature of the atmospheric layers around the flight altitude can be derived by applying a retrieval algorithm. Several questions concerning the capabilities of the MTP instrument have been investigated, establishing the quality of measurements, the range of sensitivity, and deriving the ability to determine wave characteristics from MTP measurements by answering a series of questions:

Question 1: What is the precision of the MTP temperature measurements?

This question has been answered by finding an adequate calibration strategy for the raw data recorded with the MTP. From the raw MTP measurements the noise figure was derived, needed in the interpretation of the analysis concerning GW signatures within MTP data. Since the standard retrieval algorithm is not depending on well-calibrated input, this is the first time such an exact estimation of calibration coefficients and measurement noise has been performed.

A measurement series in the laboratory was undertaken, using a cold-chamber to reproduce the varying surrounding conditions the instrument experiences during a measurement flight. It has been shown that the calibration of MTP data is sensitive to temperature changes of the surroundings of the instrument. Three calibration strategies could be identified that respect the changing instrument state during flight, and enable the calibration of MTP brightness temperatures with a precision of ~ 0.37 K, and an accuracy of 0.5 K. The latter is the accuracy of the HALO static temperature, which is used to correct systematic offsets in the calibrated data, which can be as large as 7 K.

Question 2: Which altitude region around the flight level of the research aircraft is the MTP sensitive to?

To investigate the range of sensitivity of the MTP instrument, the weighting functions, which are part of the radiation transfer (RT) equation, have been calculated, using the parameters from the HITRAN database, and the RT code GARLIC, implemented in the Py4CATS algorithm (Schreier and Gimeno García, 2013; Schreier et al., 2014). While limitations to the range of sensitivity have been indicated in earlier publications connected to the MTP, a theoretical study involving radiative transfer calculations to infer the weighting functions for the MTP instrument has not been published so far.

It could be shown that under the standard measurement settings, the weighting functions of all measurements, under all elevation angles and local oscillator frequencies, drop by $1/e$ within the first 1.5 km distance to the aircraft altitude, both above and below flight level. The resulting ~ 3 km region around flight altitude (i.e. ± 1.5 km around flight level) the instrument can collect information on temperature perturbations caused by GWs. This presents a strong limitation in the interpretation of measurement data concerning GWs, which can have vertical wavelengths that are 10-20 times larger.

A proposal to improve the measurement strategy for future missions of the MTP has been made, involving a reduction of the number of elevation angles used, and including frequencies of weaker absorption lines of the 60 GHz oxygen absorption complex. The weighting functions connected to these new measurement strategies imply that the range of sensitivity above the aircraft can be increased to 2 km, and up to ~ 6 km below the aircraft at an aircraft altitude of 11 km. However, data recorded using these new strategies can only be processed if the standard retrieval algorithm is improved, or once the best settings for the TIRAMISU retrieval, developed by Xu et al. (2016), are known. As the new measurement strategies could not be applied in any mission since the study has been conducted, existing data, recorded with the standard measurement strategy, were used to assess the MTP's abilities in measuring and characterising GWs.

Question 3: How well can various wave characteristics, such as the vertical wave length or the intrinsic frequency, be derived from existing MTP data?

The new ACHWAS algorithm to analyse MTP temperature profiles has been developed and applied to a synthetic data set, with given wave properties. When processing the input data with the TIRAMISU retrieval before applying the ACHWAS algorithm, the derived phase line orientations deviate from the true angle by as much as 10-20°, even with noise-free retrieval input. However, retrieval performance tests have revealed that the optimal settings for achieving reliable results with TIRAMISU have not yet been established. On this basis, the synthetic data study indicates that this Physics-based retrieval algorithm could be capable of providing reliable temperature data derived from MTP measurements in the future. When using the retrieval algorithm provided by NASA-JPL, which has also been used in the processing of DEEPWAVE data, the wave properties could correctly be retrieved, even from noisy synthetic data. It could be shown that the phase line orientation of GW signatures in MTP data can be derived with an accuracy of at least 30% or better, given that the amplitude of the temperature perturbation in the MTP observations is larger than 1.5K. Based on the findings in the investigation of question 1, this is five times larger than the instrument noise induced on the MTP measurements. Also, this uncertainty estimation only applies to vertical wavelengths smaller than 50 km. Larger vertical wavelengths exceed the range of sensitivity in a way, that temperature changes between the altitude layers resolved in the MTP data, are too small to be detected by the sensor. However, only GWs with vertical wavelengths of less than 30 km are observed in the atmosphere, unless they are trapped waves. This falls well within the range in which robust results can be obtained with the ACHWAS algorithm.

The uncertainty of the reconstructed temperature perturbation amplitudes is not known for atmospheric measurements, as the influence of the retrieval on the uncertainty of retrieved absolute temperatures remains unknown. Thus, large uncertainties are associated with momentum flux calculations based on the temperature fluctuations found in the MTP data. In real observations it can be estimated through the variance between multiple analysis runs of the ACHWAS algorithm, including different numbers of altitude layers around flight level. The resulting spread between the derived values depends on the amplitude of the observed temperature perturbation.

In the final Section of Chapter 5 the analysis of a set of MTP observation data from research flights within the DEEPWAVE research campaign in New Zealand, 2014, was shown. The comparison to the evaluation of flight level data analysis, as well as to studies that also use model data, is used to finally answer the question:

What contribution does the MTP make to the characterisation of gravity waves around the tropopause?

The case studies of two research flights within the DEEPWAVE campaign reveal that the MTP observations add valuable insight to the atmospheric conditions favouring or blocking propagation of GWs. While the evaluation of flight level wind data provides insight to directions of momentum and energy fluxes, it could be shown that flight level measurements are influenced by the choice of the aircraft altitude, especially in the presence of a TIL, or varying wind conditions that influence the overall wave activity of different altitudes. While derived absolute momentum flux values agree well with published leg-mean values, the extended altitude range over which MTP measurements are available is a key to correctly interpreting the possible vertical fluxes of energy and momentum. In the cases of RF12 and RF16 of the DEEPWAVE campaign, it could be shown that the flight level measurements do not produce representative values of momentum and energy fluxes for the UTLS. The MTP instrument is unique in providing measurements from which the vertical temperature profile and with it important variables such as the static stability of the same air masses as probed by in situ instruments can be derived, and insight can be gained how the wave activity on flight level compares to that of the surrounding altitude layers. Thus, MTP observations are extremely valuable in the investigation of GW propagation conditions. Those cannot be derived from flight level measurements without the additional information provided by MTP observations, and have not been shown in observational data, before.

Additionally, the ACHWAS algorithm provides a tool to investigate the contribution to the overall momentum and energy flux by individual wave-phases. It could be shown that those contributions can distinctly vary between individual wave-phases encountered during a single flight leg. While the application of the wavelet analysis to flight leg data provides insight into the amount of wave activity at different parts of a flight leg, the analysis of MTP measurements with the new ACHWAS algorithm provides the momentum flux contribution of each individual wave-phase encountered during flight.

Hence, the composition of individual flux contributions that lead to the leg-mean values derived in flight leg data analysis can be investigated.

With the proposed changes to the measurement strategy, future aircraft observations of GWs could be designed in a way that the aircraft flight level is chosen above the TIL. Then, flight level observations provide insight into momentum and energy fluxes reaching the stratosphere, while the MTP still provides information on possible wave trapping, reflection, and dissipation below flight altitude. With a larger region of sensitivity and improved retrieval settings, it could even be possible to derive altitude-dependent changes in the characteristics of a wave-phase, which could be used to quantify the deposition of momentum and energy by dissipating waves.

A Appendix

A.1 Retrieval methods

The calibrated set of brightness temperatures (BTs) measured by the MTP during one measurement cycle has to be converted to absolute temperatures of the atmosphere at different altitudes, using a retrieval software that links an absolute temperature profile to the measured BTs. The MTP measurements can be expressed as the measurement vector \vec{y} , consisting of all the single measurements belonging to one measurement cycle, recorded under different lines of sight and with different LOs. It is linked to the state of the atmosphere, \vec{x} , by the radiative transfer equation (forward model \mathbf{F}):

$$\vec{y} = \mathbf{F}(\vec{x}) \tag{A.1}$$

Since \vec{y} is given through the measurement and \mathbf{F} is known through the radiative transfer (RT) equation (see Chapter 3.1), the inversion of this equation would lead to the true state of the atmosphere. However, this is an ill-posed problem, since not only can different states of the atmosphere lead to the same measurements (Rodgers, 2000), but also the measurements in \vec{y} are usually not totally independent from each other. Thus, \mathbf{F} is not a diagonal matrix that can simply be inverted. Furthermore, all measurements include measurement errors, as discussed in Section 4.2, which can lead to a further reduction of independent information in \vec{y} . Hence, a mathematical inversion is not straightforward, and various approaches have been found in the past to retrieve an estimate of the true state of the atmosphere from measured data. The following sections will briefly introduce the most common methods used to retrieve absolute temperature profiles from remote sensing measurements, namely a statistical approach and the numerical inversion of the forward problem.

A.1.1 Statistical retrieval

The current standard MTP retrieval algorithm, provided by NASA-JPL with the purchase of the instrument (Mahoney and Gary, 2003), is based on a statistical approach, using radiosonde data as input. As stated in Denning et al. (1989), RT calculations are performed for a large number of radio soundings typical for the time and region of the scientific measurement campaign. The simulated BTs are linked to the real observations to find the best-fitting atmospheric state by a multiple regression algorithm, following Strand and Westwater (1968).

Figure A.1 shows the working principle of the retrieval algorithm, which is described in detail in the following. The retrieval algorithm includes RT calculations which are performed in the very first step of the data processing, as described below. For RT calculations the atmosphere is divided into a fixed number of 50 levels, for which absorption coefficients and opacity of the trace gases are calculated. This is based on temperature, pressure, and humidity values of the radio soundings, and the trace-gas specific characteristics found in the 1996 HITRAN database (Rothman et al., 1998). The RT calculation does not include as many trace gases as found in other RT algorithms, such as GARLIC (Schreier et al., 2014), which can also be set to use a finer altitude resolution than the RT calculations implemented in the NASA-JPL retrieval.

A large radiosonde database is the main foundation of the retrieval calculations. It contains several thousand individual radio soundings typical for the time and region of the campaign. From this database a number of templates is chosen, which are used as input to the forward RT calculations to create simulated BTs the instrument would measure, if the template atmosphere was the true state. The templates are created as the average temperature profile of 100 - 200 individual radio sonde observations (RAOBs), which are similar in their absolute temperatures and profile shapes, as compared to a chosen template basis, typically a radio sounding close to the flight track of the aircraft and at the time of the research flight. An example is shown in Fig. 4.20b. By also performing the RT calculation for each individual radio sounding of a template, a large set of equations, linking absolute temperature profiles to (simulated) BTs is created, which is solved to provide sets of so-called retrieval coefficients (RCs). These are used to link the absolute temperature at a certain altitude z to all available BTs measured by the MTP through a linear relation:

$$T(z) = \sum_{\nu=1}^{N_{\nu}} \sum_{\alpha=1}^{N_{\alpha}} \text{RC}_{\alpha,\nu} \cdot T_{\text{B}}(\alpha, \nu) \quad (\text{A.2})$$

The levels at which absolute temperatures are given in the output of the retrieval are fixed to 33 altitudes, which are defined, starting with a vertical spacing of 150 m with increasing spacing at growing distance to flight altitude. From these, only for those between ± 8 km relative to flight altitude output is created. This typically includes 28 output levels. The values of the individual RCs depend on the flight altitude, as the RT differs between varying altitudes of the instrument. Hence, the system of equations has to be solved more than once, to provide correct RCs at different aircraft altitudes. It has proven to be useful to calculate the RCs for each individual scientific flight, by using the 13 most common flight levels of this specific flight, this being the maximum number allowed by the retrieval algorithm.

Once the RCs are known, the RT calculation is performed once more, using the average temperature profile, $\langle \vec{T} \rangle_{\text{Tpl}}$, of each individual template set, creating a reference for the choice of which set of RCs to use in the conversion of the observations:

$$\vec{T}_B^{\text{TpI}} = \mathbf{F}(\langle \vec{T} \rangle_{\text{TpI}}) \quad (\text{A.3})$$

Typically, a set of 20 - 30 templates (each consisting of a set of 100 - 200 individual radio soundings) is used to process the data from one scientific campaign. Approximately 13.000 RCs are calculated for each individual template, which are stored in binary files for use during the retrieval of campaign data.

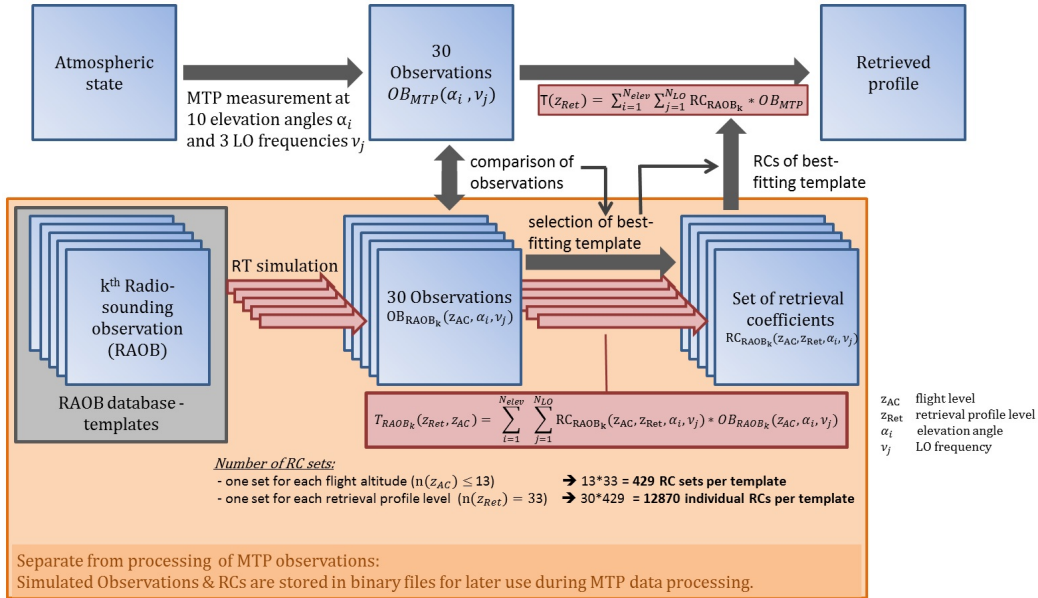


Figure A.1: Schematic of the statistical retrieval method provided by NASA-JPL.

When retrieving the absolute temperature profiles from the observation data, the algorithm chooses the best-fitting template, i.e. the one with the smallest RMS difference between \vec{T}_B^{TpI} and the current observations \vec{T}_B^{obs} . The RCs of this template are used to calculate the temperature profile, using Eq. (A.2) again, but with the real observations. For this calculation the RCs corresponding to the aircraft altitude, at which the MTP observations were made, are used. However, if those MTP observations were measured at a flight altitude different from the ones used in the RC calculation, the RCs corresponding to the processed flight levels above and below the current observation altitude are averaged (weighted with the distance to the current flight level), before Eq. (A.2) is applied.

If the \vec{T}_B^{TpI} of the second-best fitting template has a mean difference to the \vec{T}_B^{obs} with the opposite sign than that of the first, it is included in the retrieval process as well. In this case Eq. (A.2) is used twice, once with each of the RC sets. The final retrieved temperature profile is calculated as a weighted average of the two resulting absolute temperature profiles. The weights are based on the RMS difference between the observations and the templates' simulated BTs.

The major advantage of this method is that even before the campaign takes place, a representative RAOB data base can be found, using RAOBs from the same months in previous years within the region in which the research flights are planned, and choosing templates that represent the variety of atmospheric states expected during the research flights. With the RCs of these preliminary templates the measurements of a campaign flight can be converted to absolute temperature profiles shortly after the flight. Once the research flights have been made, the radio sounding data base can be updated to include the radio soundings released during the campaign, and a new calculation of RCs can be performed for later data analysis.

A weakness of this method is that the quality of the retrieved temperature profiles heavily depends on the available RAOBs. If the true state of the atmosphere the measurements took place in, is not represented in the templates, the retrieved profile will not correctly resemble the true state of the atmosphere. Instead, it will be similar to that template of which the simulated BTs are closest to those recorded during the measurement flight. Still, even those BTs can differ considerably from the measured data, leading to retrieved profiles that do not represent the actual situation well. For measurement flights over most continents that problem can be solved by adding more RAOBs or temperature profiles from model re-analyses to the database and add templates that better represent the atmospheric state during the measurements. Still, this is not always possible, since there are not always radio sounding stations close to the flight path of the research aircraft. This problem occurs especially over open ocean. Another effect of this method is that noise might be induced on the time series of retrieved profiles. This happens in the case that different templates are used for successive profiles within this time series. The different RCs associated with the templates lead to slightly varying shapes of the resulting temperature profiles. If the retrieval algorithm alternates between two or three best-fitting templates for the measurements within the time series, this can lead to reoccurring jumps in the temperature time series, which add to the overall noise and influence the results of spectral analysis of MTP data.

All in all, this relatively simple method is very fast in computing the absolute temperature profiles and can be used to get a good first impression of the measured temperatures. However, it heavily depends on the user input in form of radio soundings and the correct choice - and availability - of templates to produce reliable output. When the necessary care is taken in the choice of template radio sounding profiles, and enough a priori information is available, the retrieval can derive temperature profiles that are comparable to dropsonde measurements with deviations of less than 1 K (Davis et al., 2014).

A.1.2 Inversion of the forward problem

The weak spot of the statistical approach to the retrieval is the large dependence on the a priori knowledge of the atmospheric state that has been probed. Also, the resulting temperature profiles usually resemble the shape of the a priori template used in the retrieval calculation. A more independent approach is the inversion of the forward problem.

There are a number of implementations that also make use of some a priori knowledge, but putting different weights on the use of this a priori knowledge. Since the forward problem is a non-linear problem, a direct inversion of Eq. A.1 is not possible. Hence, an iterative approach is used, to solve for the atmospheric state \vec{x} .

All iterative methods are based on the idea to start with a first guess what the atmospheric state probably looked like (e.g. a climatological temperature profile). For this first guess the RT calculation is performed and BTs the MTP would measure in such an atmosphere are simulated. Those simulated BTs are compared to the measured data, and based on the difference the first guess temperature profile is adjusted, and the next iteration starts with the RT calculation of this adjusted temperature profile. This is repeated until a satisfactory resemblance of the measured BTs is achieved, expressed by the minimisation of a cost function. This cost function can include a number of different penalty terms, depending on the iterative method that is being used.

The following Subsections will give a brief overview of the most commonly used iterative methods, i.e. the simple method of least squares fitting, as well as optimal estimation and the Tikhonov-type regularisation that is used in the newly written retrieval algorithm for the DLR-MTP, TIRAMISU.

Least squares fitting

As stated above, the general idea of the iterative retrieval is to minimise the difference between the noisy observations \vec{y}^δ and the simulated data $\mathbf{F}(\vec{x})$ by adjusting the atmospheric state \vec{x} :

$$\mathcal{F}(\vec{x}) = \|\mathbf{F}(\vec{x}) - \vec{y}^\delta\|^2 \quad (\text{A.4})$$

This equation can be minimised, according to Rodgers (2000), by defining the atmospheric state of the following iteration \vec{x}_{i+1} as:

$$\vec{x}_{i+1} = \vec{x}_i + (\mathbf{K}_i^T \mathbf{K}_i)^{-1} \mathbf{K}_i^T [\vec{y} - \mathbf{F}(\vec{x}_i)] \quad (\text{A.5})$$

in which \mathbf{K} denotes the kernel matrix that links the i components of the observation to the j components of the (unknown) atmospheric state:

$$y_i = \sum_{j=1}^n k_{ij} x_j \quad (\text{A.6})$$

This is quite a simple method, for which a number of numerical solutions exist. However, the aforementioned effects of noise errors and reduced information content in the measurement, due to cross-correlation, make the solutions derived with this simple approach unreliable (Rodgers, 2000).

Optimal estimation

A well-described method for solving linear inverse problems is optimal estimation (Rodgers, 2000). Here, a regularisation is introduced by adding a penalty term to the cost function that is to be minimised in the iterative process. This penalty term is the a priori profile covariance matrix \mathbf{S}_y with entries

$$s_{ij} = \varepsilon\{(y_i - \bar{y}_i)(y_j - \bar{y}_j)\} \neq 0 \quad (\text{A.7})$$

using the expected value operator ε . The diagonal elements of this matrix correspond to the variance of the individual elements. The covariance matrix relates to the Gaussian distribution of the probability of \vec{y} as:

$$P(\vec{y}) = \frac{1}{(2\pi)^{n/2} |\mathbf{S}_y|^{1/2}} \exp\left(-\frac{1}{2} (\vec{y} - \langle \vec{y} \rangle)^T \mathbf{S}_y^{-1} (\vec{y} - \langle \vec{y} \rangle)\right) \quad (\text{A.8})$$

and hence resembles σ^2 of the one-dimensional case. The mean vector $\langle \vec{y} \rangle$ represents the most likely atmospheric state to expect in the measurement situation. The cost function is:

$$\mathcal{F}(\vec{x}) = (\vec{y} - \mathbf{F}(\vec{x}))^T \mathbf{S}_\varepsilon^{-1} (\vec{y} - \mathbf{F}(\vec{x})) + (\vec{x} - \vec{x}_a)^T \mathbf{S}_a^{-1} (\vec{x} - \vec{x}_a) \quad (\text{A.9})$$

with the a priori covariance \mathbf{S}_a and the observation error covariance \mathbf{S}_ε .

The optimal estimation approach relies on statistics in the form of the Bayesian theorem, which links the probability that a certain atmospheric state \vec{x} is present, if the observations \vec{y} are made, ($P(\vec{x}|\vec{y})$), to the probabilities of the atmospheric state to occur ($P(\vec{x})$), of the observation to be made ($P(\vec{y})$), and to the probability that a known atmospheric state \vec{x} causes the observations \vec{y} ($P(\vec{y}|\vec{x})$):

$$P(\vec{x}|\vec{y}) = \frac{P(\vec{y}|\vec{x})P(\vec{x})}{P(\vec{y})} \quad (\text{A.10})$$

As those expressions can be known through the RT equation, and using climatologies to find the most likely atmospheric state \vec{x} , a solution can be found, which states the probability of a certain state \vec{x} to have caused the given observations \vec{y} . The retrieval output can then be chosen, e.g. as the most likely state \vec{x} , at which $P(\vec{x}|\vec{y})$ is maximal (maximum a posteriori solution), or as the expected value:

$$\hat{x} = \int x P(x|y) dx \quad (\text{A.11})$$

Much like the statistical approach, this method is also quite sensitive to the choice of the a priori. It might fail, if no or just vague information on the probable state of the atmosphere is given. Still, this method is widely used in atmospheric sciences, in satellite retrieval algorithms (e.g. the Aura Microwave Limb Sounder (Livesey et al., 2006)), as well as ground-based applications (e.g. the TEMPERA instrument (Stähli et al., 2013)).

Tikhonov type regularisation

The Tikhonov regularisation (Tikhonov, 1963) is one more option of regularisation, which is less dependent on a priori information than the previously described methods. It is thoroughly discussed in connection with its application to MTP measurements in Xu et al. (2016). In the following, a brief overview of the main principles is given, for more information, the reader is referred to Xu et al. (2016) and references therein. Finding the regularisation parameters and minimising the cost function is more demanding on computational resources than other retrieval methods (Xu et al., 2016). As a consequence, it has not yet been used to derive atmospheric temperature profiles from airborne measurements.

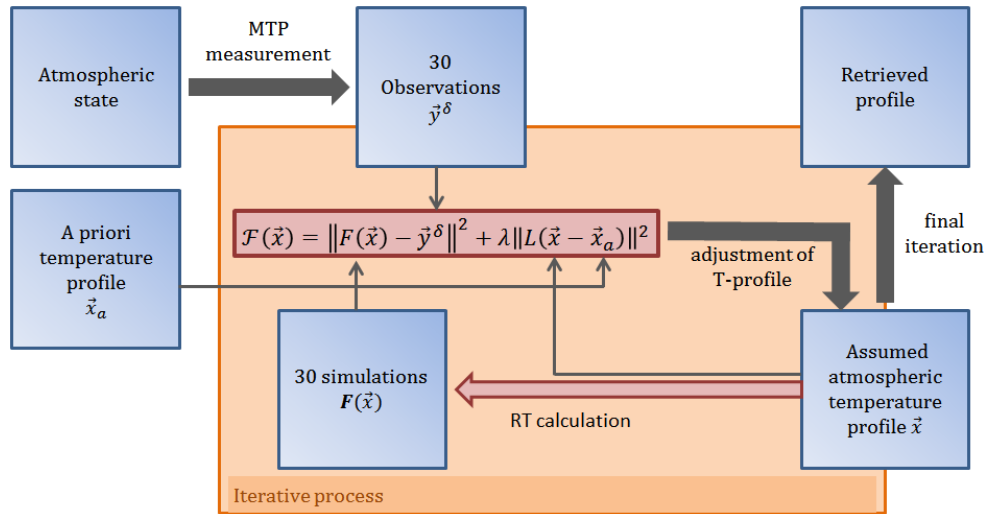


Figure A.2: Schematic of the TIRAMISU algorithm.

The main principle of setting up the cost function to be minimised in the iterative process, follows that of any iterative method, as described above. Within the Tikhonov regularisation the cost function is stated as:

$$\mathcal{F}(\vec{x}) = \|\mathbf{F}(\vec{x}) - \vec{y}^\delta\|^2 + \lambda \|\mathbf{L}(\vec{x} - \vec{x}_a)\|^2 \quad (\text{A.12})$$

again, with the state vector \vec{x} , the a priori state \vec{x}_a , and regularisation parameter λ . \mathbf{L} denotes a regularisation matrix, which can be set to choose which properties of the a priori state influence the penalty term. For example, if \mathbf{L} is chosen as identity matrix, it favours the solution to be of the same magnitude as the a priori profile. Using a regularisation matrix that has entries different from zero at other cells than those of the main diagonal, puts more weight on the shape of the profile or smoothness of the solution. It can also be constructed from the covariance matrix \mathbf{S}_{x_a} of the a priori profile. Also, there are various options to choose the regularisation parameter λ (see section (2) of Xu et al., 2016). The outcome of the algorithm depends on this choice, as it determines how much weight is given to the penalty term in Eq. (A.12). The possible choices and their performance are discussed in Xu et al. (2016).

In the applications of the TIRAMISU algorithm within this thesis, the regularisation matrix \mathbf{L} is chosen as the discrete approximation to the first-order derivative operator, implemented as:

$$L_1 = \begin{pmatrix} 1 & 0 & 0 & \cdots & 0 & 0 \\ -1 & 1 & 0 & \cdots & 0 & 0 \\ 0 & -1 & 1 & \cdots & 0 & 0 \\ \vdots & \vdots & \vdots & \ddots & \vdots & \vdots \\ 0 & 0 & 0 & \cdots & 1 & 0 \\ 0 & 0 & 0 & \cdots & -1 & 1 \end{pmatrix} \quad (\text{A.13})$$

and the regularisation parameter λ is chosen, using the expected error estimation method.

A.2 Wavelet analysis

Wavelet analysis is a method to locate periodic signals in time series of many atmospheric data sets. It allows for identification of dominant periods (wavelengths) as well as a localisation of the signal in time (space). A good introduction to the use of wavelet analysis applied to meteorological time series of data is given in Torrence and Compo (1998), in which they analyse a dataset of the time series of the El Niño- Southern Oscillation. Obviously, this method can also be applied to time series of aircraft data, as will be done when analysing MTP data.

The easiest approach to identify periodic signals in a time series of data is to apply a Fourier transform. However, processing the complete time series at once will not reveal information on the particular time (location) at which a signal of a particular frequency (scale) occurs. This information can only be extracted when using a windowed Fourier transform (WFT). Here, the Fourier analysis is performed for a smaller part of the time series at a time, shifting the focus of the analysis through the time series. The results of this method heavily depend on the chosen window length. To achieve better results, the WFT would have to be applied with a number of different window sizes, chosen by hand. The wavelet analysis is a tool that has the same advantage as an iterative WFT with different window sizes at each iteration in a much more compact mathematical way, and without dependence on a user-set scale. It is described in length in Daubechies (1990), and well summarised in Torrence and Compo (1998).

The wavelet transform of a discrete time series x_n is calculated as:

$$W_n(s) = \sum_{n'=0}^{N-1} x_{n'} \Psi^* \left[\frac{(n' - n)\delta t}{s} \right] \quad (\text{A.14})$$

using the localised time (space) index n , time-difference (distance) between two steps δt , current scale s (the equivalent of the window size in a WFT), and the complex-conjugate of the normalised wavelet function, Ψ^* . The same transform in frequency space is:

$$W_n(s) = \sum_{k=0}^{N-1} \hat{x}_k \hat{\Psi}^*(s\omega_k) e^{i\omega_k n \delta t} \quad (\text{A.15})$$

Here, the time series of data has been transformed to Fourier space via:

$$\hat{x}_k = \frac{1}{N} \sum_{n=0}^{N-1} x_n e^{-2\pi k n / N} \quad (\text{A.16})$$

In the wavelet analysis used within this thesis, a specific wavelet basis Ψ_0 , the Morlet wavelet, shown in Fig. A.3, is used:

$$\Psi_0(\eta) = \pi^{-1/4} e^{i\omega_0 \eta} e^{-\eta^2/2} \quad (\text{A.17})$$

Using normalised wavelet functions in the wavelet transform leads to results weighted only by the Fourier coefficients. Here, ω_0 denotes the wavelet parameter, that defines the resolution in time- (space-) and frequency-domain. Higher values of ω_0 result in more periods included in the time- (space-) domain (more ‘wiggles’ in the left panel of Fig. A.3), and a thinner peak in the frequency domain. As a result, the time- (spatial-) resolution is worse, but the frequency resolution is enhanced. Choosing smaller ω_0 values has the opposite effect.

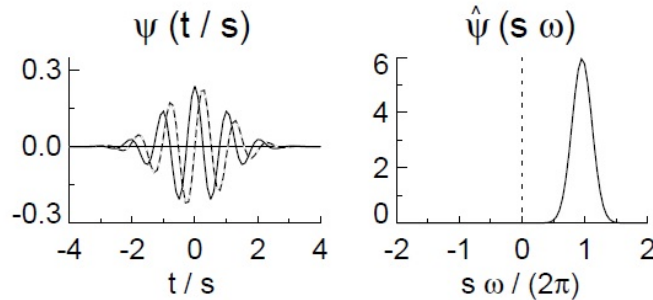


Figure A.3: Morlet wavelet basis with $\omega_0 = 6$ depicted in time-domain (left panel) and frequency domain (right panel). Adapted from Fig. 2a in Torrence and Compo (1998, ©American Meteorological Society. Used with permission.).

This effect can be seen when processing a time series of data, constructed from sine waves with different wavelengths, as shown in Fig. A.4. Here, the test signal is constructed from four sine waves of different horizontal wave lengths. Using a Morlet wavelet with $\omega_0 = 6$ (Fig. A.4b), which is the default in the wavelet analysis code provided by Torrence and Compo (1998), the four different wavelengths are found, and identified as significant signals at about the correct positions. However, the indicated regions in which the signal is considered to be significant (indicated by green lines in the colour plot), extend beyond the real positions where the sine wave is built into the time series (shown above the colour plot). Still, the global wavelet power spectrum resembles the shape of the Fourier spectrum of the input signal.

Using larger ω_0 values extends these regions in the spatial domain, yet, they become more narrow in the spectral domain (see Fig. A.4c and A.4d). On the other hand, using the wavelet base with smaller ω_0 values (e.g. $\omega_0 = 4$, as shown in Fig. A.4a) produces no usable resolution in the spectral domain, however, the region of significance in the spatial domain almost exactly resembles the location of the different wavelengths in the input signal.

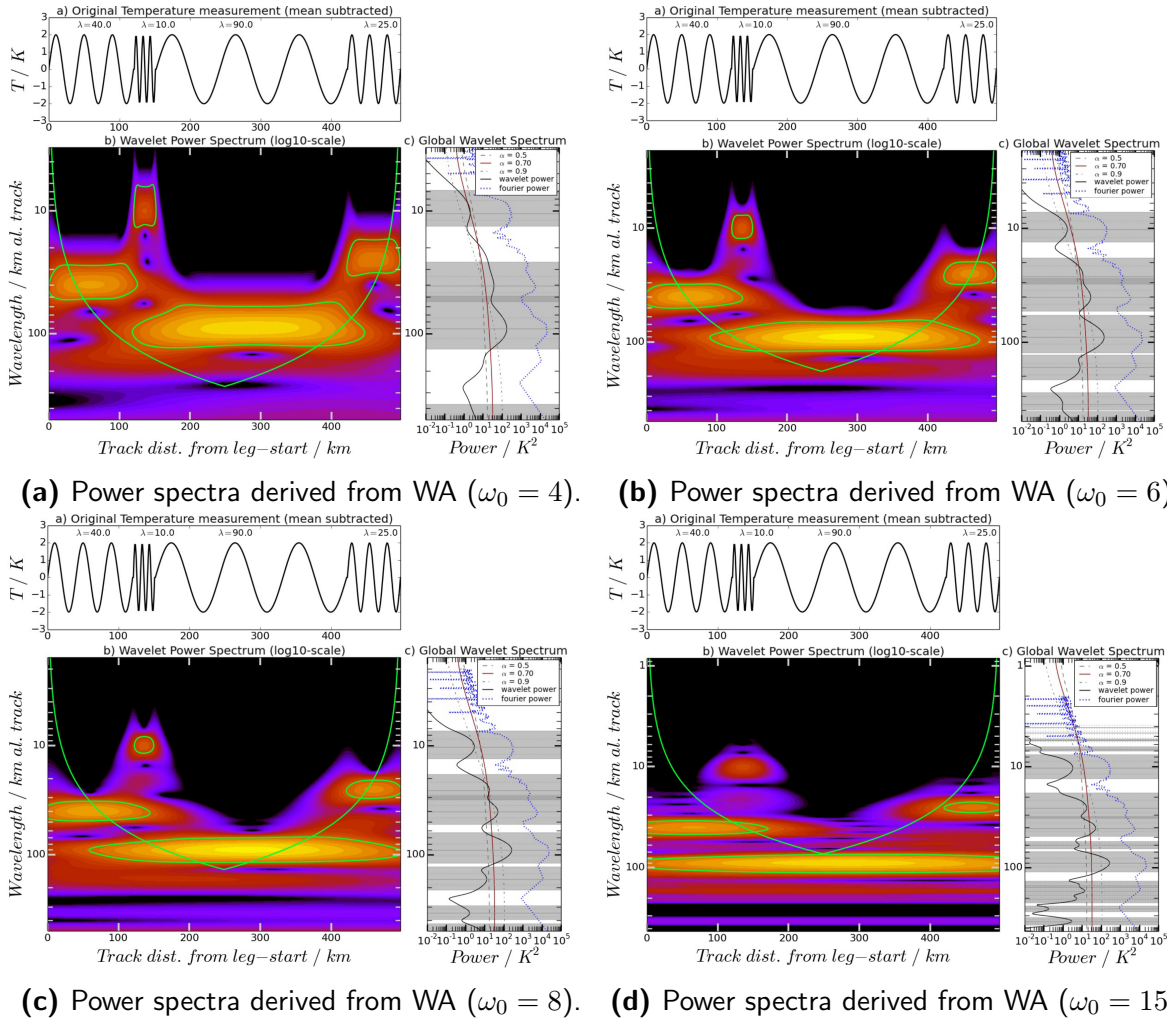


Figure A.4: Results of wavelet analysis of an artificial signal, using Morlet wavelets with (a) $\omega_0 = 4$, (b) $\omega_0 = 6$, (c), $\omega_0 = 8$, and (d) $\omega_0 = 15$. Closed green lines in colour-plots indicate the region of significance for a periodic signal found in the analysis. Trough-like green lines: Cone of influence.

Within the ACHWAS algorithm the wavelet power $|W_n(s)|^2$ is used to identify significant peaks in the frequency space, indicating periodic signals in the time series that have larger amplitudes than a theoretical noise spectrum would produce. The power spectrum of a theoretical noise signal is indicated by the red line in the power spectrum plot.

Torrence and Compo (1998) use a red noise spectrum to describe the theoretical spectral power as:

$$P_k = \frac{1 - \alpha^2}{1 + \alpha^2 - 2\alpha \cos(2\pi k/N)} \quad (\text{A.18})$$

Any peak in the normalised wavelet power spectrum that is larger than the 95 % confidence level derived from the normalised theoretical power spectrum at the respective frequency is considered significant. This threshold is derived through the variance of the time series. The coefficient α usually determines the autocorrelation between neighbouring values of a time series. A corresponding time series of red noise can be constructed using values z_n of an equally long series of Gaussian white noise. The construction follows that of a lag-1 autoregressive processes, also called Markov process:

$$x_n = \alpha x_{n-1} + z_n \quad (\text{A.19})$$

When interpreting the results of a wavelet analysis, one important quantity derived during the wavelet analysis is the so-called cone of influence (COI). This is an indication to which extent the derived wavelet spectrum is influenced by the edge of the time series. To ensure proper functioning of the transformation to the frequency domain, any data time series is padded with zeros at the beginning and the end. The larger the scales become, the bigger becomes the part of the time series influenced by boundary effects in the Fourier transform. Only the wavelet spectra outside the COI give reliable information on periodic signals in the time series, especially their amplitudes.

Obviously, as with any transformation, there is a back-transformation to restore the original signal from the wavelet coefficients, which will be used in the analysis of MTP data. Each individual point of the reconstructed time series, x_n is calculated as:

$$x_n = \frac{dj \cdot dt^{-1/2}}{\Psi_0(0)} \cdot \sum_{j=0}^J \frac{\Re\{W_n(s_j)\}}{\sqrt{s_j}} \quad (\text{A.20})$$

using $\Psi_0(0) = 0.776 \cdot \pi^{1/4}$. By applying the sum over all scales, s_j , used in the wavelet transform, the original time series can be restored. However, if reducing the number of scales that are summed up in the reconstruction, only part of the signal can be reconstructed. Thus, wave characteristics of signals at specific scales (periods or horizontal wavelengths) can be extracted from a single time series of data, and can then be further analysed separately.

It is important to note, that reconstructing the input signal within one of the intervals indicated as grey background in the global power spectra in Fig. A.4 produces different amplitudes for different wavelet bases. The reconstructed signals from wavelet transforms using wavelet bases with larger ω_0 values usually under-estimate the amplitude in the reconstructed signal, while very small ω_0 values lead to largely over-estimated amplitudes.

For example, when reconstructing the signal around $\lambda = 90$ km, the amplitude of the reconstructed signal from the wavelet transform using $\omega_0 = 4$ is 2.7 K, using the automatically chosen interval of $49 \text{ km} \leq \lambda \leq 133 \text{ km}$. Restricting the interval to $76 \text{ km} \leq \lambda \leq 133 \text{ km}$, (which is not symmetric around the correct wavelength of $\lambda = 90$ km), produces a reconstructed signal with a nearly correct amplitude of 1.9 K. The inverse problem exists with the larger ω_0 values, e.g. $\omega_0 = 8$: Reconstructing the signal around $\lambda = 90$ km, the automatically chosen interval is $62 \text{ km} \leq \lambda \leq 119 \text{ km}$, which is symmetric around $\lambda = 90$ km. Yet, the amplitude of the reconstructed signal is only 1.6 K. Only the default value of $\omega_0 = 6$ automatically chooses the reconstruction interval of $58 \text{ km} \leq \lambda \leq 124 \text{ km}$, with the correct amplitude of the reconstructed signal at 2 K. Thus, the criterion for the choice of the reconstruction interval has to be re-defined, if the the wavelet analysis is done with different settings.

A.3 DEEPWAVE model runs

For the DEEPWAVE flight RF16, two different sets of model data are available. One data set is output from high-resolution model data from the WRF model, set up with six-hourly ECMWF reanalysis data. The model run was initialised on July 3rd 2014 at 18:00 UTC and has a spacial resolution of 2 km, and temporal resolution of 5 min. The data was linearly interpolated to the flight track of RF16, and is available at 137 output levels. The other model data set results from runs with a unified model (UM)¹. According to Bramberger et al. (2017), the set-up of the model runs is using a 2 km horizontal resolution and 118 altitude layer up to 78 km. It is initialised using an operational UM analysis from July 3rd 2014 at 12:00 UTC.

Since the MTP is sensitive to much smaller part of the atmosphere than that for which model output is provided, only model data within the altitudes corresponding to the MTP measurements are used. The model data are interpolated to a 200 m grid between ± 1.5 km relative to flight altitude. This is close to the given vertical resolution of the model output, and also comparable to the vertical resolution of MTP measurements. In the following, the absolute temperatures, derived background temperatures, and resulting temperature perturbation signals, derived with the ACHWAS algorithm will be shown for each data set. Also, the reconstructed temperature perturbation signals of the ‘intermediate’ ($20 \text{ km} \leq \lambda_{\text{hor}} \leq 60 \text{ km}$) and ‘long’ ($60 \text{ km} \leq \lambda_{\text{hor}} \leq 150 \text{ km}$) wavelength scales, according to Smith et al. (2016) will be shown. As there are only two data sets of the UM the results from applying the ACHWAS algorithm will be shown in an extra plot. The following plots each show ACHWAS analysis output for individual flight legs, both for MTP data and for WRF data.

¹The UM simulations were conducted with the MONSooN system, a collaborative facility supplied under the Joint Weather and Climate Research Programme, a strategic partnership between the Met Office and the Natural Environment Research Council.

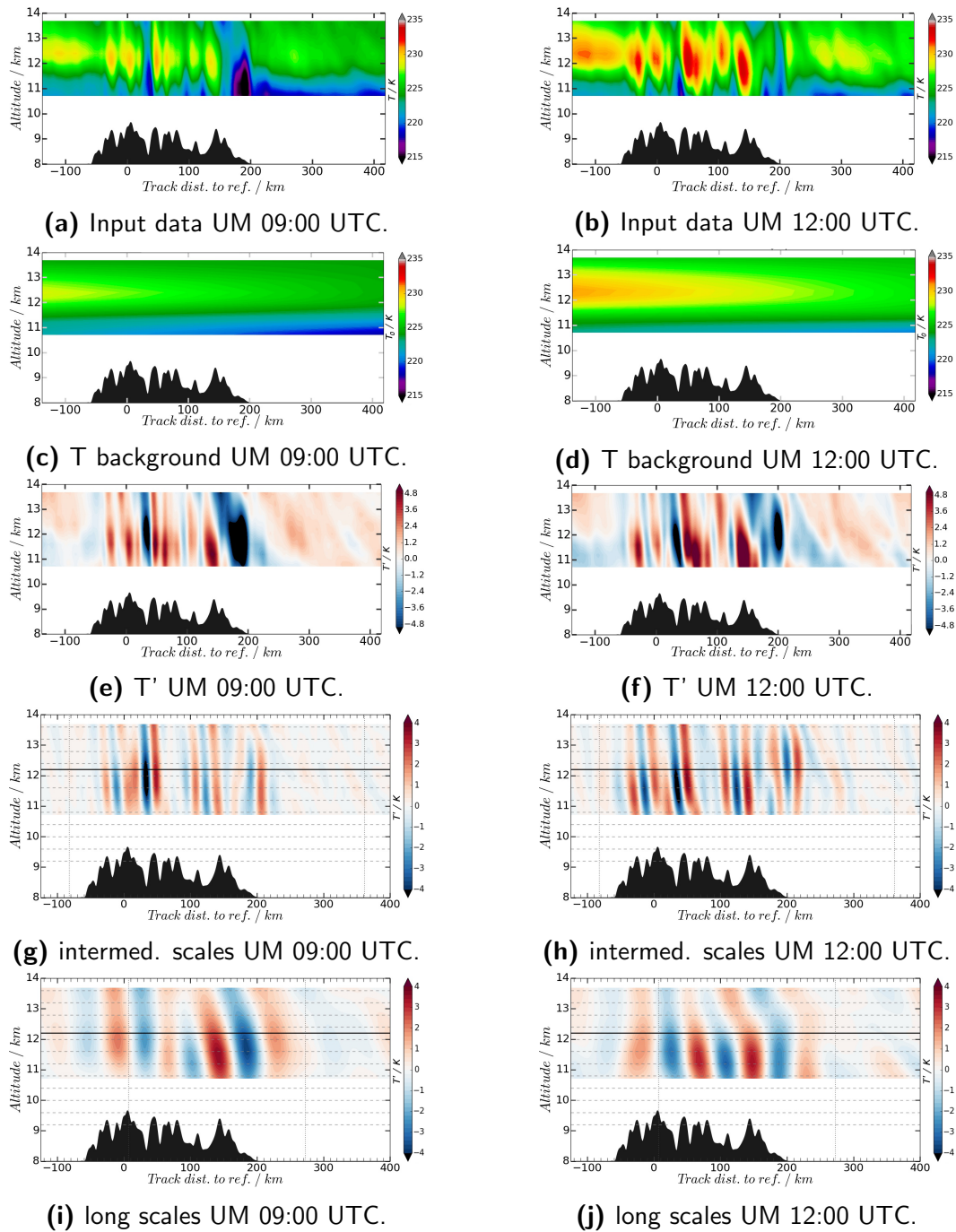


Figure A.5: Results from analysis of UM data with the ACHWAS algorithm. Left column: Analysis from 09:00 UTC; right column: Analysis from 12:00 UTC. Top row: input data; 2nd row: background temperatures; 3rd row: resulting temperature perturbations (all scales); 4th row: reconstructed T' signal of 'intermediate' scales ($20 \text{ km} \leq \lambda_{\text{hor}} \leq 60 \text{ km}$); bottom row: reconstructed T' signal of 'long' scales ($60 \text{ km} \leq \lambda_{\text{hor}} \leq 150 \text{ km}$).

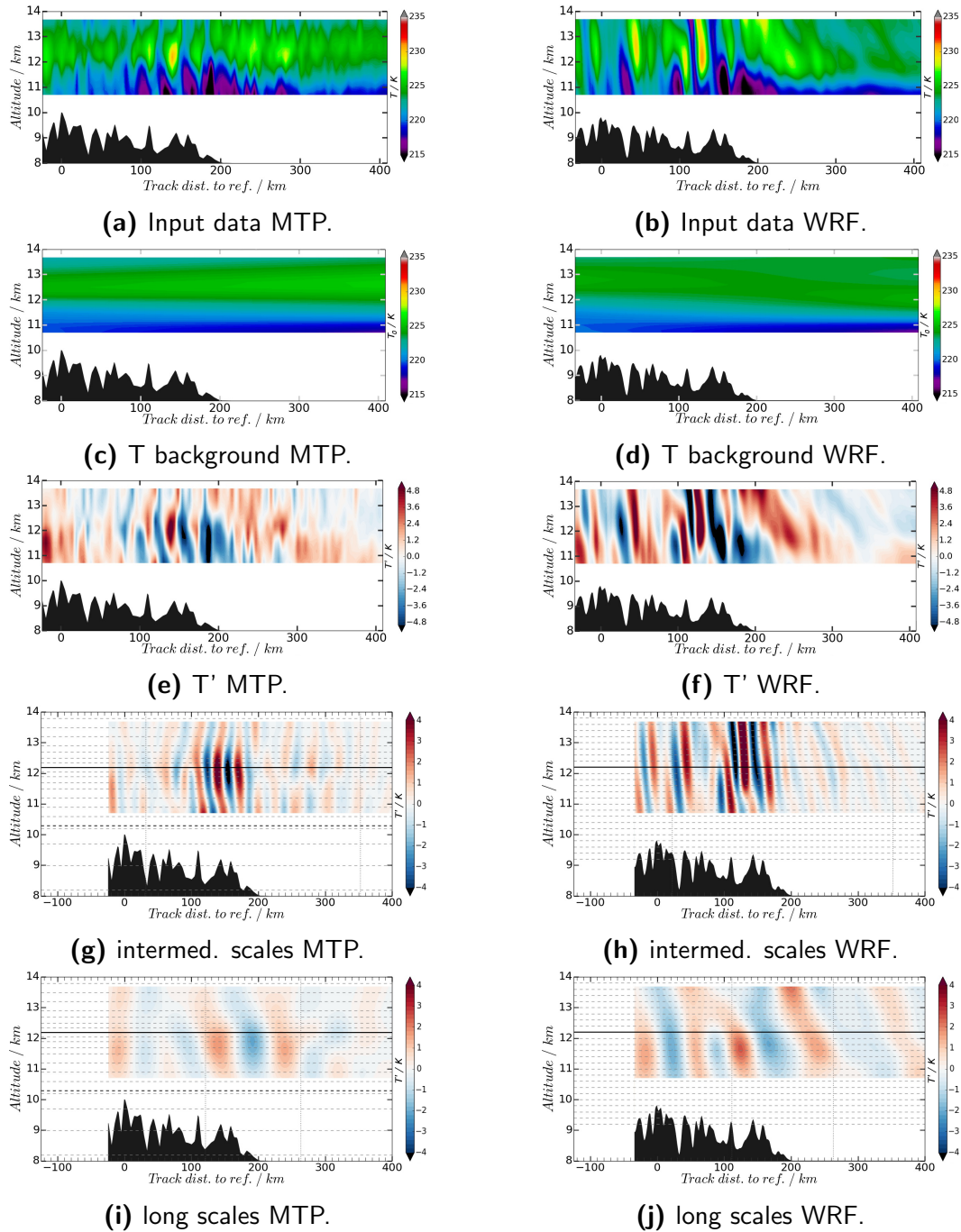


Figure A.6: Results from analysis of RF16 leg01 MTP and WRF data with the ACHWAS algorithm. Left column: Analysis of MTP data; right column: Analysis of WRF data. Top row: input data; 2nd row: background temperatures; 3rd row: resulting temperature perturbations (all scales); 4th row: reconstructed T' signal of 'intermediate' scales ($20 \text{ km} \leq \lambda_{\text{hor}} \leq 60 \text{ km}$); bottom row: reconstructed T' signal of 'long' scales ($60 \text{ km} \leq \lambda_{\text{hor}} \leq 150 \text{ km}$).

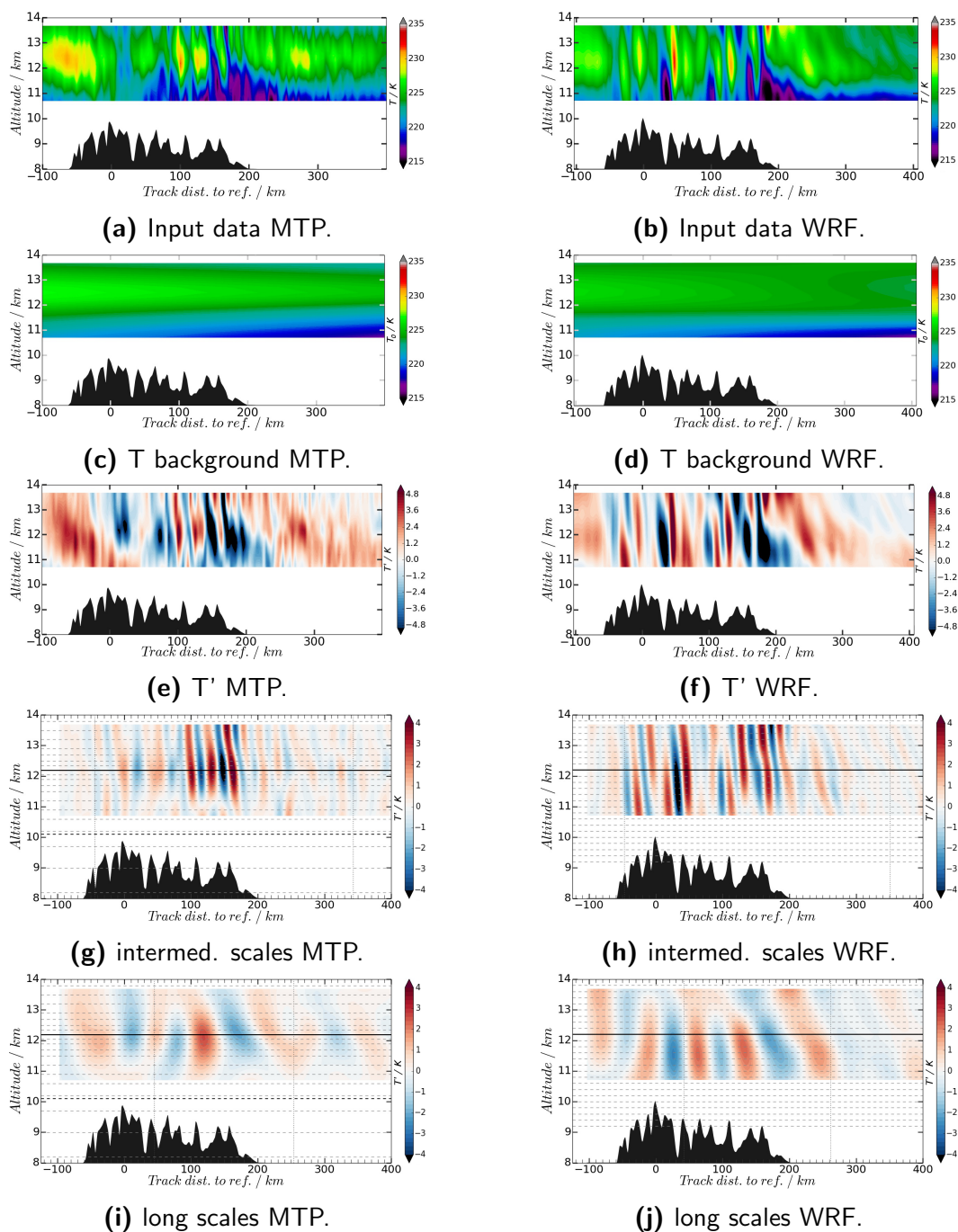


Figure A.7: Results from analysis of RF16 leg02 MTP and WRF data with the ACHWAS algorithm. Left column: Analysis of MTP data; right column: Analysis of WRF data. Top row: input data; 2nd row: background temperatures; 3rd row: resulting temperature perturbations (all scales); 4th row: reconstructed T' signal of 'intermediate' scales ($20 \text{ km} \leq \lambda_{\text{hor}} \leq 60 \text{ km}$); bottom row: reconstructed T' signal of 'long' scales ($60 \text{ km} \leq \lambda_{\text{hor}} \leq 150 \text{ km}$).

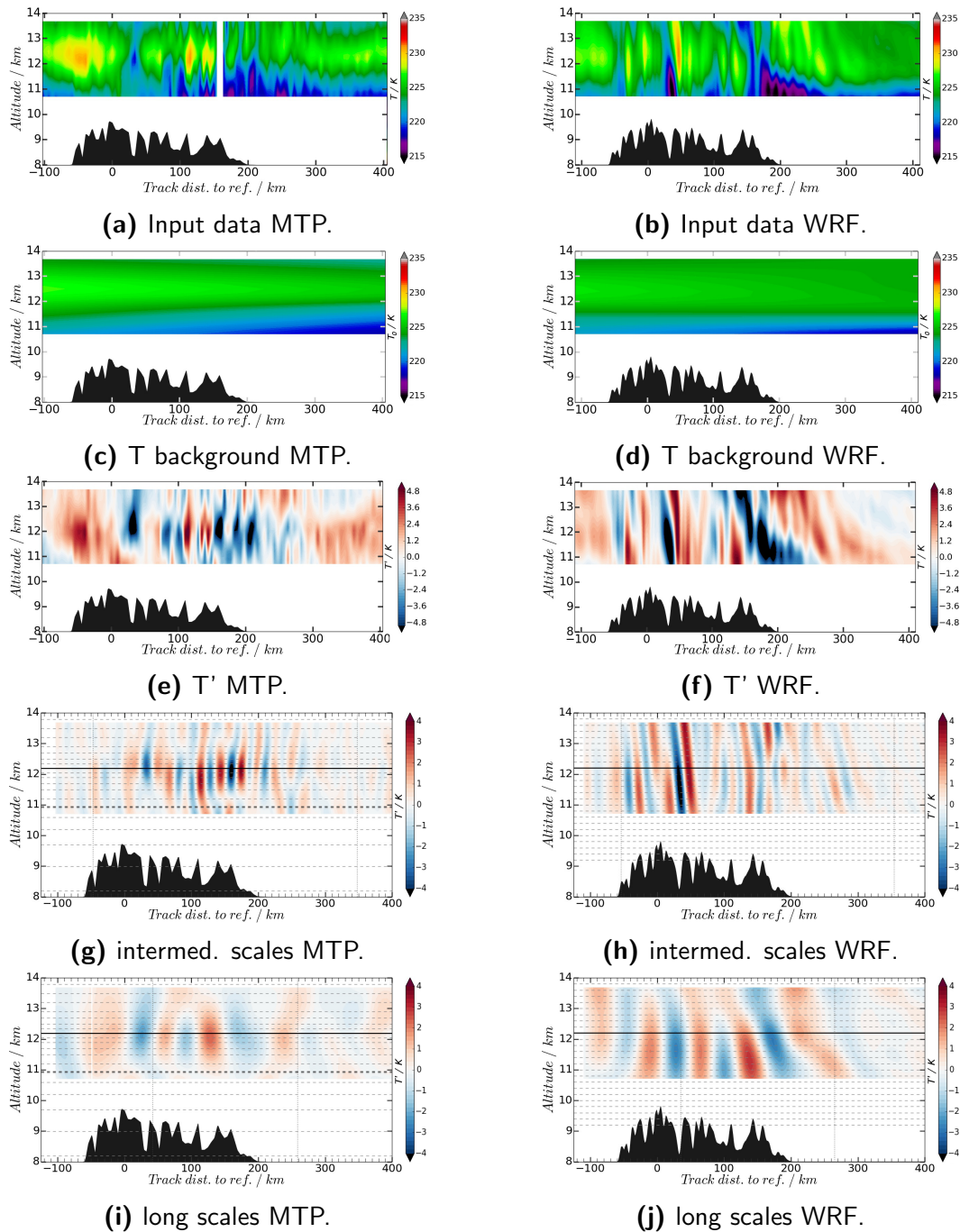


Figure A.8: Results from analysis of RF16 leg03 MTP and WRF data with the ACHWAS algorithm. Left column: Analysis of MTP data; right column: Analysis of WRF data. Top row: input data; 2nd row: background temperatures; 3rd row: resulting temperature perturbations (all scales); 4th row: reconstructed T' signal of 'intermediate' scales ($20 \text{ km} \leq \lambda_{\text{hor}} \leq 60 \text{ km}$); bottom row: reconstructed T' signal of 'long' scales ($60 \text{ km} \leq \lambda_{\text{hor}} \leq 150 \text{ km}$).

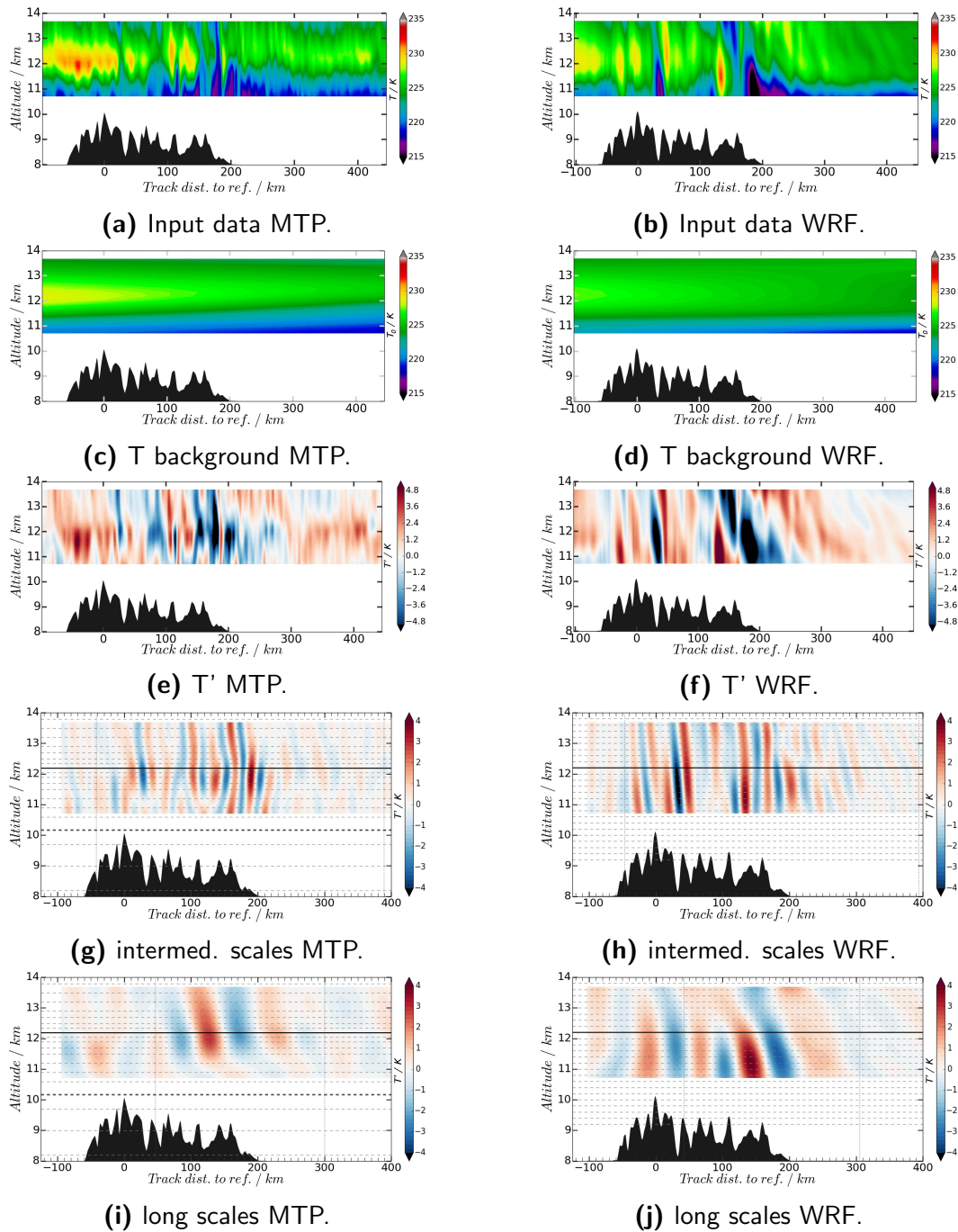


Figure A.9: Results from analysis of RF16 leg04 MTP and WRF data with the ACHWAS algorithm. Left column: Analysis of MTP data; right column: Analysis of WRF data. Top row: input data; 2nd row: background temperatures; 3rd row: resulting temperature perturbations (all scales); 4th row: reconstructed T' signal of 'intermediate' scales ($20 \text{ km} \leq \lambda_{\text{hor}} \leq 60 \text{ km}$); bottom row: reconstructed T' signal of 'long' scales ($60 \text{ km} \leq \lambda_{\text{hor}} \leq 150 \text{ km}$).

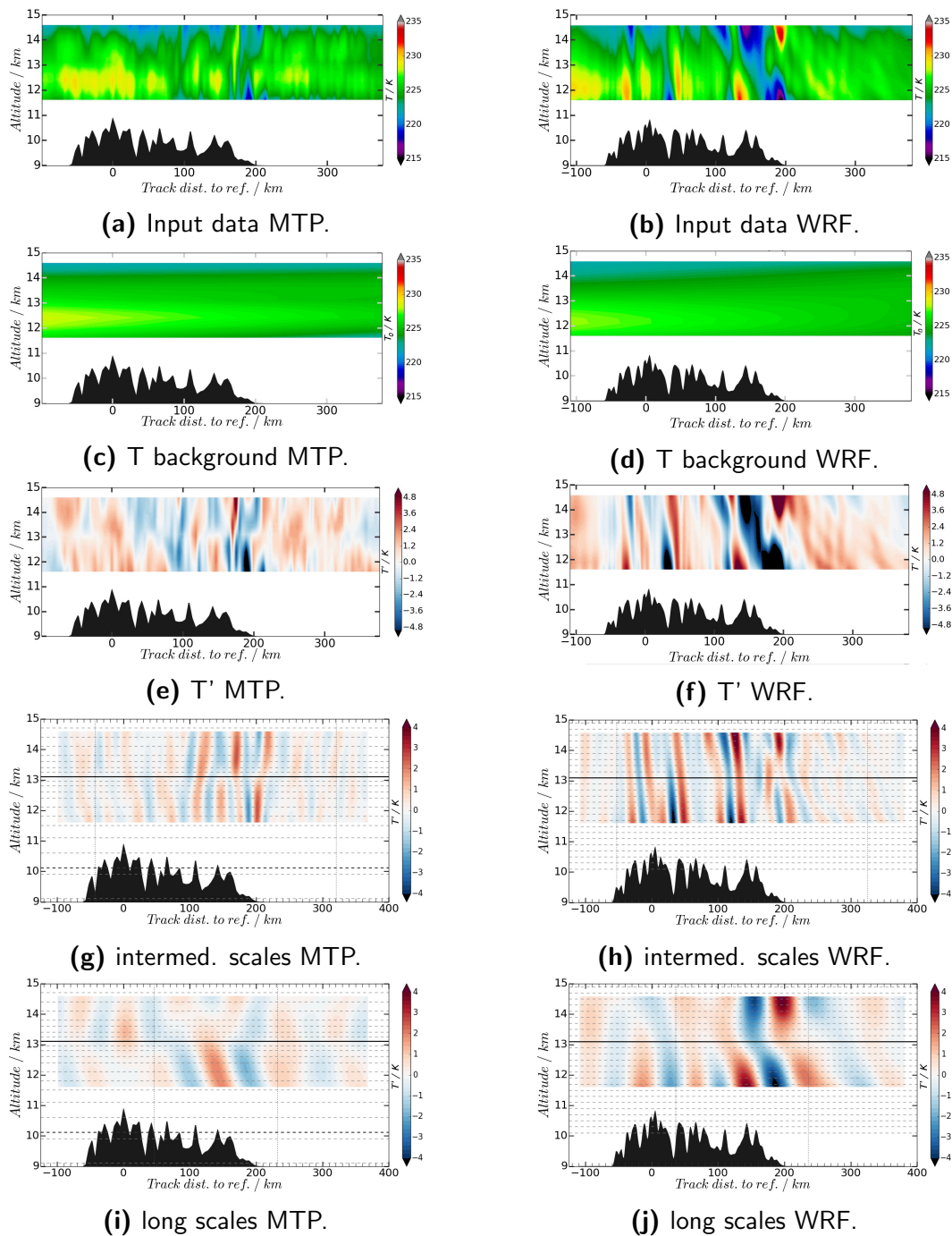


Figure A.10: Results from analysis of RF16 leg05 MTP and WRF data with the ACHWAS algorithm. Left column: Analysis of MTP data; right column: Analysis of WRF data. Top row: input data; 2nd row: background temperatures; 3rd row: resulting temperature perturbations (all scales); 4th row: reconstructed T' signal of 'intermediate' scales ($20 \text{ km} \leq \lambda_{\text{hor}} \leq 60 \text{ km}$); bottom row: reconstructed T' signal of 'long' scales ($60 \text{ km} \leq \lambda_{\text{hor}} \leq 150 \text{ km}$).

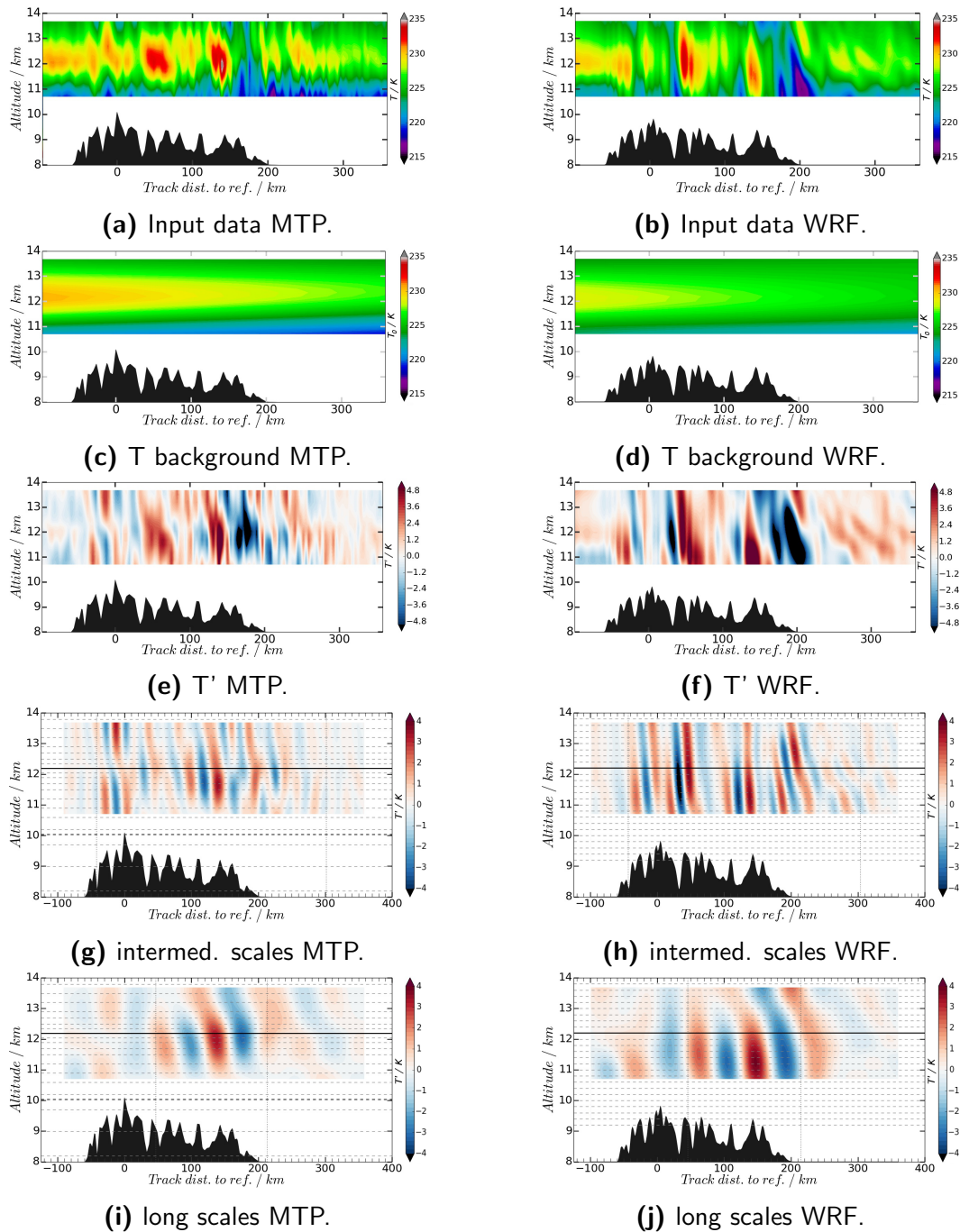


Figure A.11: Results from analysis of RF16 leg08 MTP and WRF data with the ACHWAS algorithm. Left column: Analysis of MTP data; right column: Analysis of WRF data. Top row: input data; 2nd row: background temperatures; 3rd row: resulting temperature perturbations (all scales); 4th row: reconstructed T' signal of 'intermediate' scales ($20 \text{ km} \leq \lambda_{\text{hor}} \leq 60 \text{ km}$); bottom row: reconstructed T' signal of 'long' scales ($60 \text{ km} \leq \lambda_{\text{hor}} \leq 150 \text{ km}$).

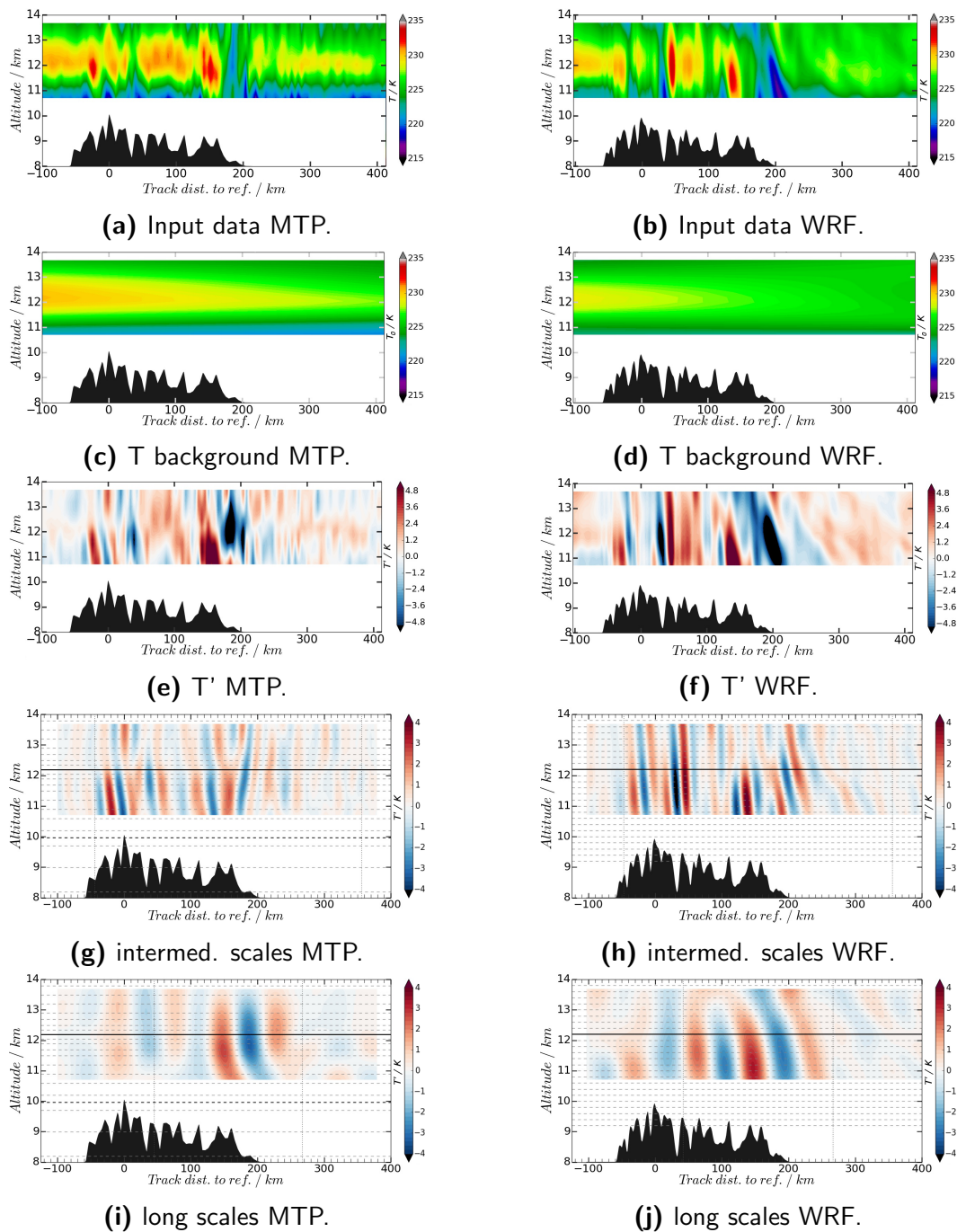


Figure A.12: Results from analysis of RF16 leg09 MTP and WRF data with the ACHWAS algorithm. Left column: Analysis of MTP data; right column: Analysis of WRF data. Top row: input data; 2nd row: background temperatures; 3rd row: resulting temperature perturbations (all scales); 4th row: reconstructed T' signal of 'intermediate' scales ($20 \text{ km} \leq \lambda_{\text{hor}} \leq 60 \text{ km}$); bottom row: reconstructed T' signal of 'long' scales ($60 \text{ km} \leq \lambda_{\text{hor}} \leq 150 \text{ km}$).

Bibliography

- Alexander, M. J., Geller, M., McLandress, C., Polavarapu, S., Preusse, P., Sassi, F., Sato, K., Eckermann, S., Ern, M., Hertzog, A., Kawatani, Y., Pulido, M., Shaw, T. A., Sigmond, M., Vincent, R., and Watanabe, S. (2010). Recent developments in gravity-wave effects in climate models and the global distribution of gravity-wave momentum flux from observations and models. *Quarterly Journal of the Royal Meteorological Society*, 136(650):1103–1124.
- Bacmeister, J., Schoeberl, M. R., Lait, L., Newman, P., and Gary, B. (1990). Small-Scale Waves Encountered During AASE. *Geophysical Research Letters*, 17:349–352.
- Bacmeister, J. T., Eckermann, S., Newman, P., Lait, L., Chan, K., Loewenstein, M., Profit, M., and Gary, B. (1996). Stratospheric horizontal wavenumber spectra of winds, potential temperature, and atmospheric tracers observed by high-altitude aircraft. *Journal of Geophysical Research*, 101:9441–9470.
- Bacmeister, J. T., Eckermann, S. D., Tsias, A., Carslaw, K. S., and Peter, T. (1999). Mesoscale Temperature Fluctuations Induced by a Spectrum of Gravity Waves: A Comparison of Parameterizations and Their Impact on Stratospheric Microphysics. *Journal of the Atmospheric Sciences*, 56:1913–1924.
- Baldwin, M. P., Gray, L. J., Dunkerton, T. J., Hamilton, K., Haynes, P. H., Randel, W. J., Holton, J. R., Alexander, M. J., Hirota, I., Horinouchi, T., Jones, D. B. A., Kinnnersley, J. S., Marquardt, C., Sato, K., and Takahashi, M. (2001). The quasi-biennial oscillation. *Reviews of Geophysics*, 39(2):179–229.
- Birner, T. (2006). Fine-scale structure of the extratropical tropopause region. *Journal of Geophysical Research: Atmospheres*, 111(D4). D04104.
- Bramberger, M., Dörnbrack, A., Bossert, K., Ehard, B., Fritts, D. C., Kaifler, B., Mallaun, C., Orr, A., Pautet, P.-D., Rapp, M., Taylor, M. J., Vosper, S., Williams, B., and Witschas, B. (2017). Does strong tropospheric forcing cause large-amplitude mesospheric gravity waves? - a deepwave case study. *Journal of Geophysical Research: Atmospheres*. in press.
- Butchart, N. (2014). The Brewer-Dobson circulation. *Reviews of Geophysics*, 52(2):157–184.

- Chan, K., Pfister, L., Bui, T., Bowen, S., Dean-Day, J., Gary, B., Fahey, D., Kelly, K., Webster, C., and May, R. (1993). A Case Study of the Mountain Lee Wave Event of January 6, 1992. *Geophysical Research Letters*, 20:2551–2554.
- Cho, J., Newell, R., Bui, T., E.V. Browell and, M. F., Mahoney, M., G.L.Gregory, Sachse, G., S.A.Vay, Kucsera, T., and A.M.Thompson (1999). Observations of convective and dynamical instabilities in tropopause folds and their contribution to stratosphere-troposphere exchange. *Journal of Geophysical Research*, 104:21,549–21,568.
- Corti, T., Luo, B., de Reus, M., Brunner, D., Cairo, F., Mahoney, M., Martucci, G., Matthey, R., Mitev, V., dos Santos, F., Schiller, C., Shur, G., Sitnikov, N., Spelten, N., Vössing, H., Borrmann, S., and Peter, T. (2008). Unprecedented evidence for deep convection hydrating the tropical stratosphere. *Geophysical Research Letters*, 35(10):L10810.
- Daubechies, I. (1990). The wavelet transform, time-frequency localization and signal analysis. *IEEE Transactions on Information Theory*, 36(5):961–1005.
- Davis, C. A., Ahijevych, D. A., Haggerty, J. A., and Mahoney, M. J. (2014). Observations of Temperature in the Upper Troposphere and Lower Stratosphere of Tropical Weather Disturbances. *Journal of the Atmospheric Sciences*, 71(5):1593–1608.
- Dean-Day, J., Chan, K., Bowen, S., Bui, T., Gary, B., and Mahoney, M. (1998). Dynamics of Rocky Mountain lee waves observed during SUCCESS. *Geophysical Research Letters*, 25:1351–1354.
- Denning, R. F., Guidero, S. L., Parks, G. S., and Gary, B. L. (1989). Instrument Description of the Airborne Microwave Temperature Profiler. *Journal of Geophysical Research*, 94(D14):16,757–16,765.
- Dörnbrack, A., Birner, T., Fix, A., Flentje, H., Meister, A., Schmid, H., Browell, E. V., and Mahoney, M. J. (2002). Evidence for inertia gravity waves forming polar stratospheric clouds over Scandinavia. *Journal of Geophysical Research*, 107:8287.
- Dunkerton, T. (1978). On the Mean Meridional Mass Motions of the Stratosphere and Mesosphere. *Journal of the Atmospheric Sciences*, 35(12):2325–2333.
- Durrán, D. (2015). MOUNTAIN METEOROLOGY - lee waves and mountain waves. In North, G. R., Pyle, J., and Zhang, F., editors, *Encyclopedia of Atmospheric Sciences (Second Edition)*, pages 95 – 102. Academic Press, Oxford, second edition.
- Eckermann, S., Dörnbrack, A., Flentje, H., Vosper, S. B., Mahoney, M. J., Bui, T. P., and Carslaw, K. S. (2006). Mountain Wave-Induced Polar Stratospheric Cloud Forecasts for Aircraft Science Flights during SOLVE/THESEO 2000. *Weather and Forecasting*, 21:42–68.
- Eckermann, S. D. and Preusse, P. (1999). Global Measurements of Stratospheric Mountain Waves from Space. *Science*, 286(5444):1534–1537.

- Ehard, B., Kaifler, B., Dörnbrack, A., Preusse, P., Eckermann, S. D., Bramberger, M., Gisinger, S., Kaifler, N., Liley, B., Wagner, J., and Rapp, M. (2017). Horizontal propagation of large-amplitude mountain waves into the polar night jet. *Journal of Geophysical Research: Atmospheres*, 122(3):1423–1436.
- Eliassen, A. and Palm, E. (1960). On the transfer of energy in stationary mountain waves. *Geofysiske Publikasjoner*, 22(3):1–23.
- Ern, M., Ploeger, F., Preusse, P., Gille, J. C., Gray, L. J., Kalisch, S., Mlynczak, M. G., Russell, J. M., and Riese, M. (2014). Interaction of gravity waves with the QBO: A satellite perspective. *Journal of Geophysical Research: Atmospheres*, 119(5):2329–2355.
- Ern, M., Preusse, P., Alexander, M. J., and Warner, C. D. (2004). Absolute values of gravity wave momentum flux derived from satellite data. *Journal of Geophysical Research: Atmospheres*, 109(D20). D20103.
- Ern, M., Trinh, Q. T., Kaufmann, M., Krisch, I., Preusse, P., Ungermann, J., Zhu, Y., Gille, J. C., Mlynczak, M. G., Russell III, J. M., Schwartz, M. J., and Riese, M. (2016). Satellite observations of middle atmosphere gravity wave absolute momentum flux and of its vertical gradient during recent stratospheric warmings. *Atmospheric Chemistry and Physics*, 16(15):9983–10019.
- Fritts, D. C. and Alexander, M. J. (2003). Gravity wave dynamics and effects in the middle atmosphere. *Reviews of Geophysics*, 41(1). 1003.
- Fritts, D. C., Smith, R. B., Taylor, M. J., Doyle, J. D., Eckermann, S. D., Dörnbrack, A., Rapp, M., Williams, B. P., Pautet, P.-D., Bossert, K., Criddle, N. R., Reynolds, C. A., Reinecke, P. A., Uddstrom, M., Revell, M. J., Turner, R., Kaifler, B., Wagner, J. S., Mixa, T., Kruse, C. G., Nugent, A. D., Watson, C. D., Gisinger, S., Smith, S. M., Lieberman, R. S., Laughman, B., Moore, J. J., Brown, W. O., Haggerty, J. A., Rockwell, A., Stossmeister, G. J., Williams, S. F., Hernandez, G., Murphy, D. J., Klekociuk, A. R., Reid, I. M., and Ma, J. (2016). The Deep Propagating Gravity Wave Experiment (DEEPWAVE): An Airborne and Ground-Based Exploration of Gravity Wave Propagation and Effects from Their Sources throughout the Lower and Middle Atmosphere. *Bulletin of the American Meteorological Society*, 97(3):425–453.
- Gamblin, B., Toon, O., Tolbert, M., Kondo, Y., Takegawa, N., Irie, H., Koike, M., Balenthin, J., Hunton, D., Miller, T., Viggiano, A., Anderson, B., Avery, M., Sachse, G., Podolske, J., Guenther, K., Sorenson, C., and Mahoney, M. (2006). Nitric acid condensation on ice: 1. Non-HNO₃ constituent of NO_y condensing cirrus particles on upper tropospheric. *Journal of Geophysical Research*, 111:D21203.
- Gary, B. (2006). Mesoscale temperature fluctuations in the stratosphere. *Atmospheric Chemistry and Physics*, 6:4577–4589.

- Gary, B. (2008). Mesoscale temperature fluctuations in the Southern Hemisphere stratosphere. *Atmospheric Chemistry and Physics*, 8:4677–4681.
- Gary, B. L. (1989). Observational Results Using the Microwave Temperature Profiler During the Airborne Antarctic Ozone Experiment. *Journal of Geophysical Research*, 94(D9):11,223–11,231.
- Geller, M. A., Alexander, M. J., Love, P. T., Bacmeister, J., Ern, M., Hertzog, A., Manzini, E., Preusse, P., Sato, K., Scaife, A. A., and Zhou, T. (2013). A Comparison between Gravity Wave Momentum Fluxes in Observations and Climate Models. *Journal of Climate*, 26(17):6383–6405.
- Gisinger, S., Dörnbrack, A., Matthias, V., Doyle, J. D., Eckermann, S. D., Ehard, B., Hoffmann, L., Kaifler, B., Kruse, C. G., and Rapp, M. (2017). Atmospheric conditions during the deep propagating gravity wave experiment (deepwave). *Monthly Weather Review*, 145(10):4249–4275.
- Haggerty, J., Schick, K., Mahoney, M. J., and Lim, B. (2014). The NCAR Microwave Temperature Profiler: Data applications from recent deployments. In *2014 13th Specialist Meeting on Microwave Radiometry and Remote Sensing of the Environment (MicroRad)*, pages 133–135.
- Hartmann, D., Chan, K., Gary, B., Schoeberl, M., Newman, P., Martin, R., Lowenstein, M., Podolske, J., and Strahan, S. (1989). Potential Vorticity and Mixing in the South Polar Vortex During Spring. *Journal of Geophysical Research*, 94(D9):11,223–11,231.
- Heller, R., Voigt, C., Beaton, S., Dörnbrack, A., Kaufmann, S., Schlager, H., Wagner, J., Young, K., and Rapp, M. (2017). Mountain waves modulate the water vapor distribution in the utls. *Atmospheric Chemistry and Physics Discussions*, 2017:1–32.
- Hoffmann, L., Grimsdell, A. W., and Alexander, M. J. (2016). Stratospheric gravity waves at Southern Hemisphere orographic hotspots: 2003–2014 AIRS/Aqua observations. *Atmospheric Chemistry and Physics*, 16(14):9381–9397.
- Hoffmann, L., Xue, X., and Alexander, M. J. (2013). A global view of stratospheric gravity wave hotspots located with Atmospheric Infrared Sounder observations. *Journal of Geophysical Research: Atmospheres*, 118(2):416–434.
- Holton, J., Haynes, P., McIntyre, M., Douglas, A., Road, R., and Pfister, L. (1995). Stratosphere-troposphere exchange. *Reviews of Geophysics*, 33:403–439.
- Holton, J. R. (1982). The Role of Gravity Wave Induced Drag and Diffusion in the Momentum Budget of the Mesosphere. *Journal of Atmospheric Sciences*, 39.
- Holton, J. R. (1983). The Influence of Gravity Wave Breaking on the General Circulation of the Middle Atmosphere. *Journal of Atmospheric Sciences*, 42(6).

- Jensen, E., Pfister, L., Bui, T.-P., Lawson, P., and Baumgardner, D. (2010). Ice nucleation and cloud microphysical properties in tropical tropopause layer cirrus. *Atmospheric Chemistry and Physics*, 10(3):1369–1384.
- Jones, E., Oliphant, T., Peterson, P., et al. (2001). SciPy: Open source scientific tools for Python. [Online; accessed 16-Oct-2014].
- Kaifler, B., Kaifler, N., Ehard, B., Dörnbrack, A., Rapp, M., and Fritts, D. C. (2015). Influences of source conditions on mountain wave penetration into the stratosphere and mesosphere. *Geophysical Research Letters*, 42(21):9488–9494.
- Kaifler, N., Kaifler, B., Ehard, B., Gisinger, S., Dörnbrack, A., Rapp, M., Kivi, R., Kozlovsky, A., Lester, M., and Liley, B. (2017). Observational indications of downward-propagating gravity waves in middle atmosphere lidar data. *Journal of Atmospheric and Solar-Terrestrial Physics*.
- Karbou, F., Aires, F., Prigent, C., and Eymard, L. (2005). Potential of advanced microwave sounding unit-a (amsu-a) and amsu-b measurements for atmospheric temperature and humidity profiling over land. *Journal of Geophysical Research: Atmospheres*, 110(D7):D07109.
- Krisch, I., Preusse, P., Ungermann, J., Dörnbrack, A., Eckermann, S. D., Ern, M., Friedl-Vallon, F., Kaufmann, M., Oelhaf, H., Rapp, M., Strube, C., and Riese, M. (2017). First tomographic observations of gravity waves by the infrared limb imager GLORIA. *Atmospheric Chemistry and Physics Discussions*, 2017:1–21.
- Kruse, C. G. and Smith, R. B. (2015). Gravity Wave Diagnostics and Characteristics in Mesoscale Fields. *Journal of the Atmospheric Sciences*, 72(11):4372–4392.
- Kruse, C. G., Smith, R. B., and Eckermann, S. D. (2016). The Midlatitude Lower-Stratospheric Mountain Wave “Valve Layer”. *Journal of the Atmospheric Sciences*, 73(12):5081–5100.
- Leutbecher, M. and Martin, H. V. (2000). The Propagation of Mountain Waves into the Stratosphere: Quantitative Evaluation of Three-Dimensional Simulations. *Journal of the Atmospheric Sciences*, 57:3090–3108.
- Liebe, H., Rosenkranz, P., and Hufford, G. (1992). Atmospheric 60-GHz oxygen spectrum: New laboratory measurements and line parameters. *Journal of Quantitative Spectroscopy and Radiative Transfer*, 48(5):629 – 643.
- Lim, B., Mahoney, M., Haggerty, J., and Denning, R. (2013). The Microwave Temperature Profiler performance in recent airborne campaigns. In *2013 IEEE International Geoscience and Remote Sensing Symposium - IGARSS*, pages 3363–3366.
- Lindzen, R. S. (1981). Turbulence and stress owing to gravity wave and tidal breakdown. *Journal of Geophysical Research: Oceans*, 86(C10):9707–9714.

- Livesey, N. J., Snyder, W. V., Read, W. G., and Wagner, P. A. (2006). Retrieval algorithms for the EOS Microwave Limb Sounder (MLS). *Journal of Geoscience and Remote Sensing*, 44:1144–1155.
- Mahoney, M. (2004). Where is the Tropopause? In *SOFIA upper Deck Science Opportunities Workshop*. NASA ames research center.
- Mahoney, M. and Denning, R. (2009). A State-of-the-Art Airborne Microwave Temperature Profiler (MTP) . In *33rd International Symposium on the Remote Sensing of the Environment*.
- Mahoney, M. and Gary, B. (2003). DC-8 MTP Calibration for SOLVE-2. In *SOLVE2/Vintersol Science Team Meeting*.
- Marcy, T., Popp, P., Gao, R., Fahey, D., Ray, E., Richard, E., Thompson, T., Atlas, E., Loewenstein, M., Wofsy, S., Park, S., Weinstock, E., Swartz, W., and Mahoney, M. (2007). Measurements of trace gases in the tropical tropopause layer. *Atmospheric Environment*, 41(34):7253 – 7261.
- Melsheimer, C., Verdes, C., Buehler, S. A., Emde, C., Eriksson, P., Feist, D. G., Ichizawa, S., John, V. O., Kasai, Y., Kopp, G., Koulev, N., Kuhn, T., Lemke, O., Ochiai, S., Schreier, F., Sreerekha, T. R., Suzuki, M., Takahashi, C., Tsujimaru, S., and Urban, J. (2005). Intercomparison of general purpose clear sky atmospheric radiative transfer models for the millimeter/submillimeter spectral range. *Radio Science*, 40(1). RS1007.
- Murphy, D. and Gary, B. (1995). Mesoscale Temperature Fluctuations and Polar Stratospheric Clouds. *Journal of Atmospheric Sciences*, 52:1753–1760.
- Nappo, C. (2013). *An Introduction to Atmospheric Gravity Waves*. International geophysics series. Academic Press/Elsevier.
- Nielsen-Gammon, J., Powell, C., Mahoney, M., Angevine, W., Senff, C., White, A., Berkowitz, C., Doran, C., and Knupp, K. (2008). Multisensor Estimation of Mixing Heights over a Coastal City. *Journal of Applied Meteorology and Climatology*, 47:27–43.
- Pfister, L., Chan, K., Bui, T., Bowen, S., Legg, M., Gary, B., Kelly, K., Proffitt, M., and Starr, W. (1993). Gravity Waves Generated by a Tropical Cyclone During the STEP Tropical Field Program: A Case Study. *Journal of Geophysical Research*, 98:8611–8638.
- Plougonven, R. and Zhang, F. (2014). Internal gravity waves from atmospheric jets and fronts. *Reviews of Geophysics*, 52(1):33–76.
- Popp, P., Marcy, T., Jensen, E., Karcher, B., Fahey, D., Gao, R., Thompson, T., Rosenlof, K., Richard, E., Herman, R., Weinstock, E., Smith, J., May, R., Wilson, J., Heymsfield, A., Mahoney, M., and Thompson, A. (2006). The observation of nitric-acid containing particles in the tropical lower stratosphere. *Atmospheric Chemistry and Physics*, 6:601–611.

- Portele, T., Dörnbrack, A., Wagner, J., and Rapp, M. (2017). Mountain Wave Propagation under Transient Tropospheric Forcing - A DEEPWAVE Case Study. Submitted, under review.
- Rodgers, C. D. (2000). *Inverse methods for atmospheric sounding theory and practice*. World Scientific, Singapore River Edge, N.J.
- Rothman, L., Rinsland, C., Goldman, A., Massie, S., Edwards, D., Flaud, J.-M., Perrin, A., Camy-Peyret, C., Dana, V., Mandin, J.-Y., Schroeder, J., McCann, A., Gamache, R., Wattson, R., Yoshino, K., Chance, K., Jucks, K., Brown, L., Nentchinov, V., and Varanas, P. (1998). THE HITRAN MOLECULAR SPECTROSCOPIC DATABASE AND HAWKS (HITRAN ATMOSPHERIC WORKSTATION): 1996 EDITION. *J. Quant. Spectrosc. Rad. Transfer*, 60(5):665–710.
- Sato, K., Watanabe, S., Kawatani, Y., Tomikawa, Y., Miyazaki, K., and Takahashi, M. (2009). On the origins of mesospheric gravity waves. *Geophysical Research Letters*, 36(19). L19801.
- Schreier, F., García, S. G., Hedelt, P., Hess, M., Mendrok, J., Vasquez, M., and Xu, J. (2014). {GARLIC} — a general purpose atmospheric radiative transfer line-by-line infrared-microwave code: Implementation and evaluation. *Journal of Quantitative Spectroscopy and Radiative Transfer*, 137:29 – 50.
- Schreier, F. and Gimeno García, S. (2013). Py4CATS – Python tools for line-by-line modelling of atmospheric radiative transfer. In Cahalan, R. F. and Fischer, J., editors, *Radiation Processes in the Atmosphere and Ocean (IRS2012): Proceedings of the International Radiation Symposium (IRC/IAMAS)*, volume 1531 of *AIP Conference Proceedings*, pages 123–126. American Institute of Physics.
- Schumann, U., Kiemle, C., Schlager, H., Weigel, R., Borrmann, S., D’Amato, F., Krämer, M., Matthey, R., Protat, A., Voigt, C., and Volk, C. (2017). Long-lived contrails and convective cirrus above the tropical tropopause. *Atmospheric Chemistry and Physics*, 17(3):2311–2346.
- Schwarz, J., Spackman, J., Fahey, D., Gao, R., Lohmann, U., Stier, P., Watts, L., Thomson, D., Lack, D., Pfister, L., Mahoney, M., Baumgardner, D., Wilson, J., and Reeves, J. (2008). Coatings and their enhancement of black carbon light absorption in the tropical atmosphere. *Journal of Geophysical Research: Atmospheres*, 113(D3):D03203.
- Siskind, D. E. (2014). Simulations of the winter stratopause and summer mesopause at varying spatial resolutions. *Journal of Geophysical Research: Atmospheres*, 119(2):461–470.
- Sitnikova, V., Sitnikov, N., Ulanovskii, A., Shur, G., Lukyanov, A., and F. Ravegnani, M. M. (2009). Estimation of the Tropospheric Air Ratio near the Thermal Tropopause Using the Aircraft Measurements. *Russian Meteorology and Hydrology*, 34(8):510–514.

- Skamarock, W. C., Dudhia, J. B. K. J., Gill, D. O., Barker, D. M., Duda, M. G., Huang, X.-Y., Wang, W., and Powers, J. G. (2008). A description of the advanced research WRF version 3. NCAR/TN-475+STR.
- Skamarock, W. C. and Klemp, J. B. (2008). A time-split nonhydrostatic atmospheric model for weather research and forecasting applications. *Journal of Computational Physics*, 227:3465 – 3485.
- Smith, R. B. and Kruse, C. G. (2017). Broad-Spectrum Mountain Waves. *Journal of the Atmospheric Sciences*, 74(5):1381–1402.
- Smith, R. B., Nugent, A. D., Kruse, C. G., Fritts, D. C., Doyle, J. D., Eckermann, S. D., Taylor, M. J., Dörnbrack, A., Uddstrom, M., Cooper, W., Romashkin, P., Jensen, J., and Beaton, S. (2016). Stratospheric Gravity Wave Fluxes and Scales during DEEPWAVE . *Journal of the Atmospheric Sciences*, 73(7):2851–2869.
- Smith, R. B., Woods, B. K., Jensen, J., Cooper, W. A., Doyle, J. D., Jiang, Q., and Grubišić, V. (2008). Mountain Waves Entering the Stratosphere. *Journal of the Atmospheric Sciences*, 65(8):2543–2562.
- Spinei, E., Cede, A., Herman, J., Mount, G., Eloranta, E., Morley, B., Baidar, S., Dix, B., Ortega, I., Koenig, T., and Volkamer, R. (2015). Ground-based direct-sun DOAS and airborne MAX-DOAS measurements of the collision-induced oxygen complex, O₂O₂, absorption with significant pressure and temperature differences. *Atmospheric Measurement Techniques*, 8(2):793–809.
- Stähli, O., Murk, A., Kämpfer, N., Mätzler, C., and Eriksson, P. (2013). Microwave radiometer to retrieve temperature profiles from the surface to the stratopause. *Atmospheric Measurement Techniques*, 6(9):2477–2494.
- Strand, O. N. and Westwater, E. R. (1968). Statistical estimation of the numerical solution of a fredholm integral equation of the first kind. *Journal of the ACM*, 15(1):100–114.
- Swenson, G. R., Alexander, M. J., and Haque, R. (2000). Dispersion imposed limits on atmospheric gravity waves in the mesosphere: Observations from OH airglow. *Geophysical Research Letters*, 27(6):875–878.
- Szajkowski, M. (2016). Development of pre- and post-processing tools for the analysis of microwave temperature profiling observations.
- Tabazadeh, A., Toon, O., Gary, B., Bacmeister, J., and Schoeberl, M. (1996). Observational constraints on the formation of type ia polar stratospheric clouds. *Geophysical Research Letters*, 23(16):2109–2112.
- Thornton, B. F., Toohey, D. W., Tuck, A. F., Elkins, J. W., Kelly, K. K., Hovde, S. J., Richard, E. C., Rosenlof, K. H., Thompson, T. L., Mahoney, M. J., and Wilson, J. C.

- (2007). Chlorine activation near the midlatitude tropopause. *Journal of Geophysical Research: Atmospheres*, 112(D18):D18306.
- Tikhonov, A. (1963). On the solution of incorrectly stated problems and a method of regularization. *Dokl Acad Nauk SSSR*, 151:501–504.
- Torrence, C. and Compo, G. P. (1998). A Practical Guide to Wavelet Analysis. *Bulletin of the American Meteorological Society*, 79(1):61–78.
- Tuck, A., Baumgardner, D., Chan, K., Dye, J., Elkins, J., Hovde, S., Kelly, K., Loewenstein, M., Margitan, J., May, R., Podolske, J., Proffitt, M., Rosenlof, K., Smith, W., Webste, C., and Wilson, J. (1997). The Brewer-Dobson Circulation In the Light of High Altitude In Situ Aircraft Observations. *Quarterly Journal of the Royal Meteorological Society*, 123:1–69.
- Tuck, A., Hovde, S., Kelly, K., Mahoney, M., Proffitt, M., Richard, E., and Thompson, T. (2003). Exchange between the upper tropical troposphere and the lower stratosphere studied with aircraft observations. *Journal of Geophysical Research*, 108:4734.
- U. Schumann (ed.) (2012). *Atmospheric Physics, Research topics in Aerospace*. Springer-Verlag Berlin Heidelberg.
- Ulaby, F., Moore, R., and Fung, A. (1981). *Microwave remote sensing: active and passive. Volume I: microwave remote sensing fundamentals and radiometry*. Addison-Wesley; Remote Sensing Series 2.
- Ungermann, J., Blank, J., Dick, M., Ebersoldt, A., Friedl-Vallon, F., Giez, A., Guggenmoser, T., Höpfner, M., Jurkat, T., Kaufmann, M., Kaufmann, S., Kleinert, A., Krämer, M., Latzko, T., Oelhaf, H., Olchewski, F., Preusse, P., Rolf, C., Schillings, J., Suminska-Ebersoldt, O., Tan, V., Thomas, N., Voigt, C., Zahn, A., Zöger, M., and Riese, M. (2015). Level 2 processing for the imaging Fourier transform spectrometer GLORIA: derivation and validation of temperature and trace gas volume mixing ratios from calibrated dynamics mode spectra. *Atmospheric Measurement Techniques*, 8(6):2473–2489.
- Urbanek, B., Groß, S., Schäfler, A., and Wirth, M. (2017). Determining stages of cirrus evolution: a cloud classification scheme. *Atmospheric Measurement Techniques*, 10(5):1653–1664.
- Voigt, C., Schumann, U., Minikin, A., Abdelmonem, A., Afchine, A., Borrmann, S., Boettcher, M., Buchholz, B., Bugliaro, L., Costa, A., Curtius, J., Dollner, M., Dörnbrack, A., Dreiling, V., Ebert, V., Ehrlich, A., Fix, A., Forster, L., Frank, F., Fütterer, D., Giez, A., Graf, K., Groß, J.-U., Groß, S., Heimerl, K., Heinold, B., Hüneke, T., Järvinen, E., Jurkat, T., Kaufmann, S., Kenntner, M., Klingebiel, M., Klimach, T., Kohl, R., Krämer, M., Krisna, T. C., Luebke, A., Mayer, B., Mertes, S., Molleker, S., Petzold, A., Pfeilsticker, K., Port, M., Rapp, M., Reutter, P., Rolf, C., Rose, D., Sauer, D., Schäfler, A., Schlage, R., Schnaiter, M., Schneider, J., Spelten, N., Spichtinger, P., Stock, P., Walser,

- A., Weigel, R., Weinzierl, B., Wendisch, M., Werner, F., Wernli, H., Wirth, M., Zahn, A., Ziereis, H., and Zöger, M. (2017). ML-CIRRUS: The Airborne Experiment on Natural Cirrus and Contrail Cirrus with the High-Altitude Long-Range Research Aircraft HALO . *Bulletin of the American Meteorological Society*, 98(2):271–288.
- Wagner, J., Dörnbrack, A., Rapp, M., Gisinger, S., Ehard, B., Bramberger, M., Witschas, B., Chouza, F., Rahm, S., Mallaun, C., Baumgarten, G., and Hoor, P. (2017). Observed versus simulated mountain waves over Scandinavia – improvement of vertical winds, energy and momentum fluxes by enhanced model resolution? *Atmospheric Chemistry and Physics*, 17(6):4031–4052.
- Wang, L., Alexander, M., Bui, T., and Mahoney, M. (2006). Small-scale gravity waves in ER-2 MMS/MTP wind and temperature measurements during CRYSTAL-FACE. *Atmospheric Chemistry and Physics*, 6:1091–1104.
- Waters, J. (1976). Absorption and Emission by Atmospheric Gases. *Methods in Experimental Physics*, 12:142 – 176.
- Wendisch, M., Pöschl, U., Andreae, M. O., Machado, L. A. T., Albrecht, R., Schlager, H., Rosenfeld, D., Martin, S. T., Abdelmonem, A., Afchine, A., Araùjo, A. C., Artaxo, P., Aufmhoff, H., Barbosa, H. M. J., Borrmann, S., Braga, R., Buchholz, B., Cecchini, M. A., Costa, A., Curtius, J., Dollner, M., Dorf, M., Dreiling, V., Ebert, V., Ehrlich, A., Ewald, F., Fisch, G., Fix, A., Frank, F., Fütterer, D., Heckl, C., Heidelberg, F., Hüneke, T., Jäkel, E., Järvinen, E., Jurkat, T., Kanter, S., Kästner, U., Kenntner, M., Kesselmeier, J., Klimach, T., Knecht, M., Kohl, R., Kölling, T., Krämer, M., Krüger, M., Krisna, T. C., Lavric, J. V., Longo, K., Mahnke, C., Manzi, A. O., Mayer, B., Mertes, S., Minikin, A., Mollenker, S., Münch, S., Nillius, B., Pfeilsticker, K., Pöhlker, C., Roiger, A., Rose, D., Rosenow, D., Sauer, D., Schnaiter, M., Schneider, J., Schulz, C., de Souza, R. A. F., Spanu, A., Stock, P., Vila, D., Voigt, C., Walser, A., Walter, D., Weigel, R., Weinzierl, B., Werner, F., Yamasoe, M. A., Ziereis, H., Zinner, T., and Zöger, M. (2016). ACRIDICON-CHUVA Campaign: Studying Tropical Deep Convective Clouds and Precipitation over Amazonia Using the New German Research Aircraft HALO. *Bulletin of the American Meteorological Society*, 97(10):1885–1908.
- Witschas, B., Rahm, S., Dörnbrack, A., Wagner, J., and Rapp, M. (2017). Airborne Wind Lidar Measurements of Vertical and Horizontal Winds for the Investigation of Orographically Induced Gravity Waves. *Journal of Atmospheric and Oceanic Technology*, 34(6):1371–1386.
- Woodhouse, I. H. (2005). *Introduction to Microwave Remote Sensing*. CRC press.
- World Meteorological Organization (1957). Meteorology A Three-Dimensional Science: Second Session of the Commission for Aerology . *WMO Bulletin*, 4(4):134–138.

-
- Xu, J., Schreier, F., Doicu, A., and Trautmann, T. (2016). Assessment of Tikhonov-type regularization methods for solving atmospheric inverse problems. *Journal of Quantitative Spectroscopy and Radiative Transfer*, 184:274 – 286.
- Zhang, J. (2016). Estimation of atmospheric temperature using airborne microwave remote sensing.

Acronyms

AAOE	Airborne Antarctic Ozone Experiment
AASE II	Airborne Arctic Stratospheric Experiment
ACHWAS	<u>A</u> ltitude-resolved <u>ch</u> aracterisation of <u>w</u> aves in <u>a</u> tmospheric sounding
ACRIDICON	<u>A</u> erosol, <u>C</u> loud, Precipitation, and <u>R</u> adiation <u>I</u> nteraction and <u>D</u> ynamics of <u>C</u> ONvective Cloud Systems
AMSU-A	Advanced Microwave Sounding Unit-A
BT	brightness temperature
CAT	clear air turbulence
CIRA	COSPAR International Reference Atmosphere
COI	cone of influence
COSPAR	Committee on Space Research
DEEPWAVE	Deep Propagating Gravity Wave Experiment
DLR	German Aerospace Center, [Deutsches Zentrum für Luft- und Raumfahrt e.V.]
ECMWF	European Centre for Medium-Range Weather Forecasts
FWHM	full width half maximum value
GARLIC	Generic Atmospheric Radiation Line-by-line Infrared Code
GPS	Global Positioning System
GW	gravity wave
GWPED	gravity wave potential energy density per mass
HAIS	HIAPER Airborne Instrumentation Solicitation
HALO	High Altitude and Long Range Research Aircraft
HALO TS	HALO static temperature
HATPRO	<u>H</u> umidity <u>A</u> nd <u>T</u> emperature <u>P</u> ROfilers
HITRAN	<u>h</u> igh-resolution <u>t</u> ransmission molecular absorption database
IOP	intensive observation period
LIDAR	<u>L</u> ight <u>D</u> etection <u>A</u> nd <u>R</u> anging
LO	local oscillator frequency
ML CIRRUS	Mid-Latitude CIRRUS experiment

MSTF	mesoscale temperature fluctuation
MTP	Microwave Temperature Profiler
NASA	National Aeronautics and Space Administration
NASA-JPL	Jet Propulsion Laboratory
NCAR	National Center for Atmospheric Research
NCAR GV	NCAR Gulfstream-V
ND	noise diode
NSF	National Science Foundation
NZ	New Zealand
PLO	phase line orientation
PSC	polar stratospheric clouds
Py4CATS	<u>Python</u> scripts for <u>Computational</u> <u>AT</u> mospheric <u>S</u> pectroscopy
QBO	quasi-biennial oscillation
RADAR	<u>RA</u> dio <u>D</u> etection <u>A</u> nd <u>R</u> anging
RAOB	radio sonde observation
RC	retrieval coefficient
RF	research flight
RMS	root mean square
RT	radiative transfer
SI	South Island
STEP	Stratospheric-Tropospheric Exchange Project
TIL	tropopause inversion layer
T-REX	Terrain-Induced Rotor Experiment
TEMPERA	<u>Temperature</u> <u>R</u> adiometer
TIRAMISU	<u>Temperature</u> <u>I</u> nve <u>R</u> sion <u>A</u> lgorithm for <u>MI</u> crowave <u>So</u> unding
UM	unified model
UTC	Coordinated Universal Time
UTLS	upper troposphere and lower stratosphere
WF	weighting function
WFT	windowed Fourier transform
WRF	Weather Research and Forecasting

Danksagung

Mein Dank gilt meinem Doktorvater Prof. Dr. Markus Rapp, der durch offene Ohren und guten Rat meine Arbeit unterstützt hat. Ich habe es genossen, im Zuge von wissenschaftlichen Kampagnen und Konferenzen die Welt erkunden zu dürfen und die Freiheit zu haben mit ‘meinem’ Messgerät ‘mein Ding’ machen zu dürfen.

Gleiches gilt für meine wissenschaftlichen Betreuer Dr. Andreas Dörnbrack und Dr. Andreas Fix. Sie haben mich nicht nur rein wissenschaftlich mit offenen Ohren und tatkräftiger Unterstützung auf Kampagnen und daheim begleitet. Den vielen Korrekturlesern und Korrekturleserinnen sei hiermit noch einmal herzlich für ihre Zeit und Unterstützung während der End-Phase meiner Arbeit gedankt. Insbesondere danke ich hier Dr. Bernd Kaifler. Weiterhin gilt mein Dank den vielen lieben Kollegen des PA, die sowohl während, als auch außerhalb der Arbeit mein Leben bereichern. Hier sind natürlich besonders die Büro-Kolleginnen (‘Razupaltuff!’), die gesamte Abteilung 4 und große Teile der Abteilungen 2 und 6 zu nennen, die Kaffeepausen, Mittagessen und Abendgestaltung einen Sinn gegeben haben. Besonders erwähnen möchte ich auch Dr. Manfred Birk, der mich während der ganzen Zeit unterstützt hat - durch wertvolle Diskussionen über die Mess-Technik, den Retrieval-Algorithmus, oder andere wichtige Fragen, aber auch ganz praktisch bei der Beschaffung von Stickstoff für die Kalibration.

Des Weiteren gibt es viele Menschen, denen ich an dieser Stelle danken möchte, weil sie durch planerische, handwerkliche und wissenschaftliche Fertigkeiten meine Arbeit erleichtert haben. Daher ein großer Dank an die Kollegen des Flugbetriebs und die Werkstatt der LIDAR Abteilung. Für die Entwicklung des Retrieval codes TIRAMISU und die Zusammenarbeit während dessen Entwicklung und darüber hinaus, möchte ich mich bei Prof. Dr. Trautmann, Dr. Franz Schreier und Dr. Jian Xu bedanken, bei denen ich alles fragen durfte und immer Antworten bekam. Gleiches gilt für Harald Czekala von RPG.

Ebenso gilt mein Dank Dr. Peichl und seiner Gruppe, im Besonderen Matthias Jirousek, am DLR-HR für Unterstützung und Input zu Fragen zur Messtechnik, und die Ausführung der Messungen, die für die Entwicklung meines Retrieval inputs unverzichtbar waren.

Julie Haggerty war maßgeblich an meinem Verständnis des Messgerätes und des Retrieval codes beteiligt, und war mir während der ganzen Zeit eine wertvolle Unterstützung und Diskussionspartnerin. Ihre Mess-Daten sind Grundlage meines letzten Kapitels, das zeigt, dass meine Mühen sich gelohnt haben.

Kein Projekt ist erfolgreich, wenn es nicht Menschen gäbe, die einen durch moralische Tiefs begleiten und Erfolge mit feiern. Für ihre Geduld, frundschaftlichen Rat, Ablenkungsmanöver zur rechten Zeit, das ‘Betreute Promovieren’ und jede Menge Verständnis möchte ich meinem Partner, meiner Familie und meinen Freunden herzlich danken. Im besonderen gilt das für die Gilchinger Kantorei und die Handball-Damen des TSV Gilching, die meine Fehl-Zeiten tolerierten und mich in ihren Reihen so herzlich willkommen geheißen haben, dass mir in den Jahren meiner Promotion eine richtige neue Heimat entstanden ist.

